Accretion Processes in Magnetic Cataclysmic Variables - a detailed study of UZ Fornacis

Zwidofhelangani Ndamulelo Khangale

10 June 2022

A thesis presented in full fulfillment of the degree of Doctor of Philosophy in Astronomy at the University of Cape Town

Supervisor: Prof. Patrick Alan Woudt and
Co-supervisor: Dr Stephen Brian Potter*

*South African Astronomical Observatory and visiting Professor at the University of Johannesburg

To my dearly-departed sister Sukumani Asnath Khangale Mutengwe and my grandmother Vho-Nyatshisevhe Mbedzi Tshilamatanda.

Abstract

This thesis presents a multi-wavelength exploration of the emissions from magnetic cataclysmic variable (mCV) stars with specific focus on the eclipsing AM Her system, UZ Fornacis (hereafter UZ For). The main objective of this thesis is to investigate the underlying emission mechanisms as well as the accretion dynamics in this system with the intention of increasing our understanding of this class of objects as a whole. The presence of a strong magnetic field in UZ For makes it an interesting object in terms of how the magnetic field dominates the accretion dynamics and its influence on the emission processes. The eclipsing characteristics of this system, with a clearly defined ingress and egress of the main accretion spot, can be exploited to gain further insights through precise eclipse timings.

The first part of this thesis presents 33 new mid-eclipse times spanning eight years of observations on UZ For. The new observations are used to test the two-planet model previously proposed to explain the periodic variations in the eclipse times of UZ For measured over the past ∼35 years. The results show that the proposed model does indeed follow the general trend of the new eclipse times. However, there are significant departures. In order to accommodate the new eclipse times, the two-planet model requires that one or both of the planets have highly eccentric orbits, i.e. $e \geq 0.4$. Such multiple planet orbits are considered to be unstable. Whilst our new observations are consistent with two cyclic variations as previously predicted, significant residuals remain. This study explores the possibility that either additional cyclic terms, possibly associated with more planets, or other mechanisms, such as the Applegate mechanism are contributing to the eclipse time variations.

The second part of this thesis presents phase-resolved spectroscopy of UZ For which allowed us to do a detailed Doppler tomography study of this target. The averaged blue spectrum is dominated by single- and/or double-peaked emission from HeII 4686 Å and the Balmer lines, as well as weak emission from HeI lines and the CIII/NIII blend at 4650Å. The averaged red spectrum shows strong emission from CaII lines at 8498 Å and 8542 Å and possibly weak emission from the NaI doublet at 8183 Å and 8194 Å. The strength of HeII 4686 Å line is comparable to that of Hβ line and this is typical for AM Her systems in a high state of accretion. The ratio of Hγ/Hβ $\simeq$ 1 implying that these emission lines were formed in an optically thick region, that is, a region of high optical depth in the lines. Doppler tomography of the strongest features in the blue, HeII 4686Å and the Balmer lines (e.g. Hβ line), using both the standard and inside-out maps, revealed the presence of three

emission regions: 1) the irradiated face of the secondary star, 2) the ballistic stream and the threading region, and 3) the magnetically confined accretion stream. The Doppler maps of emission lines in the red spectrum show the presence of emission from the irradiated face of the secondary star as well as emission from various parts of the ballistic and magnetically confined accretion stream. Also presented are the respective modulation Doppler maps of each line. These show that both the ballistic and magnetically confined accretion stream are modulated as well as the irradiated face of the secondary star.

In addition to the above, the first simultaneous optical and MeerKAT radio observations of the eclipsing AM Her system UZ For are also presented. The optical data include SALT circular spectropolarimetry taken around the eclipse and SHOC and MeerLICHT photometry. The total intensity spectrum shows broad emission features with the continuum that rises in the blue. The percentage circularly polarized spectra show that UZ For is negatively polarized (up to $\sim -8\%$) in the blue and decreasing gradually towards the red. The circularly polarized spectrum shows the presence of three cyclotron emission features at $\sim$4500 Å, 6000 Å and 7700 Å, corresponding to harmonic numbers 4, 3 and 2, respectively. These features are dominant before the eclipse and disappears after the eclipse. The harmonics are consistent with the magnetic field strength of $\sim$57 MG seen at a viewing angle of 70°. To aid with the interpretation of the circular spectropolarimetry, simultaneous circular and linear photopolarimetric observations of UZ For obtained with the HIPPO instrument several weeks leading to the SALT observations were also analysed. The results show that UZ For is $\sim -5\%$ circularly and 5% linearly polarized before the eclipse. A burst of linear polarization is seen just after the eclipse reaching $\sim$10%. After the eclipse, negative circular polarization reaching $\sim -5\%$ is observed. Both linear and circular polarization are consistent with zero after phase 1.1. The MeerKAT radio observations show a faint source which has a peak flux density of 30.7 ± 5.4 μJy/beam at 1.28 GHz (L-band) at the position of UZ For. This marks the first detection of UZ For at L-band.

This study demonstrates that multi-wavelength observations are essential to understanding the various emission processes that are at work in mCVs. The results presented in this thesis shows that UZ For is one of the most interesting AM Her systems known to date. The circular spectropolarimetry results are consistent with those from literature and shows that the SALT telescope will be able to observe other systems like this for detailed analysis. Furthermore, the eclipse times of this system is consistent with the presence of two planets and makes UZ For the second AM Her system after HU Aqr shown to harbour planets and in which additional observations still support earlier conclusions. The radio detection of this system with MeerKAT opens a window to studying other low flux density AM Her systems at L-band radio frequencies in the southern sky.

Preface

This thesis investigates the emission mechanisms and accretion processes in magnetic cataclysmic variables − a subclass of cataclysmic variables − specifically the accretion dynamics in the highly magnetic system (i.e. the AM Her system or polar) UZ Fornacis. Generally, their relatively short periods (few hours) and the presence of strong magnetic fields make the AM Her systems an interesting group of CVs and allow us to study the influence of strong fields on both accretion dynamics and emission processes. Chapter 1 provides an overview of CVs including their formation and evolution as well as their classification and space density. The remainder of Chapter 1 focuses on the review of the AM Her systems including their fundamental properties such as: spectroscopic properties, polarimetric and photometric properties, X-ray properties and cyclotron emission properties.

Chapter 2 focuses on long-term photometric monitoring of the eclipsing polar, UZ For. The individual light curves of UZ For, spanning eight years and bringing the total coverage of over three decades, are presented and their mid-eclipse times measured. Detailed analysis of the mid-eclipse times of this target reveal that the ephemeris of UZ For deviate from linear and quadratic terms which can be explained by either the magnetic cycle activities of the secondary star − known as the Applegate mechanism − or the presence of circumbinary planets in orbit around the binary.

Spectroscopic observations obtained over two epochs and covering both blue (∼4050–5150 Å) and red (∼7550–8650 Å) wavelengths is presented in Chapter 3. From this, Doppler tomography of UZ For is undertaken using both the standard and inside-out projection. This is the first time Doppler maps of this system is presented in full. In addition, flux modulation using spectra covering half the phase is used to construct Doppler maps in order to investigate emission variation with the orbital phase.

Chapter 4 presents simultaneous optical and radio observations of UZ For obtained using four telescopes: SALT, SAAO 1.9-m, MeerLICHT and MeerKAT. Although this is the first time such observations were conducted in South Africa, we hope that this will be a norm for the future. For these observations, SALT was operated in its circular spectropolarimetry mode. The results show strong cyclotron emission before the eclipse with polarization reaching $\sim -8\%$. The cyclotron spectra of UZ For show three negative cyclotron humps which we modelled with the magnetic field strength of 57 MG. This system was detected in radio wavelengths using MeerKAT at a frequency of 1.28 GHz.

I summarise the results of my investigation of high-speed photometry, inside-out Doppler tomography and flux modulation mapping and simultaneous radio and optical observations of UZ For in Chapter 5. I conclude the chapter with an overview of some future work that will build on the work done for this thesis.

During the course of my PhD, I was afforded a chance to spend a week at the SAAO 1.9-m telescope in Sutherland to get some observing experience. The telescope was equipped with the HIPPO instrument. In addition to the above, I was involved in several publications which not only include the publications of my major results from this work, but also a couple of conference proceedings and at least one co-authored article.

List of refereed first-author articles:

1. "High-speed photometry of the eclipsing polar UZ Fornacis", Khangale, Z. N., Potter, S. B., Kotze, E. J., Woudt, P. A., and Breytenbach, H., **2019, A&A, 621, A31.**

2. "A spectroscopic, photometric, polarimetric, and radio study of the eclipsing polar UZ Fornacis: the first simultaneous SALT and MeerKAT observations", Khangale Z. N., Potter S. B., Woudt P. A., Buckley D. A. H., Semena A. N., Kotze E. J., Groenewald D. N., Hewitt D. M., Pretorius M. L., Fender R. P., Groot P., Bloemen S., Klein-Wolt M., Körding E., Le Poole R., McBride V. A., Townsend L., Paterson K., Pieterse D. L. A., and Vreeswijk P., **2020, MNRAS, 492, 4298.**

3. "A spectroscopic analysis of the eclipsing nova-like EC 21178-5417 – discovery of spiral density structures", Khangale Z. N., Woudt P. A., Potter S. B., Warner B., Kilkenny D., and van der Heyden K., **2020, MNRAS, 495, 637.**

List of conference proceedings:

1. "Phase-resolved Spectroscopy and Photometry of the Eclipsing Polar UZ Fornacis", Khangale Z. N., Potter S. B., and Woudt P. A., **2019, IAU Symposium, 339, 314–317.**

2. "Multi-wavelength study of the eclipsing polar UZ Fornacis", Khangale Z. N., Potter S. B., and Woudt P. A., **2021, Proceeding of Science, in The Golden Age of Cataclysmic Variables and Related Objects V. 2–7 September 2019. Palermo. p. 19.**

List of co-authored articles:

1. "Analysis of spiral structure in the accretion disc of the nova-like cataclysmic variable EC21178-5417" Ruiz-Carmona R., Khangale Z. N., Woudt P. A. and Groot P. J., **2020, MNRAS, 491, 344.**

In addition to academic duties, I have also served as an Astronomy Student Departmental Representative in 2018 followed by a year-long service in the Faculty of Science as a General Secretary of the Science Postgraduate Students' Council in 2019 – both roles at the University of Cape Town (UCT). I have also helped coordinate the National Astrophysics and Space Science Programme (NASSP) winter school, a role which include planning, recruitment and day-to-day operations of the school as well as mentoring students thereafter.

Acknowledgements

Firstly, I would like to thank my wonderful two supervisors, **Dr Stephen Brian Potter** and **Prof. Patrick Alan Woudt**, not only for giving me the opportunity to conduct this project but for motivating, supporting and guiding me throughout my PhD. Without them, this PhD would have not been possible. Thank you for believing in me, for your patience, for your kindness, and for providing invaluable guidance throughout my PhD studies. Apart from my supervisors, I wish to extend my gratitude to Dr Enrico Kotze, Dr Danièl Groenewald and Dr David Buckley for their support, guidance and providing the much needed feedback on my writing when I was preparing manuscripts for publication. I would like to acknowledge all my collaborators; with special mention to Hannes Breytenbach, Dante Hewitt, Dr Lee Townsend and Dr Andrey Semena, whose data reduction expertise contributed greatly in further improving the quality of my work and therefore contributed to the success of this PhD study. I would also like to acknowledge the Southern African Large Telescope (SALT) team under the leadership of Dr Encarni Romero-Colmenero and the South African Radio Astronomy Observatory (SARAO) team under the leadership of Dr Fernando Camilo and the MeerLICHT team under the leadership of Prof. Paul Groot, whose simultaneous observations form the cornerstone of this thesis.

I would like to thank the former and current head of department of astronomy at the University of Cape Town (UCT), **Emiritus Prof. Renée C. Kraan-Korteweg** and **Prof. Patrick Alan Woudt**, and the director at South African Astronomical Observatory (SAAO) **Prof. Petri Väisänen**, not only for welcoming me into their respective institutions but for providing the with the much needed office space and equipment, etc., so I could focus on my research. A special thank you goes to my mentors: **Prof. Saalih Allie**, **Prof. Thebe Medupe** and Dr Rudi Kuhn, for always lending me their ears in times of hardship and supporting me during my PhD journey. I would also like to thank Dr Ramotholo Sefako, Dr Marissa Kotze, Prof. Patricia Whitelock, Associate Prof. Sarah Blyth, Dr Kurt van der Heyden, Emiritus Prof. Brian Warner, Dr Vanessa McBride and Dr Shazrene Mohamed, for sharing their academic-life experiences as well as insightful suggestions with me on how to succeed in astronomy and also encouraging me to work smart in order to get something done. I won't forget to express the gratitude to the rest of the astronomers at both the Astronomy Department at UCT and the SAAO, for sharing their experiences with me as well as encouraging me to go an extra mile in order to succeed.

I am forever grateful to my **family**, relatives and friends with special mention of my **mother**, my number one fan and uncle (**Mr Edward Nethonzhe**), my dearest sisters (**Fulufhelo**, Mashudu, Tuwani and Nakisani), my brothers: Nthabeliseni, Phumudzo, Matamela and Emmanuel, and my favourite niece Beauty. Their support, encouragement and motivation helped me to accomplish my personal goal of becoming a scientist and a better person. A special mention and thank you goes to my best friend, **Mpulukeng**, who stayed by my side and always encouraged me to hang on and push for a little longer.

I would like to extend my gratitude to the administrative staffs at both UCT: **Roslyn Daniels**, Rushana Fagodien, Nicky Walker, Nomphelo Lungisa and Carol Marsh; and SAAO: **Valencia Cloete**, Linda Tobin, Eugene Lakey, Glenda Snowball, Nazli Mohammed, Dalene Fischer, Siphosethu Claassen, and their colleagues (past and presents). Your endless support and guidance is hard to come by and I will cherish the friendship we shared throughout my life. Before I forget, I would like to thank my friends and/or present or past colleagues at both UCT and SAAO with special mention of the following people: Michael, Antoine, Orapeleng, Miriam, Blaise, Itumeleng, Elias, Bynish, Palesa, Nkateko, Sibusiso, **Dr Tshiamiso Makwela**, Reikatseone, Julia, Mponeng, Nazir, Mokhine, Kerry, Hope, Sim, Bellinda, Chaka, and other past and present NASSP colleagues, for all the stimulating discussions we shared over the years and for always encouraging each other from day one but most of all for sharing this journey with me. I would like to give a special thanks to the library staffs at SAAO: Theresa and Zuthobeke, who provided me with the books and articles that were inaccessible to me. And without forgetting to mention Siphelo at UCT and the IT department at SAAO: Irwaan, Malibongwe, Lucian and Chantal, who always solved my computer problems. Last but not least, I would like to acknowledge the following people (past and present) from various departments at SAAO: Dr Christian Hettlage, Sivuyile, Thembela, Cedric, Buzani, Natalie Jones, Nhlavutelo, Andrew, Ayanda, who either taught me a lot about astronomy or made my life at SAAO easier.

I greatly acknowledge the financial assistance from the National Research Foundation (NRF) of South Africa, an agency of the Department of Science and Innovation (DSI), for funding my studies through an NRF Innovation Doctoral Scholarship. This work was carried out in part using facilities and data processing pipelines developed at the Inter-University Institute for Data Intensive Astronomy (IDIA). IDIA is a partnership of the Universities of Cape Town, of the Western Cape and of Pretoria. We thank the American Association of Variable Star Observers (AAVSO) observers who made the observations on which this project is based, the AAVSO staff who archived them and made them publicly available, and the developers of the Variable Star Visualisation and Analysis (VSTAR) package which we used for analysis.

Declaration of Authorship

The work presented in this thesis was done in collaboration with various people who provided some of the observations and in some cases contributed to the data reduction, analysis and discussion. This thesis contains research that has already been published in peer-reviewed journals:

1. Chapter 2 is based on the first paper entitled "High-speed photometry of the eclipsing polar UZ Fornacis" has been published in the Astronomy & Astrophysics Journal; **Z. N. Khangale**, S. B. Potter, E. J. Kotze, P. A. Woudt, and H. Breytenbach, **2019, A&A, 621, A31.**

   "We present 33 new mid-eclipse times spanning approximately eight years of the eclipsing polar UZ Fornacis. We have used our new observations to test the two-planet model previously proposed to explain the variations in its eclipse times measured over the past ∼35 years. We find that the proposed model does indeed follow the general trend of the new eclipse times, however, there are significant departures. In order to accommodate the new eclipse times, the two-planet model requires that one or both of the planets require highly eccentric orbits, that is, $e \geq 0.4$. Such multiple planet orbits are considered to be unstable. Whilst our new observations are consistent with two cyclic variations as previously predicted, significant residuals remain. We conclude that either additional cyclic terms, possibly associated with more planets, or other mechanisms, such as the Applegate mechanism are contributing to the eclipse time variations. Further long-term monitoring is required."
   For this Chapter 2, the observations and data reductions from the HIPPO instrument, mentioned in Section 2.3.1, were obtained by Dr Stephen B. Potter. Dr Stephen B. Potter, Dr Enrico J. Kotze* and Mr Hannes Breytenbach† did all the observations and reductions of the SHOC data listed in Section 2.3.2. It is worth mentioning that Mr Hannes Breytenbach's interest in this object was focused on quasi-periodic oscillations and not on eclipse timings. I measured all the 33 mid-eclipse times mentioned in this publication and did all the analysis, utilizing the least-square fit code written by Potter et al. (2011), and all the write-up of the paper with guidance from Dr S. B. Potter and Prof. P. A. Woudt. The other co-authors provided constructive comments on my

*Dr Erico J. Kotze was a PhD candidate at UCT and supervised by Dr S. B. Potter.
†Mr Hannes Breytenbach is a PhD candidate at UCT under the supervision of Prof. P. A. Woudt.

drafts resulting in the acceptance of this paper.

2. Chapters 3 titled "Phase-resolved spectroscopy and Doppler tomography of UZ Fornacis" and 4 titled "Optical and radio observations of UZ Fornacis" are based on the second paper entitled "A spectroscopic, photometric, polarimetric and radio study of the eclipsing polar UZ Fornacis: the first simultaneous SALT and MeerKAT observations" has been published in the MNRAS Journal; **Z. N. Khangale**, S. B. Potter, P. A. Woudt, D. A. H. Buckley, A. N. Semena, E. J. Kotze, D. N. Groenewald, D. M. Hewitt, M. L. Pretorius, R. P. Fender, P. Groot, S. Bloemen, M. Klein-Wolt, E. Körding, R. Le Poole, V. McBride, L. Townsend, K. Paterson, D. L. Pieterse and P. Vreeswijk, **2020, MNRAS, 492, 4298.**

   We present phase-resolved spectroscopy, photometry and circular spectropolarimetry of the eclipsing polar UZ Fornacis. Doppler tomography of the strongest emission line using the inside-out projection revealed the presence of three emission regions: from the irradiated face of the secondary star, the ballistic stream and the threading region, and the magnetically confined accretion stream. The total intensity spectrum shows broad emission features and a continuum that rises in the blue. The circularly polarized spectrum shows the presence of three cyclotron emission harmonics at ∼4500 Å, 6000 Å and 7700 Å, corresponding to harmonic numbers 4, 3, and 2, respectively. These features are dominant before the eclipse and disappear after the eclipse. The harmonics are consistent with magnetic field strength of ∼57 MG. We also present phase-resolved circular and linear photopolarimetry to complement the spectropolarimetry around the times of eclipse. MeerKAT radio observations show a faint source which has a peak flux density of 30.7 ± 5.4 μJy/beam at 1.28 GHz at the position of UZ For.

   For Chapter 3, the observations (Section 3.4 were taken with SALT between 2013 and 2014 and Dr S. B. Potter wrote the proposal for this. I did all the reductions and analysis shown in Section 3.4.2 and 3.5. I also did all the Doppler tomography (3.6, using the code of Dr E. J. Kotze (Kotze et al. 2016) and the analysis that follows from this. Dr S. B. Potter and Dr E. J. Kotze, provided very constructive comments on my draft of the paper.

   For Chapter 4, Dr Andrey Semena observed and reduced UZ For observations listed in Section 4.3.2.1. I converted this times to Barycentric Julian Date (BJD) and plotted the final light curve. Prof. P. A. Woudt and Dr Lee Townsend observed UZ For with MeerLICHT (mentioned in Section 4.3.2.2) on the night and the former helped retrieving the observations from MeerLICHT database. I converted the times to BJD and plotted the final light curve. The spectropolarimetry observations (Section 4.3.2.3) were made with SALT under Dr D. A. H. Buckley's Large Science Proposal, I reduced and analyzed the data with the help from Dr D. Groenewald and Dr S. B. Potter. Radio observations of UZ For, Section 4.3.2.4, were coordinated by Prof. P. A. Woudt with MeerKAT under ThunderKAT proposal and data reduction, analysis, plotting,

etc., was done by Mr D. M. Hewitt. Dr S. B. Potter observed UZ For with HIPPO on 2018 October 4, he reduced the data and sent me the results. I converted the times to BJD and also plotted and analyzed the results. For this paper, I helped in putting all the sections together as well as discussion and conclusions and literature review. Overall, all the co-authors contributed in these two chapters. I got very strong comments from Dr D. A. H. Buckley, Dr M. L. Pretorius, Dr D. Groenewald, Dr E. J. Kotze, Prof. P. Groot and Dr K. Paterson.

Plagiarism Declaration

I, Zwidofhelangani Ndamulelo Khangale, hereby declare that the work on which this thesis is based is my original work (except where acknowledgements indicate otherwise) and that neither the whole nor any part of it has been, is being, or is to be submitted for another degree in this or any other university. I authorise the University to reproduce for the purpose of research either the whole or any portion of the contents in any manner whatsoever.

Contents

List of Figures

List of Tables

Acronyms

Chandra Chandra X-ray Observatory. 39, 196

2MASS The Two Micron All Sky Survey. 170

AAVSO American Association of Variable Star Observers. vi, x, 12, 24, 166, 167, 188

ASAS-SN All-Sky Automated Survey for SuperNovae. x, 123, 124, 166, 167, 196

ASCA Advanced Satellite for Cosmology and Astrophysics. 18

ASTRO-H Astro-H. 197

ASTROSAT Astronomy Satellite. 196

ATCA Australian Telescope Compact Array. 57, 58

BJD Barycentric Julian Date. xv, 14, 15, 85, 108, 168, 170, 173

BVIT Berkeley Visible Image Tube. 122, 123

CASA Common Astronomy Software Applications. 172, 185

CRTS Catalina Real-time Transient Survey. x, 30, 123, 166, 167, 196

DSI Department of Science and Innovation. 12

Einstein Einstein (HEAO 2) X-ray Observatory. 18

eROSITA extended ROentgen Survey with an Imaging Telescope Array. 196

EUVE Extreme Ultraviolet Explorer. 64, 78

EXOSAT European X-ray Observatory Satellite. 18, 36–38, 60, 77, 160

GAIA Global Astrometric Interferometer for Astrophysics. 7, 104, 107, 124, 161, 185, 199

GALEX The Galaxy Evolution Explorer. 170

GEMS Gravity and Extreme Magnetism Small Explorer. 197

GINGA Ginga X-ray Satellite. 41

GPS Global Positioning System. 81, 82, 173

HEAO-1 High Energy Astronomy Observatories. 39

HET Hobby Eberly Telescope. 121

HIPPO HIgh-speed Photo-Polarimeter. ii, iii, vii, x, xv, 6, 8, 13, 15, 79–84, 160, 162, 172, 173, 175, 185, 189, 194

HRS High-Resolution Spectrograph. 122, 123

HST Hubble Space Telescope. 65

IAU International Astronomy Union. 60, 120

IDIA Inter-University Institute for Data Intensive Astronomy. 12

IDL Interactive Data Language. 85, 94

INTEGRAL International Gamma-Ray Astrophysics Laboratory. 196

IXO International X-ray Observatory. 197

JBI Jodrell Bank BroadBand Interferometer. 58

JD Julian Date. 85, 168, 170, 173

MASTER Mobile Astronomical System of Telescope-Robots. 123, 196

MAXI Monitor of All-sky X-ray Image. 196

MCMC Markov Chain Monte Carlo. 195

MeerKAT Karoo Array Telescopes. iii, iv, x, 6, 7, 14, 60, 69, 70, 159, 160, 162–165, 167–169, 171–173, 184, 185, 188, 190, 194–199

MeerLICHT MeerLICHT. iii, iv, x, xv, 6, 7, 11, 14, 162, 164–166, 168–171, 173, 174, 185, 188, 195

MIGHTEE MeerKAT International GHz Tiered Extragalactic Exploration. 189, 198

MIT Massachusetts Institute of Technology. 82

MORIS Massachusetts Institute of Technology Optical Rapid Imaging System. 82

NASA-IRTF NASA Infrared Telescope Facility. 82

NASSP National Astrophysics and Space Science Programme. 9, 12

NRF National Research Foundation. 12

NSF National Science Foundation. 56, 161

NuSTAR The Nuclear Spectroscopic Telescope Array. vi, 24, 196

OGLE Optical Gravitational Lensing Experiment. 124

PanSTARRS The Panoramic Survey Telescope And Rapid Response System. 170

Parkes Parkes Radio Telescope. 57

PIPT Principal Investigator Proposal Tool. 125

POETS Portable Occultation, Eclipse, and Transit Systems. 82

RASS ROSAT All Sky Survey. 7, 8, 199

RBS ROSAT Bright Survey. 8

ROSAT ROentgen SATellite. 7, 18, 37–39, 41, 64

ROSAT-NEP ROSAT North Ecliptic Pole. 8

RSS Robert Stobie Spectrograph. x, xv, 112, 122, 124, 125, 159, 162, 163, 168, 170, 185, 199

RXTE Rossi X-ray Timing Explorer. 18

SAAO South African Astronomical Observatory. vii, xv, 7, 8, 11, 12, 79–83, 121, 125, 164, 168, 172, 185, 195

SALT Southern African Large Telescope. iii, ix, x, xv, 6, 7, 11, 14, 69, 70, 111, 121–126, 150, 159, 162, 168–171, 173, 185, 189, 190, 194, 195, 197, 199

SALTICAM SALT Imaging Camera. 122

SARAO South African Radio Astronomy Observatory. 11, 163, 171

SDSS Sloan Digital Sky Survey. 7, 8, 170

SHOC Sutherland High-speed Optical Camera. iii, iv, vii, x, xv, 6, 13, 79, 80, 82–84, 162, 168–171, 173, 185, 197

SKA Square Kilometre Array. 163, 164

SkyMapper SkyMapper Southern Survey. 170

Swift/BAT Burst Alert Telescope onboard Neils Gehrels Swift Observatory. 8, 18, 196

TDB Barycentric Dynamical Time. xv, 85, 108

ThunderKAT The Hunt for Dynamic and Explosive Radio Transients with MeerKAT. 171, 172, 189, 196

UCT University of Cape Town. 9, 11–13

USNO United State Naval Observatory. 168, 173

UTC Coordinated Universal Time. 85, 170, 171, 174

VLA Very Large Array. x, 56–58, 60, 161, 167, 188, 190, 197, 199

VSTAR Variable Star Visualisation and Analysis. 12

XMM-Newton X-ray Multi-mirror Mission Newton Space Observatory. vi, 18, 24, 35–37, 39–41, 64, 196

Chapter 1

Introduction

1.1 Cataclysmic variable stars

Cataclysmic variables (CVs) are semi-detached mass transferring binaries consisting of a white dwarf (WD) primary accreting mass from a low-mass secondary companion via Roche lobe overflow (see e.g. Warner 1995a). The secondary companion in CVs is usually an unevolved low-mass main-sequence star (Patterson 1984, Warner 1995b). Some CVs do however have a slightly evolved companion (Goliasch & Nelson 2015) or a degenerate companion (Kalomeni et al. 2016). The WD and the secondary star are tidally locked together in such a way that the companion star repeatedly presents the same hemisphere towards the WD. This results in the distortion of the secondary companion into a "tear-like" shape due to the gravitational pull of the primary.

CVs show two types of light variability namely extrinsic and intrinsic variations ranging from time scales as short as seconds to decades. The short time scale variations include flickering and quasi-periodic oscillations. The long-term variability includes repeated outbursts, particularly those occurring in dwarf novae, recurrent novae and classical novae (see section 1.2) on time scales that range from a few days to centuries. Therefore, understanding CVs leads to a wealth of knowledge that is essential to understanding other types of variability in a wide range of astronomical objects that vary over time scales ranging from thousands to millions of years.

There are many reasons for studying CVs. For example, CVs offer astronomers a laboratory to study a wide range of phenomenon including: the physics of accretion onto compact objects such as WDs, the formation and evolution of close binaries – including common-envelope processes as well as their population synthesis by studying a large sample of these systems. Their rapid variability on a variety of time scales (e.g. from a few seconds to decades) allow us to study and understand their long and short time scale variabilities which are directly linked to the variation in mass transfer from the companion star to the WD. For CVs which contain an accretion disc, e.g. dwarf novae and nova-likes, understanding the physics of accretion disc in these systems on short time scales directly gives

us clues to understanding other astronomical objects with accretion discs such as active galactic nuclei and tidal disruption events. CVs with strong magnetic fields, such as polars and intermediate polars, allow us to study the effects of magnetic fields on accreting WDs and also the physics of accretion onto these systems. Novae offer us an opportunity to study stellar thermonuclear processes and the abundance of elements in the Galaxy. Some CVs have recently been observed to exhibit variations in their eclipse arrival times and this was attributed to either magnetic cycle activities of the secondary star or the presence of circumbinary planets. Therefore, continued monitoring of these systems may reveal more information about the formation and evolution of planetary systems in close binary systems and the universe as a whole.

In this thesis, I present an optical and radio wavelength study of the eclipsing polar UZ Fornacis (UZ For) using observations obtained between 2011 and 2018. This chapter contains an introduction and literature review of various aspects of magnetic CVs and Section 1.8 contains a review of UZ For. In the next sections (1.1.1 and 1.1.2), I will focus on the formation and evolution of CVs. See also Zorotovic & Schreiber (2020) and Pala et al. (2020) for recent reviews and developments on the formation and evolution of CVs.

1.1.1 Formation of CVs

The origin of CVs is thought to be from detached binary systems consisting of two main-sequence stars − separated by few million to hundreds of millions of kilometers − where one star is more massive than the other. The more massive star will evolve faster and become a giant or supergiant, since stars in the main-sequence follow the mass-luminosity relation (see e.g. Ritter 2010). The presence of the secondary "less massive" star limits the size up to which the primary star can grow without losing mass to its companion. Mass transfer to the secondary star begins when the massive star has filled its Roche lobe resulting in the decrease of the orbital separation and shrinking of the Roche limit and radius of the secondary star in order to conserve angular momentum of the system. The more massive star, however, keeps expanding due to the negative adiabatic and thermal-equilibrium mass-radius exponents (see e.g. Webbink 1985) and keeps on losing mass at high rates to its companion. On the other hand, the secondary star expands rapidly in response to high mass transfer rates from the primary (e.g. Kippenhahn & Meyer-Hofmeister 1977, Neo et al. 1977). The rapid expansion of the two stars results in the binary system evolving into deep contact known as the common envelope phase. The end product is a binary system consisting of the core of the massive star and the original mass of the companion star deep in the common envelope (e.g. Iben & Livio 1993).

Frictional interaction between the binary system and the material in the common envelope forces the two stars to spiral inwards resulting in a drastic decrease in the orbital separation. The spiralling-in eventually produces differential rotation in the largely convective common envelope, which results in the formation of a powerful magnetic dynamo (Regős & Tout 1995). According to Nordhaus et al. (2011), frictional energy release will unbind the common envelope in some cases, but not all, resulting in the formation of a close binary

consisting of the former primary's degenerate core and secondary. The core of the primary contracts as it evolves to become a fully degenerate WD. As mentioned in Ritter (2012), the mass of the WD component can in theory, be anywhere between the lowest possible value resulting from stellar evolution ($\sim$0.15 $M_{\odot}$) and the Chandrasekhar mass limit (M_{CH}) $\approx$1.4 $M_{\odot}$ (e.g. Chandrasekhar 1931). Zorotovic et al. (2011) reported that the observed mean masses of WDs amongst CVs is 0.83 $\pm$ 0.23 $M_{\odot}$, whereas the mean mass of WDs in pre-CVs is 0.67 $\pm$ 0.21 $M_{\odot}$.

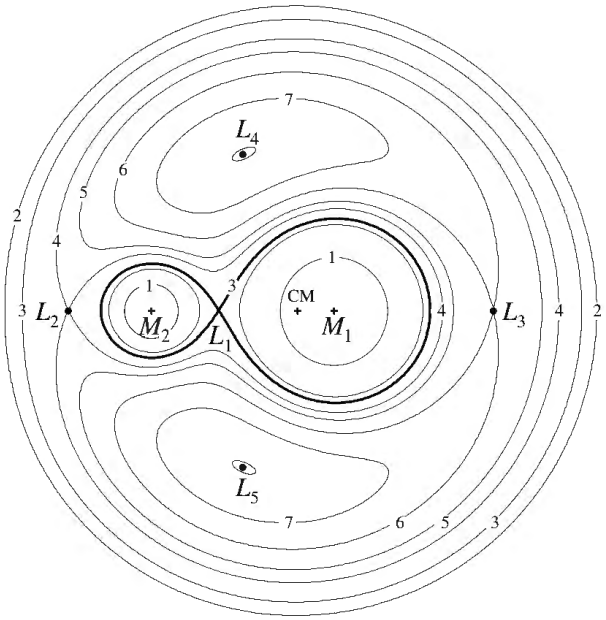

Figure 1.1: A schematic through the orbital plane showing the Roche equipotentials for a binary system with mass ratio $q = \frac{M_2}{M_1} = 0.5$, where M_1 is the primary and M_2 is secondary. The centre of mass of each component is marked with plus (+) sign while that of the binary system is marked with CM. The Lagrange points are marked from $L_1 - L_5$ and the numbers 1$-$7 mark the Roche equipotentials in increasing order with 3 being the Roche surface. Adopted from Figure 4.3 of Frank et al. (2002).

At this stage the detached binary system continues to lose orbital energy due to magnetic wind braking (Huang 1966, Verbunt & Zwaan 1981, Rappaport et al. 1983) and gravitational wave radiation (Paczyński 1967, Faulkner 1971, Paczynski & Sienkiewicz 1981) resulting in a further decrease of the orbital separation until the secondary star fills its Roche lobe and mass transfer via Roche lobe overflow is initiated. The resulting semi-detached system is considered to be a CV. The material from the secondary star starts flowing through the inner Lagrangian point (L_1, see Figure 1.1) into the Roche lobe of the WD. The flow of material is now reversed, that is, from the secondary star to the WD – the opposite of what was mentioned earlier when this binary was forming. However, the material from the secondary star does not fall directly onto the WD but follows a ballistic stream trajectory in the direction of the WD. Depending on the magnetic field strength of the WD, the ballistic

stream may result in the formation of an accretion disc around the WD at the circularization radius or the material gets accreted onto the magnetic poles of the WD. For CVs where the field strength of the WD is less than 10 MG, the material from the secondary forms a disc around the WD and accretion occurs in the inner edge of the disc or through the accretion curtain. On the other hand, systems where the magnetic field strength of the WD is greater than 10 MG, the material from the secondary star is forced to follow the field lines when reaching the magnetosphere of the WD and accretion takes places close to the magnetic poles of the WD. Therefore, the magnetic field strength of the WD plays a vital role in defining a class of CVs.

1.1.2 Evolution of CVs

The evolution of CVs is not well-understood, but as Schaefer (2020) asserts, it is what allow us to relate the different classes to each other, their similarities and differences, and to understand their histories and futures. There were different theories that were used to explain the evolution of CVs in the past, but there are two prominent ones such as the hibernation model (Prialnik & Shara 1986, Shara et al. 1986, Livio & Shara 1987, Shara 1989) and the magnetic braking model (Rappaport et al. 1982, Patterson 1984, Knigge et al. 2011). According to the hibernation model (see e.g. Schaefer 2020), a CV system evolves from a classical nova, to a dwarf nova, to a quiescent disconnected binary, to a dwarf nova, to a classical nova and so on, as the accretion rate changes. Therefore, a typical CV will evolve through the various stages on a time scale of approximately a million years. For this model, the evolution of CVs is governed by the detachment brought about by an unexpected change in orbital period resulting from the mass lost during a nova eruption. Hillman et al. (2020) presented a unified theory of CV evolution based on simulations and modelling of nova eruptions and their results support the hibernation model.

According to the magnetic braking model, however, the evolution of CVs is governed by the loss of orbital angular momentum from the binary (Rappaport et al. 1983, Paczynski & Sienkiewicz 1983, Spruit & Ritter 1983), resulting in evolution from long to short orbital periods. The magnetic braking model requires that orbital periods of all CVs must be decreasing due to various mechanisms that extract angular momentum from the binary orbit and the period changes over billions of years. Both, the hibernation and magnetic braking model, require that the orbital period must be changing. The changes in orbital period of CVs can be determined using long-term observations. For example, some novae have photometric measurements dating back to 1889 ($\sim$130 years ago). These data can be used to investigate various things including: orbital period changes, accretion rate changes and the changes from the nova eruptions, which are critical in describing and interpreting the evolutionary changes of CVs.

On the other hand, CVs have photometric light curves covering one or two decades at best and astronomers rely on other parameters such as orbital period in order to piece together their evolution. The orbital period distribution of CVs, e.g. Figure 1.3, has been used in the past to explain the evolution of CVs and this led to the development of the standard

model of CV evolution known as the disrupted magnetic braking model (see e.g. Verbunt 1984, Knigge et al. 2011) in order to explain the evolution of CVs. In accordance with the disrupted magnetic braking model, CVs evolve from long to short orbital periods and their evolution is governed by orbital angular momentum loss from the binary system and by the internal structure of the companion (Rappaport et al. 1983, Paczynski & Sienkiewicz 1983, Spruit & Ritter 1983, Knigge et al. 2011). According to Pala et al. (2020), the time scale in which the secondary star loses mass is similar to its thermal time scale, and this results in a donor star which is hotter, bloated and slightly out of thermal equilibrium, compared to an isolated main sequence star of the same mass. Therefore, the deviation from thermal equilibrium is understood to be the origin of the major features such as the period gap and period minimum seen in the orbital period distribution of CVs. The orbital period distribution diagram, Figure 1.2, reveals two most obvious features that are (i) the period gap between 2.15 and 3.18 h (Knigge 2006); (ii) a sharp cut-off around a period minimum ($P_{\rm min} \sim 80$ min). These features are discussed below.

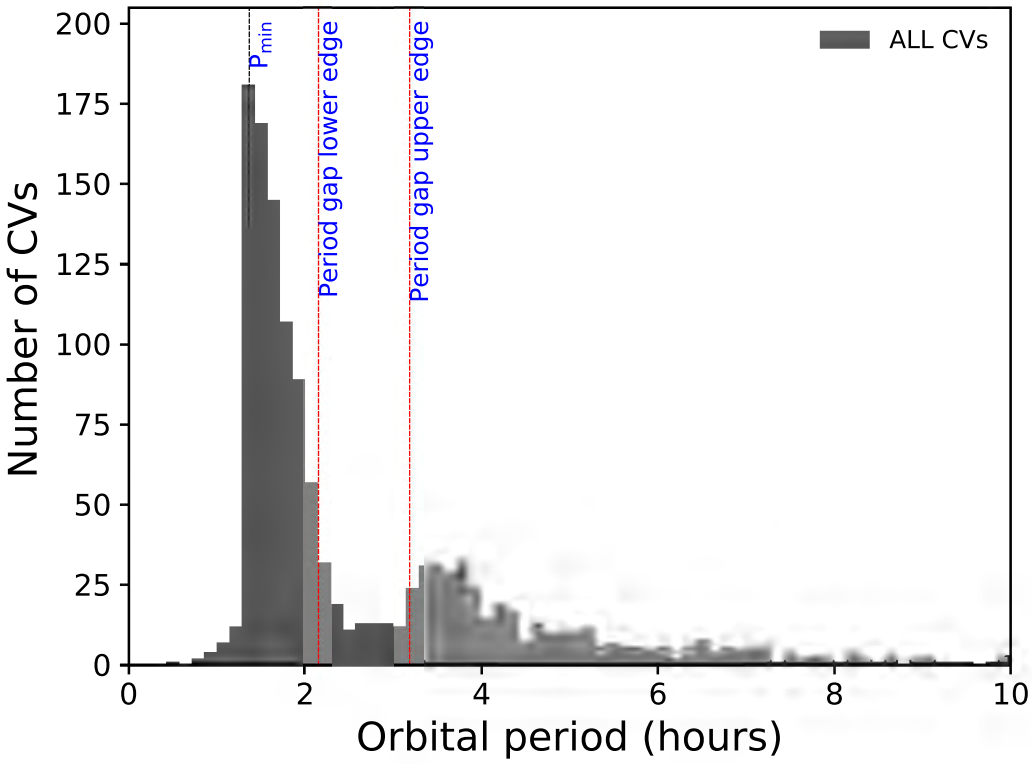

Figure 1.2: The orbital period distribution of 1340 confirmed and suspected CV candidates (dwarf novae, nova-likes and magnetic CVs) from the Ritter & Kolb (2003) catalogue version 7.24 of CVs. The black dashed line marks the period minimum ($P_{\rm min} \sim 82$ min) whereas the red dashed lines mark the lower and upper edge of the period gap.

At longer orbital periods ($P_{\rm orb} \geq 3$ h), CV evolution is driven by angular momentum loss due to magnetic wind braking and gravitational radiation. However, continued mass

transfer from the secondary star to the WD results in the secondary star becoming fully convective at $P_{\rm orb} \backsimeq 3$ h. At this stage, the secondary star detaches from the Roche lobe as a result of a re-configuration of its magnetic field which greatly reduces the effectiveness of magnetic wind braking as the system evolves to shorter orbital periods. This reduces the mass transfer from the secondary star to the WD. Therefore, the system continues to lose angular momentum due to gravitational wave radiation in the period gap (2 h $< P_{\rm orb} <$ 3 h) and evolves towards shorter periods as a detached binary. The observed orbital period distribution of CVs shows the lack of systems in the 2−3 h period range. The scarcity of CVs in the period gap is understood as the result of mass transfer that turns off when the system changes from being magnetic wind braking dominated to gravitational wave radiation dominated. Schreiber et al. (2010) found strong evidence for disrupted magnetic wind braking at the fully convective boundary from observational studies of 670 post common envelope binaries. In another study conducted by Zorotovic et al. (2016), based on the orbital period distribution diagram of 52 detached CVs, a clear peak was seen within the period range 2−3 h, corresponding to the period gap in CVs. Their results agree with predictions from the theory of disrupted magnetic braking but requires that an assumption that CVs are crossing the period gap as detached binaries to be made in order to match with binary population models. They concluded that CVs become detached binaries at $P_{\rm orb} \backsimeq$ 3 h and this supports the hypothesis that magnetic wind braking becomes inefficient at the fully convective boundary. This is also in agreement with the studies of Knigge et al. (2011) who constructed evolutionary path followed by CVs based on the observed mass-radius relationship of their donor stars. Knigge et al. (2011) found that their results match the data quite well if one assumes that angular momentum loss above the period gap is described by magnetic wind braking and that angular momentum loss below the period gap is solely driven by gravitational wind radiation. Howver, they found that the normalization factors derived for their best-fit donor evolution sequence are 2.47 $\pm$ 0.22 below the orbital period gap and 0.66 $\pm$ 0.05 above the orbital period gap, respectively. This results implies that angular momentum loss is stronger than pure gravitational radiation in CVs below the period gap but weaker than a typical magnetic braking in CVs above the period gap.

Upon reaching the lower-edge of the period gap, $P_{\rm orb} \backsimeq 2$ h, the orbital separation is such that the secondary star fills its Roche lobe again and mass transfer to the WD resumes with angular momentum loss driven by gravitational wave radiation. Further loss of angular momentum from the system shrinks the orbital separation and keeps the companion star filling its Roche lobe and mass transfer becomes stable again. CVs below the period gap keep evolving towards shorter orbital periods until the period minimum, $P_{\rm orb} \backsimeq 82$ min, is reached. At this stage, the secondary star becomes a sub-stellar type object whose radius increases as further mass is lost. That is, the time scale at which the secondary star loses mass becomes shorter compared to its thermal time scale and as a result, the secondary star is driven out of thermal equilibrium and stops shrinking as further mass is lost. At this stage the CV starts evolving towards longer orbital periods. CVs that have reached the period minimum and have started evolving towards longer periods are called period

bouncers (Patterson 1998). According to Amantayeva et al. (2021), there are 14 confirmed and/or suspected period bouncers (see their Table 5). Period bouncers are expected to be predominant below the period gap at least according to CVs' evolution estimations and Galaxy age (Kolb & Baraffe 1999). But these objects are associated with low rates of mass transfer and this makes them less luminous and difficult to detect.

The evolution described above is true for most CVs but there is uncertainty in the evolution of magnetic CVs, especially polars. According to Li et al. (1994), angular momentum loss may not be as effective in polars as it is in non-magnetic or weakly magnetic CVs in bringing the two stars together. This is due to the fact that the stellar wind from the secondary star in polars is trapped within the magnetosphere of the WD. This phenomenon consequently slows down the loss of angular momentum from the system due to the reduced number of open field lines which results in reduced mass transfer rates and leads to longer evolutionary time scales (e.g. Briggs et al. 2018). Note that polars have reduced number of open field because the magnetic field lines from the donor star form closed loops or connect with the field lines from the WD, resulting in the reduction of the magnetic flux in the open field lines responsible for magnetic braking. The disrupted magnetic braking mechanism discussed in this section offers a simple interpretation for the observed high incidence of magnetic systems among CVs (Araujo-Betancor et al. 2005b). For more details on formation and evolution of CVs, the reader is directed to Ferrario et al. (2020) and Pala et al. (2020).

1.1.2.1 Space density of CVs

In the past, CVs were discovered through a variety of methods including: optical variability, optical colours, emission line spectrum and X-ray surveys such as those conducted by the ROentgen SATellite (ROSAT, Truemper 1982, Pfeffermann et al. 1987). The majority of the CV systems discovered from X-ray surveys are magnetic CVs, e.g. ROSAT All Sky Survey (RASS, e.g. Thomas et al. 1998), whereas the majority of the non-magnetic CVs population were discovered at optical wavelengths, e.g. Sloan Digital Sky Survey (SDSS, Szkody et al. 2002). However, these surveys suffer from selection effects as objects discovered from different surveys suffer from selection bias. There are several ways to make sense of these catalogs and one such method is through deriving the space densities of the various subclasses, either through volume or flux-limited samples, assuming that the distances to the individual objects are known to some accuracy.

Recently, Pala et al. (2020) presented a "volume-limited sample of 42 CVs within 150 pc", albeit with known parallaxes from the Global Astrometric Interferometer for Astrophysics (GAIA; Gaia Collaboration 2018) second data release (DR2), in order to study the space density and population properties. They derived the space density of $4.8^{+0.6}_{-0.8} \times 10^{-6}$ pc^{-3} for the galactic CV population. However, their derived space density is lower compared to the values of $\sim 2 \times 10^{-5} - 2.0 \times 10^{-4}$ pc^{-3} predicted in the binary population synthesis studies of zero age CVs of de Kool (1992) and Politano (1996), respectively. Several attempts were made recently to derive or improve the space density measurements of CVs

from different CV populations. For example, Goliasch & Nelson (2015) and Belloni et al. (2018) derived the space density for the present-day population of CVs, assuming nuclear evolution, of $\backsimeq(1.0\pm0.5)\times10^{-5}$ pc^{-3} and $\lesssim2\times10^{-5}$ pc^{-3}, respectively. Their results agree to those reported in the literature (e.g. de Kool 1992, Politano 1996).

It has been reported that the predicted space density of CVs is larger than those derived from observations (see e.g. Briggs et al. 2018). For example, Thomas & Beuermann (1998) inferred a space density of $\backsimeq6.1\times10^{-7}$ pc^{-3} for polars discovered in the RASS, while a space density of $1.3^{+0.6}_{-0.4}\times10^{-6}$ pc^{-3} was suggested by Pretorius et al. (2013) for magnetic CVs based on the analysis of the complete "X-ray flux limited" ROSAT Bright Survey (RBS, Schwope et al. 2000b) and the ROSAT North Ecliptic Pole (ROSAT-NEP, Pretorius et al. 2007) survey. Hernández Santisteban et al. (2018) used eclipsing CVs from the Stripe82 sample from SDSS (York et al. 2000) to estimate the upper limit to the space density of period bouncer CVs of $\backsimeq2\times10^{-5}$ pc^{-3}.

Schwope (2018) presented the space density of CVs from the complete X-ray selected and flux-limited RBS and ROSAT-NEP sample and that of intermediate polars from Swift/BAT (Burst Alert Telescope onboard Neils Gehrels Swift Observatory; Gehrels et al. 2004, Barthelmy et al. 2005). They derived the space density of intermediate polars and non-magnetic CVs to be $<1.3\times10^{-7}$ pc^{-3} and $<5.1\times10^{-7}$ pc^{-3}, respectively. There are several caveats that exist in these studies, e.g. the distance to the individual CVs and the scale height of the Galactic distribution of CVs. Pretorius et al. adopted a scale height of 120 pc and 260 pc, for the long-period (relatively young) and short-period (old) CVs. These assumptions were reasonable but their space density will need to be revised once better distance estimates are available. These studies have shown a strong link between the X-ray luminosity function and space density of CVs. See section 8 of Mukai (2017) for more details on this topic.

1.2 Classification of CVs

As mentioned in Warner (1995a), the early classifications of CVs were based on morphology of light curve, that is, the observed outbursts that characterise each class. The current classification of CVs has been broadened to include spectroscopic and magnetic properties since the discovery of recurrent novae and later realization that the recurrence times and outburst ranges of recurrent novae and dwarf novae overlap. CVs are divided into several groups, namely: classical and recurrent novae, dwarf novae, nova-likes, magnetic CVs and AM CVn stars. The magnetic CVs are the basis of this thesis and, therefore, I will only define the various types of CVs and refer the reader to the appropriate literature for information.

Classical novae are binary systems with only one observed novae outburst. Their outbursts have amplitudes ranging from 6 to 20 magnitudes. The outburst amplitudes in classical novae are strongly correlated to the rate at which the outburst fades, this give rise to a further classification into fast or slow novae. The outbursts in classical novae are thought to arise as a result of thermonuclear runaways of the hydrogen-rich material accreting onto the WD primary. DQ Her and BT Mon are two examples of classical novae (see e.g. Schaefer

2020). The former, DQ Her, is a well-observed nova which was first observed in 1934 December (see, Stratton 1934) and it is an excellent test case for models of nova eruptions. The latter, BT Mon, is an eclipsing nova that went novae outburst in 1939 (see Robinson et al. 1982, and references therein). **Recurrent novae**, on the other hand, are binary systems that are observed to have more than one novae outburst or recurrent outbursts on time scales of decades, e.g. U Sco and CI Aql (Schaefer 2011). The outburst amplitudes of recurrent novae are generally smaller than those of classical novae. The outbursts in recurrent novae are understood to arise from the ejection of a substantial shell of material around the WD at high velocities.

Dwarf novae are close binary systems characterized by outbursts typically varying from 2-10 magnitudes (Thorstensen 2020a) which repeat on time scales ranging from ten days to tens of years (See chapter 3 of Warner (1995a) for comprehensive review). It is worth noting that the time scales between each type of dwarf novae outburst is well defined. The outbursts in dwarf novae are thought to arise from the instability in the accretion disc which occurs when the material accumulating in the accretion disc reaches a critical optical depth (Meyer & Meyer-Hofmeister 1981, Smak 1984). Based on the morphology of their outburst light curve, dwarf novae are further subdivided into Z Cam, SU UMa and U Gem stars.

Nova-likes are disc-dominated close binary systems that are like dwarf-novae in constant outbursts and they are associated with a high mass transfer rate. However, there are other nova-likes, e.g. VY Scl systems, that show occasional low states due to the reduction in mass transfer rate. Before magnetic CVs were known, all the systems that did not fall in the above groups were classified as nova-likes. Based on their spectroscopic and photometric properties, nova-likes are subdivided into four groups, namely: UX UMa, RW Tri, SW Sex and VY Scl stars. The dwarf novae and nova-likes are commonly classified as non-magnetic CVs since the WD in these systems have magnetic fields < 1 MG. See chapter 4 of Warner (1995a) for more details on this subject.

Magnetic CVs are close binary systems where the WD is strongly magnetic ($B \geq 1$ MG). The magnetic field of the WD can partially or completely disrupt the formation of an accretion disc around the WD, depending on the magnetic field strength. Magnetic CVs are further divided into two groups: the higher field polars − so-called following the recommendation by the Polish astronomers Krzeminski & Serkowski (1977) due their high degree of polarization − and lower field intermediate polars. Section 1.3 discusses these two groups which make up magnetic CVs in detail.

AM CVn stars are named after the prototype AM CVn and are compact close binaries in which a Helium, Carbon or Oxygen WD accretes from hydrogen-deficient companion stars, which is also believed to be Helium WD. Typical orbital periods of AM CVn range from 10 to 65 minutes (Nelemans 2005). The optical spectra of AM CVns show that the accretion discs in these systems are helium-dominated and hydrogen-free.

1.3 Magnetic cataclysmic variables

As already mentioned in Section 1.2, magnetic CVs (hereafter mCVs) are divided into two sub-classes, namely: polars or the AM Herculis systems (named after the prototype AM Her (Tapia 1977a); and hereafter AM Her systems) and the intermediate polars or the DQ Herculis systems (named after the prototype DQ Herculis, see Walker 1956, Patterson 1994; and hereafter DQ Her systems). The classification into AM Her systems and DQ Her systems is based on the magnetic field of the WD amongst other properties. For example, the WD in AM Her systems have strong magnetic fields ranging 7−230 MG (see e.g. Wickramasinghe & Ferrario 2000b, Ferrario et al. 2015; 2020) – which prevent the formation of an accretion disc. In addition to the strong field, the WD and the companion star in AM Her systems are locked together in synchronous rotation − which occur as a result of the interaction between the magnetic field of the WD and that of the secondary companion (Frank et al. 1992).

Typical orbital periods of AM Her systems range from 78 min for CV Hyi (Burwitz et al. 1997) and 79.69 min for EV UMa (Osborne et al. 1994) to 7.98 h for V1309 Ori (Harrop-Allin et al. 1997). However, there are other AM Her system candidates with shorter orbital periods, e.g. RBS0490 has an orbital period of 46 min (see e.g. Thorstensen et al. 2006, Harrison & Campbell 2015). Recent study conducted by Joshi et al. (2022) indicates that the most probable orbital period for RBS0490 is 1.689 h. There are a number of known AM Her systems in which the WD's spin and orbital period is slightly out of synchronism, e.g. V1432 Aql (Friedrich et al. 1996a), BY Cam (Mason et al. 1998), V1500 Cyg (e.g. Pavlenko et al. 2018), CD Ind (see Littlefield et al. 2019, Hakala et al. 2019), V4633 Sgr (Lipkin & Leibowitz 2004; 2008), Paloma (Schwarz et al. 2007, Joshi et al. 2016), IGR J19552+0044 (Tovmassian et al. 2017) and RX J0838−2827 (Rea et al. 2017). The two periods differ by less than 2% in most of these asynchronous systems except in the case of Paloma and IGR J19552+0044 where desynchronization differ by more than 3%. According to Norton et al. (2004), the cause of desynchronization is thought to be a recent nova eruption (e.g. V1500 Cyg went nova in 1975). However, Pagnotta & Zurek (2016) found no evidence of a recent nova shell around the remaining three asynchronous AM Her systems. The lack of a recent nova does not disprove the nova as the cause of asynchronism. Warner (2002) estimated a mean time of synchronisation of ∼300 years and this implied a nova recurrence time for all AM Her systems should be ∼5000 years in order to explain the presence of four asynchronous systems amongst 68 AM Her type systems known at that time.

On the other hand, the magnetic field strength of DQ Her systems range from 1 to 10 MG (e.g. BG CMi, Chanmugam et al. 1990) – and is strong enough to disrupt and truncate the inner part of the accretion disc which is formed around the WD. One of the defining characteristics of DQ Her systems is that their WD rotates rapidly and their spin period is always less than or a fraction of the binary's orbital period. Typical spin periods of the WD in DQ Her systems range from 33 s for AE Aqr (Patterson 1979) to 4021 s for EX Hya (Vogt et al. 1980, Warner & McGraw 1981), whereas their orbital periods range between 81.08 min (e.g. V455 And, Araujo-Betancor et al. 2005a) to 47.92 h (e.g. GK Per, (Watson

et al. 1985, Crampton et al. 1986)). Recently, a spin period of 29 s has been detected for the WD in CTCV J2056−3014 (Lopes de Oliveira et al. 2020) and this makes it the shortest WD spin ever recorded since AE Aqr. A further example of the shortest WD spin for a DQ Her system of 24.9 s was recently reported for LAMOST J024048.51+195226.9 (CRTS J024048.5+195227) (see e.g. Littlefield & Garnavich 2020, Pelisoli et al. 2022). The DQ Her systems show two types of optical variability: orbital variability due to rotation of the binary system and the spin variability as the WD rotates about its axis with one or two accretion columns (cf. Breus et al. 2019).

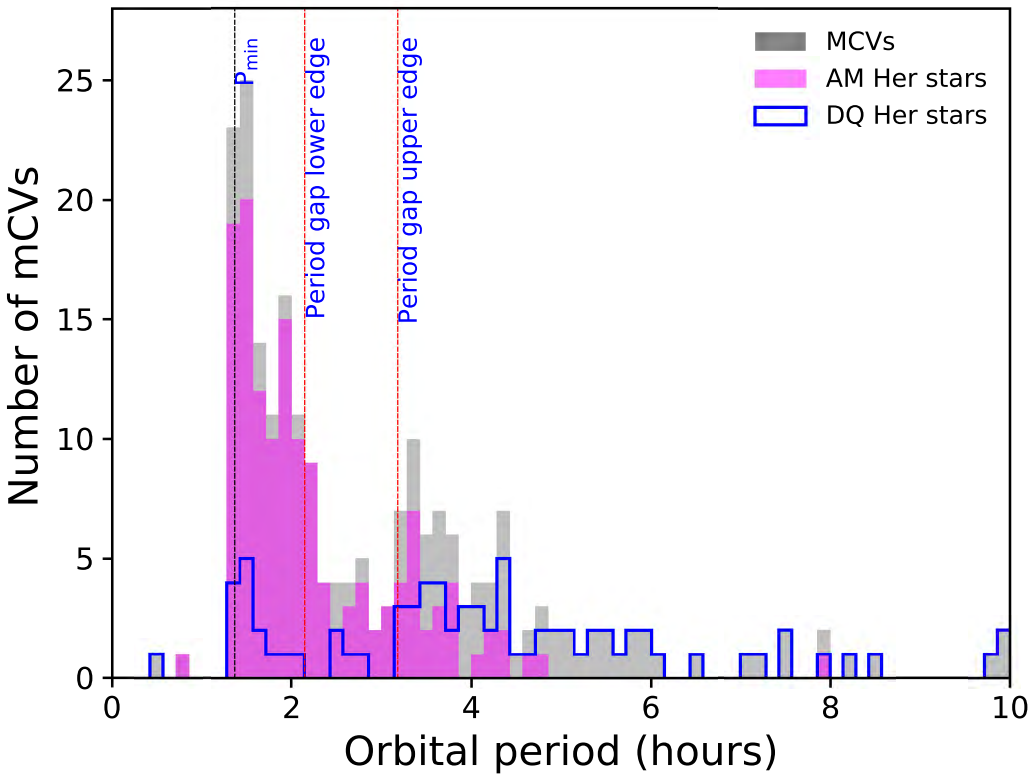

Figure 1.3: The orbital period distribution of confirmed mCVs (grey) from the Ritter & Kolb (2003) catalogue version 7.24 consisting of AM Her systems (magenta) and DQ Her systems (solid blue line). The black dashed line marks $P_{\rm min} \sim 82$ min whereas the red dashed lines mark the lower and upper edge of the period gap.

It has been reported that mCVs comprise ∼20−25% of all known CVs and that their orbital period distribution is similar to those of non-magnetic CVs (Ferrario et al. 2015). However, these numbers are constantly changing since a number of CVs are discovered every month and also there are not enough data to further classify these systems into their respective classes. The final version (7.34, 2016) of the Ritter & Kolb (2003) catalogue of CVs (and hereafter RK*) contains more than 170 mCVs (Ferrario et al. 2015) and this is almost a threefold increase from the 60 systems recorded in Wickramasinghe & Ferrario

*See https://wwwmpa.mpa-garching.mpg.de/RKcat/cbcat for more details.

(2000b) – in the last two decades. According to Joshi et al. (2020), the RK catalogue (version 7.24, 2016) contains 119* confirmed AM Her systems while a further 31 candidates are uncertain. Their Figure 11 shows the distribution of 122 AM Her systems of which 30% are eclipsing binaries. On the other hand, there are over 50 confirmed DQ Her systems in our Galaxy and majority of them are listed in the RK catalogue (Worpel et al. 2020) and over 60 are uncertain candidates. The recently updated catalogue† (version 2) of DQ Her stars produced by Koji Mukai list 71 confirmed and over 79 are uncertain candidate systems.

Figure 1.3 shows an example of the orbital period distribution diagram of 224 mCVs (grey histogram) with the associated distribution of AM Her systems (magenta histogram) and DQ Her systems (blue solid line) constructed based on the version 7.24 of Ritter & Kolb (2003) catalogue of CVs. It is clear from the figure that the AM Her type systems dominate the distribution of mCVs at orbital periods less than 4 h whereas the DQ Her systems dominate the population at longer orbital periods. Also shown in Figure 1.3 is the orbital period distribution of 142 confirmed AM Her systems. At least 29 of the AM Her systems are eclipsing binaries, where the secondary star orbits close enough to the line of sight in such a way that the secondary star occults the accretion stream and the WD i.e. the inclination of the system is greater than 72° (see e.g. Mason et al. 2019). In addition, 34 of the AM Her systems are found in the period gap. On the other hand, Figure 1.3 shows the distribution of 82 confirmed DQ Her systems in RK catalog. At least five of the DQ Her systems are found in the period gap. Mason et al. (2019) showed that at least seven of the DQ Her systems are in the period gap. Further discussion in this chapter is confined to various aspects of AM Her systems that are relevant to this thesis. But first, we briefly discuss one of the most useful imaging technique that has been used to study AM Her systems.

1.4 Doppler tomography

The size of CVs, a few solar radii, makes it impossible to study with direct imaging techniques since they subtend a few micro-arcseconds on the sky as observed from Earth and also they are found at typical distances of hundreds of parsecs (Pretorius et al. 2013). Therefore, to study these objects, astronomers have to rely on indirect imaging techniques such as Doppler tomography (Marsh & Horne 1988), eclipse mapping (Horne 1985, Baptista 2016), Roche tomography (Rutten & Dhillon 1994, Morin et al. 2016), Stokes imaging (Potter et al. 1998, Potter 2016) and accretion stream mapping (Hakala 1995, Vrielmann & Schwope 2001, Hakala et al. 2002).

Doppler tomography is an indirect imaging technique that was developed by Marsh & Horne (1988) which uses orbital phase-resolved spectra to construct a two-dimensional image of astrophysical objects (e.g. CVs) in velocity space. This technique was developed

*Worpel lists 129 confirmed AM Her systems in their website http://haukeworpel.altervista.org/polars_list.html.

†Koji Mukai lists 71 confirmed and 79 unceratin DQ Her systems in their website https://asd.gsfc.nasa.gov/Koji.Mukai/iphome/catalog/alpha.html.

to interpret emission line profile variations of the accretion discs in non-magnetic CVs and has made it possible to visualise the main emission regions, such as the irradiated face of the secondary, accretion discs and other accretion flows. Doppler tomography is governed by five axioms outlined in Marsh (2001) and repeated below as follows:

1. all points in the system are equally visible at all times;
2. the flux from each point in the frame of rotation is constant;
3. all motion is parallel to the orbital plane and is mapped accordingly;
4. all velocity vectors co-rotate with the system; and
5. the intrinsic line profile width is negligible.

The first and second axioms above are easily violated since the exact geometry of the system in CVs are generally unknown. For high-inclination systems, the effect of self-eclipse is seen as a violation, although the violation is apparent in eclipsing systems. If the first axiom is violated, then the second axiom is violated by default. In addition, the second axiom is violated by any emission anisotropy in the system, such as that induced by shocks and density waves in the accretion disc, or system outbursts. The third axiom assumes that all the material in the binary moves in the orbital plane of the binary. However, this is not true for AM Her systems since the motion of the material in the magnetic-confined accretion stream is out of the orbital plane of the binary. The fifth axiom is satisfied for most systems since Doppler shift produced by orbital motion and accretion flows translates to a velocity of hundreds of km/s whereas broadening produced by random thermal motions translates to only a few tens of km/s. Doppler tomography has been reviewed by Marsh (2001; 2005) and most recently by Marsh & Schwope (2016) and we refer the readers to these studies for much in-depth explanation of this method. The following paragraphs discusses the basic equations and the various projection methods that are used in Doppler tomography today.

A given point in the binary system can be defined by its spatial position such as its velocity (V_x, V_y), assuming two-dimensional for simplicity. For CVs, it is customary to define the x-axis to point from the WD to the donor star and the y-axis to point in the direction of motion of the donor star. With this in mind and defining the orbital phase zero as the time when the donor star is closest to the observer, then the radial velocity (V_R) of the point in question at orbital phase ϕ is given by (Eq. 3 of Marsh 2001) as follows:

$$V_R = \gamma - V_x \cos 2\pi\phi + V_y \sin 2\pi\phi \tag{1.1}$$

where γ is the systemic velocity or radial velocity of the centre of mass of the system. The use of a single value of γ is equivalent to assuming that all motion is parallel to the orbital plane of the binary, axiom three above. Equation 1.1 is the origin of Kraft's "S-waves" (Kraft et al. 1962) and is fundamental to Doppler imaging. For example, emission from the secondary star is red-shifted when moving away from an observer and blue-shifted when

moving towards an observer. If the binary has a circular orbit, the emission line profile from the secondary will move back and forth in a characteristic S-wave pattern. In addition, Eq. 1.1 shows that if one measures V_R as a function of the orbital phase (ϕ) and fit sinusoid plus a constant, one can then deduce accurate values of the closely-related duos, (V_x, V_y) – assuming that the γ is known.

An image in velocity space of the system can be defined as the strength of emission as a function of velocity, i.e. $I(V_x, V_y)$. Therefore, the flux observed from the system that comes from the velocity element bounded by V_x to $V_x + dV_x$ and V_y to $V_y + dV_y$ is given by $I(V_x, V_y)dV_xdV_y$. The line flux observed from the system between the radial velocities V and $V + dV$ at orbital phase ϕ can now be obtained by integration over all regions of the image that have the correct radial velocity using Eq. 4 of Marsh (2001) as follows:

$$\int_{-\infty}^{\infty}\int_{-\infty}^{\infty} I(V_x, V_y)[g(V - V_R)dV]dV_xdV_y, \tag{1.2}$$

where g is a function of velocity representing a line profile from any point in the image and V_R is given by Eq. 1.1 above. The velocity width is divided out to obtain flux density and the line profiles now are expressed using Eq. 5 of Marsh (2001) as

$$f(V, \phi) = \int_{-\infty}^{\infty}\int_{-\infty}^{\infty} I(V_x, V_y)g(V - V_R)dV_xdV_y \tag{1.3}$$

Here the profile f has the units of power per unit area per velocity interval. Doppler tomography is only effective if the broadening function g is relatively narrow compared to the width of the emission region. Therefore, in the ideal case g is a delta function, $g(V) = \delta(V)$, and the above equation 1.3 can be seen as selecting a set of lines in two-dimensional velocity space defined by a condition $V = V_R$ with the lines labelled by the particular velocity V in the profile to which they contribute. Therefore, Eq. 1.1 can be written as

$$aV_x + bV_y = c \tag{1.4}$$

where $a = -\cos 2\pi\phi$, $b = +\sin 2\pi\phi$ and $c = V - \gamma$ are all constants for a particular phase ϕ and thus define a set of parallel lines. The profiles of Eq. 1.3 are thought to as a projection of the two-dimensional image along the direction defined by $\mathbf{P} = (\sin 2\pi\phi, \cos 2\pi\phi)$, a position that rotate clockwise as the orbital phase advances. This is also thought to be the direction with which the Earth rotates as seen from the rotating frame of the binary.

To emphasise the above statements, Eq. 1.3 can be re-written with V_R term expanded and the broadening function set to a delta function as follows (Eq. 11.8 of Marsh & Schwope 2016):

$$f(V, \phi) = \int_{-\infty}^{\infty}\int_{-\infty}^{\infty} I(V_x, V_y)\delta(V - \gamma + V_x\cos 2\pi\phi - V_y\sin 2\pi\phi)dV_xdV_y \tag{1.5}$$

The profile formation described by Eqs 1.3 and 1.5 implies that a series of line profiles taken at different phases around the binary orbit is the equivalent of a series of projections of a

two-dimensional image along straight lines into one-dimensional.

Different inversion methods had been used over the years, e.g. filtered-back projection (e.g. Rowland 1979), maximum entropy method (Marsh & Horne 1988, Marsh 2001) and fast maximum entropy method (Spruit 1998). The concept of maximum entropy estimate which is a statistical inference for finding a probability distribution based on partial knowledge was introduced by Jaynes (1957). Marsh & Horne (1988) applied the maximum entropy method to find the emission distribution in velocity coordinate frame that is consistent with the input data, that is, the Doppler-shifted spectra at a number of observed phases of the binary system. To achieve this, the maximum entropy method uses an iteration algorithm, which is a slight modified version of that described in Lucy (1994), related to the Richardson-Lucy iteration (Richardson 1972, Lucy 1974). The fast maximum entropy algorithm is described in Spruit (1994) and is used for eclipse mapping Horne (1985) and has been used to construct Doppler maps (Spruit 1998). It is faster than any other algorithms used in maximum entropy method applications (e.g. Skilling & Bryan 1984).

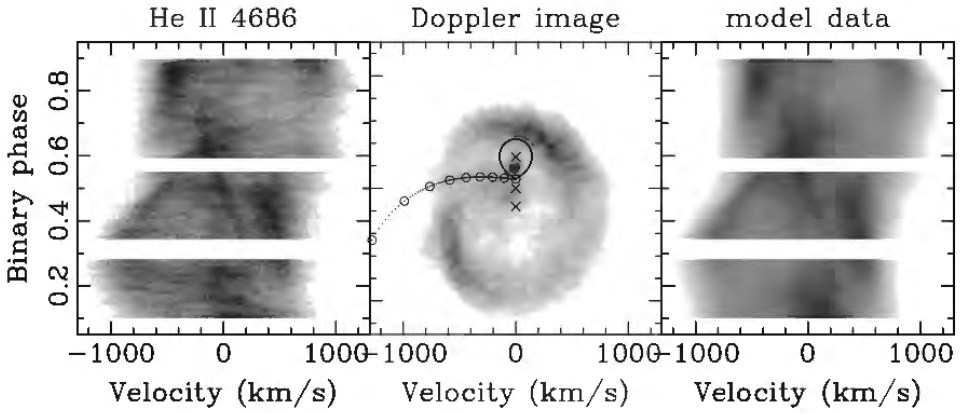

Figure 1.4: Example of observed and reconstructed trailed spectra (left and right) and Doppler map (centre) of IP Peg using HeII 4686 Å emission line obtained during high state. Adopted from Figure 2 of Harlaftis et al. (1999).

Examples of Doppler maps of CVs produced using the maximum entropy method and filtered back projections are shown in Figures 1.4 and 1.5, respectively. Also shown are the observed and reconstructed trailed spectra from these systems. From the figures, a clear distinction between the Doppler map of a dwarf nova (a disc-dominated system) and an AM Her system (a discless system). The overlaid models show the best-fit that describe the data and can be used to constrain the binary parameters in case where the these parameters are not well known. The Doppler map of IP Peg shows a ring-like structure associated with an accretion disc whereas the tomograms of AM Her show complex structure with emission concentrated in the vicinity of the secondary and the accretion stream. The Doppler maps of AM Her shown in Figure 1.5 were constructed using the HeII 4686 Å and Hβ emission lines from the observations obtained during a high state. The Doppler maps and trailed

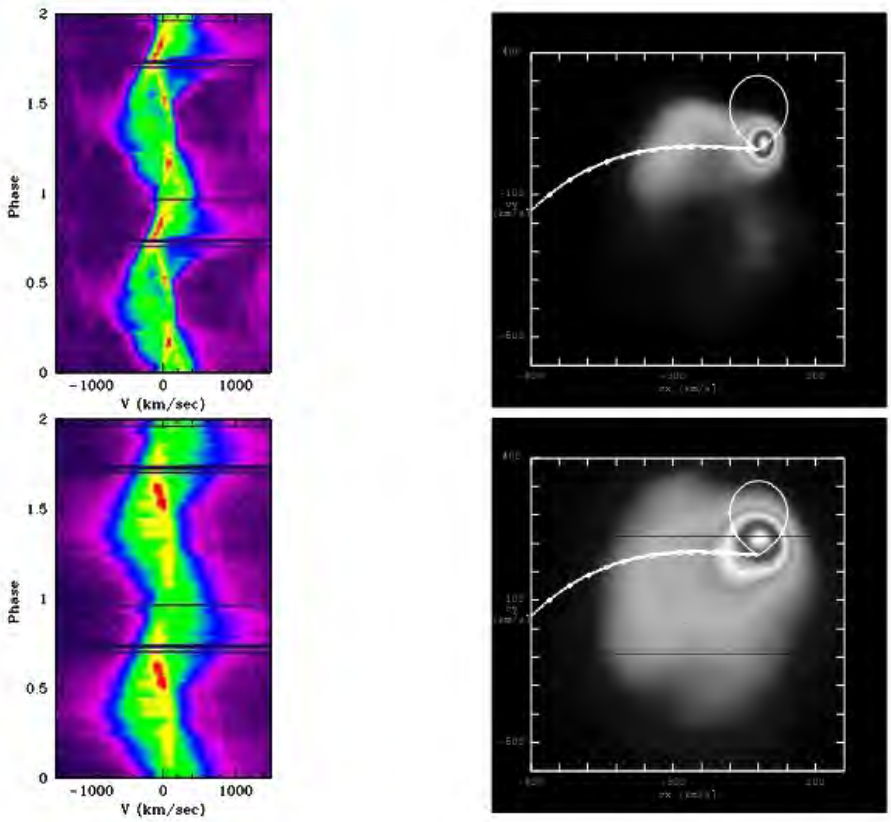

Figure 1.5: Example of observed trailed spectra (left panels) and Doppler map (right panels) of AM Her using HeII 4686 Å (top) and Hβ emission lines obtained during high state. Adopted from Figure 2 of Staude et al. (2004).

spectra of these two line are different in structure. The differences in the trailed spectrum and Doppler maps of HeII from those of the Hβ line were explained as due to shielding of the incident radiation by the accretion stream (see Staude et al. 2004, for further discussion). The observed structure in the Doppler map of HeII resembles the ballistic stream but the stream model overlaid in the tomogram does not trace this feature. The location of the ballistic stream, as per the model, is different. This was explained as a result of the motion of the stream as it leaves the orbital plain. As a further example, Figure 11.9 of Marsh & Schwope (2016) show the Doppler maps of HU Aqr using HeII 4686 Å line from the observations in two different states: the 1993 high state and the 1996 intermediate state. The high-state Doppler maps were dominated by emission from the donor star whereas that of the intermediate state is dominated by emission from both the donor star and the ballistic stream. These studies reveal that the Doppler maps of AM Her systems are interesting since they show different line structures since the emission lines in these systems trace various parts of the accretion flow. In addition, these systems undergo various states of mass accretion and this can be captured and investigated with the use of Doppler tomography. Chapter 3 is based on the implementation of Doppler tomography techniques on one of the eclipsing

polar, UZ Fornacis. Therefore, more details and history of Doppler tomography in AM Her systems will be reviewed in Chapter 3.

1.5 Fundamental properties of AM Her systems

The AM Her prototype, AM Herculis, was discovered as a variable star in 1924 and listed as a nova-like because of its slow variation in brightness (∼3 mag) and its emission line spectrum. Berg & Duthie (1977) suggested that AM Her could be the optical counterpart of the Uhuru X-ray source 3U 1809+50. The optical spectra and X-ray observations of this source revealed an orbital period of 3.09 h (Hearn et al. 1976, Cowley & Crampton 1977). The same orbital period was discovered in linear (up to 7%) and circular (varying from −9% to +3%) polarization at optical wavelengths by Tapia (1977a). The high degree of circular polarization led Tapia to suggest that the WD in AM Her must be strongly magnetic and subsequently estimated the field strength of $\sim 2\times10^8$ G. Studies conducted later showed that the polarized emission arises from cyclotron harmonics (Visvanathan & Wickramasinghe 1979) and this reduced the inferred field strength by a factor of ∼5. Campbell et al. (2008b) derived a magnetic field of 13.6 MG from the infrared spectra of AM Her.

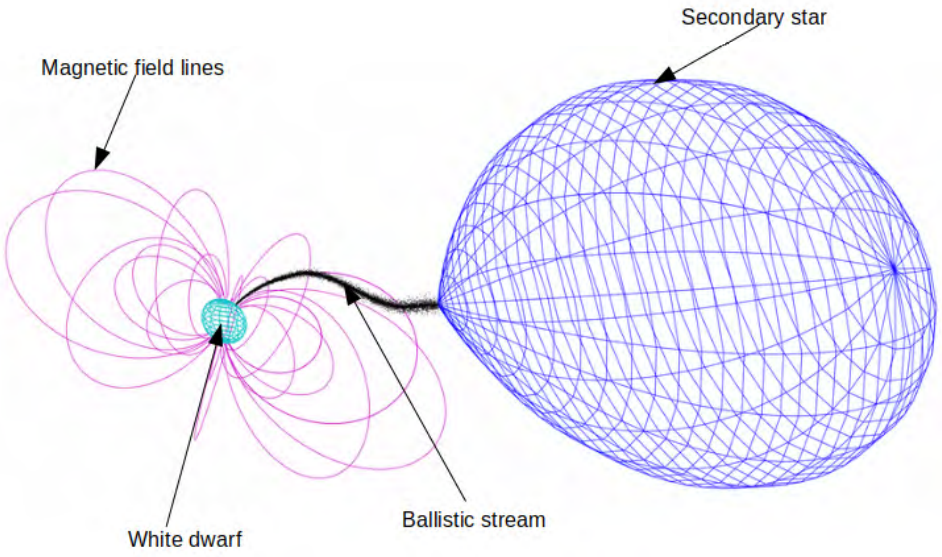

Figure 1.6: A schematic of an AM Her system. See text for more details. The code used to produce this figure is available at https://github.com/astromancer/mCV. Adopted from Figure 1 of Breytenbach et al. (2015).

The radial velocity variations (see e.g. Cowley & Crampton 1977) of the optical spectroscopy and the intensity variations of the X-ray photometry (see e.g. Hearn et al. 1976) of AM Her were found to have identical periods (i.e. 3.09 h), suggesting that the WD rotates at the same rate as the orbital motion, making it phase-locked in the reference frame of the

binary. After the discovery of AM Her, a search for polarization in other "nova-likes" was carried out. This led to the discovery of another two AM Her type systems, e.g. VV Pup (Tapia 1977b) and AN UMa (Krzeminski & Serkowski 1977). These three AM Her type systems, AM Her, AN UMa and VV Pup were found to show common characteristics from linear and circular polarization, optical flux and spectral features, which varies with the orbital period (Stockman 1977). The current definition of AM Her type systems requires that the WD and the companion be phase-locked or be slightly asynchronous due to nova eruption (see e.g. Warner 1995a). The other defining characteristics of AM Her type systems will be reviewed in the next three sections (Section 1.5.1 to 1.5.3). Since then, the AM Her type systems have grown in number to over 150 systems including both confirmed and suspected systems (Ferrario et al. 2020). The majority of these systems were discovered by blind or dedicated all sky X-ray surveys conducted by the Einstein (HEAO 2) X-ray Observatory (Einstein; Giacconi et al. 1979), European X-ray Observatory Satellite (EXOSAT; Taylor et al. 1981), ROSAT, Rossi X-ray Timing Explorer (RXTE; Bradt et al. 1993, Levine et al. 1996, Jahoda et al. 1996), Advanced Satellite for Cosmology and Astrophysics (ASCA; Tanaka et al. 1994), X-ray Multi-mirror Mission Newton Space Observatory (XMM-Newton; Jansen et al. 2001) and Swift/BAT. A model of the AM Her type system is shown in Figure 1.6 with the main components labelled, namely: the secondary star, the ballistic and magnetically confined accretion stream, the WD and its strong magnetic fields.

The ballistic stream

As already mentioned in Section 1.1.1, when one star in a binary fills its Roche lobe, the material will spill over to its companion. The existence of a stream of gas in CVs was suggested by Crawford & Kraft (1956) based on the observation of broad and strong emission lines in the spectra of AE Aqr. In the context of mCVs (specifically AM Her systems), when the secondary star has filled its Roche lobe, a ballistic stream of partially ionized gas is ejected into the Roche lobe of the WD. Upon leaving the inner Lagrangian point (L_1), the material from the secondary star follows a ballistic stream trajectory and accelerates to supersonic speeds towards the WD until, at some distance from the WD, the magnetic pressure overwhelms the ram pressure of the ballistic stream at the magnetosphere. The region where the magnetic pressure overwhelms the ram and gas pressure is called the threading region and sometimes the stagnation region. The exact location of the threading region depends on the balance of the ram and gas pressure of the ballistic stream and magnetic pressure of the WD. The equilibrium radius from the primary at which the magnetic field lines dominates the ballistic flow is known as the Alfvén (or magnetospheric) radius. Generally, it is assumed that the field in AM Her systems is a dipole; even if it is not, the dipole term of the field will dominate at large distances from the WD surface. In some AM Her systems, a strong shock is formed in the vicinity of the threading region. The bright threading region has been seen in the eclipse mapping of UZ For (Stockman & Schmidt 1996, Kube et al. 1999) and has also been detected in the light curves of HU Aqr modelled by Vrielmann & Schwope (2001). In addition, Littlefield et al. (2015a) presented evidence of the varying threading region in

the asynchronous AM Her system V1432 Aql – varying at spin-orbit beat period.

At the threading region, the ballistic stream is interrupted due to the balance between ram pressure and magnetic pressure, and diverted from the orbital plane of the binary and follows a trajectory along the magnetic field lines of the WD before being accreted. The stream in AM Her type systems is made up of two components: the ballistic part from L_1 to the threading region and the magnetically confined part from the threading region to the WD surface at either or both poles. Also, if the accretion is predominantly to the upper pole, then the magnetically confined accretion stream will be curved above the orbital plane. On the other hand, if the accretion is predominantly to the lower pole, then the magnetically confined accretion stream will be curved below the orbital plane. Note that the locations of the threading region and the accretion shock are determined by the complex interaction between the accretion flow and the magnetic fields of the WD (see e.g. Mukai 2017). The stream in AM Her systems is responsible for the absorption dips seen in the light curves of high inclination systems in optical, infrared and X-ray regime. The absorption dip occurs when the accretion stream passes between the line of sight between the observer and the accretion spot(s) on the surface of the WD.

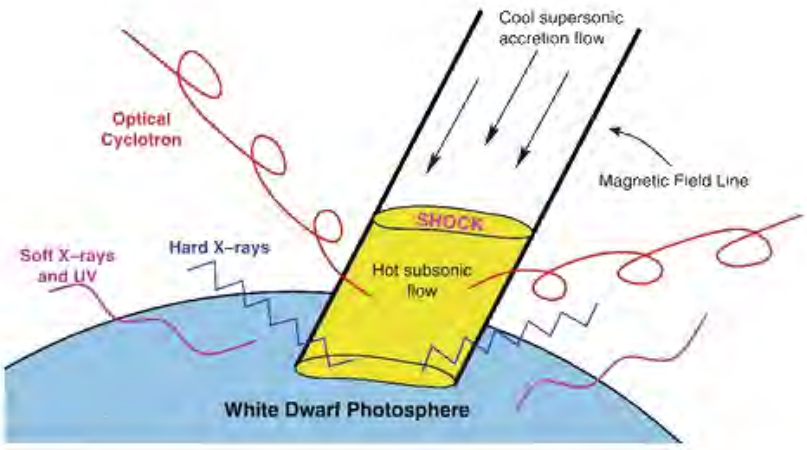

Figure 1.7: The schematic showing the accretion shock of a magnetic CV near the accreting pole of the WD. Adopted from Figure 2 (10.2) of Potter (2016).

Accretion shock

The magnetically confined accretion stream is ionized due to collisions within the stream and also by ultraviolet and X-ray photons from the accretion region on the surface of the WD. The stream is first accelerated to supersonic velocities (of the order of a few 1000 km/s) as it moves along field lines and suddenly decelerated by a factor of $\sim$4 at some height above the WD surface. The sudden deceleration, from supersonic to subsonic, results in the formation of a strong shock (Aizu 1973) above the WD's surface near the magnetic pole(s) (Lamb & Masters 1979, King & Lasota 1979). A schematic of an accretion column near the

WD's surface is shown in Figure 1.7. The typical temperatures of the material in the shock reaches 10−95 keV (e.g. Hellier 1996, Kuulkers et al. 2006, De Martino et al. 2008) and this results in the gas being highly ionized. The heated plasma cools down, due to thermal and cyclotron cooling which is extremely efficient in AM Her systems (Lamb & Masters 1979, Woelk & Beuermann 1992), as it settles onto the surface of the WD resulting in a stratified post-shock region. The high density and temperatures in the post-shock region force the electrons to gyrate around the magnetic field lines emitting cyclotron radiation which is highly polarized. In the optical and near-infrared bands, this radiation is dominated by the cyclotron emission (Wu et al. 1994, Cropper et al. 1999). Cyclotron radiation (see Section 1.6) is thought to be caused by cyclotron emission from a hot plasma in a magnetic field of greater than 10 MG (Chanmugam & Dulk 1981, Meggitt & Wickramasinghe 1982).

The AM Her type systems are recognized for their high degree of polarization, e.g. AM Her (Tapia 1977a). EV UMa has the highest recorded circular polarization, ranging from −20% to 50%, for an AM Her system (Hakala et al. 1994). The post-shock region is responsible for the emission of hard X-rays via bremsstrahlung (Fabian et al. 1976, Lamb & Masters 1979), which dominates over line emission. However, about half of the Bremsstrahlung and cyclotron flux is absorbed by the WD's photosphere and re-emitted as soft X-rays and/or extreme-ultraviolet radiation. The soft X-ray photons are mostly emitted near the base of the post-shock flow and thus a majority of the AM Her systems are found to show a soft X-ray excess (see e.g. Joshi et al. 2020). The soft X-ray excess or rather the soft problem is discussed in detail in Section 1.5.3.2. AM Her systems are associated with high ratios of soft-to-hard X-ray luminosity. On the other hand, the soft X-rays and extreme-ultraviolet emissions in DQ Her systems is emitted from an optically thick boundary layer (Patterson & Raymond 1985). Accretion onto the WD occurs over a small extended area on the surface of the WD near one or both the magnetic poles. For a review on AM Her systems see, for example, Cropper (1990), Warner (1995a) and Frank et al. (2002). Some properties of AM Her systems are reviewed in Ferrario et al. (2015; 2020).

The secondary star

The secondary companion in CVs is a low-mass main-sequence star, usually a red dwarf. Its mass can be determined directly from the orbital period of the binary (see e.g. Eq. 9 of Smith & Dhillon 1998). The secondaries in longer orbital period CVs, especially high inclination, are sufficiently luminous for their absorption lines to be seen in the blue and yellow spectral region. For these systems, their spectral type can be estimated, e.g. Catalán et al. (1999) estimated a spectral type of M4V for the secondary in QQ Vul. For systems with shorter orbital periods, the secondary star's absorption lines such as NaI and TiO are seen in the near infrared spectra. The optical and near-infrared spectra of the secondaries in mCVs show absorption from the NaI doublet at 8190 and emission from HeII, OI, MgII, CI, NI, CaII and Paschen series, e.g. QQ Vul (Catalán et al. 1999). From the use of Doppler tomography techniques, Catalán et al. (1999) showed that the Balmer lines, HeII, CI and OI emission lines had a narrow component originating from near L_1 point and strong component

from the ballistic stream. The MgII and CaII emission lines, however, originate solely from the hemisphere of the companion star facing the WD, i.e. the illuminated hemisphere of the red dwarf. On the other hand, the absorption lines from NaI doublets were shown to originate from the non-illuminated hemisphere of the red dwarf (see e.g. Schwope et al. 2000a). See Knigge et al. (2011) for further details in this topic.

1.5.1 Photometric (and polarimetric) properties

The photometric and polarimetric properties of AM Her systems have already been discussed in detail in the literature, e.g. Chapter 6 (Section 6.3) of Warner (1995a). Here in this section I review some of the defining photometric properties of the AM Her systems. The AM Her systems show strong orbital and long-term variation in their optical and infrared photometric light curves, i.e. the optical and infrared light curves are modulated at the same orbital period. The brightness variations in AM Her systems have been recorded on time scales ranging from seconds to years (see e.g. Kafka et al. 2005a, Wu & Kiss 2008). Some of the behaviour observed in these systems were explained in terms of star spots on the secondary star, instabilities at the L_1 point, blob fragmentation in the magnetic threading region and shock oscillations in the accretion region (Livio & Pringle 1994, Schmidt 2004). The other factor contributing to the optical variability of these systems is that the material leaving from L_1 takes minutes to reach the WD, since there is no accretion disc to store the gas or dilute the accretion luminosity. Therefore, the photometric variations in optical light portrays the effects of instabilities and turbulence that arises en route.

1.5.1.1 Polarimetric properties

Generally, the defining characteristics of AM Her systems is that their emission is strongly and variably circularly and linearly polarized in optical and infrared wavelengths due to cyclotron emission from the accretion region(s) (Cropper 1990). Typical levels of linear and circular polarization ranges from -25% to $+25\%$, however, circular polarization reaching 50% has been recorded in the literature (e.g. EV UMa, Hakala et al. 1994). The cyclotron emission dominates in AM Her systems and can contribute a significant fraction to the overall optical light of the binary system. The reason for this is that cyclotron radiation is highly beamed and appears brightest when the observer's line of sight is perpendicular to the fields of the emitting material; therefore, its contribution to the observed light is highly variable as the viewing angle of the cyclotron-emitting region changes across the orbital period (see e.g. Gänsicke et al. 2001a). Thus, the orbital light curves of AM Her systems can exhibit rapid, high-amplitude variations seldom seen in non-magnetic CVs (e.g. Littlefield et al. 2018a). Some AM Her systems undergo a sudden drop in optical brightness when the accretion region goes behind the limb of the WD, e.g. VV Pup, AM Her, or is eclipsed by the secondary star, e.g. HU Aqr, DP Leo.

In the case of VV Pup, the percentage of linear polarization reaches about 9% during the faint phase (Bailey 1978) whereas the percentage of circular polarization peaks in the

bright phase (∼8%) – consistent with those reported by Tapia (1977b) and Liebert et al. (1978). For AM Her, Bailey et al. (1978) reported polarization reaching 1.5% at phase 0.94 and 2.5% at phase 0.05. During the high state of AM Her, Crosa et al. (1981) reported circular polarization reaching −6% at phases 0.2 and 0.8, whereas the linear polarization was 6%. Piirola et al. (1994) reported detection of both linear (<1%) and positive and negative circular (from ∼ −2 to ∼ +12.5%) polarization from BY Cam in their UBVRI photometry. The presence of both negative and positive circular polarization in BY Cam implies that there are two accretion regions on the surface of the WD. However, the presence of both negative and positive circular polarization in an AM Her system does not necessarily mean that it is a two-pole accreting system, e.g. AM Her (Tapia 1977a, Stockman et al. 1977). The sign of polarization depends on the angle between the direction of the magnetic field lines in the accretion region and the line of sight of the observer among other properties.

Potter et al. (2004) used Stokes Imaging described in Potter et al. (1998) to model the polarimetric observations of V834 Cen obtained during the high state. Their results, based on modelling of this source, reveal that one emitting region is visible throughout the orbital cycle and is responsible for the high degree of polarization. The location of the accretion region determined from Stokes imaging is consistent with the location determined from extreme ultraviolet observations by Mauche (2002). Potter et al. (2005) presented photopolarimetric observations of CTCV J1928−5001 and found that, in addition to the orbital period modulation of 101 min, the circular polarization of CTCV J1928−5001 was ranging from −8% to +12% in the red and 0 to 5% in the blue – consistent with a two-pole accretion system. Furthermore, two pulses of linear polarization were seen at orbital phases where there is a reversal in circular polarization. The reversal in circular polarization in mCVs is understood to result from the appearance and/or disappearance of the accreting region(s) over the limb of the WD with the magnetic field lines inclined away from the observer. The deep brief reversal at the end of the bright phase hump, like that seen in VV Pup (Cropper & Warner 1986), is due to viewing the main accretion region from behind instead of in front with the field lines inclined away from the observer for a short time. The other scenario is that of at least two accreting regions of opposite magnetic polarity introduced when Piirola et al. (1987) discovered that more than three pulses of linear polarization were occasionally present for VV Pup. In another study, Potter et al. (2006) presented photometric and polarimetric observations of SDSS J205017.84−053626.8. This source shows circular polarization ranging from −10% to +4% and this is consistent with a two-pole accretor.

Rodrigues et al. (2006) presented optical polarimetry of 1RXS J161008.0+035222 and 1RXS J231603.9−052713. In the case of 1RXS J161008.0+035222, both linear (4%) and circular (15%) polarization were observed and were consistent with a one-pole accreting system where the accretion pole is always visible. For 1RXS J231603.9−052713, linear and circular polarization reaching 6% and 20% were observed for this system. However, the circular polarization had a complex structure with the main peak at phase 0.3 and possibly another peak around phase 0.95. Another form of Stokes Imaging is presented by

Costa & Rodrigues (2009) which considers a three-dimensional region with the electronic density and temperature varying following a shock-like profile and a dipolar magnetic field. Oliveira et al. (2019) recently applied this to the polarimetric observations of V348 Pav. Their results shows circular polarization reaching 30% and modelling of this system yielded a magnetic field strength of 28 MG and system parameters consistent with those deduced from radial velocity measurements. It is worth mentioning that Potter & Buckley (2018) used photopolarimetric observations to show that AR Sco is highly linearly polarized, with the linear polarization reaching 40%, although, it is argued that this system is not an accreting CV.

1.5.1.2 Optical, infrared and ultraviolet light curves

Other defining characteristics of AM Her systems is that their optical, infrared and ultraviolet light curves are modulated on the same orbital period. The examples of optical, infrared and ultraviolet light curves of AM Her systems are shown in Figures 1.8 (top two panels), 1.9 (left panels) and 1.11 and they all show modulation at the orbital period. The AM Her systems show two types of photometric variations: short-term variations on timescales of seconds and minutes to hours and long-term variations on timescales of days and months to years. The short-term variations are made of small-amplitude variations such as flickering, modulation on the orbital period and eclipse of the accretion region by the companion or the WD. The photometric light curves of AM Her systems come in different shapes, from simple light curves with a faint phase and a bright phase to double-humped light curves and complex ones.

The simple light curves of AM Her systems showing the faint and bright phases have been reported in literature, e.g. VV Pup (Bailey 1978, Szkody et al. 1983), MT Dra (Schwarz et al. 2002), SDSS J032855.00+052254.2 (Worpel et al. 2016), PTF1J2224+17 (Schwope & Thinius 2020), to name a few. The bright phases in these systems are explained as a result of cyclotron emission from the accretion region which is seen during the bright phase and is self-eclipsed by the WD during the faint phase. Therefore, the orbital light curves, the emission line structures and circular polarization of these systems are the functions of these states. The presence of a single hump in these systems does not mean that the second pole is not contributing to the overall emission of the system. For example, the light curve of VV Pup obtained during the high states is characterized by strong line emission and a hump with height of up to two magnitudes lasting ∼0.4 of the orbital cycle (Smak 1971, Warner & Nather 1972). In addition, polarimetry taken during the high states of VV Pup show positive circular polarization during the hump phases whereas during the faint phase negative circular polarization is observed (Liebert & Stockman 1979). During the low states of VV Pup, the hump and line emission disappears and positive circular polarization is observed during the hump phases and zero polarization elsewhere (Smak 1971, Liebert et al. 1978). According to Liebert & Stockman (1979), the high state in VV Pup was interpreted as a result of accretion onto two poles whereas the low states of this system was interpreted as a result of accretion onto one pole (i.e. the main accreting pole emitting positive polarization).

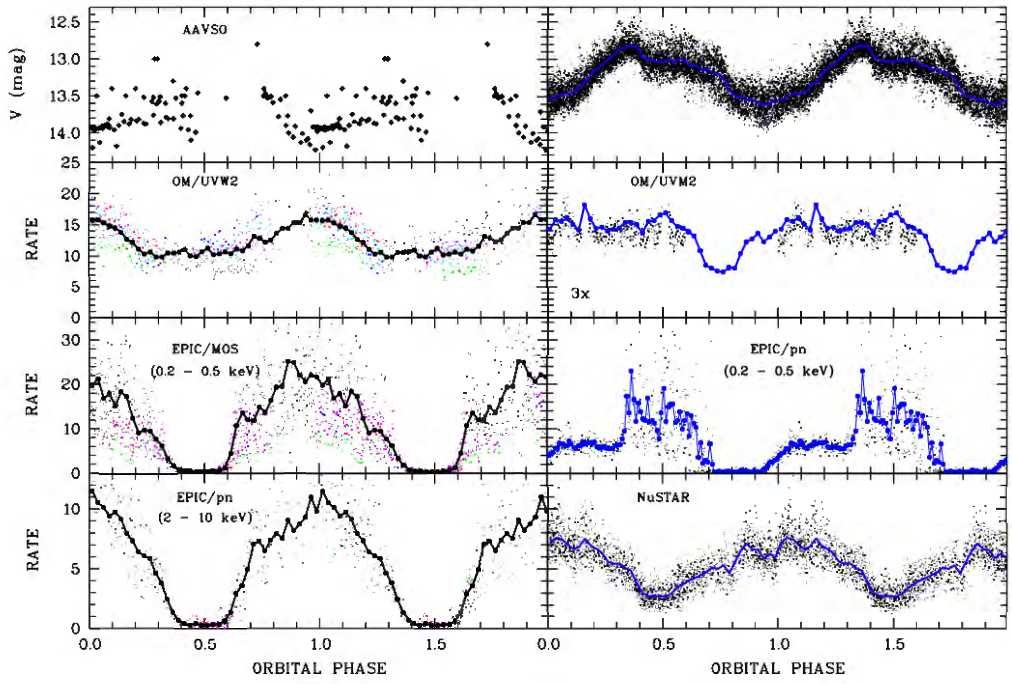

Figure 1.8: Multi-wavelength light curves of AM Her obtained in 2005 (left) and 2015 (right) from top to bottom showing the optical (AAVSO), ultraviolet (XMM-Newton), soft X-ray (XMM-Newton) and hard X-ray (XMM-Newton (left) and NuSTAR (right)). Adopted from Figure 4 of Schwope et al. (2020b).

The double-hump shape of the light curves of AM Her systems has been explained as a result of emission from two accretion regions. For example, the optical and infrared light curves of AM Her show two humps and two minima, with the first hump occurring at phase ∼0.3 and the second hump occurring at phase ∼0.7 (e.g. Bailey et al. 1978, Mazeh et al. 1986, Schwope et al. 2020b) and this was interpreted as a result of accretion onto two poles. For AM Her, however, the optical emission originates from the pole opposite to the X-ray emitting pole, see Figure 1.8 and discussion by Schwope et al. (2020b). The high states orbital light curves of HY Eri also shows two humps (see Figure 1.9). Another example of a double-hump light curves with two partially overlapping humps of unequal amplitude as well as two minima of different depths is presented by Littlefield et al. (2015b; 2018a) for MASTER OT J132104.04+560957.8. However, for this system they notice that the secondary maximum alternates between weak and strong from one cycle to another.

Complex light curves in AM Her systems have been reported for e.g., QQ Vul (Kafka & Honeycutt 2003), EF Eri (Bailey et al. 1982), V834 Cen (e.g. Mouchet et al. 2017), AN UMa, MN Hya (Wang et al. 2018) and 2XMMi J225036.9+573154 (Ramsay et al. 2009). The photometric light curves of QQ Vul presented by Kafka & Honeycutt (2003) show a flat continuum sometimes with one or two dips at phase 0.5 and phase 0.9. The light curves of

V834 Cen show a *nearly* sinusoidal variation with a pronounced minimum (Mouchet et al. 2017). The bright phase of V834 Cen is dominated by strong and variable flickering and/or flaring whereas the faint phase or minimum sometimes show a broad dip superposed on the minimum. However, the white light photometric light curves of this source had previously shown light curves changing shapes from double-humps (Osborne et al. 1987a) to saw tooth shape (Cropper 1989).

For eclipsing AM Her systems, their photometric light curves show a structured eclipse profile where the WD, the accretion region and the accretion streams are occulted by the secondary star (e.g. Joshi et al. 2020). The presence of the eclipse offers a simple reference time which can be used to study any phase-dependent phenomenon since several orbital cycles of the binary can be observed in one night. In addition, the short orbital cycles of AM Her systems allow for investigation of the short time scale phenomenon which are observed in the light curves of these systems (Bridge 2004). Figure 1.9 (left panels) show examples of photometric light curves of an eclipsing AM Her system, HY Eri ($P_{\rm orb}$ = 2.85 h), showing orbital modulation that are interrupted by the eclipse of the WD and the accretion region(s). The orbital light curves of HY Eri are characteristic of AM Her systems exhibiting two accretion regions which is also shaped by cyclotron emission. This system changes from high state (top and second rows) through intermediate state (third row) to low states (bottom panel) of accretion (see Beuermann et al. 2020, for more details).

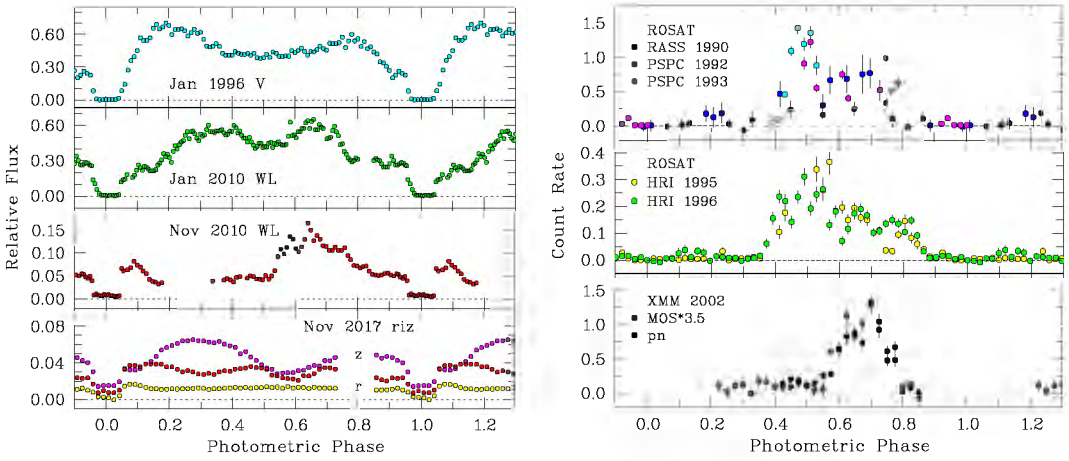

Figure 1.9: Examples of optical (left) and X-ray (right) light curves of HY Eri obtained over multiple epochs showing orbital and long-term variability. Adopted from Figure 1 of Beuermann et al. (2020).

The eclipse profiles contain information about the structure and the brightness distribution along the accretion stream. As the eclipse progresses, different parts of the binary (i.e. the WD and the accretion regions) are eclipsed at slightly different times and these allow for the precise measurements of these events. Also, when the WD and the accretion regions are eclipsed, the accretion stream becomes the dominant source of observed brightness although

there is some small contribution from the secondary star. Therefore, the eclipse allows us to study the changing brightness along the trajectory of the accretion stream from which, if constrained, the location of emission can be inferred. Furthermore, the eclipse profiles can provide constraints on a number of system parameters such as the inclination of the system, the size of the WD and the size and location of the accretion region(s) (Bridge 2004). Therefore, modelling of the eclipse profiles provides information about the spatial structures and the binary parameters of the system (e.g. Joshi et al. 2020). As an example, Schwope et al. (2001) estimated the size of the accretion region to be 4° (450 km) based on the egress measured in soft X-ray light curves of HU Aqr. They estimated that the spot extended vertically by $\leq 0.015 R_{\rm wd}$. Their comparison of the width of the stream dip and the extent of the accretion spot revealed that only the inner 60−80% of the stream are dense enough to produce soft X-rays. Figure 1.10 shows the eclipse profiles of HY Eri showing various stages of the eclipse ingress and egress when different emission regions are being occulted by the secondary star. These are unique characteristics of AM Her systems since there is no accretion disc, therefore, studying the eclipse profiles allows us to determine system parameters and other physics.

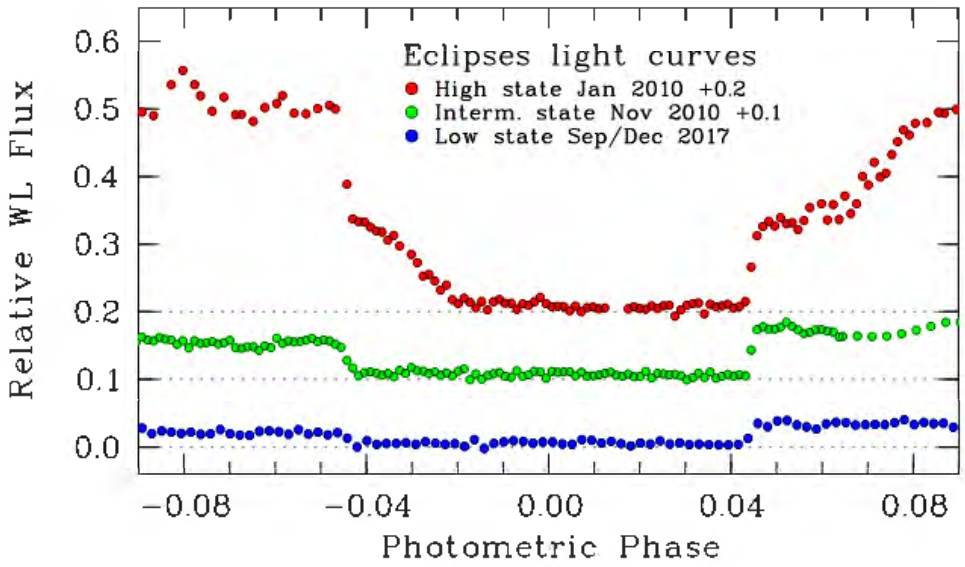

Figure 1.10: Optical eclipse profiles of an AM Her system, HY Eri, showing three different shapes associated with the various states of this system. Adopted from Figure 2 of Beuermann et al. (2020).

The optical light curves of AM Her systems sometimes show a narrow dip (see e.g. Patterson et al. 1981, Mason 1985, Watson et al. 1989) in the middle of the bright phase for non-eclipsing systems or just before the primary eclipse for eclipsing systems where the magnitude of the system drops by a few tens of percent, e.g. VV Pup (Vennes et al. 1995),

AR UMa (Szkody et al. 1999) and HU Aqr (Schwope et al. 2001), MT Dra (Schwarz et al. 2002), FL Cet and CSS 081231: 071126+440405 (Katysheva & Shugarov 2012). These dips are sometimes not seen in the light curves of these systems, see e.g. HU Aqr (Schwope et al. 2001). The dips seen in these systems are interpreted as the result of obscuration of the accretion region on the magnetic WD by the magnetically confined accretion stream. As an example, Breytenbach et al. (2019) reported that the magnitude of MASTER OT J061451.70−272535.5 drops by ∼50% leading to the primary eclipse.

Mauche (2002) gives ultraviolet light curves of V834 Cen and they reveal two maxima: a broad maximum at phase 0.55 and a narrow maximum at phase ∼1.0. In addition, the ultraviolet light curves of V834 Cen show a secondary minimum situated between the two maxima and a strong asymmetric eclipse centred at phase 0.88. What is more interesting is that the ultraviolet light curves of this system differs slightly from one observation to the next. Furthermore, the ultraviolet light curves are significantly different from the X-ray light curves.

The infrared JHK light curves of AM Her presented by Kafka et al. (2005b) shows that the infrared light is wavelength-dependent, showing variability from a simple sinusoidal variation in the J band to a highly modulated light (non-sinusoidal) in the H and K bands. These were explained as due to cyclotron radiation which dominates in the infrared for AM Her systems. Similarly, the infrared light curves of VV Pup differs from the optical in that they show double-sinusoid and not single hump as observed in optical (Szkody et al. 1983). For example, the optical and ultraviolet light curves of AI Tri shown in Figure 2 of Traulsen et al. (2010) show similar light variation between the two bands. However, the variability in X-ray is different.

Campbell et al. (2008b) found that the J and H band light curves of AM Her, Figure 1.11 top and middle panels, show strong ellipsoidal variations whereas the K band (bottom panel) light curve were explained as a result of the combination of ellipsoidal variation and cyclotron emission. In the early studies, the mid-infrared light curves of AM Her systems were found to show infrared excess (see e.g. Brinkworth et al. 2007) and these were interpreted as possibly due to circumbinary discs.

1.5.1.3 Long-term photometric light curves

The long-term photometric light curves of AM Her systems show total brightness variations of ∼3 magnitude or more (Warner 1995a). An example of a long-term optical light curve of AM Her from Šimon (2016) is shown in Figure 1.12 and reveal two distinct photometric states: a high state with V ∼12.5 mag and a low state with V ∼15.5 mag. The low states in these system are attributed to accretion onto the WD via stellar wind and the luminosity due to accretion onto the WD is reduced at optical, X-ray and ultraviolet wavelengths. During the high states, accretion occurs via the Roche lobe over flow and the luminosity of the system is enhanced. Several processes have been suggested to explain the low and high states observed in AM Her systems and these include the following: variations in mass transfer rate, star spots on the secondary star, instabilities at the L_1 point, blob fragmentation in the

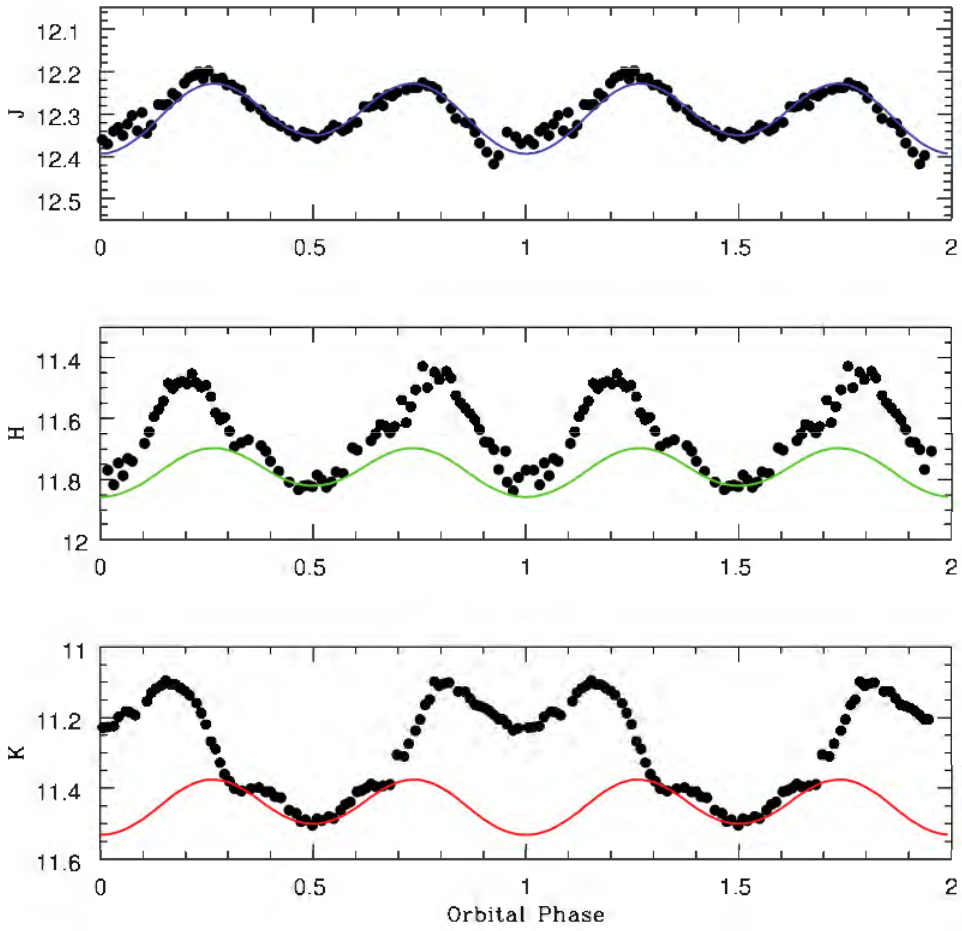

Figure 1.11: The JHK photometry of AM Her obtained during a low state and the solid lines overplotted is the light curve model for inclination of 50°. Adopted from Figure 1 of Campbell et al. (2008b).

magnetic threading region and shock oscillations in the accretion region (Livio & Pringle 1994, Schmidt 2004). Therefore, the long-term photometric studies of these systems are essential in order to reveal any characteristics based on stellar activity and/or mass transfer (e.g. Kalomeni 2012).

The long-term light curve of the AM Her prototype has been presented in the literature by different authors (Hessman et al. 2000, Kafka et al. 2005a, Wu & Kiss 2008) and dates back to 1890. The long-term optical light curve obtained between 1977 and 1998 and presented by Hessman et al. (2000) reveal that AM Her spends about 25% of its time in the high state and that the low states of this system is random. The low-state of this system was attributed to star spot near the L_1 point. Kafka et al. (2005a) found that the long-term low-state photometric light curve of this source shows flaring events lasting about 15 to 90 minutes. Further low-state studies presented by Kalomeni & Yakut (2008) show the presence of short-term, low-amplitude light variations of about 0.02-0.03 mag. In addition, brightness

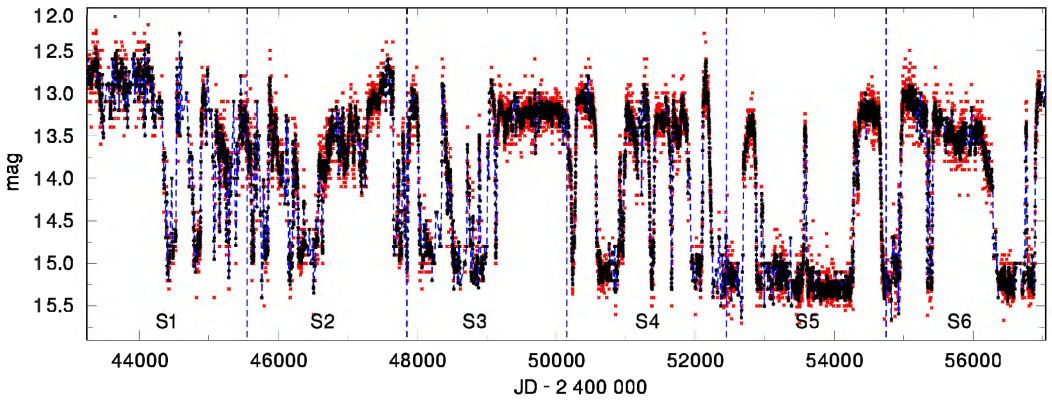

Figure 1.12: Long-term V magnitude light curve (black circles) of AM Her spanning from 1977 to 2015 showing the mean one-day brightness (red crosses) and moving average (blue dashes). The vertical dashed lines divide the light curve into equal segments marked S1 to S6. Adopted from Figure 2 of Šimon (2016).

variations ranging from 0.7 to 2 mag, which they attributed to the stellar activity of the secondary star, were also detected. On the other hand, Wu & Kiss (2008) show that AM Her has a 63% high state duty cycle, from the observations stretching from 1892 to 2005 and that there appears to be a pattern of long and short duty cycle alternation (i.e. the high and low state alternates) which they attribute to the change in magnetic field configuration in the system. According to Wu & Kiss (2008), the star-spot model of Hessman et al. (2000) has highlighted the importance of magnetism in the role for the high and low states and the state transition of the AM Her systems, analyses have shown that the model has fallen short of satisfactorily explaining the 100-year data of optical brightness variations of the system AM Her.

Further long-term light curves of AM Her spanning from 1977 to 2015 are presented in e.g. Kafka & Hoard (2009), Dai et al. (2013), Šimon (2016) and Schwope et al. (2020b). These studies revealed that the long-term light curve of AM Her shows alternating low and high states of different lengths, displaying transitions between the two states, characterized by low state transient events. In addition, Kafka & Hoard (2009) found an intermediate state which lasted two months that occurred while AM Her was transitioning from a prolonged low state. However, the transition from low to high state for this event was identical in speed and duration to any other normal transition from low to high state. Furthermore, Šimon (2016) found that the high states in the long-term light curve of AM Her are not well-defined but represented narrow levels of brightness. The light curve features can be explained by activities on the donor star, mass transfer rate variation, star spots and their migration caused by differential rotation.

Kafka & Honeycutt (2005) reported that the transitions to and from low states, based on long-term light curves, of some AM Her systems (e.g. AM Her, ST LMi, MR Ser, AR UMa and AN UMa) were similar to that of VY Scl type stars. Their results show that the speeds and shapes of the transitions of both disc-systems and magnetic systems above the period

gap suggest that the low states in these systems are due to star spots on the secondary star drifting in front of the L_1 point. The speeds and shapes of the transitions of magnetic systems below the period gap point to X-ray irradiation on the L_1 point as the cause of the low states. A follow-up study of ST LMi by Kafka et al. (2007) shows a prolonged low state followed by a period of alternating high and low states.

Kalomeni (2012) presented a long-term study of five AM Her systems (AM Her, AN UMa, AR UMa, DP Leo and V1309 Ori) and found variations of 170, 218 and 180 days for AM Her, AN UMa and AR UMa, respectively. They attributed the periodicities as maybe due to modulation of the mass-transfer rate resulting from magnetic cycles in the secondary stars. In addition, Mason & Santana (2015) analyzed long-term light curves of 44 AM Her systems from the Catalina Real-time Transient Survey (CRTS; Drake et al. 2009) database spanning nine years. Their results show that the long-term light curves of AM Her systems could be classified into different categories, namely: systems with distinctive repeatable low states (e.g. AM Her, EF Eri, ST LMi, etc.); low accretion rate AM Her systems (e.g. WX LMi, MQ Dra, V379 Vir, etc.); systems dipping to, but not remaining in low states (e.g. EK UMa, V834 Cen, EQ Cet, etc.); systems showing complex multi-state behaviour (e.g. CE Gru, GG Leo, FR Lyn, etc.); systems remaining mostly in high states (e.g. CD Ind, AN UMa, AI Tri, etc.) and eclipsing systems (e.g HU Aqr, DP leo, HS Cam, etc.). However, they argued that this classification is not unique since some systems fell into more than one category, e.g. EQ Cet. There are other AM Her systems whose long-term light curves have been presented in literature, e.g. BY Cam (Andreev et al. 2013), QQ Vul (Kafka & Honeycutt 2000) and most recently MASTER OT J132104.04+560957.8 (Littlefield et al. 2018a).

1.5.1.4 Quasi-periodic oscillations

Some AM Her systems show quasi-periodic oscillations (QPOs) in their optical and polarimetric light curves. These QPOs are thought to be produced by intensity variations of the emitted radiation originating at the post-shock region. The structure and the dynamical properties of the accretion region is reviewed in Bera & Bhattacharya (2018). For example, Middleditch (1982) reported detection of optical QPOs with amplitudes of 1−5% ranging from 1.25−2.5 s from the light curves of AN UMa and V834 Cen. A recent study conducted by Mouchet et al. (2017) for V834 Cen reveals QPOs on the three filters used, however, their r filter showed QPOs at all orbital phases with the high relative amplitude observed during the bright phase. In another study, Larsson (1987) reported detection of optical QPOs of 2−3 s in the light curve of EF Eri. Another AM Her system that had been found to show QPOs of order of a few seconds in its light curve is VV Pup (Larsson 1989). A recent study on VV Pup by Bonnet-Bidaud et al. (2020) reveals the presence of QPOs in the three filters used with a mean period of 1.5 s and mean amplitude of 1%. In addition, Middleditch et al. (1997) reported detection of broad and narrow QPOs with amplitudes of ∼1−4% and periods of 5 s and 1.25 s from the high-speed photometric light curves of BL Hyi. QPOs have also been detected in polarimetric light curves of AM Her systems at least on one occasion.

For example, Potter et al. (2010) reported detection of photometric and polarimetry QPOs of the order 5−6 minutes in the photopolarimetry and circular polarimetry observations of IGR J14536−5522 on two separate occasions.

1.5.2 Spectroscopic properties

The spectroscopic properties of AM Her type systems have been reviewed in Chapter 5 of Warner (1995a). Here I review some of the defining spectroscopic properties of these systems. The optical and near infrared spectra of AM Her systems show strong emission lines from the Balmer lines along with HeI, HeII and the Bowen fluorescence blend CIII/NIII blend (Schachter et al. 1991) at 4650 Å superposed on a non-photospheric continuum. The Bowen blend is indicative of high excitation of the emission line region (Mukai 1988). The emission line profiles of AM Her systems show multiple narrow and broad emission line components which are associated with emission from the ballistic stream, magnetically confined accretion stream and the irradiated face of the secondary star. The high-excitation feature, HeII 4686 Å emission line, is prominent in AM Her systems and is a signature for strong fields. Therefore, the HeII 4686 Å emission line is a defining feature of AM Her type systems. The existence of singly-ionized Helium (e.g. HeII 4686 Å) in AM Her systems point to the presence of an ionizing source on the surface of the WD. Note that the ionization potential of Helium is 54 eV. The low-excitation lines, the Balmer series and neutral Helium (HeI), are recombination lines and originate primarily from low-density regions along the accretion flow. The strength of the HeII 4686 Å emission line is comparable or can exceed that of the Hβ emission line in intensity. The Balmer emission lines mostly show an inverted decrement with Hγ or Hδ the strongest. An example spectrum covering from the near-ultraviolet to the near-infrared obtained on 1988 July 17 is presented in Figure 3 of Schachter et al. (1991). The full list of emission lines is listed in their Table 2.

Generally, the spectra of AM Her systems, during the high state, is dominated by emission lines superposed on a continuum that rises strongly in the ultraviolet and may also rise in the near infrared. Two further examples of the spectra of AM Her systems obtained while these systems were in a different states of accretion are shown in Figures 1.13 and 1.14 for CSS 080228: 081210+0403 (Thorstensen et al. 2020) and RX J1007−2017 (Thomas et al. 2012), respectively. The high-state spectra show prominent emission from Balmer and Helium lines with continuum that seems to rise in the blue. The middle spectra of RX J1007−2017 obtained in 1992 January and shown in Figure 1.14 shows the intermediate state. This spectrum shows prominent emission from Balmer and Helium lines superposed on a more flat continuum and also seen is a moderate increase in cyclotron emission.

The spectra of AM Her systems obtained during the low state show emission lines with significantly reduced strength and their continuum is dominated by emission from the photosphere of the WD and its companion (Gänsicke 1997). The spectra of CSS 080228: 081210+0403 (bottom left of Figure 1.13) and that of RX J1007−2017 (bottom of Figure 1.14) were taken when these systems were in their low state of accretion. For the former, the strength of the Balmer lines is significantly reduced compared to their strength when

they were observed in the high state. In addition, the HeI lines are not seen while HeII 4686 Å is still present in emission. For RX J1007−2017, however, the low-state spectra taken in 1997 March show the absence of prominent Balmer and helium emission lines. The presence of weak Balmer lines and intense cyclotron emission lines indicate that low-level accretion is still taking place. Further to that, the red part of the spectrum is dominated by TiO bands of the secondary star.

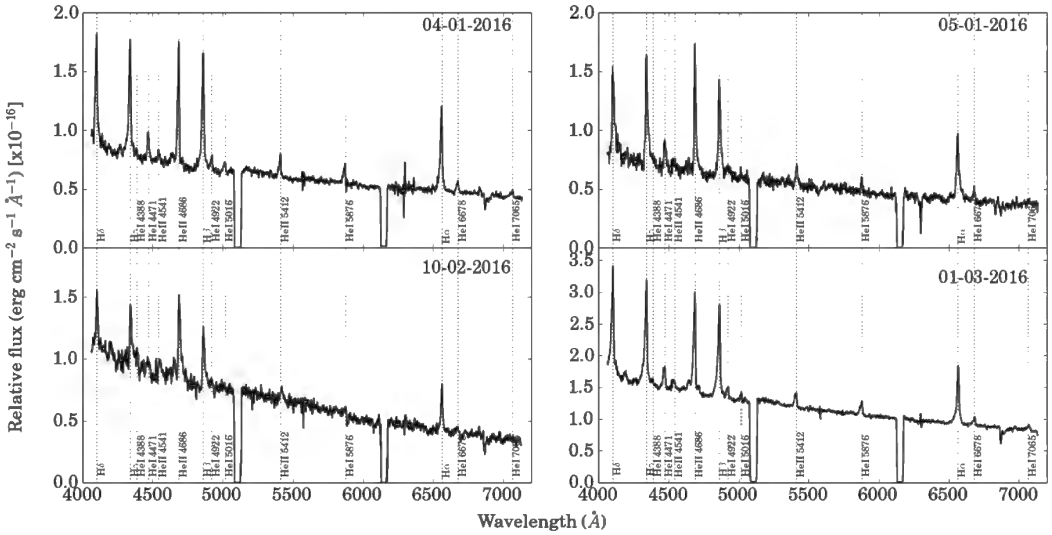

Figure 1.13: The spectra of CSS 080228:081210+040352 obtained with SALT and taken at four different epochs. Adopted from figure 9 of Thorstensen et al. (2020).

The spectra of AM Her systems show variability on time scales ranging from a few days to years. For example, the spectra of CSS 080228:081210+040352 shown in Figure 1.13 show this source undergoing various accretion states within a three-month period. On the other hand, the spectra of RX J1007−2017 shown in Figure 1.14 show spectral variability on time scales of a few years, i.e. from low state (March 1997) to high state (February 2000) within a period of three years.

The ultraviolet spectra of AM Her type systems is characterized by strong emission lines from HeII 1640 Å, CIV 1550 Å, SiIV 1400 Å and NV 1240 Å (Warner 1995a) with occasional MgII at 2800 Å (e.g. V834 Cen, Sambruna et al. 1994). Other lines seen in the ultraviolet spectra of AM Her systems include CIII 1176 Å, CII 1333 Å and SiIII at 1207 Å and the SIII multiplet at 1295−1303 Å. These features have been observed in the spectra of CD Ind, UW Pic and AN UMa (see e.g. Araujo-Betancor et al. 2005b). Sometimes semi-forbidden lines such as NIV 1486, OIII 1663 and NIII 1750 are seen in the ultra-violet spectra of AM Her systems, e.g. MR Ser (Echevarría et al. 1988). The CIV 1550 Å is always the strongest emission feature in ultraviolet spectra of AM Her systems, in both low and high states (Bonnet-Bidaud & Mouchet 1987, Araujo-Betancor et al. 2005b). For example, the ultraviolet spectra of V1432 Aql presented by Friedrich et al. (1996b) show strong emission lines of CIV 1550Å, NV 1240 Å, SiIV 1400 Å and HeII 1640 Å, with CIV 1550Å being the

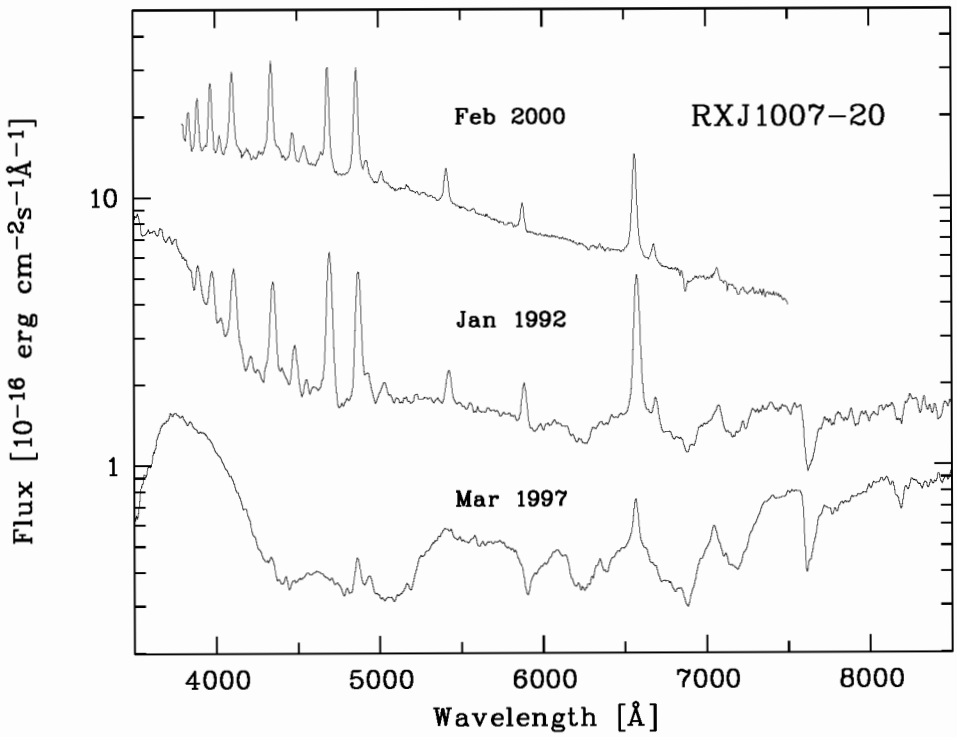

Figure 1.14: The mean spectra of a high-field polar, RX J1007−2017, taken at three different epochs. Adopted from figure 1 of Thomas et al. (2012).

strong feature. The slope of the ultraviolet continuum can be used to determine the surface temperature of the WD whereas the equivalent widths of the emission lines can be used to derive the inclination of the system. Figure 1 of Araujo-Betancor et al. (2005b) shows the far ultraviolet spectra of eleven AM Her systems, three of which were observed in high state. Their high-state spectra (of CD Ind, UW Pic and AN UMa) are dominated by emission from CIV 1550Å, NV 1240 Å, SiIV 1400 Å and HeII 1640 Å, CIII 1176 Å, CII 1333 Å and SiIII at 1207 Å. However, the spectra obtained during low-state show a broad Lyman α absorption feature at 1216 Å with weak emission lines with the exception of MR Ser and V834 Cen, which show a featureless continuum perhaps dominated by cyclotron emission.

The spectra of AM Her type systems are mainly characterized by cyclotron humps observed at infrared and optical wavelengths (Wickramasinghe et al. 1991, Cropper et al. 1989, Kalomeni et al. 2005, and references therein). The intermediate and low-state spectra of RX J1007−2017, Figure 1.14, show cyclotron emission from the accretion column. Modelling of the cyclotron features tell us more about the magnetic strength of the emission region. This topic will be discussed in detail in Section 1.6.

1.5.3 X-ray properties of AM Her systems

The X-ray properties of AM Her systems have been reviewed by different authors (see e.g. Cropper 1990, Warner 1995a) and most recently by Mukai (2017) and de Martino et al. (2020). The post-shock region in AM Her systems produces radiation in a wide range of wavelengths including cyclotron in optical and bremsstrahlung in X-rays and emission from the base of the accretion shock which is absorbed and re-emitted as soft X-ray and ultraviolet radiation (Cropper 1990). For DQ Her systems, however, the accretion curtain is responsible for the emission of optical, X-ray and ultraviolet radiation with little emission in optical. This section gives an overview of some of the X-ray properties of AM Her systems.

Generally, X-ray photons are defined as those photons with energy ranging between 0.1−100 keV and these are more often divided into three components: soft X-rays (0.1−2 keV), medium energy (2−10 keV) and hard X-ray (10−100 keV) bands (Mukai 2017). The medium and high-energy hard X-ray photons are sometimes collectively referred to as hard X-rays, especially when dealing with CVs or AM Her type systems. The X-rays from CVs are mostly emitted through thermal processes either through optically thick (optical depth, $\tau > 1$) or optically thin ($\tau < 1$) emissions. However, this is a clear simplification since most accreting WDs have regions of intermediate optical depth, $\tau \sim 1$ (see Mukai 2017, for a recent review). The hard X-ray light curves from AM Her systems are predominantly shaped by the eclipse of the accretion region, since they are emitted in an optically thin region above the surface of the WD. On the other hand, the soft X-rays are emitted from the surface that is optically thick and therefore limb-darkening effects are also important. The X-ray luminosities of mCVs range from a few $\sim 10^{30}$ erg s^{-1} to $\sim 10^{34}$ erg s^{-1}, and as such, they are the brightest X-ray emitting CVs known (e.g. de Martino et al. 2020).

1.5.3.1 X-ray light curves

Generally, the X-ray light curves of CVs show variability on a variety of time scales ranging from seconds to tens of years. X-ray light curves of synchronous AM Her systems show strong modulation at the orbital period since in these systems the spin and orbital period are the same, e.g. AM Her (Heise et al. 1985), AN UMa (Mason & Gray 2004) and RS Cae (Traulsen et al. 2014). The bottom two panels of Figure 1.8 show examples of X-ray light curves of AM Her that show modulation at the orbital period. Another example of X-ray light curves are shown in the top and bottom panels of Figure 1.15 for AN UMa and reveal strong modulation of X-rays at the orbital period (Ramsay & Cropper 2004a). Figure 2 of Traulsen et al. (2014) shows similar behaviour of modulation of X-rays at the orbital period for RS Cae.

On the other hand, the X-ray (and ultraviolet) emission from asynchronous AM Her systems show variability on two periods, the spin period of the WD and orbital period of the binary. For example, Joshi & Pandey (2019) detected two orbital variations from the X-ray (and ultraviolet) light curves of CD Ind which they attribute to the orbital and spin periods of the WD (see their Figure 4). In addition, Rea et al. (2017) found three periods:

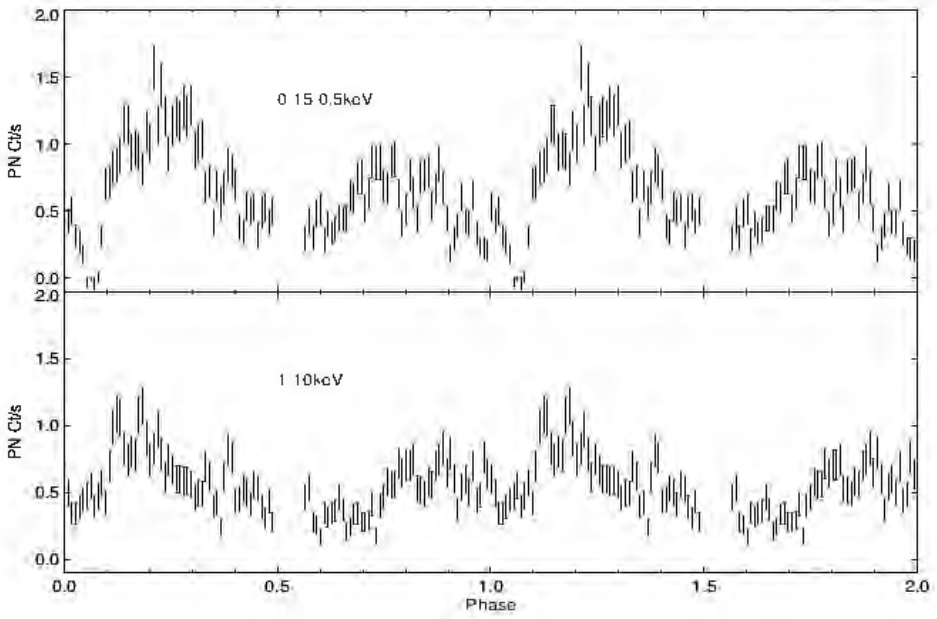

Figure 1.15: The soft (top panel) and hard (bottom panel) X-ray light curves of AN UMa taken with XMM-Newton. Adopted from Figure 2 of Ramsay & Cropper (2004a).

1.64 h, 1.47 h and 1.52 h, in the optical and X-ray light curves of RX J0838−2827 which they attributed to orbital period of system (1.64 h) and spin period of the WD (1.47 h) and the period of 1.52 was interpreted as a beat period. The X-ray spectra of RX J0838−2827 show modulation on these two periods (see their Figure 10).

The shapes of the orbital X-ray light curve of AM Her systems vary from a simple one consisting of a faint phase − during which the source is hardly detected − and a bright phase − where X-ray emission is maximum − to double-peaked shapes and light curves with complex structure. The simple structure of X-ray light curves has been recorded in the literature for e.g. AM Her (Heise et al. 1985, Schwope et al. 2020b, see Figure 1.8), VV Pup (e.g. Mason 1985, Bonnet-Bidaud et al. 2020), ST LMi (Figure 2 of Mason 1985), CSS081231:071126+440405 (Worpel & Schwope 2015) and HY Eri (Beuermann et al. 2020, see Figure 1.9). The faint phase in these systems lasts over half the orbital cycle, indicating that the accretion occurs predominantly in the lower pole − assuming that one pole is visible for part of the orbital cycle. In the case of AM Her, however, the faint phase lasts ∼0.2 of the orbital cycle and this implied that accretion was mainly occurring in the upper pole that suffers a short self occultation (see e.g. Matt et al. 2000). In another study, Bernardini et al. (2014) found that the faint and bright phases of Swift J2218.4+1925 lasts 30% and 70% of the orbital cycle, respectively. The faint phase is understood as due to self-occultation as the accretion region, emitting X-rays, is eclipsed by the WD. In Bernardini et al. (2019), the light curve of 2PBC J0658.0−1746 also shows modulation at the orbital period with a bright and faint phase, typical of AM Her systems and produced by the accretion flow above the main accretion pole that comes into and out of view. However, the faint phase counts

are non-zero suggesting that either the main accretion pole does not disappear completely behind the limb of the WD or there is a second emitting region also producing X-rays. Recently, Schwope et al. (2020a) found 3XMM J000511.8+634018, a new AM Her system discovered in the XMM-Newton catalogue (Rosen et al. 2016), to show a simple X-ray light curve consisting of a faint phase and bright phase lasting 0.55 of the orbital phase − showing similar behaviour to that of VV Pup and ST LMi.

The faint phase in the X-ray light curves of AM Her systems is sometimes not observed. For example, Priedhorsky et al. (1987) reported the disappearance of the faint phase in both the soft and hard X-ray light curves of AM Her during an unusual high state. In addition to that, the observations obtained with EXOSAT and presented by Heise et al. (1985) showed that AM Her was in its reverse soft X-ray mode, with hard and soft X-ray differing by 180° in phase. However, its hard X-ray light curve was similar to those seen during the normal mode, but its soft X-rays were brighter for about half a cycle centered on what is normally the faint phase. Mazeh et al. (1986) found that the optical light curves of AM Her obtained in the reversed mode of accretion were surprisingly similar to those seen during the normal mode. Similarly, Schwope et al. (2020b) reported that AM Her was found in the reverse soft X-ray mode in 2015 (see Figure 1.8) with the soft and hard X-ray light curves differing by 180° in phase. While the reverse soft X-ray mode reported by Heise et al. (1985) showed nonzero flux, that of Schwope et al. (2020b) show a faint phase lasting ∼0.2 of the cycle where the flux is substantially reduced and consistent with zero. Furthermore, the reversed soft X-ray state of AM Her is more complex and appears different each time.

The complex X-ray light curves of AM Her systems comes in a variety of shapes and have been reported for a number of systems including, QQ Vul and EF Eri (Mason 1985), V834 Cen (Sambruna et al. 1991) and AN UMa (Ramsay & Cropper 2004a). The hard X-ray light curve of EF Eri, Figure 1 of Mason (1985), shows a sinusoidal shape with absent faint phase. Similar behaviour was observed in the soft X-ray light curves of V834 Cen as reported by Sambruna et al. (1991) and Ramsay et al. (2004). The soft and hard X-ray light curves of AN UMa show two humps centred around phase 0.3 and 0.8 and this is reminiscent of accretion onto two poles. There are other systems that show double-humps in their X-ray light curves, e.g. MN Hya (Buckley et al. 1998) and XMM J2250+5731 (Ramsay et al. 2009). The former shows aperiodic flaring activities, a pre-eclipse dip and evidence of a second stream flowing to the second magnetic pole. The absence of the faint phase in these systems was attributed to either the active pole is always visible or accretion takes place on both poles.

In addition to complex structures, the shapes of X-ray light curves of some AM Her systems exhibit different structures from one epoch to another. For example, the X-ray light curves of QQ Vul (Mason 1985) and V834 Cen (Sambruna et al. 1991) and those presented by Osborne et al. (1987b) and Sambruna et al. (1994) for the same systems are different in structures or shapes. The cause for this is additional factors other than multiple emission regions in these systems. In the case of QQ Vul, the 1983 October and 1985 June soft X-ray light curves showed two peaks; a broad peak at phase 0.8–1.0 and a narrower

peak at 0.45–055. But the soft X-ray light curve obtained on 1985 September showed two peaks with similar strength centred at phases 0.25 and 0.65. While for V834 Cen, the soft X-ray light curves obtained in 1984, 1985 and 1986 (Figure 1 of Sambruna et al. 1994) vary in shape from asymmetrical to double-humped, with a broad minimum occurring at phase range $\sim 0.3-0.5$. The hard X-ray light curves of this source, Figure 2 of Sambruna et al. (1994), appear to be sinusoidal with the common feature being the dip between phase 0.9 and 0.1, which is almost consistent with the soft X-ray light curves. The optical light curves, taken simultaneously with the EXOSAT observations, also show similar changes in shape from asymmetric to double humped (see Osborne et al. 1987a). According to Mukai (2017), these changes observed within a few years, can not be explained by the change in magnetic field but can be attributed to other factors that can change from one epoch to another, e.g. mass transfer rate. Furthermore, they argued that in order to interpret such complex X-ray light curves of AM Her systems, it is recommended to treat each peak as representing a distinct emission region and this would possibly require a complex magnetic field geometry beyond a simple dipole (see e.g. Mukai 2017). However, the presence of multiple emission regions does not necessarily mean that the WD has a complex magnetic field geometry.

Similar to their photometric counterparts, some of the soft X-ray light curves of AM Her systems show a narrow dip lasting $\sim$0.1 of the orbital cycle and which is attributed to the occultation of the emitting region by the magnetic stream towards the upper pole (King & Williams 1985). These dips have been observed in the X-ray light curves of e.g., MN Hya (Schwarz et al. 2002), AN UMa (see Figure 1.15, Mason & Gray 2004), V834 Cen (see Figure 1 of Mason (1985)), CE Gru (Ramsay & Cropper 2002), Swift J2218.4+1925 (Bernardini et al. 2014) and most recently in CSS081231:071126+440405 (Worpel & Schwope 2015) and 2PBC J0658.0−1746 (Bernardini et al. 2019). For 2PBC J0658.0−1746, however, this feature was prominent during the strongest two bright phases observed. In addition to the above, the X-ray light curves of AM Her systems were suspected to show quasi-periodic oscillations (QPOs) and aperiodic variability. For example, Bonnet-Bidaud et al. (1991) reported detection of X-ray QPOs in the light curves of AM Her with periods of 250-280 s. In another study, Beardmore et al. (1995) reported that the X-ray spectra of QQ Vul exhibit 450 s QPOs with amplitude of $\sim$30 percent from the ROSAT observations. However, following recent observations with XMM-Newton, Bonnet-Bidaud et al. (2015) and Bonnet-Bidaud et al. (2020) reported non-detection of QPOs in the X-ray light curves of AM Her and VV Pup.

1.5.3.2 The soft X-ray problem

The post-shock region releases kinetic energy in the form of thermal Bremsstrahlung (hard X-rays) and cyclotron radiation, which is highly polarized. However, about half of the Bremsstrahlung and cyclotron flux is absorbed by the WD's photosphere and re-emitted as soft X-rays. The following relation (i.e. equation 1 of Lamb 1985) holds,

$$L_{\rm SX} \simeq L_{\rm tb} + L_{\rm cyc} \tag{1.6}$$

where $L_{\rm SX}$ is the soft X-ray luminosity, $L_{\rm tb}$ is the luminosity of the thermal Bremsstrahlung radiation and $L_{\rm cyc}$ is the luminosity of the cyclotron radiation. However, the observed soft X-ray flux in some if not most AM Her systems exceeds the sum of thermal Bremsstrahlung and cyclotron radiation by a large factor (see e.g. Beuermann & Schwope 1994, Ramsay et al. 1994). According to the standard model of the shock region, the ratio of the re-processed radiation (e.g. L_{SX}) to that directly emitted by the shock (e.g. L_{tb}) should be $L_{reprocessed}/L_{shock} = L_{SX}/L_{tb} \sim$0.5 (see e.g. Lamb & Masters 1979, King & Lasota 1979). However, the observations of AM Her systems made with EXOSAT and ROSAT between 1983 and 1999 found that a number of these systems showed a large soft X-ray excess, i.e. the ratio was well in excess of that predicted by the standard model (e.g. Cropper 1990, Ramsay et al. 1994, Beuermann & Burwitz 1995). For example, the ratio of soft X-ray to hard X-ray of AR UMa and V884 Cen was estimated to be $\simeq$50–1000 (Szkody et al. 1999). This deviation from the predictions is known as the "soft X-ray puzzle" or "soft X-ray excess" and had been the subject of investigation in the late 1980s and 1990s (Cropper 1990). For example, Ramsay et al. (1994) found that when bolometric luminosities were used, a significant number of AM Her systems (e.g. UZ For, VV Pup, AN UMa, QS Tel, etc.,) nevertheless showed large soft X-ray excesses. In addition, they found that a number of objects were consistent with a model which includes radiative heating only. Radiative heating involves absorption, scatterings, and re-emissions of photons. On the other hand, reprocessing of X-rays refers to the process by which the emitted radiation interacts with the matter surrounding the WD and is re-emitted. In another study, Beuermann & Burwitz (1995) calculated the ratio of soft-to-hard X-ray luminosity from the ROSAT band (0.1–2.4 keV) and found that the soft X-ray excess is significantly reduced if one assumes that cyclotron radiation dominates the emission for AM Her systems with magnetic field strengths $\gtrsim$30 MG. Note that cyclotron radiation is a cooling the shock unlike thermal Bremsstrahlung. Therefore, the luminosity ratio will be lower. It is worth mentioning that some DQ Her systems also show soft X-ray excess, e.g. V2400 Oph (Joshi et al. 2019).

Different models were proposed to explain the soft X-ray excess in mCVs, these include nuclear burning on the surface of the WD (Raymond et al. 1979, Papaloizou et al. 1982), accretion energy being transported by electron conduction into the WD and being re-emitted as soft X-rays (Fabian et al. 1976, King & Lasota 1980, Frank et al. 1988) and the bombardment model (Kuijpers & Pringle 1982, Thompson & Cawthorne 1987). However, none of these models could account for the soft X-ray excess in AM Her systems. The most accepted solution to the soft X-ray problem is the "blobby" accretion first proposed by Kuijpers & Pringle (1982) and further developed by different authors (e.g. Frank et al. 1988, Lichfield & King 1990, Frank et al. 2002). According to this model, soft X-rays could be produced by dense blobs that penetrate the WD's photosphere resulting in a buried shock. The hard X-rays emitted by the shock are thermalized in the photosphere of the WD, with the energy eventually released as soft X-rays. According to Cropper et al. (2000), soft X-rays can also be produced near the base of the post-shock region. Heise & Verbunt (1988) found that in the reversed on-state of AM Her, the ultraviolet and the hard X-ray maxima were sometimes

in anti-phase with the soft X-rays minima. This led them to conclude that the reprocessed component is emitted in the extreme-ultraviolet rather than as soft X-rays. Schmidt (2004) argued that the ratio of soft X-ray or extreme-ultraviolet emission reprocessed off the WD surface to Bremsstrahlung is almost 50:50.

Ramsay & Cropper (2004b) demonstrated the dependence of the soft-to-hard X-ray luminosity ratios on calibration, geometrical effects and spectral models. This was achieved by using accretion column models of Cropper et al. (1999) to recalibrate the ROSAT and XMM-Newton data. Ramsay & Cropper (2004b) came to the conclusion that fewer systems show a distinct soft X-ray excess than originally estimated from the ROSAT observations. Recently, XMM-Newton has uncovered a number of AM Her systems without a distinct soft X-ray component (see e.g. Ramsay & Cropper 2004b, Ramsay et al. 2004, Worpel et al. 2016, Bernardini et al. 2017). This suggests that if the reprocessed component exists in these systems, it should have a low temperature, shifting the emission towards the ultraviolet and extreme ultraviolet ranges. Based on these new findings, de Martino et al. (2020) suggest that AM Her systems should not be characterized as soft X-ray emitting sources any longer. Furthermore, XMM-Newton – with its high sensitivity – has increased the number of DQ Her systems showing a soft blackbody component from three systems (discovered with ROSAT) to 19 and this represents ∼30% of all known DQ Her systems (e.g. Bernardini et al. 2017). See Mukai (2017) and de Martino et al. (2020) for further details on the soft X-ray problem as well as X-ray reviews of mCVs.

1.5.3.3 X-ray spectra

This section gives a general review of X-ray spectral properties of AM Her systems together with a few examples. See Mukai (2017) and de Martino et al. (2020) for recent developments in this topic. Generally, the spectra of mCVs are characterized by a multi-temperature optically thin plasma which is indicated by the presence of 6−7 keV iron complex with H-like Fe XXVI at ∼6.9 keV and He-like Fe XXV Kα line at 6.7 keV (see e.g. de Martino et al. 2020). The other lines seen in the spectra of mCVs include weaker K-shell features of less heavier elements and a neutral Fe Kα fluorescent component. Recent observations of mCVs conducted with XMM-Newton and *Chandra* (Weisskopf 1999, Weisskopf et al. 2000) grating spectra have shown that at least three DQ Her systems show the presence of O VII absorption edge in their X-ray spectra (e.g. de Martino et al. 2008). An example X-ray spectrum of an AM Her system is shown in Figure 1.16 with prominent emission lines labelled.

The first X-ray spectra of an AM Her system was obtained by the HEAO-1 (Fishman 1977, Nugent et al. 1983) satellite in 1978 for AM Her covering energies from 0.1−150 keV. The spectra in discussion were analyzed by Rothschild et al. (1981). The X-ray spectra of AM Her showed two components: a soft X-ray component falling rapidly between 0.2 and 0.4 keV and a hard X-ray component above 2 keV. The spectra were devoid of features except for a prominent emission feature at 6.5 ± 0.15 keV and this was explained as due to fluorescence from the WD by the bremsstrahlung from a small thin shocked region. The emission feature

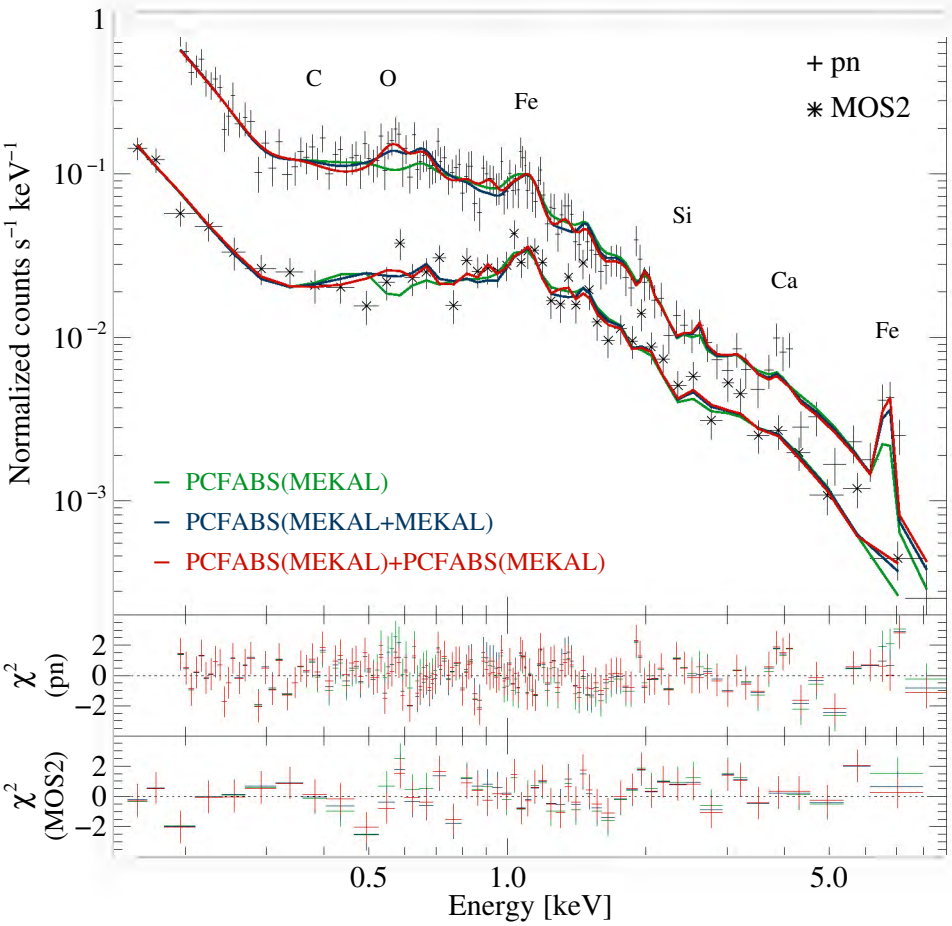

Figure 1.16: The X-ray spectrum of QS Tel obtained in 2006 September with XMM-Newton. Adopted from Figure 3 of Traulsen et al. (2011).

at 6.4 keV in the X-ray spectra of mCVs is now identified as fluorescence from iron Kα line, e.g. V834 Cen (Sambruna et al. 1994), CSS081231:071126+440405 (Worpel & Schwope 2015) and VV Pup (e.g. Bonnet-Bidaud et al. 2020). In at least one example, Bernardini et al. (2019) noted that the fluorescent line at 6.4 keV was not observed in the X-ray spectra of 2PBC J0658.0−1746. But they attributed this to the faintness of the source and low signal-to-noise data from XMM-Newton. A recent study of 19 mCVs conducted by Eze (2015) resolved the 6.4 keV, 6.7 keV and 7.0 keV Fe Kα emission lines. They attributed the 6.7 keV and 7.0 keV emission lines to collisions in the vicinity of the WD arising from the shock front. Their results suggest that the 6.4 keV line emission is likely created by a combination of reflection of hard X-rays from the WD's surface and absorption-induced fluorescence. The reflection, either at the WD surface or in the pre-shock flow of mCVs, is confirmed by the presence of fluorescent Fe at 6.4 keV (Ezuka & Ishida 1999).

For AM Her, the soft X-ray spectra were fitted with a blackbody and exponential shapes including absorption from the cold gas in the intervening area. The hard X-ray spectra,

i.e. spectra above 2 keV, were fitted with a power law and a bremsstrahlung continuum model which included photoabsorption by cool gas and the effect of the emission at 6.4 keV. Rothschild et al. (1981) noted that different energy ranges of the hard X-ray spectra of AM Her needed to be fitted with different power laws and they also found that no single-temperature thermal bremsstrahlung continuum could explain all the data from the different detectors used. This study demonstrated that modelling of X-ray spectra of mCVs requires complexities at low energies due to the presence of complex absorption from neutral material located in the pre-shock flow with column densities reaching $\sim 10^{23}$ cm^{-2} (see e.g. Mukai 2017) and multi-temperature optically thin or thick models. Therefore in order to make sense of the spectra of AM Her systems, models such as blackbody, exponential, thermal bremsstrahlung continuum and power laws, etc., are required to fit the X-ray spectra of mCVs. In some cases, however, simple models consisting of a bremsstrahlung continuum plus iron line emission, with absorption, have been found to adequately describe the GINGA (e.g. Makino & ASTRO-C Team 1987, Swinbanks 1987) hard X-ray spectra seen in mCVs, e.g. Ishida (1991).

As an example, Sambruna et al. (1994) used a blackbody model to fit the low-energy X-ray emission from V834 Cen, while the medium-energy X-ray spectra were fitted with absorbed bremsstrahlung and power-law spectral models. The Fe feature at 6.4 keV was fitted with a Gaussian profile. Figure 1.16 shows an X-ray spectrum of QS Tel obtained in 2006 and presented by Traulsen et al. (2011) which is fitted with a black-body component and two partially absorbed plasma components. In another study, Elkholy & Nouh (2015) used a three multi-models: a soft X-ray blackbody, hard X-ray thermal bremsstrahlung and an intermediate component or a simple Gaussian line, to fit the X-ray spectra of VV Pup obtained with ROSAT covering energy from 0.1−2 keV. VV Pup was observed by XMM-Newton in 2007 by Bonnet-Bidaud et al. (2020) and its X-ray spectrum showed an Fe line at 6.76 keV. The X-ray spectra was first modelled using the sum of a blackbody (0.14 keV) and a high temperature ($\sim$ 39 keV) bremsstrahlung component, with absorption by cold matter and fitted the Fe line at 6.76 keV with a Gaussian profile. However, the final X-ray spectra model for VV Pup was achieved by using an *ipolar*[*] model in addition to a blackbody component, a bremsstrahlung component with high temperature and the Gaussian profile. In another study, Worpel & Schwope (2015) presented an X-ray spectra of CSS081231:071126+440405 obtained with XMM-Newton. Their spectra was fitted with a multi-temperature model including blackbody-like and a hot thermal component. Other recent studies of AM Her systems exist in the literature, e.g. those of Joshi et al. (2020) and Schwope et al. (2020b) which employ similar techniques of multi-temperature and multi-model fitting as discussed above.

[*]The ipolar model was developed for DQ Her systems and it allows for specifying of the capture point of the material by the magnetic field lines in terms of the WD radius.

1.6 Cyclotron radiation

Cyclotron radiation is emitted when a non-relativistic electron gyrates about the magnetic field giving off energy. It is emitted at the frequency of gyration called gyrofrequency (ω_o). In order to understand cyclotron radiation, we consider a charged particle, i.e. an electron with a charge e, moving at a velocity $\vec{v}$ in a uniform magnetic field $\vec{B}$ as shown below in Figure 1.17.

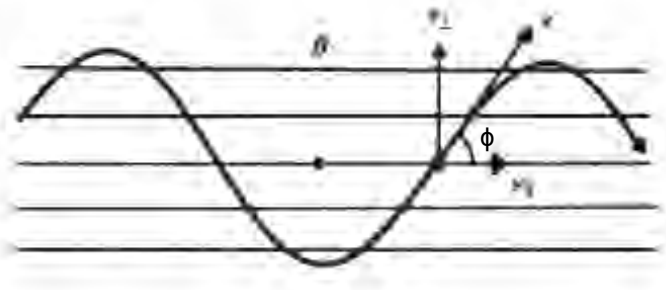

Figure 1.17: A schematic showing the motion of an electron gyrating around the uniform magnetic field. Adopted from Figure 7.1 of Longair (2011).

The charged particle will experience a Lorentz force given by

$$\vec{F}_e = e\left(\frac{\vec{v}}{c} \times \vec{B}\right) \tag{1.7}$$

where c is the speed of light and assuming negligible electric field $\vec{E}$ so that $e\vec{v}\dot{E} = 0$ implying that the magnitude of $\vec{v}$ is constant. Note that the direction of the Lorentz force (Eq. 1.7) is perpendicular to both $\vec{v}$ and $\vec{B}$ and its magnitude is given by e.g. equation 8.25 of Irwin (2007) shown below:

$$F_e = \frac{ev}{c} B \sin\phi = \frac{ev}{c} B_\perp \tag{1.8}$$

where ϕ is the angle between $\vec{v}$ and $\vec{B}$, which is also known as the pitch angle and $B_\perp = B\sin\phi$. It follows from Eq. 1.7 that

$$m_e\gamma\frac{d\vec{v}}{dt} = \frac{e\vec{v}}{c} \times \vec{B} \tag{1.9}$$

where γ is the Lorentz factor of the electron given by $\gamma = 1/\sqrt{1 - v^2/c^2}$. Separating the velocity components, $\vec{v}_{||}$ – velocity of the electron along the magnetic field and $\vec{v}_\perp$ – velocity of the electron in a plane normal to the magnetic field gives

$$\frac{d\vec{v}_{||}}{dt} = 0, \quad \frac{d\vec{v}_\perp}{dt} = \frac{e}{\gamma m_e c}\vec{v} \times \vec{B}. \tag{1.10}$$

Equation 1.10 implies that both $\vec{v}_{||}$ and $\vec{v}_\perp$ are constant and result in a uniform circular motion of the charged particle on the normal plane (see Figure 1.18(a)). On the other hand,

the combination of circular motion and constant uniform motion along the magnetic field result in a helical motion of the electron (see Figure 1.18(c)). Thus the electron will produce a spiral motion around the magnetic field and, therefore, it will have both velocity components, that is, $\vec{v}_{||}$ and $\vec{v}_{\perp}$. Here $\vec{v}_{||}$ is the velocity of the electron parallel to the magnetic field and therefore not affected by it. The perpendicular component of the velocity is $\vec{v}_{\perp} = v \sin \phi$. Figure 1.18 will be discussed in detail in Section 1.7.

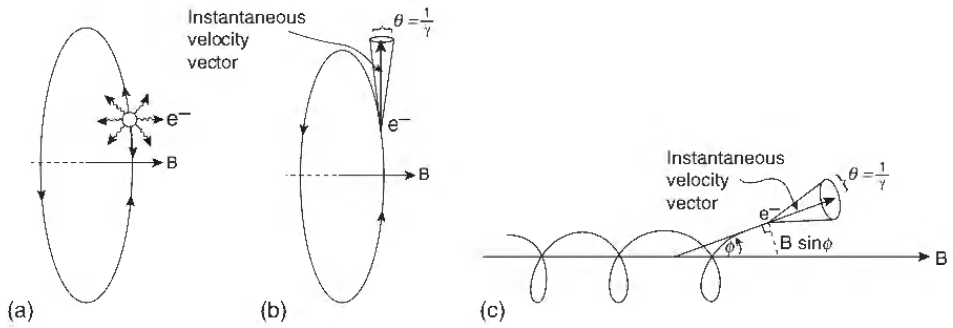

Figure 1.18: A schematic showing radiation given off by an electron with initial speed, $\vec{v}$, gyrating around field lines of strength, B. See text for more details. Adopted from Figure 8.10 of Irwin (2007).

The Lorentz force (Eq. 1.8) can be equated to the centrifugal forces to give:

$$F_e = \frac{ev_{\perp}}{c} B_{\perp} = \frac{\gamma m_e v_{\perp}^2}{r_o} \tag{1.11}$$

where r_o is the orbital radius that is perpendicular to the magnetic field, called gyroradius or radius of gyration. Solving for r_o from the above equation and equating it to the expression ($r_o = v_{\perp}T/2\pi$, given by the relation between velocity, distance and time) and substituting $T = 1/\omega_o$, we get:

$$r_o = \frac{\gamma m_e v_{\perp} c}{eB} = \frac{v_{\perp} T}{2\pi} = \frac{v_{\perp}}{2\pi\omega_o} \tag{1.12}$$

where T is the period of gyration. It follows for Eq. 1.12 that the gyrofrequency or radius of gyration of the electron (ω_o) is given as follows

$$\omega_o = \frac{eB}{2\pi\gamma m_e c}. \tag{1.13}$$

Therefore, an isolated electron will gyrate at gyrofrequency ω_o given by Eq. 1.13 above and emit radiation at all harmonics (n), that is, integer multiples (n = 1,2,3, ...) of this fundamental frequency. The energy of the electron affects the frequencies at which the radiation is emitted and also the distribution of the energy amongst the harmonics. That is, the more energetic the electron the higher the harmonics at which the radiated power is emitted. The emitted radiation is circularly polarized if viewed along the magnetic field lines and linearly polarized if viewed perpendicular to the magnetic field lines. Generally, cyclotron

radiation is emitted at an intermediate angle (ϕ) and therefore it is elliptically polarized (see Drummond & Rosenbluth 1963). The intensity of the radiation is also dependent on the direction of the magnetic field lines and on the harmonic of the radiation. That is, at high harmonics the anisotropy in the intensity is very pronounced with the radiation being restricted to a narrow beam centred on the orbital plane of the electrons circular motion. Near the fundamental frequency the anisotropy is less pronounced.

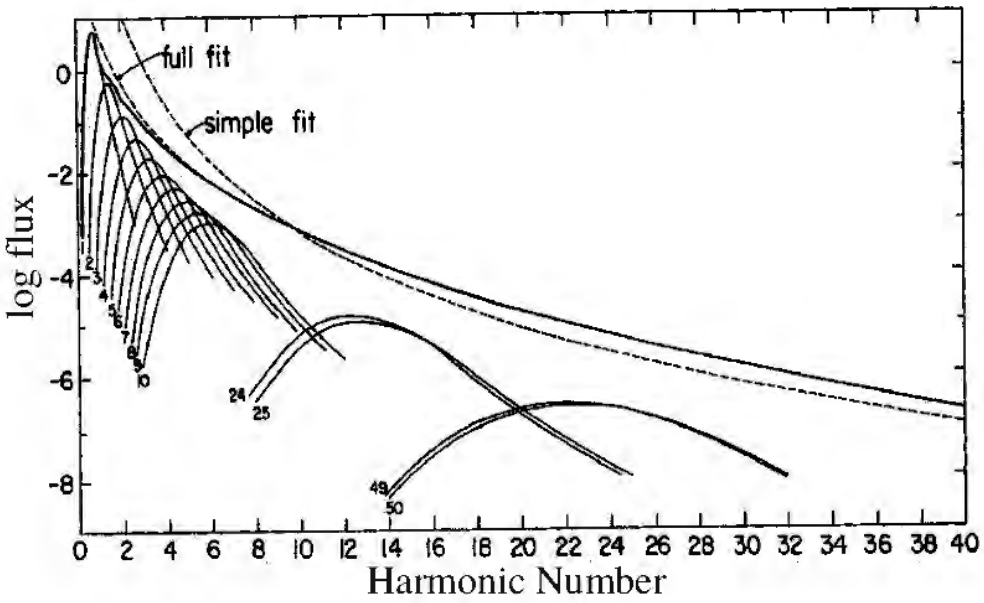

Figure 1.19: Distribution of the energy amongst the first 50 harmonics for a viewing angle $\phi = 0.16$. Adopted from Masters (1978).

Thus the emission from a group electrons will have a distribution of energies resulting in the broadening of the harmonics. The low energy electrons (i.e. $\gamma \simeq 1$) will emit cyclotron radiation near the frequencies $n\omega_c$, where ω_c is the cyclotron frequency. On the other hand, the highly energetic electrons (i.e. $\gamma \gg 1$) will radiate at frequencies $n\omega_o = n\omega_c/\gamma \ll n\omega_c$. In general, the line width due to this relativistic mass increase would be of the order of the square of the electron's thermal energy. However, the more energetic electrons emit cyclotron radiation at higher harmonics. Therefore, the higher harmonics will be broader than the lower ones and shifted towards lower frequencies (see Figure 1.19). The distribution of Doppler shifts of radiation from electrons moving towards and away from the observer is also an important broadening mechanism at angles of $\phi = 0°$. At high temperatures the broadening mechanism is partly compensated by the beaming of the radiation, most of the radiation being emitted in the direction of the motion (Masters 1978, Meggitt & Wickramasinghe 1982). It is worth mentioning that towards higher harmonics (and shorter wavelengths), the cyclotron emission becomes optically thin. While at lower harmonics, the cyclotron emission is optically thick since the excess flux is absorbed resulting in the

loss of any cyclotron hump information. Lamb & Masters (1979) pointed it out that at lower harmonics, the cyclotron emission would be greater than the Raleigh-Jeans tail of the blackbody emission. The spacing of any two adjacent cyclotron humps in the spectrum also provides a direct measurement of the magnetic field in the accretion region. This will be demonstrated in Chapter 4.

Faraday mixing and cyclotron absorption coefficients

As already mentioned above, cyclotron radiation will generally be elliptically polarized and becoming circularly polarized when viewed emitted along the magnetic field lines or linearly polarized when emitted orthogonal to the field lines. However, as the physical depth (s/s_o) of the plasma increases two mechanism becomes important. Firstly, Faraday mixing coefficients (f, h) can change the ratio of linear to circular polarization and plays an important role only if it dominates over cyclotron absorption coefficients (q, v). Note that cyclotron absorption coefficients are dependent on the physical depth. At intermediate and high harmonics ($n \geq 5$ in this temperature range) we get:

$$f^2 + h^2 \gg q^2 + v^2.$$

When the above approximation is valid, the ratio of linear to circular polarization is independent of the depth s. Thus for $\omega/\omega_c \geq 5$, the linear polarization is confined to angles near $\phi = 90°$ giving the appearance of a pulse. Meggitt & Wickramasinghe (1982) noted that at sufficiently low harmonics, where large values of the opacity are encountered, the values of the cyclotron absorption coefficients are comparable with or even exceed the Faraday mixing coefficients. In these circumstances the dominant effect is depolarization with Faraday mixing terms playing a minor role. Secondly, the total polarization decreases to zero as the intensity approaches the Plank function, that is to say, one can not have more intensity than given by the Plank function. As mentioned in Meggitt & Wickramasinghe (1982), there is a third regime of large optical depth in which the intensity approaches the Plank function and so does not vary with angle. However, the radiation in this regime is completely unpolarized.

The two effects mentioned above give rise to a number of interesting conclusions. Foremost, the lower harmonics become depolarized quickly at low optical depths without any appreciable Faraday mixing as a result of their high opacity. Thus the computations for ω/ω_c of the lower harmonics, such as those of Meggitt & Wickramasinghe (1982), do not show the confinement of linear polarization around $\phi = 90°$. While for intermediate and high harmonics ($n \geq 5$ at 20 keV) with a moderate path length of material, Faraday mixing results in the production of linear polarization at angles near $\phi = 90°$. However, as the path length is increased the linear polarization gradually disappears as a result of depolarization. As mentioned in Meggitt & Wickramasinghe (1982), the linear polarization persists for a larger range of values of s/s_o at $\omega/\omega_c = 15$ than at $\omega/\omega_c = 5$ due to the general decrease in opacity with frequency. In addition, the increase in opacity with temperature means

that shorter path lengths are required to depolarize the radiation. The observation of an intermittent linear polarization pulse in AM Her systems is understood as a result of of the change in the extent of the emitting region (or path length). Furthermore, the existence of a persistent linear pulse in highly variable system may imply high harmonic radiation. Generally, opacity decreases greatly as the angle from the magnetic field approaches zero making it necessary for the path lengths to be larger to depolarize the radiation. As a result some circular polarization will persist in most circumstances, in contrast to the situation with linear polarization.

Further details on cyclotron radiation, polarization and cyclotron absorption coefficients, etc., can be obtained in the following studies: Meggitt & Wickramasinghe (1982), Barrett & Chanmugam (1984), Wickramasinghe & Meggitt (1985) and Chanmugam et al. (1989), to name a few. It is worth mentioning that the calculations of Meggitt & Wickramasinghe (1982) did not include the effects of free-free opacity whereas that of Wickramasinghe & Meggitt (1985) included the effects of free-free opacity. However, Wickramasinghe & Meggitt (1985) did not include the difficult problem of electron scattering since they reasoned that the variation in the optical depths of electron scattering, free-free opacity and cyclotron opacity, with viewing angle respect to the direction of magnetic field, shows that scattering can not be dominant. On the other hand, Chanmugam et al. (1989) used two methods: the first of which is an improved version of that of Chanmugam & Dulk (1981) which uses single particle method and the second one is based on dielectric formulation of Tamor (1978).

Generally, the observation of cyclotron harmonics in the spectra of AM Her systems provides information about the magnetic field strength and the physical conditions in the accretion region. For one-pole accretion, the cyclotron emission is only seen during the bright phase when the emitting region is in view although it is contaminated by other sources such as the emission from the ballistic and magnetically confined accretion stream as well as the irradiated secondary star. Therefore, before analysing the cyclotron spectra, it must first be decontaminated. One such technique that has been used in the past was stream-emission subtraction whereby a spectrum from the faint phase was subtracted from the spectra from the bright phase (see e.g. Schwope & Mengel 1997). This technique assumes that the spectra from the faint phase represent all the additional components of radiation which obfuscate the cyclotron emission. The spectra of the secondary star changes slowly with phase and cannot be completely subtracted from the bright-phase spectra.

1.6.1 Modelling cyclotron radiation

Magnetic fields play an important part in determining both the gas dynamics of mass transfer and the radiation properties in mCVs (Wickramasinghe & Ferrario 2000a). When the mass transfer rate drops below a certain level, the WD photosphere is revealed. The Zeeman intensity and polarization spectra (when available) allow strong constraints to be placed on the surface averaged field and on field structure. In addition, cyclotron spectroscopy provides direct information on magnetic field strengths at the accretion shocks.

Several attempts at modelling the observations of AM Her have been made. For example, Chanmugam & Dulk (1981) performed the calculations for cyclotron radiation from a hot plasma in a temperature of 0.2−20 keV. On the other hand, Meggitt & Wickramasinghe (1982) provide the calculations of the intensity and polarization of the cyclotron radiation from emission regions of uniform temperature, density and magnetic field. Detailed modelling began with Barrett & Chanmugam (1984) who assumed that the post-shock region is uniform, semi-infinite and plane parallel. In other attempts, Wickramasinghe & Meggitt (1985) assumed that the post-shock region is a point source. These models failed or could not explain several observational features that are common to many AM Her systems. Wickramasinghe & Ferrario (1988) constructed models characterized by cylindrically extended cyclotron emission regions displaced from the magnetic poles and with a temperature and density structure across the shock. Their model closely agreed with some of the observed properties of AM Her stars but could not reproduce other properties such as the asymmetries observed in the light and polarization curves. Ferrario & Wickramasinghe (1990) introduced arc-shaped cyclotron emission regions constructed by dividing the cyclotron region into elements, each with its own temperature, optical depth and magnetic field. The model allows inhomogeneities in temperature and density to be introduced along the linearly extended region. This model is more successful and was applied to several systems including ST LMi and V834 Cen (Wickramasinghe & Ferrario 1995) as well as MN Hya (Buckley et al. 1998). Schwope (1990) developed a constant-lambda (Λ) models (Schwope et al. 1990) in order to model cyclotron emission from mCVs. This model depends on four global parameters: magnetic field, the plasma temperature, the viewing angle of the magnetic pole and the size parameter which is closely linked to the column density along the line of sight through the accretion region. The constant-lambda model has been used to model spectra of several systems, e.g. AM Her and ST LMi (Campbell et al. 2008b), V1500 Cyg (Harrison & Campbell 2018) and recently on RX J0859.1+0537, RX J0749.1−0549, and RX J0649.8−0737 (Joshi et al. 2020).

1.6.2 The model of stratified accretion shock

For this thesis in Chapter 4, however, we will use the model of stratified accretion shocks described in Potter et al. (2002) as well as Chapter 2 and 4 of Potter (1998) and applied to both AM Her systems e.g. ST LMi (Potter 2000) and DQ Her systems e.g. PQ Gem (Potter et al. 1997) to model circularly polarized spectra of UZ For in order to determine the magnetic field strength of this system. The model of stratified accretion shock uses the hydrodynamic model of Cropper et al. (1999) to determine the structure of the post-shock region. The intensity and polarization of the emission are calculated from the four Stokes formulation for cyclotron opacity and radiative transfer described in Meggitt & Wickramasinghe (1982) and Wickramasinghe & Meggitt (1985). Note that the cyclotron absorption coefficients of Meggitt & Wickramasinghe (1982) and Wickramasinghe & Meggitt (1985) were found to be unreliable by Chanmugam et al. (1989). This thesis, specifically in Section

4.4.3.3, used cyclotron absorption coefficients* from Potter et al. (2002) obtained from their accretion shocks modelling and shown in their Figure 1 as contour plots. As demonstrated in Figure 5.4 of Potter (1998), a single-temperature model is insufficient in reproducing the cyclotron spectrum in ST LMi. They noted that a lower temperature and possibly a lower density region is required to reproduce the cyclotron humps in the optically thick part of the spectrum and a higher temperature and density region to reproduce the correct spectral slope. Therefore, multiple temperature models are required in order to reproduce the cyclotron humps in the spectrum. Their combined spectrum (bottom panel of Figure 5.4) is a significant improvement over the single temperature model in that the spectral slope and the general morphology of the cyclotron humps are reproduced.

1.6.3 Magnetic field strength in AM Her systems

There are three methods by which the magnetic field of the WD in AM Her systems can be determined. As mentioned in Ferrario et al. (2015), indirect measurements of the magnetic field strength of the WDs in these systems can be obtained through one of the following methods: modelling of cyclotron emission features, through Zeeman splitting of the photospheric hydrogen absorption lines observed during low states and through studying non-photospheric (or halo) Zeeman features (see e.g. Bailey 1995). The list† of known (114) or suspected AM Her systems with measured magnetic field strength and the methods used are given in Table 2 of Ferrario et al. (2015). The above-mentioned methods are discussed in Section 1.6.3.1 to 1.6.3.3 and we give some examples. Note that there are AM Her systems whose magnetic field strengths has been measured using two different methods. At least three systems (BL Hyi, V834 Cen and MR Ser) have had their magnetic field strengths determined from the three methods mentioned above.

1.6.3.1 Cyclotron spectroscopy

Cyclotron features are seen as a series of broad humps in the optical (3000 Å <= λ <= 7000 Å) and near-infrared (7000 Å <= λ <= 14000 Å) spectrum of AM Her systems during intermediate and high accretion states (e.g. Wickramasinghe & Ferrario 2000b). In other instances, extending the observations into the infrared (1.0 μm <= λ <= 2.4 μm), where the lower harmonics are seen, allow for the application of this method. Cyclotron features occur at harmonics of the cyclotron frequency and were first seen in the spectra of VV Pup (Visvanathan & Wickramasinghe 1979). However, thermal Doppler broadening can smear out the higher harmonics into a featureless continuum, but in favourable circumstances individual harmonics may be resolved. Cyclotron features has been identified in at least 71 of the 114 AM Her systems listed in Table 2 of Ferrario et al. (2015) and this has led to the determination of the filed strengths in these systems.

*The cyclotron absorption coefficients from Potter et al. (2002) were never published as Tables as does Chanmugam et al. (1989) and Vaeth & Chanmugam (1995).

†Table 2 listed 104 confirmed AM Her systems and 10 pre-AM Her systems up to 2015.

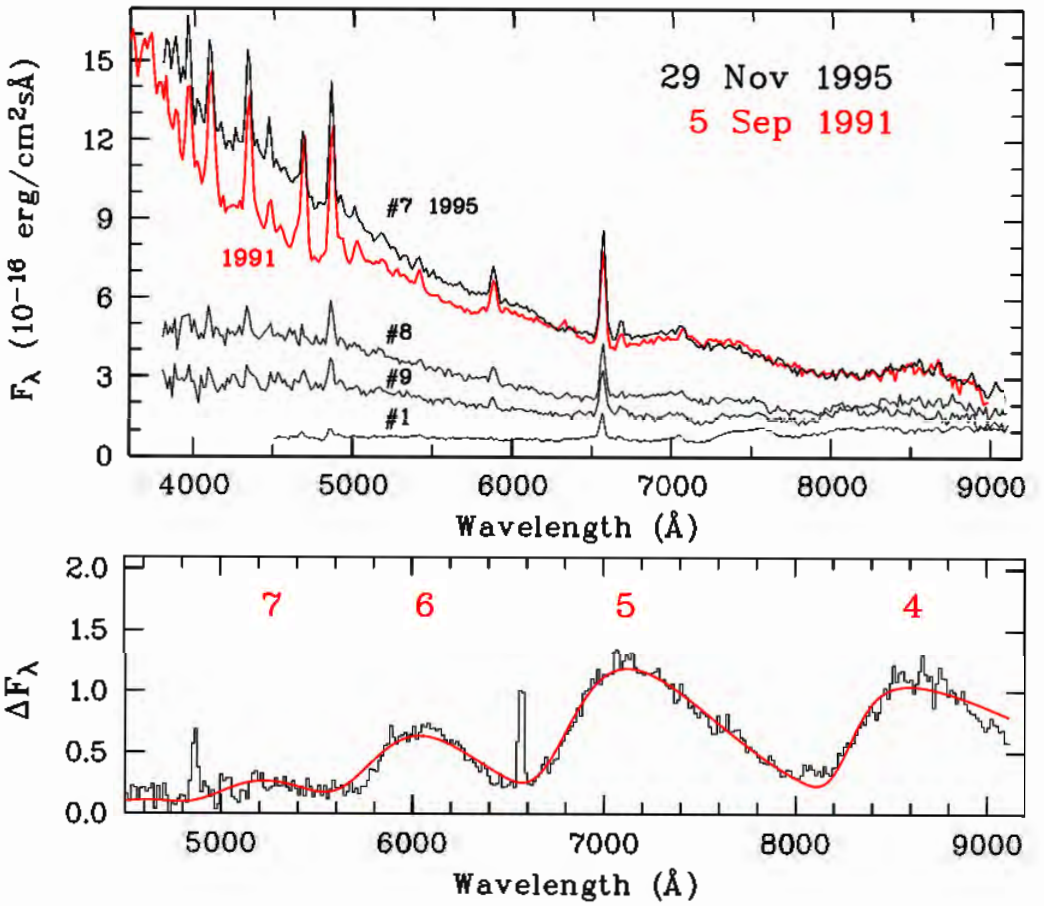

Figure 1.20: An example spectrum of V358 Aqr showing cyclotron humps. Adopted from Figure 4 of Beuermann et al. (2017).

The bottom panel of Figure 1.20 shows an example of a cyclotron spectrum of V358 Aqr presented by Beuermann et al. (2017). The cyclotron spectra of V358 Aqr shows the presence of four cyclotron humps and was fitted with a model of isothermal plasma from Chanmugam & Dulk (1981) with a field strength of 31.8 ± 0.2 MG in a temperature (kT) of 9.5 ± 1.0 keV and thickness parameter (log Λ) of 3.5 ± 0.2 and a viewing angle of 72.4 ± 1.0°. The four cyclotron humps were identified with harmonic numbers 4th to 7th as shown in the Figure. According to Beuermann et al. (2017), the main accreting pole emitting cyclotron radiation in V358 Aqr is permanently visible whereas the second pole in hidden throughout the orbital phase. This makes this target a one-pole accreting system. The majority of the systems (∼50) listed in Table 2 of Ferrario et al. (2015) are one-pole accreting systems, e.g. EK UMa (see e.g. Cropper et al. 1990), V834 Cen (see e.g. Schwope & Beuermann 1990, Ferrario et al. 1992), PZ Vir (Szkody et al. 2003), V1309 Ori (Harrop-Allin et al. 1997) and BL Hyi (Ferrario et al. 1996), to name a few. The magnetic field strengths determined from cyclotron modelling of the spectra of these systems ranges from ∼7 MG (e.g. V379 Vir

Farihi et al. 2008) to 150 MG (e.g. V884 Her Schmidt et al. 2001). Recently, Littlefield et al. (2018a) used the homogeneous cyclotron-emission model of Chanmugam & Wagner (1979) and Wickramasinghe & Meggitt (1985) to constrain the magnetic field strength of the WD in MASTER J132104.04+560957.8 from its optical spectra. This was done in the absence of multiple or visible cyclotron harmonics and concluded that MASTER J132104.04+560957.8 is a one-pole accreting AM Her system. Further examples of one-pole accreting AM Her systems include the following: PTF1J2224+17 (Schwope & Thinius 2020) and Gaia18aya (Thorstensen et al. 2020).

Some AM Her systems show detectable cyclotron features from more than one accreting region and this led to determination of the field strengths from both poles. AM Her systems that show these behaviour are commonly called two-pole accreting systems. At least eleven AM Her systems listed in Table 2 of Ferrario et al. (2015) exhibit these kind of behaviours and include the following systems: EQ Cet (Campbell et al. 2008a), EF Eri (Ferrario et al. 1996), VV Pup (see e.g. Wickramasinghe et al. 1989, Schwope & Beuermann 1997), DP Leo (e.g. Cropper & Wickramasinghe 1993), ST LMi (Ferrario et al. 1993, Campbell et al. 2008b), AR UMa (Schmidt et al. 1996, Gänsicke et al. 2001b), V347 Pav (Ramsay et al. 1996b, Potter et al. 2000), QS Tel (Schwope et al. 1995a), WX LMi (Reimers et al. 1999), HS 0922+1333 (Reimers & Hagen 2000). In the case of MN Hya, Buckley et al. (1998) suggested this source to be a two-pole accreting AM Her system with one emission region partially visible at all orbital phases. However follow-up study by Ramsay & Wheatley (1998) seems to suggest this system to be a one-pole accreting system. There are other AM Her systems recently shown to be two-pole accretors, e.g. CSS081231: 071126+440405 also known as CRTS CSS081231 J071126+440405 (Worpel & Schwope 2015, Kolbin et al. 2019), V1500 Cyg (Harrison & Campbell 2018) and HY Eri (Beuermann et al. 2020), to name a few. For two-pole accreting systems, the magnetic field strengths in the main spot are generally below 60 MG, however, there are other AM Her systems were the field strength is far greater than that. For example, Gänsicke et al. (2001b) determined the field strength in AR UMa to be in the region of 160 MG and 240 MG from modelling of cyclotron features from the ultraviolet spectrum of this system. Other examples of systems with field strength exceeding 60 MG for the main accreting regions include HS 0922+1333, WX LMi and V1500 Cyg. Cyclotron emission is not limited to optical and infrared wavelengths only, there are a few AM Her systems with highest field strength that also show cyclotron emission in the ultraviolet e.g. QS Tel (Rosen et al. 2001) and AR UMa (Gänsicke et al. 2001b, Ferrario et al. 2003). Part of Chapter 4 will present recent circular **spectropolarimetry** observations and modelling of the polarized cyclotron spectra and/or flux of UZ For.

1.6.3.2 Photospheric Zeeman splitting

During low accretion states, the photospheres of the two stars, the WD and the Donor star, contribute a significant amount of radiation to the total luminosity of the system. Therefore, it is possible to discern the Zeeman splitting in the Balmer lines of the WD's photosphere. The Zeeman splitting features are seen as both absorption lines in the total intensity and

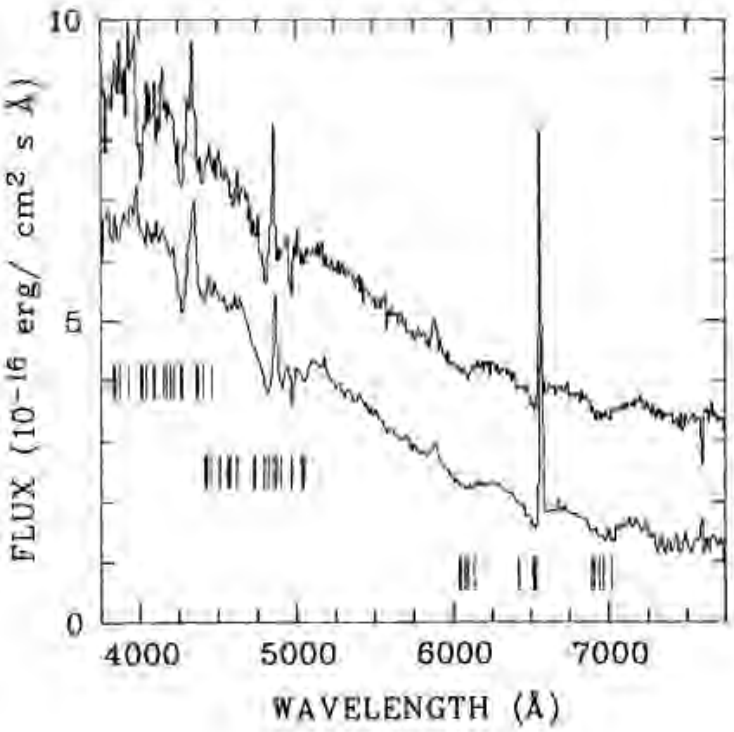

Figure 1.21: An example of a photospheric Zeeman splitting of the Balmer lines observed during the low state of BL Hyi. Adopted from Figure 5 of Schwope et al. (1995b).

also as corresponding polarization features (see e.g. Bailey 1995) in the spectra of AM Her systems. The first direct measurements of the magnetic field in an AM Her system was made by Schmidt et al. (1981) who detected evidence of Zeeman-splitting absorption in the Balmer lines of AM Her. They estimated the field strength of ∼10 MG at the equator and ∼20 MG at the poles. Latham et al. (1981) found similar results for the same system but with the mean surface magnetic field of 13 MG. However, the modelling of this line by Wickramasinghe & Martin (1985) with an offset dipole model yielded the field strength of 14 MG. Of the 114 AM Her systems listed in Table 2 of Ferrario et al. (2015), eleven of them have field strength determined by using this method. A typical spectra of an AM Her system (i.e. BL Hyi) showing photospheric Zeeman splitting is shown in Figure 1.21. It is worth mentioning that the first spectra of BL Hyi showing Zeeman absorption components due to hydrogen from the underlying magnetic WD were initially reported by Wickramasinghe et al. (1984) and this is consistent with a magnetic field of 30 MG. In addition to the two above mentioned systems (AM Her and BL Hyi), there are a number of AM Her systems that have field strengths determined from Zeeman splitting and these include ST LMi (Schmidt et al. 1983, Bailey et al. 1985), V834 Cen (e.g. Ferrario et al. 1992), AR UMa (Schmidt et al. 1996), MR Ser (e.g. Schwope et al. 1993, Araujo-Betancor et al. 2005b), AP CrB (e.g Gänsicke et al. 2004, Schwope et al. 2006), QS Tel (Schwope et al. 1995a), HU Aqr (Glenn et al. 1994), CP Tuc (Beuermann et al. 2007) and SDSS J030308.35+00544.1 (Parsons et al.

2013). Recently, Littlefield et al. (2020) detected Zeeman features from the AM Her type system Tau 4 (RX J0502.8+1624) and this was attributed to the field strength of 15 ± 2 MG.

1.6.3.3 Non-photospheric or halo Zeeman features

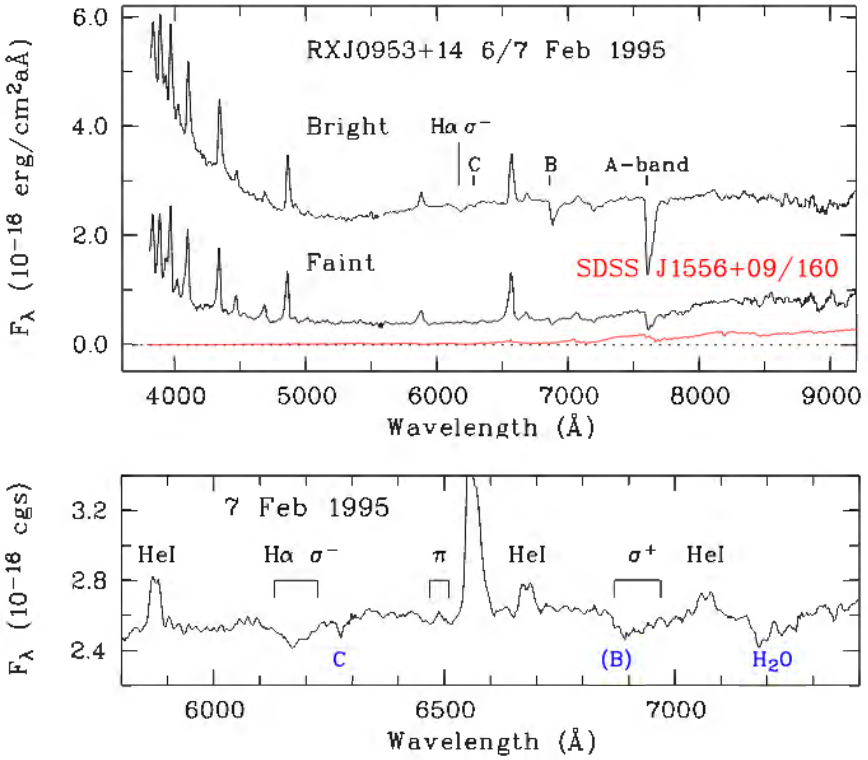

Figure 1.22: An example of Zeeman features of Hα in the bright phase spectrum (top panel) of RX J0953.1+1458. The bottom panel shows enhanced Zeeman features obtained by subtracting faint phase spectrum from the bright phase spectrum. Adopted from Figure 7 of Beuermann et al. (2021).

The non-photospheric or halo Zeeman features are seen during the bright phases of some AM Her systems and are thought to arise from the halo of matter surrounding the accretion shock. These features are seen in absorption against the cyclotron emission. The first direct measurements of field lines of an AM Her system from Zeeman absorption features were made by Wickramasinghe et al. (1987) from the spectra of V834 Cen and this led to determination of magnetic field strength of 20–25 MG for this system. Follow-up studies conducted by Schwope & Beuermann (1990) and Achilleos et al. (1992) placed the field strengths of this source at similar values to that of Wickramasinghe et al. (1987). Figure 1.22 shows an example of Zeeman splitting absorption features of Hα obtained by Beuermann et al. (2021) for RX0953.1+1458 with both the Hα π and σ^- components are undisturbed while the σ^+ component coincides with the atmospheric band. This particular spectrum

was obtained during the bright phase and it was modelled with the field strengths of 19 MG. RX0953.1+1458 is listed in Table 2 of Ferrario et al. (2015) but had no known field strengths when this Table was published. We note that there are eight AM Her systems in Table 2 of Ferrario et al. (2015) that have field strengths determined from this method. These includes BL Hyi (e.g. Schwope et al. 1995b, Araujo-Betancor et al. 2005b), V834 Cen (Wickramasinghe et al. 1987, Schwope & Beuermann 1990, Achilleos et al. 1992), MR Ser (Schwope et al. 1993), EF Eri (Achilleos et al. 1992), V393 Pav (Thomas et al. 1996), V2301 Oph (Ferrario et al. 1995), V884 Her (Schmidt et al. 2001) and EP Dra (Schwope & Mengel 1997). The field strength determined from non-photospheric Zeeman features ranges from 7 MG (for V2301 Oph) to 150 MG (for V884 Her). It is worth mentioning that in most cases the field strength determined from non-photospheric Zeeman features is consistent with the other methods used at least in the following systems: EF Eri, V834 Cen, MR Ser, V884 Her. For BL Hyi, the field strength determined from this method is almost half the field strength measured from the other two methods. The three remaining systems: V2301 Oph, EP Dra and V393 Pav, has field strengths determined from non-photospheric Zeeman features only, therefore has no other comparison.

1.7 Radio observations of CVs

Radio emission has been reported in a wide range of astrophysical objects, including CVs. Generally, CVs, especially mCVs, have long been suspected to emit in radio wavelengths. For example, Chanmugam & Wagner (1978) estimated the radio luminosity of CVs due to cyclotron radiation. However, their radio luminosity was well below the sensitivity of any radio telescopes that were being used in 1978. Based on a wide range of properties observed for these systems, Coppejans et al. (2015) concluded that more than one emission mechanism such as optically thick synchrotron emission, gyrosynchrotron emission or electron cyclotron maser emission, is responsible for radio emission in non-magnetic CVs. On the other hand, Barrett et al. (2020b) argued that the likely emission mechanism in highly polarized mCVs is cyclotron maser emission while the emission from unpolarized sources could be explained with gyrosynchrotron emission. The three radio emission mechanisms that are associated with radio emission from CVs are briefly explained below.

Synchrotron emission

Synchrotron radiation is a non-thermal radiation generated by the emission of high energy relativistic ($\gamma > 5$, where $\gamma = (1/\sqrt{1 - v^2/c^2})$ charged particles such as electrons gyrating in a magnetic field. This is the same process responsible for the radio emission of our Galaxy, supernova remnants and extra-galactic radio sources (Longair 2011). The source of relativistic electrons is the electron component of the cosmic/photon rays which are always changing direction. The radiation emitted is confined to a narrow cone in the direction of the motion of the charged particles and hence it is beamed. Synchrotron radiation is frequently

called non-thermal radiation meaning continuum radiation of a distribution of particles with a non-Maxwellian energy spectrum.

To understand synchrotron radiation, we consider a charged particle (e.g. an electron e) moving at a velocity $\vec{v}$ in a magnetic field $\vec{B}$. The charged particle (e) will experience a Lorentz force which, assuming negligible electric field $\vec{E}$, is given by Eq. 1.7. As already mentioned in Section 1.6, the direction of the Lorentz force is perpendicular to both $\vec{v}$ and $\vec{B}$ and the magnitude of this force is given by Eq. 8.25 of Irwin (2007) the following equation:

$$\mathrm{F_e} = \frac{ev}{c} B \sin\phi = \frac{ev}{c} B_{\perp} \tag{1.14}$$

where ϕ is the angle between $\vec{v}$ and $\vec{B}$, which is also known as the pitch angle and $B_{\perp} = B \sin\phi$. Its velocity along the field lines is constant whilst it gyrates about the magnetic field direction at a relativistic gyrofrequency (ω_o) given by the following relation:

$$\omega_o = \frac{eB}{2\pi\gamma m_e} \tag{1.15}$$

here γ is the Lorentz factor of the electron given by $\gamma = 1/\sqrt{1 - v^2/c^2}$.

The geometry that gives rise to synchrotron radiation is shown in Figure 1.18. If $\vec{B}$ is perpendicular to $\vec{v}$ (Figure 1.18(b)), $\sin\,\phi = 1$, the electron will experience the maximum Lorentz force. The force acting on the electron is perpendicular to both $\vec{v}$ and $\vec{B}$ and causes the electron to gyrate about the field lines giving-off synchrotron radiation. The emitted radiation is highly beamed in the forward direction into a cone of angular radius, $\phi = \frac{1}{\gamma}$. Thus, synchrotron radiation will only be seen when the cone is pointing in the direction of the observer. If $\vec{B}$ is parallel to $\vec{v}$, $\sin\,\phi = 0$, the electron will experience no Lorentz force and therefore will not gyrate about the field line and no radiation is emitted. In reality, case (c) in Figure 1.18, the electron's initial velocity is in any arbitrary direction, that is, it will have components of its velocity both parallel and perpendicular to field lines and therefore it will spiral around field lines emitting synchrotron radiation. However, the speed of the electron does not change over the period of gyration due to the force, but only its direction changes and constitutes an acceleration and therefore will radiate. Note that any charged particle, ions and protons, experience this behaviour, however, synchrotron emission from the ions and protons is negligible compared to that of electrons.

Since the magnetic field in mCVs is strong (>1 MG), the motion of the charged particles results in the formation of magnetized plasma. Therefore, the gyrating charged particles will be coupled to the field lines, that is, trapped by it. Thus if the field line is curved, the charged particle will follow through the curvature and any emission emitted by the charged particle can be used to map out the magnetic field configuration. Synchrotron emission allows for the map out the magnetic field where electrons are relativistic. According to Björnsson (2019), synchrotron emission can be eliminated in the case of high polarized and short duration emission from mCVs since it generates a broad continuous spectrum and polarization of less than 40%.

Gyrosynchrotron emission

Gyrosynchrotron emission was first proposed by Dulk et al. (1983) and is understood to be caused by emission from mildly relativistic ($1 < \gamma < 5$) electrons with energy ∼500 keV gyrating in a magnetic field of the WD during quiescent state (Dulk et al. 1983, Chanmugam & Dulk 1982, Chanmugam 1987) or the red dwarf (Dulk et al. 1983, Chanmugam & Dulk 1982). Gawroński et al. (2018) found that for AM Her, there is a correlation between the quiescent radio luminosity and the activity level of the binary. They argued that in the case of AM Her, the accretion stream provides, at lest partially, the electrons responsible for the gyrosynchrotron emission even when the accretion has dropped significantly (low rate). Recently, Barrett et al. (2020b) found that fourteen mCVs from their sample of 122 showed unpolarized continuum emission with a very high temperature brightness. This kind of emission is characteristic of an incoherent radiative process in an optically thick plasma. They attributed the radio emission from these systems to gyrosynchrotron radiation from midly ($1 < \gamma < 5$) relativistic electrons gyrating in a magnetic field. They argued that the source of the few tens of keV to few MeV electrons are magnetic reconnection events between the WD and the donor star or near the surface of the donor star.

Electron cyclotron maser emission

Electron cyclotron maser emission was first proposed by Melrose & Dulk (1982) in order to explain high brightness temperatures ($\geq 10^{10}$ K) and high degrees of circular polarization in the solar microwave spikes and radio bursts from some stars. Maser emission is caused by flaring of energetic electrons near the surface of the WD or the red dwarf (Dulk et al. 1983). As mentioned in Barrett et al. (2020b), the characteristics of cyclotron maser emission in a constant magnetic field are high polarization (>80%), short timescales (<600 s) and narrow band emission. They found both high polarization and short timescales emission in the ten minutes observations of LW Cam and V603 Aql (Nova and IP candidate). However, they attributed the absence of narrow band emission in these systems to emission from a broad range of magnetic fields and multiple emission regions. Maser emission is thought to arise from energetic electrons with a relatively mild loss-cone anisotropy. Earlier, Treumann (2006) argued that it is reasonable to assume that the electron cyclotron maser would be responsible for the emission in dwarf M stars but at that time it could not be decided whether or not the loss-cone or the shell maser is at work in these objects. Recent study of mCVs conducted by Barrett et al. (2020b) revealed that cyclotron maser emission is responsible for highly polarized emission in three quarters of the system showing radio emission. The cyclotron maser emission favours the loss-cone instability whereby a plasma of relativistic electrons with an isotropic velocity distribution is confined to a magnetic flux tube. The converging magnetic field creates a magnetic mirror causing most of the electrons to be reflected, while the highest energy electrons precipitate out. The loss cone anisotropy causes the index of refraction of the plasma to be negative. The magnetoionic modes of the plasma are then amplified with the extraordinary mode typically growing much faster than

the ordinary mode. This mechanism results in highly polarized radiation.

The following two sections (Section 1.7.1 and 1.7.2) present an overview of studies that have been conducted for both non-magnetic CVs and mCVs over the past four decades. See a recent review by Coppejans & Knigge (2020) for a general review of radio emission in CVs and proposed radio emission mechanisms. Barrett et al. (2020b) provides an overview of radio emission in mCVs.

1.7.1 Radio emission from non-magnetic CVs

Radio emission has been reported across all types of non-magnetic CVs, including dwarf novae (e.g. Benz et al. 1983, Benz & Guedel 1989, Körding et al. 2008, Coppejans et al. 2016b) and nova-likes (e.g Körding et al. 2011, Coppejans et al. 2015, Hewitt et al. 2020). Fuerst et al. (1986) reported observations of eight CVs in high state, seven dwarf novae and one classical nova, with the NSF's (National Science Foundation*) Karl G. Jansky Very Large Array (VLA); none of these sources had flux densities greater than 0.1 and 0.3 mJy. Prior to 2008, only three non-magnetic CVs were detected at radio wavelengths, SU UMa (Benz et al. 1983), EM Cyg (Benz & Guedel 1989) and TY Psc (Turner 1985).

In the case of dwarf novae, one of the likely emission mechanisms is synchrotron from a jet. For example, Körding et al. (2008) and Russell et al. (2016) reported radio observations of SS Cyg during outbursts and their results were consistent with synchrotron emission from a transient radio jet. EM Cyg is the other dwarf nova that also shows circularly polarized flare events with polarization reaching 81% (Benz & Guedel 1989). Coppejans et al. (2016b) presented a further observation of five dwarf novae during outbursts (RX And, U Gem and Z Cam) and super-outbursts (SU UMa and YZ Cnc). Their results show that the observed radio emission vary on time scales of minutes to days and that it was likely synchrotron emission. In addition, they found no correlation between radio luminosity and optical luminosity, orbital period, CV class or outburst type however, they recommended that higher cadence data was necessary to test this. The lack of radio detection in the past were linked to timing (Körding et al. 2008) and sensitivity (Coppejans et al. 2015) of the radio telescopes. According to Coppejans & Knigge (2020), recent theoretical and observational advances suggest that CVs do indeed launch jets. In particular, it was demonstrated that the accretion-outflow cycle of CVs is analogous to that of the X-ray Binaries (XRBs). For example, radio observations of CV SS Cyg have consistently shown radio flaring equivalent to that observed in XRBs that marks a transient jet.

Nova-likes on the other hand, have been shown to be significant radio emitters, (see e.g. Körding et al. 2011, Coppejans et al. 2015), with luminosities that are not too different from those seen in dwarf novae (Coppejans et al. 2016a). For V3885 Sgr, Körding et al. (2011) concluded that the most likely source of the radio emission is optically thin synchrotron emission originating in a jet. In a study of four nova-likes, Coppejans et al. (2015) detected

*The National Science Foundation is an independent agency of the United States government that supports fundamental research and education in all the non-medical fields of science and engineering.

three nova-likes (TT Ari, RW Sex and V603 Aql) and these were found to show a range of properties, including flaring and variability on both short (∼200 s) and longer term (days) time scales, as well as circular polarization levels of up to 100%. For example, TT Ari was observed to show a flaring event lasting ∼10 min and this source was found to show circular polarization exceeding 75%. The wide range of properties observed for these systems suggest that more than one emission mechanism is responsible for radio emission in non-magnetic CVs. Recent study of eleven nova-likes conducted by Hewitt et al. (2020), they detected four systems (V3885 Sgr, IM Eri, RW Sex and V603 Aql) with IM Eri being detected for the first time in radio. Based on the systems observed, radio emission is only detected in systems with a high specific optical luminosity $\gtrsim 2.2 \times 10^{18}$ erg s^{-1}Hz^{-1} at the radio detection limits (corresponding to $M_V \lesssim 6.0$). In addition, they noted that the X-ray and radio emission from the detected sources lie on the same power law that has previously been proposed for non-pulsating neutron stars in low-mass XRBs ($L_X \propto L_R^{\sim 0.7}$).

Radio emission has also been detected in one of the AM CVns observed using the VLA, RX J0806.3+1527 (e.g. Ramsay et al. 2007). The other two systems, RX J1914+24 and ES Cet, observed with the VLA and the Australian Telescope Compact Array (ATCA; Frater & Brooks 1992) only gave 3σ upper limits. For AM CVns, Wu et al. (2002) predicts that radio emission should be produced due to electron-cyclotron maser emission (Willes & Wu 2004, Willes et al. 2004). And also that circularly polarized radio emission should be detected provided that these systems are observed at an appropriate viewing angle.

1.7.2 Radio emission from mCVs

The first radio observations of an AM Her system were made with the VLA for AM Her at 4.9 GHz and a flux density of 0.67 mJy was detected (Chanmugam & Dulk 1982). However, they did not detect any circular polarization despite the observations being taken in full polarization mode. A follow-up study of AM Her and five other systems (EF Eri, VV Pup, MR Ser, ST LMi and AN UMa) conducted by Dulk et al. (1983) at 4.9 GHz showed a 100% circularly polarized radio flare from AM Her with a peak flux of 9.7 mJy lasting about ten minutes. The other systems (EF Eri, VV Pup, MR Ser, ST LMi and AN UMa) were non-detections; Dulk et al. placed an upper limits of ∼0.2 mJy for these sources. The radio emission from AM Her was attributed to gyrosychrotron emission from energetic electrons trapped in the magnetosphere of the WD. The radio flare was attributed to an electron-cyclotron maser that operates near the surface of the red dwarf in a magnetic field of ≈1 kG.

The second radio detection of a mCV was made by Wright et al. (1988) for V834 Cen using the 64-m diameter Parkes Radio Telescope (Ables et al. 1986) at 8.4 GHz. They found V834 Cen to be variable on time-scales as short as one minute and reaching peak flux densities of 35 mJy. The emission from V834 Cen was attributed to an electron-cyclotron maser, although the maser emission suggestions in AM Her systems have recently been challenged by Kurbatov et al. (2019). Instead they suggest the radio emission arises from Alfvenic turbulence. AE Aqr was the first DQ Her system to show radio emission (see e.g.

Bookbinder & Lamb 1987, Bastian 1987, Bastian et al. 1988). This source was observed with the VLA in 1985 and 1987 at four frequencies (1.5, 4.9, 15 and 22.5 GHz) and was detected in all four frequency bands. AE Aqr was found to be a variable radio source on time scales less than 5 minutes, showed circular polarization less than 15% and showing flux densities of 3–5 mJy at 1.4 GHz, 8–16 mJy at 4.9 GHz and 1−12 mJy at 15 GHz. Its radio light curve shows flare-like variations but no significant circular polarization was detected from AE Aqr. The radio emission of AE Aqr shows similarities to the low-level flares from Cygnus X-3 (Spencer et al. 1986).

Several radio surveys of mCVs have been carried out in the past three decades by different authors. For example, Beasley et al. (1994) observed 37 mCVs (22 previously unobserved and 15 previously observed sources) using both the VLA and ATCA, and both at an observing frequency of 8.4 GHz. Their results yielded non-detection of any radio emission from the 37 targets. In addition, their observations included an extensive pointing of V834 Cen, suggesting that the results presented by Wright et al. (1988) were incorrect or the source produces occasional transients emission. A survey of 21 mCVs conducted by Pavelin et al. (1994) using the Jodrell Bank BroadBand Interferometer (Padin et al. 1987) at 5 GHz yielded five detections of mCVs, amongst these were three new detection: BG CMi (2.2 ± 0.7 mJy), ST LMi (2.0 ± 0.3 mJy) and DQ Her (1−4 mJy).

In addition to the above-mentioned surveys, a few pointed observations were conducted between 1990−2010. For example, Mason et al. (1996) reported observations of the asynchronous AM Her system BY Cam with the VLA telescope at three frequencies: 1.4 GHz, 4.9 GHz and 8.3 GHz, respectively. Their results only gave upper limits to the flux densities of 0.059 mJy at 1.4 GHz, 0.023 mJy at 4.9 GHz and 0.137 mJy at 8.3 GHz. Much of the radio observations that were done prior to 2004 have been reviewed in Mason & Gray (2004). By 2004, only six mCVs, three AM Her systems (AM Her, V834 Cen and ST LMi) and three DQ Her systems (AE Aqr, DQ Her and BG CMi), were reported to be radio emitters. In another study, Mason & Gray (2007) observed nine mCVs within 100 pc between 2003 and 2004, including AR UMa, with the VLA telescope at a frequency of 8.436 GHz. They found AR UMa to be a strong radio emitter with peak flux densities of 0.422 ± 0.060 mJy and 0.734 ± 0.095 mJy for the two epochs obtained between 2003 and 2004. AM Her was also observed in low state and detected with a flux density of 0.586 ± 0.074 mJy and this was consistent with previous observations.

Recently, Barrett et al. (2017; 2020b) conducted a multi-semester snapshot (lasting a few minutes per frequency band) survey of 122 mCVs observed with the VLA "with improved sensitivity" and operating at three frequency bands (C-band (4–6 GHz), X-band (8–10 GHz) and K-band (18–22 GHz), respectively) at full polarization. Some of the targets were observed at more than one epoch. It is worth mentioning that a fourth frequency, Q-band (40–44 GHz) was used for some observations. They detected radio emission from 33 mCVs (see Table 1 of Barrett et al. (2020b)), where some systems detected at more than one frequency band, with fluxes ranging from 6 μJy to 8 mJy. A staggering 28 targets are new radio sources and thus increasing the number of known radio-detected mCVs to more that

40. They reported that fourteen of the radio detections from 33 detected show unpolarized continuum emission with a very high brightness temperature. According to Barrett et al. (2020b), this kind of emission is characteristic of an incoherent radiative process in an optically thick plasma. They attributed the radio emission from these unpolarized systems to gyrosynchrotron emission from mildly ($1 < \gamma < 5$) relativistic electrons gyrating in a magnetic field. On the other hand, they found that 24 of 33 systems detected show highly circularly polarized radio emission of short duration. They ruled out cyclotron and gyrosynchrotron emission since it is unlikely to be the responsible for radio emission observed in highly polarized mCVs since specific conditions are needed to produce high polarization. This is because this kind of radiation must be emitted along the magnetic field lines in a relatively homogeneous plasma (Barrett & Chanmugam 1985). They attributed the high degree of circular polarization in these sources to electron cyclotron maser emission originating from the lower corona of the donor star and not from a region between the two stars. This is because maser emission allows for a more direct estimate of the mean coronal magnetic field of the donor star which they estimated to be between 1–4 kG assuming a magnetic filling factor of 50%. For example, radio observations of EF Eri presented by Barrett et al. (2020a) shows that this source is 100% circularly polarized at 8−12 GHz for several minutes. They concluded that for EF Eri, the most likely emission mechanism is electron cyclotron maser emission in a 4 kG magnetic field based on the high degree of polarization and short-duration emission. Furthermore, they attributed the detection of multiple emission features to the presence of multiple low-density plasma regions near the WD or in the corona of the secondary star.

LW Cam is another example of AM Her system that has been studied extensively in radio wavelengths by Barrett et al. (2020b) and was found to show 100% circularly polarized. These authors rebinned the X-band (8–12 GHz, see Figure 2 of Barrett et al. (2020b)) spectrum into several bins with a total bandwidth of 256 MHz each and average the flux value of two adjacent 128 MHz spectral windows. The rebinned spectrum revealed the presence of at least one narrow band (<300 MHz) emission feature at a frequency of ∼10.295 GHz which they attributed to pronounced electron maser event. The event was associated with the magnetic field strength of ≈3.6 kG for the plasma assuming that maser emission was at the fundamental harmonic. The remaining polarized emission was attributed to the sum of many smaller events with a range of magnetic fields. They ruled out the accretion stream as the origin of the radio emission in LW Cam since emission seems to arise from the third of the distance from the WD to L_1 point. However, this doesn't rule out the possibility of maser emission from the low density regions within the WD's magnetosphere. They argued that the most likely site of polarized emission is in the lower corona of the donor star where the plasma density and frequency are low enough to allow cyclotron emission to escape (see Dulk et al. 1983, Dulk 1985). The emission site is probably near the footprints of one or more coronal loops with the source of the high energy electrons being from magnetic reconnection events in stellar flares.

Most recently Pretorius et al. (2021)* reported detection of radio emission from the second AE Aqr-like system (a propeller system), LAMOST J024048.51+195226.9†, at lower frequency centred at 1.28 GHz using MeerKAT. LAMOST J024048.51+195226.9 was found to be bright radio source with a flux density of 0.60 ± 0.02 mJy and spectral index of −0.6 ± 0.2 at 1.284 GHz, and show variability on time scales of tens of minutes. The radio luminosity of this source was found to be 2.7×10^{17} erg s^{-1} Hz^{-1} and is the second highest yet reported for a CV, and even higher than radio luminosity of AE Aqr. Barrett (2022) presents further radio observations of LAMOST J024048.51+195226.9 conducted with the VLA on two separate occasions. The first of these observations were a one hour across five radio bands from 2–26 GHz measuring the radio spectrum. The radio spectrum of this source show a negative spectral index between 2–26 GHz. The second observations were an on-source pointing at C-band (4–8 GHz) lasting about two hours. The radio light curve of this source shows that the flux density and circular polarization vary randomly on time scales of a few minutes. Overall, the radio observation of LAMOST J024048.51+195226.9 reveals that this source is dissimilar to AE Aqr in that it shows negative spectral index and its radio light curve shows emission with periods of high circular polarization. Note that AE Aqr show positive spectral index (∼0.5) and unpolarized radio emission (e.g. Bookbinder & Lamb 1987). Part of Chapter 4 will present recent **MeerKAT radio observations** of UZ For at 1.28 GHz.

1.8 Review of UZ For

UZ For is an eclipsing CV, belonging to the AM Her type class of mCVs, discovered as a fortuitous X-ray source, EXO 033319−2554.2, from the observations obtained in 1983 and 1986 with the EXOSAT (Taylor et al. 1981) and reported in a series of International Astronomy Union (IAU) circulars (Giommi et al. 1987, Beuermann et al. 1987, Ferrario et al. 1988). Its X-ray and optical properties were strongly suggesting that this source was an AM Her type binary system. During its discovery, UZ For was found to show 100% modulation in its soft X-ray flux with on-off behaviour at the orbital period of 127.7 ± 3.0 min (Giommi et al. 1987, Osborne et al. 1988). Also detected was an eclipse like feature at the end of the bright phase. They also reported that the bright phase of this source lasts 55% (0.55) of the orbital phase and was cut by an eclipse-like feature lasting ∼8 min with unresolved ingress and egress.

The AM Her membership of UZ For was confirmed in part from spectroscopic observations obtained on 1987 October 21−26, 1987 November 27 and 1987 December 9 (Beuermann et al. 1987; 1988, Ferrario et al. 1988; 1989, Allen et al. 1989) which show emission from the Balmer lines and HeII 4686 Å, whose line strength varies from one epoch to another. The spectral type of the companion star was estimated to be dM4.5 (Boeshaar 1976).

*The article was published after the first submission of this thesis.

†The Large Sky Area Multi-Object Fibre Spectroscopic Telescope (LAMOST), also known as the Guo Shoujing Telescope after the 13th-century Chinese astronomer, is a meridian reflecting Schmidt telescope, located in Xinglong Station, Hebei Province of China.

The spectroscopic properties of UZ For are reviewed in greater detail in Section 3.2. The magnetic membership was confirmed from polarimetric observations with the detection of strong circular (−25% to +10%) and linear (∼5%) polarization and decreasing with increasing wavelength (Bailey et al. 1987, Berriman & Smith 1988, Ferrario et al. 1989, Bailey & Cropper 1991). Detailed polarimetric properties as well as magnetic field strengths determined over the years of UZ For are given in Section 4.1. Beuermann et al. (1988) gives the first estimate of the distance to UZ For and this was found to be 240 ± 50 pc. Their integrated flux, from spectrophotometry, showed recurrent dips which indicate an orbital period of 126.5 ± 0.5 min and the eclipse width of 7.5 ± 0.3 min. UZ For was the second eclipsing AM Her type system to be discovered after DP Leo (Biermann et al. 1985) and the first AM Her system to be found in the period gap. The first estimate of the WD mass in UZ For was made by Hameury et al. (1988). They find that the WD in UZ For to be 1.09 ± 0.01 $M_{\odot}$ and this was significantly larger than other AM Her systems by 0.25−0.6 $M_{\odot}$ and close to the Chandrasekhar mass limit.

1.8.1 Optical light curves of UZ For

The first light curves of UZ For were derived by Beuermann et al. (1988) from the 2 min spectrophotometry exposures obtained in 1987 October 20 and 22. Their light curves, equivalent of B, V and I, show the presence of pronounced dips in the B and V bands − the eclipse of the primary by the companion star − recurring at an orbital period of 127 min and consistent with the X-ray light curve of Osborne et al. (1988). Interestingly, the light curves of UZ For showed a typical light curve of AM Her systems consisting of a bright and faint phase. Beuermann et al. (1988) noted that the maximum light during the bright phase, in both B and V bands, was centred on phase 0.87 and that the bright phase lasted about 51%(0.51) of the cycle. The centre of the bright phase was consistent with that seen in the X-ray light curves reported by Osborne et al. (1988). Allen et al. (1989) presented photometric light curves of UZ For obtained on 1987 December 6, their results showed clear ingress and egress of the main accretion spot. They reported that ∼75% of the total light was extinguished within 5 s and this implied that the size of the cyclotron emission region must be ∼2.6×10^{8} cm in diameter. In a separate study, Ferrario et al. (1989) presented optical light curves of UZ For taken on 1987 December 15 which also show a narrow eclipse with a width of ∼8 min and occurring at the end of the bright phase.

UZ For has been the subject of several high-speed photometric studies in optical (Bailey & Cropper 1991, Imamura & Steiman-Cameron 1998, Perryman et al. 2001, de Bruijne et al. 2002), ultraviolet (Stockman & Schmidt 1996) and extreme ultraviolet (Warren et al. 1995) and X-rays (Bailey 1995). Fortunately, much of these observations were taken in different states of mass transfer and helped in further understanding the physical and geometrical properties of this system. The shape of the optical light curves of UZ For can be divided into three categories: low state, faint high state and high state (see Figure 2 of Imamura & Steiman-Cameron 1998). The high-state light curves (Figure 1.23) are dominated by the accretion stream, which contributes a significant fraction of the overall luminosity of

the system. During the high-state, the gradual decline after the ingress and steep rise to and from minima is longer and the flatter minimum is shorter. The low-state light curves (Figure 1.24), however, are dominated by emission from the accretion region and the WD's magnetosphere. During the low-state, the gradual decline and rise to and from minimum is shorter and the flatter minimum is longer.

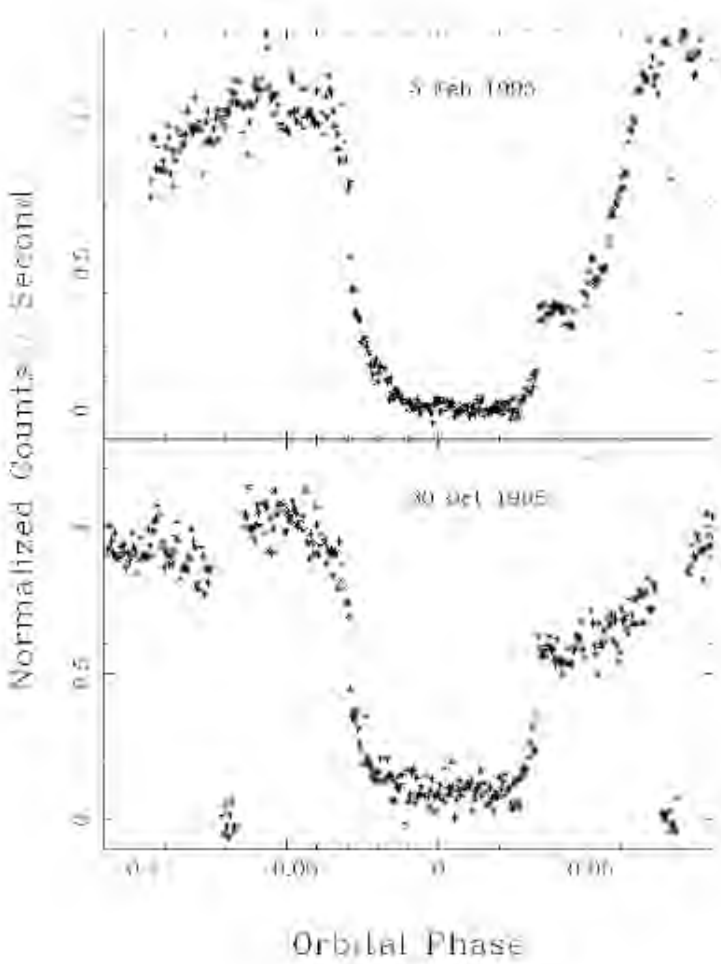

Figure 1.23: Eclipse profiles of UZ For obtained during the high state. Adopted from Figure 6 of Imamura & Steiman-Cameron (1998).

The typical eclipse profiles of UZ For are shown in Figures 1.23 and 1.24. They show the presence of various stages in both the ingress and egress of the eclipse profiles (see e.g. Bailey & Cropper 1991, Imamura & Steiman-Cameron 1998, for details). The ingress showed a rapid drop followed by a gradual decline to minimum and the egress showed an initial slow rise followed by a rapid rise. The rapid drop and rise were attributed to emission from the accretion spot responsible for the cyclotron radiation on the surface of the WD. The gradual decline and slow rise were associated with the eclipse of the WD's photosphere. The measured duration of the sharper ingress and egress are $\sim$3 s and 5$-$6 s, respectively.

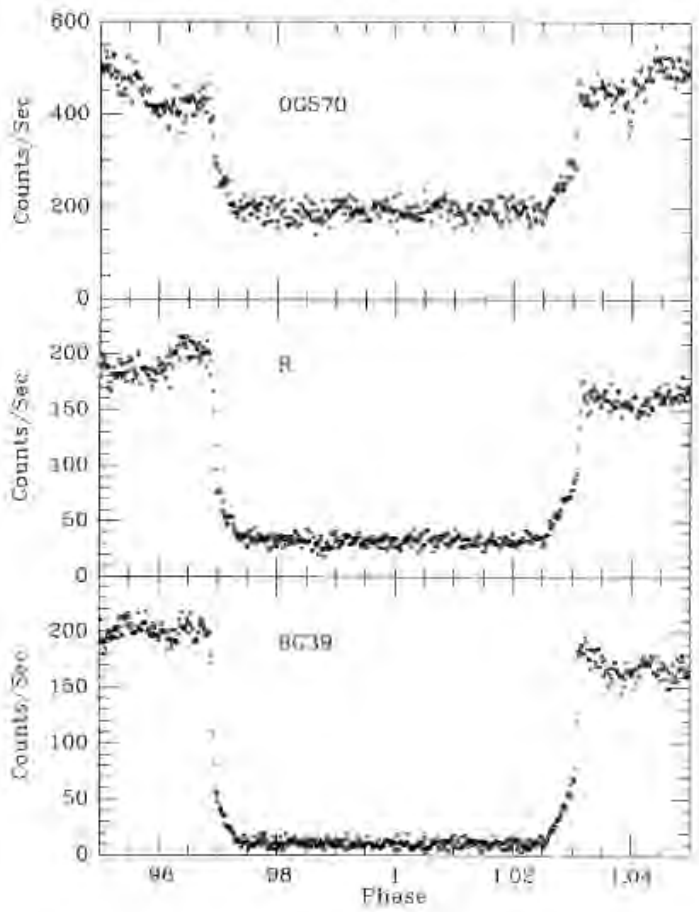

Figure 1.24: Eclipse profiles of UZ For obtained during the low state. Adopted from Figure 2 of Bailey & Cropper (1991).

However, the optical light curves of UZ For presented by Perryman et al. (2001) show clear two-stages in both the ingress and egress which they attribute to the presence of two accretion regions located close to the poles of the WD. Their modelling place the first of this accretion regions in the lower hemisphere, consistent with the location seen in optical (Bailey & Cropper 1991), extreme ultraviolet (Warren et al. 1995) and X-rays (Bailey 1995). Therefore, the first accretion region is responsible for emission of cyclotron radiation. The second accretion region is located in the upper hemisphere close to the rotation axis of the WD and no evidence of emission is seen in X-rays.

The time of ingress and/or egress of CVs (UZ For included) can be measured with great precision. These has led to the realization that the orbital period in some CVs were changing from one epoch to another either decreasing or increasing. The variations in the orbital periods is explained as either due to magnetic cycle activities of the secondary star known as Applegate mechanism (Applegate 1992) or the presence of circumbinary planet(s) in orbit around the binary (Brinkworth et al. 2006). The former mechanism is reviewed in Section

2.1.1 whereas the latter is reviewed in Section 2.1.2. The times of mid-eclipse of UZ For has been measured for over three decades (see detailed review in Section 2.2). Earlier eclipse timings of this system (by e.g. Beuermann et al. (1988) and Allen et al. (1989)) showed no significant period changes, however, follow-up studies conducted by Bailey & Cropper (1991), Ramsay (1994) and Imamura & Steiman-Cameron (1998) showed departure from linear and quadratic ephemeris with residuals of ±50 s. The quadratic term pointed at an increasing orbital period of UZ For, the opposite of what was being observed in other systems, see e.g. DQ Her (Warner 1988). This led Perryman et al. (2001) to exclude some of the mid-eclipse times when updating the ephemeris of this system citing untraceable inconsistencies. Follow-up eclipse timing studies of UZ For conducted by Dai et al. (2010) and Potter et al. (2011) show that the deviation from a linear and quadratic ephemeris has continued over the years and the residuals can be explained either due to the presence of circumbinary planets around the binary or Applegate mechanism. Chapter 2 is based on the modelling of the eclipse timings residuals of UZ For in order to establish the mechanism responsible.

1.8.2 X-ray, ultraviolet and extreme-ultraviolet

The soft X-ray light curves of UZ For presented by Osborne et al. (1988) also showed a dip before the eclipse, similar to EF Eri, V834 Cen, etc, (see Section 1.5.3.1), of width 0.06 of the orbital cycle attributed to the eclipse of the accretion region by the accretion stream. Further X-ray light curves of this source obtained with ROSAT (Truemper 1982, Pfeffermann et al. 1987) on two separate occasions are presented by Ramsay et al. (1993) and Ramsay et al. (1996a). These observations revealed that UZ For was still emitting X-rays during the faint phase, suggesting that there was a second weaker region also emitting X-rays. In addition, the rise to bright phase took longer (∼260 s), implying that the source of cyclotron radiation was extended. Other X-ray observations of UZ For were made with XMM-Newton (Jansen et al. 2001) during the low state (see e.g. Still & Mukai 2001, Pandel & Córdova 2002). The analysis performed by Still & Mukai (2001) did not show any X-rays from the source, suggesting that the accretion rate either decreased or accretion onto the WD has stopped. However, the analysis by Pandel & Córdova (2002) shows occasional flares in both X-rays and ultraviolet and for these observations, UZ For was ∼800 times fainter in X-rays than the high state recorded by ROSAT (Ramsay et al. 1993). In addition, a transient event lasting ∼900 s was detected simultaneously in X-ray, ultraviolet and optical monitors. During this event, the X-ray flux increased by a factor of ∼30. They attributed the transient event to the impact of gas on the main accreting region on the surface of the WD.

Warren et al. (1993; 1995) and Sirk et al. (1994) presented the extreme ultraviolet observations of UZ For obtained using the Extreme Ultraviolet Explorer satellite (EUVE, Bowyer & Malina 1991) between 1992 and 1993, see Figure 1.25. They reported detection of a narrow absorption dip (at phase 0.9) in the extreme ultraviolet light curve of UZ For which they attributed to the emission from the accretion stream at the location of the threading region

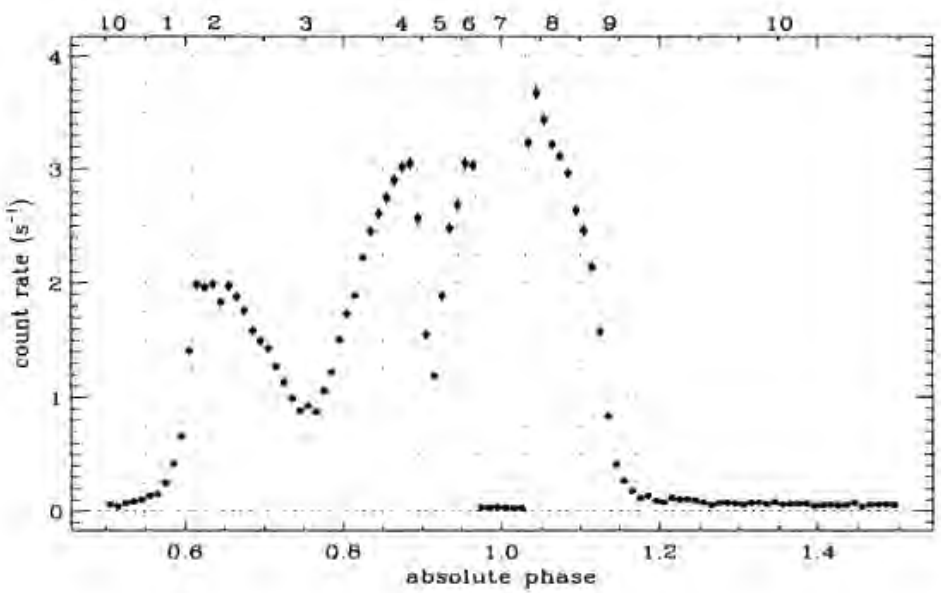

Figure 1.25: An example of an extreme ultraviolet light curve of UZ For showing faint and bright phases. Adopted from Figure 2 of Warren et al. (1995).

many WD radii away from the accretion spot. They also detected a broad dip at phase 0.75 caused by absorption much closer to the WD surface. Both narrow and broad absorption effects were variable in time and phase and this was used to conclude that the angular size of accretion spot must be $<5^\circ$ – based on the time scales of the secondary star's ingress and egress. In addition, in order to explain the light curve phase duration, given the small spot size, they suggested that the extreme-ultraviolet must be raised vertically by $\approx 5^\circ$ of the WD radius.

Stockman & Schmidt (1996) presented ultraviolet observations of UZ For obtained with the Hubble Space Telescope (HST) during the high state. Their eclipse light curves could be decomposed into three components: the WD, a hot photospheric emission region on the WD and the ultraviolet bright accretion stream. Detailed eclipse modelling places the majority of the ultraviolet emission in the accretion ballistic stream between the WD and the circularization radius. Note that the circularization radius is the radius at which the Kepler specific angular momentum equals that of matter accreting through the L_1 (i.e. inner Lagrangian point). In addition, they presented an ultraviolet spectrum which shows strong emission lines from NV, CIV, HeII and SiIV. Their ultraviolet spectra were used in computational modelling by Kube et al. (1999), where they model the CIV light curve of UZ For and found that the stagnation region in the magnetosphere of the WD was a prominent source of emission lines.

The properties of UZ For discussed above have led to the model schematic of this system shown in Figure 1.26 and this was first produced by Ferrario et al. (1989). Similar sketches of the geometry of the accretion region of this system is presented in Figure 3 of Schwope (1990) and also in Figure 5 of Warren et al. 1995. The model of Ferrario et al. (1989) is

based on polarization, eclipsing and radial velocity behaviours of this system. The physical size of the binary components are arbitrary in Figure 1.26 and most notably, is the absence of the magnetically confined accretion stream. However, this model accounts for most of the observed properties of this system. The sketch of Schwope (1990) is based on similar characteristics as that of Ferrario et al. (1989) but only shows an edge-on or line of sight view of the WD. On the other hand, the model of Warren et al. (1995) is based on extreme ultraviolet observations and X-rays analysis. The main differences between the two models is the viewing angle. In the sketches of Ferrario et al. (1989), the binary is viewed from the bottom whereas that of Warren et al. (1995) shows a side view projection of the binary at different orbital phases. From these figures, it is immediately obvious that accretion onto the WD occur at the main accreting region which is located below the orbital plane (i.e. line of sight of the observer). It is worth mentioning that the main accreting region on the WD is self-eclipsed by the WD for about 50% of the orbital cycle.

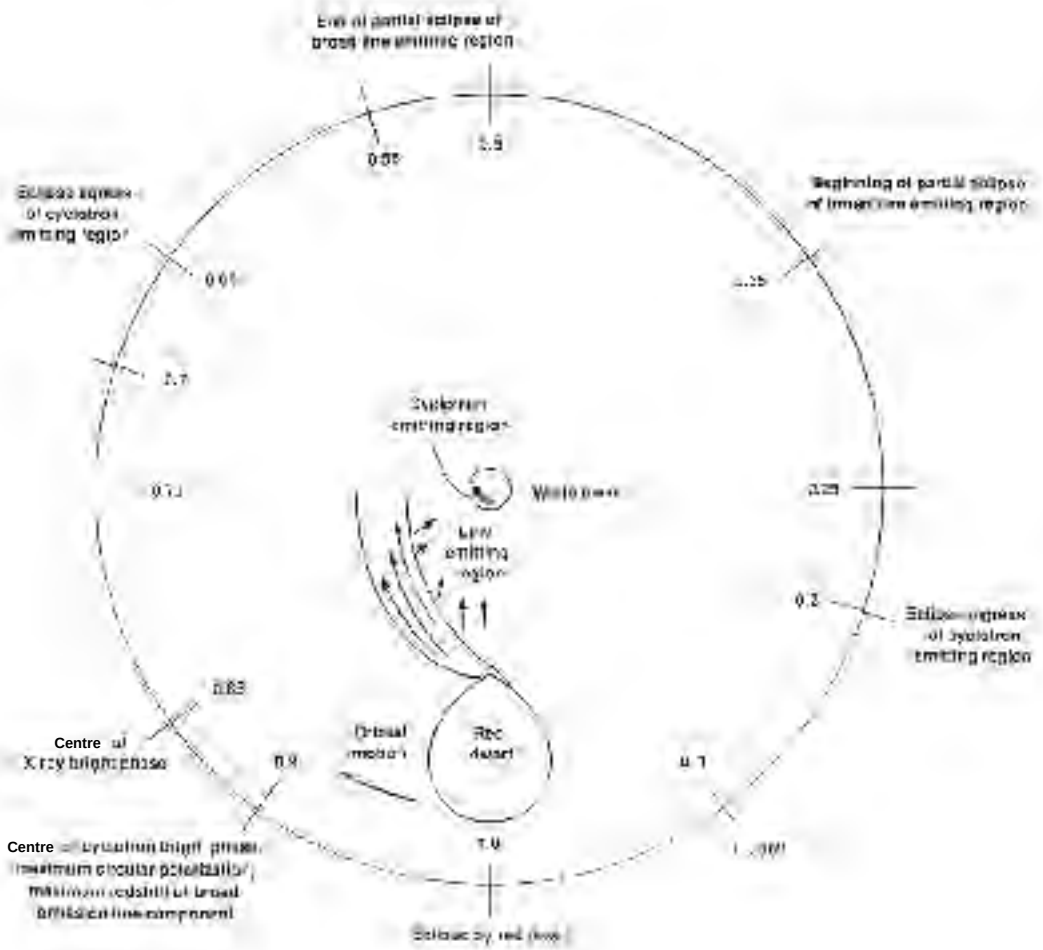

Figure 1.26: The geometry of UZ For proposed by Ferrario et al. (1989) based on polarization, eclipsing and radial velocity behaviour. Adopted from Figure 8 of Ferrario & Wickramasinghe (1989).

1.8.3 Doppler map of UZ For

Figure 1.27 shows the observed trailed spectra and Doppler map of UZ For constructed using HeII 4686 Å emission while this system was in a low state (Schwope et al. 1999). The Doppler map and/or the trailed spectra of this system were reproduced in Figure 7 of Schwope (2001) and most recently in Figure 11.13 of Marsh & Schwope (2016). The low-state trailed spectra of UZ For (Figure 1.27, left panel) shows a complex structure similar that of HU Aqr (Schwope et al. 1997a) showing emission from three distinct components: the narrow emission component (green), the broad mid-velocity (green) and underlying high-velocity (blue) components. The narrow emission component is associated with the emission from the donor star whereas the two broad components are attributed to emission from the ballistic and magnetically confined accretion stream. Earlier, Schwope (1995) conducted a radial velocity study of emission lines from phase-resolved spectra of HU Aqr. The multi-components in the emission line of AM Her systems were first studied in detail by Schwope (1995). They fitted emission line profiles from the high state observations of HU Aqr with triple Gaussian plus a continuum component thereby extracting the radial velocity of each component. Schwope (1995) noted that the narrow emission component which was associated with the reprocessing/illumination by the accretion spot followed a perfect sine-curve and was only visible on phase 0.25–0.75 while the radial velocity curves of the remaining two components (the high-velocity component and the broad base component) were complex. These results have led to understanding the complex line profiles of AM Her systems and it is now general knowledge that these line profiles are consist of multiple-components from different parts of the accretion flow.

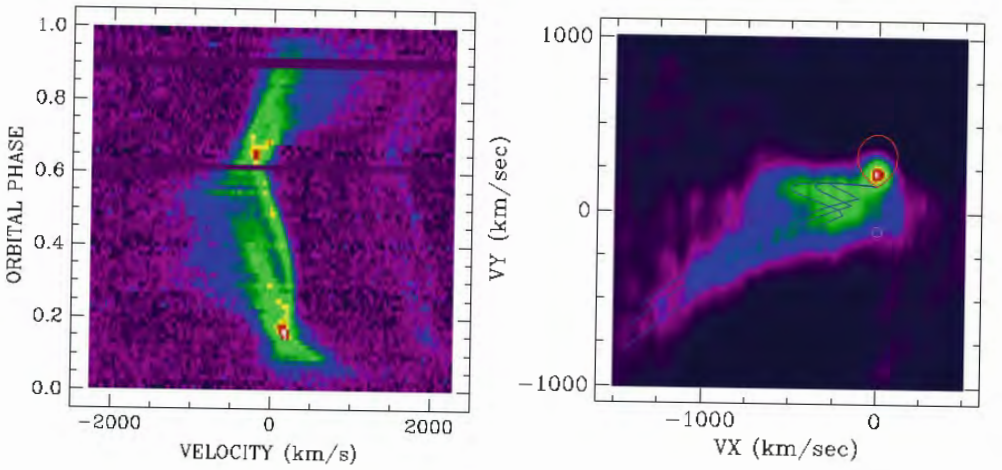

Figure 1.27: The trailed spectra and Doppler map of UZ For using HeII 4686 Å emission line obtained during low state. Adopted from Figure 11.13 of Marsh & Schwope (2016).

The Doppler map of UZ For (Figure 1.27, right panel) shows emission concentrated in the top left region of the tomogram. These were associated with emission from the ballistic part of the accretion stream and while the majority of the emission centred on y-axis was

attributed to the irradiated face of the secondary star. The cometary tail-like feature in the bottom left region of the map were attributed to the magnetically dominated part of the accretion stream. These features are traced well by overlaid model with the mass ratio of 0.2, inclinations (of 81°), and the ballistic and magnetically confined accretion stream trajectories to the Doppler map.

All the Doppler maps mentioned so far in this thesis were constructed using either filtered-back projection or any variation of the maximum entropy method and in addition, they were all in cartesian (V_x, V_y) coordinates. Recently, Kotze et al. (2015; 2016) presented a new projections method called the inside-out method based on the fast maximum entropy method of Spruit (1998). The inside-out method uses polar coordinates and is reviewed in Chapter 3. As already mentioned in Section 1.4, the structure of the Doppler maps of AM Her systems depend on the state of accretion during the time of observation. Their appearances tells more about the underlying emission mechanisms at work from different components. Modelling of the Doppler maps allow for the constraint of the various components such as the extent of the ballistic stream and accretion curtains. Chapter 3 of this thesis presents medium resolution spectroscopy and Doppler maps of UZ For based on both the standard and inside-out projections and extend the scope of the Doppler maps to other emission lines. Furthermore, we present for the first time the modulation maps of this system.

1.9 Thesis overview

1.9.1 Research aims or objectives

The purpose of this research is three-folds. Firstly, this thesis tests the viability of the two-planetary system suggested to explain the variation in the mid-eclipse time residuals of UZ For presented in Potter et al. (2011). UZ For is one of many other close binary systems, e.g. NN Ser (Beuermann et al. 2010), HU Aqr (Qian et al. 2011) and DP Leo (Beuermann et al. 2011), that show variation in their eclipse times and the cause of the variability was attributed to either magnetic cycle activities of the secondary star (i.e. Applegate mechanism) or the presence of single- or multiple-planetary systems in orbit around the binary. A detailed review on the eclipse time variations in CVs is presented in Section 2.1. To summarize, for some of these systems when new observations are included in the fitting, the new data deviate or disprove the planetary system hypothesis. But there are a few of these systems that have been shown to be consistent with the circumbinary planets model when new observations are added in their analysis, e.g. NN Ser (Goździewski et al. 2015) and HU Aqr (Bours et al. 2016). In the case of UZ For, Dai et al. (2010) reported slightly over a decade ago that the variations in the mid-eclipse times could be explained by the presence of an extra-solar planet orbiting the binary with an orbital period of 23 years. A follow-up study by Potter et al. (2011), with data spanning 27 years, showed that the mid-eclipse time variations were best explained with a two-planet model, with orbital periods of ∼5 and ∼15 years, respectively. This study extends the baseline of observations of UZ For

by a further eight years, from 27 to 35 years. In summary, this thesis presents additional 33 mid-eclipse observations of UZ For obtained between 2011 and 2018 and brings the total combined mid-eclipse times to 75. All the mid-eclipse times (75) were used in fitting with a quadratic plus two elliptical terms in order to investigate if a two-planet model is still viable or not in order to explain the residuals of UZ For.

Secondly, a detailed study of the emission in UZ For, through the use of Doppler tomography is conducted. Doppler tomography is an imaging technique in which spectra taken consecutively and covering an orbital phase of the binary system are transformed into a Doppler image in velocity space (Marsh & Horne 1988). This technique was developed to unravel the structures of the accretion disc in non-magnetic CVs but has also been used in magnetic CVs. Although the first results were not promising for AM Her systems, there were other promising results, e.g. HU Aqr (Schwope et al. 1997a) and V834 Cen (Potter et al. 2004). Recently, Kotze et al. (2015; 2016) presented a complementary extension to the standard Doppler tomography technique called the inside-out projection. In addition, this technique is particularly effective at revealing the high-velocity magnetic accretion flow not seen in the standard tomograms of AM Her systems. The first Doppler map of UZ For was presented by Schwope et al. (1999) and their results showed several emission components. In this thesis, phase-resolved spectroscopy from SALT is used to compute Doppler tomography using the inside-out projection and flux modulation mapping in order to reveal detailed emission components and consequently broadening our knowledge of the accretion dynamics in AM Her systems.

Lastly, this thesis presents simultaneous multi-wavelength observations of UZ For with the aim of studying the system variability in different wavelengths. UZ For has been studied extensively in a wide range of wavelengths including optical (e.g. Allen et al. 1989, Schwope et al. 1990, Bailey & Cropper 1991), X-ray (e.g. Still & Mukai 2001), ultraviolet (Stockman & Schmidt 1996), extreme-ultraviolet (e.g. Warren et al. 1995) and most recently in radio regime by Barrett et al. (2017; 2020b). The strength of the magnetic field around the WD in UZ For, determined from cyclotron modelling, was a hot topic in the late 1980s, see e.g. (Beuermann et al. 1988, Ferrario et al. 1989, Schwope et al. 1990). Also, it has been shown that UZ For shows one or two pole accretion depending on accretion state (see e.g. Bailey & Cropper 1991). All these studies gave a clear picture of what is happening around UZ For even though the observations were not taken simultaneously. This thesis presents the first simultaneous optical (photometry and circular spectropolarimetry) and radio observations of this target taken with world-class telescopes such as SALT and MeerKAT. SALT spectropolarimetric observations are used to investigate the magnetic field of UZ For and MeerKAT is used to investigate the simultaneous radio emission. The SALT observations form part of the commissioning of the circular spectropolarimetry mode.

1.9.2 Thesis outline

This thesis is organised as follows. In Chapter 2, I show that the two-planetary system plus some form of the Applegate mechanism may be sufficient in explaining the residuals of UZ

For. In Chapter 3, I show that with the use of the inside-out Doppler tomography technique, the emission components contained in the spectra of UZ For can be broken into three main components as opposed to one component in the standard tomograms. Finally, in Chapter 4, I show that simultaneous multi-wavelength observations, of an AM Her system, UZ For, is essential in interpreting different emission mechanism that operates in mCVs. Through the first circular spectropolarimetry from SALT, we were able to detect cyclotron features in the spectra of UZ For and modelling of these features allowed us to estimate the magnetic field strength of 57 MG. Our results are consistent with the findings reported over three decades ago by Schwope et al. (1990). In addition, we detected UZ For in radio wavelengths at 1.28 GHz using the MeerKAT telescope. This thesis ends in Chapter 5 with the summary, conclusion derived from each chapter and possible future work.

Chapter 2

High-speed photometry of the eclipsing AM Her system UZ Fornacis

This chapter presents an analysis of high-speed photometry of the eclipsing AM Her type system, UZ For. This work has been published in the form of a paper in the **Astronomy and Astrophysics Journal** in 2019 with the same title (Khangale et al. 2019b). This chapter focuses on the analysis of new photometric observations of the eclipsing UZ For system spanning an additional eight years with the aim of investigating the purported cyclic variations reported in Potter et al. 2011 (hereafter Paper I) based on photometric observations spanning 27 years. According to Paper I, the mid-eclipse times of UZ For show departures from simple linear or quadratic trends with amplitudes of ∼60 s. The departures are strongly suggestive of two cyclic variations of 16(3) and 5.25(25) years. The two favoured mechanisms to derive such periodicities are either the presence of two giant extrasolar planets in the orbit around the binary or the Applegate mechanism due to magnetic cycle activity of the secondary star. However, in Paper I they argued that Applegate's mechanism would require the entire radiant energy output of the secondary and therefore this mechanism seems to be the least likely of the two to explain the mid-eclipse times. Also, there is no observational evidence that the entire radiant energy of the secondary star has been redirected to any mechanism such as the Applegate's mechanism. They found that the two-planet model provides realistic solutions but it does not quite capture all of the eclipse times measurements. Also, a highly eccentric orbit for the outer planet is required in order to get a good fit to the data. Generally, solutions with high eccentric orbits are deemed unstable and planetary systems of this nature do not last long. For example, Horner et al. (2012b) found that the two-planet solutions of Lee et al. (2009) proposed for the circumbinary around HW Vir were stable for less than a few 10^4 years. Stable circumbinary planetary systems have been reported in the literature. For example, Song et al. (2019)

found two-planet solutions with eccentricity $e \sim 0.15$ which are stable for 10^8 years for NY Vir. It is also possible that the periodicities are driven by some combination of both mechanisms.

The aim of this chapter is to address the following three points:

- the proposed model of cyclic variations predicts a maximum in observed-minus-calculated (O−C) diagram of UZ For between 2010 to 2012 and a minimum in O−C between 2016 and 2018.
- to investigate, with added data, if the proposed model is still sufficient to describe the updated O−C diagram, and,
- if the proposed model is insufficient to explain the observations, what else can be invoked to explain the results.

This chapter is structured as follows. Section 2.1 contains a literature review on eclipse times variations in eclipsing binaries and the mechanisms that have been suggested to explain these variabilities. Section 2.2 contains a brief review on UZ For and Section 2.3 gives an account of all the observations obtained for this study as well as the details of the instruments and data reduction methods. The results are presented in Section 2.4, including the new fitting parameters, the updated O−C diagram and the proposed mechanisms. The final results are discussed in Section 2.5. Section 2.6 gives the summary and conclusion based on the results.

2.1 Eclipse time variations in CVs

An interesting phenomenon that had been found to occur in a wide range of binary systems, is the cyclic modulations in the orbital periods of systems containing a late-type companion star, i.e. spectral type later than F5 (e.g. Hall 1989). These variations can be induced by several processes such as: mass transfer, angular momentum transfer or loss (e.g. Rappaport et al. 1983), magnetic activity (Applegate 1992), light travel time effect (e.g. Schwarz et al. 2011), apsidal motions, spurious signals or stellar evolution.

The mass transfer, from the secondary star in CVs, is highly variable and the majority of these systems change from a high state to a low state and back over time scales ranging from days to months and years. These variations range from both flickering, typical of CVs on time scales of minutes, to significant changes in the overall shape of the light curves. A number of factors can contribute to those variations which include the activity and the shape of the secondary star. The loss of angular momentum from the binary, due to either magnetic wind braking and/or gravitational radiation, are generally what define CVs. But these changes either result in an increase or decrease of the orbital period and therefore are aperiodic.

Apsidal motions are also ruled out for explaining the period variations in CVs since the orbital eccentricity is negligible and also both the primary and secondary minima show

identical residuals. The spurious signals can arise from star spots and other effects that distort the eclipsing binary light curve (e.g. Haghighipour 2015). While some of these are aperiodic signals, a few of them such as apsidal motions or the light travel time effect requires that the modulation in the orbital period should be strictly periodic. On the other hand, magnetic activities on the surface of the secondary star produces period changes up to 5–10 times the binary period (Applegate 1992). Sections 2.1.1 and 2.1.2 below review the two processes or mechanisms: the Applegate mechanism and circumbinary planets, that have been advanced in order to explain the variation in eclipse times observed in CVs.

2.1.1 Magnetic cycle mechanisms

Magnetic activities in the secondary star have long been suspected to be the cause of orbital period variation in close binaries. Matese & Whitmire (1983) proposed a mechanism to account for the cyclic period variation of the gravitational quadrupole moment of the secondary components and this was linked to dynamo action by Applegate & Patterson (1987). In another study, Warner (1988) linked the cyclic variations of the orbital period of the nova remnant, DQ Her, to variations in the radii of the companion star caused by solar-type (sunspot) magnetic cycles.

In the 1990s, Applegate (1992) proposed a model, now termed "Applegate mechanism", which can account for the period modulation in some eclipsing binaries over time scales of decades or longer. According to this mechanism, the period variations in CVs result from quasi-periodic changes in the quadrupole moment of the secondary star due to solar-like magnetic cycle activities. In this model, it is assumed that a strong magnetic field is produced by a dynamo cycle resulting in the redistribution of the angular momentum within the interior of the secondary star. This change, in the quadrupole moment of the secondary star, then leads to the variation of the orbital period. However, since the Applegate mechanism suggests magnetic activities as the main cause of period changes and magnetic activity requires convection, therefore the orbital period variation should only be observed in binaries with at least one convective star. Earlier, Hall (1989) conducted a study of 101 Algols and found that 31 of these systems showed evidence of period modulation and these also contained a convective companion. Based on these, Applegate (1992) suggested that there is a strong connection between the orbital period variations and the presence of magnetic activity.

The original Applegate model linking magnetic activity to orbital period variations has been reviewed by different authors. For example, Lanza et al. (1998) considered effects of an azimuthal magnetic field on the gravitational quadrupole moment of an active star. They identified the cause of the period variations with the magnetic dynamo of the active star, which transforms a portion of the outflowing energy generated in the nuclear burning regions into magnetic energy. They argue that this dynamo can not be of the $\alpha\Omega$-type (where Ω is the angular velocity of rotation and α is the correlation coefficient) as described in Applegate (1992), but is more likely to be an $\alpha^2\Omega$ dynamo. The Applegate mechanism was further developed by Lanza & Rodonò (1999) who considered the variation of the quadrupole

moment with the changes of kinetic and magnetic energy of the stellar hydromagnetic dynamo. This was applied to a sample of 46 close binaries with late-type components and their results are consistent with Hall's hypothesis that orbital period modulation is related to magnetic activity of the companion stars. Also, the presence of period variations in CVs below the period gap and in other magnetic active systems, suggests that the period variation is produced by a distributed dynamo working in the convection zone. This is because CV secondaries below the period gap have donors which are regarded as fully convective. As an example, Subebekova et al. (2020) found that the residual diagram of RW Tri shows a periodic variation with a period of ∼42 years and this is comparable with the mean value (40−50 years) of the change in quadrupole moment in magnetically active companions. This led them to conclude that the Applegate mechanism can be used to explain the variation in RW Tri, however, they did not rule out circumbinary planets as the other cause of eclipse time variations. Lanza (2006) found that for RS CVns, the hypothesis proposed by Applegate was not adequate to explain the orbital period modulation of close binary systems with a late-type secondary.

In another study, Völschow et al. (2016) presented an improved version of Applegate's mechanism which now includes the angular momentum exchange between a finite shell and the core of the star to derive the general conditions under which the Applegate's mechanism can operate. They find that, out of the 16 systems that were analysed, only four systems (e.g. QS Vir, DP Leo, V471 Tau, BX Dra) could be explained by the improved Applegate's mechanism. For the remaining systems, more than the total energy generated by the secondary star is necessary to power the binary's period variations. They note that for UZ For and three other systems, the ratio of energy required to power the improved Applegate mechanism to the total energy generated by the secondary star is almost unity. In the case of NN Ser, the ratio of energy required to power the improved Applegate mechanism to the total energy generated by the secondary star is greater than unity, implying that it can not be explained by magnetic activity. Furthermore, Völschow et al. (2018) described in detail the physics giving rise to the modulation of the orbital period due to kinetic and magnetic fluctuations. Their model shows that the resulting orbital period variations in binaries are one or two orders of magnitude lower than the observed values in RS CVns like systems. These support earlier conclusions, from existing theoretical work, that the Applegate mechanism may not be enough to produce the observed variations in these systems. However, they find that low-mass post-common-envelope binaries, such as CVs, with orbital separations less than one solar radius and secondary masses in the range of 0.30−0.36 $M_{\odot}$ are promising Applegate candidates.

2.1.1.1 Spectral type of the companion star

Bours et al. (2016) carried out a long-term programme of eclipse measurements on 67 WDs in close binaries in order to detect any period variations. Their results show that binary systems with baselines exceeding ten years and with companions of spectral types M5 or earlier, appear to show greater eclipse times variations than systems with companions of

spectral types later than M5. They found this to be consistent with an Applegate-type mechanism. However, they also considered it reasonable to assume that some planetary systems could exist around evolved WDs binaries, for example NN Ser (Beuermann et al. 2013, Hardy et al. 2016). A recent study by Pulley et al. (2018) agrees with the earlier conclusion by Bours et al. (2016) that higher values of the residuals are found with secondary companions of spectral type M5/6 or possibly earlier as a result of an Applegate mechanism. The spectral type of UZ For is dM4.5 (Beuermann et al. 1988) suggesting that an Applegate-type mechanism could be significant in this system.

2.1.2 Circumbinary planets

Circumbinary substellar objects have long been suspected to exist around main-sequence binary stars and close WD−main-sequence binaries. The presence of circumbinary planets in orbit around the binary will perturb the centre of mass of the binary system and cause a light-time delay along the line of sight (Irwin 1959). These delays can cause eclipses to appear earlier or later compared to a simpler linear ephemeris. That is, the observed and calculated eclipse times differ by an amount ranging from a few seconds to ∼100 s. The residuals between the observed and calculated eclipse times vary as the binary orbits the centre of mass of the system. These variations in the eclipse times appear as periodic variations in the residual diagrams due to the light travel time effect. Recently, Doyle et al. (2011) reported the detection of a transiting circumbinary planet around the main-sequence binary star, Kepler-16, with an orbital period of 229 days. The first substellar companion, a brown dwarf, was announced almost two decades ago around the post common-envelope binary V471 Tau (Guinan & Ribas 2001). At present, circumbinary planets have been claimed for a number of eclipsing, close compact binaries consisting of various companions, below we explain some of those binaries that have been suggested to host circumbinary planets. For a complete review on this topic, up to 2013, see Zorotovic & Schreiber (2013). According to Marsh (2018), eclipse time variations has been reported for over 30 binaries. Circumbinary planets has been suggested on at least ten systems as the main driver of the eclipse times variations. For six of these systems two or more planets were required to model the eclipse times variations. Recently, there has been a growing number of suspected circumbinary planets in post common-envelope binaries (see e.g. Mai & Mutel 2022, and references therein). Some of the binaries that have been suspected to host circumbinary planets are reviewed below.

Circumbinary planets have been suggested to explain the eclipse times variations in CVs, e.g. DP Leo (Qian et al. 2010, Beuermann et al. 2011), HU Aqr (Qian et al. 2011, Goździewski et al. 2015), UZ For (Dai et al. 2010, Potter et al. 2011) and pre-CV NN Ser (e.g. Beuermann et al. 2011). In the case of DP Leo, Qian et al. (2010) suggested that the cyclic variations is due to the presence of an exoplanet orbiting the binary with a period of 23.8 years. A follow-up study conducted by Beuermann et al. (2011) showed that the extrasolar companion to DP Leo was orbiting the binary with an orbital period of 28 years. For HU Aqr, Qian et al. (2011) proposed that the decrease in the orbital period

is due to the presence of two circumbinary planets orbiting the binary at 6.54 and 11.96 years, respectively − with the possibility of the third planet. However, Horner et al. (2011) found that the proposed planetary systems of HU Aqr were dynamically unstable on a time scale less than 5×10^3 years. They argued that if there is a second or third planet in the HU Aqr system, then their orbits are dramatically different from those suggested by Qian et al. (2011). Wittenmyer et al. (2012) re-analysed all the available eclipse times of HU Aqr at that time and deduced a two-planet solution which did not require the presence of additional planet(s) within the system. However, their dynamical analyses showed that the derived two-planet model was unstable on short time scales of 10^4 years. The eclipse times of HU Aqr was again re-analysed by Hinse et al. (2012) and they also found that the best-fitting model requires dynamically unstable solutions with high eccentric orbits for two planets. In both studies, Wittenmyer et al. (2012) and Hinse et al. (2012) noted that dynamically stable solutions are possible for HU Aqr if the orbits are non-coplanar, highly eccentric as well as retrograde. In a follow-up study, Goździewski et al. (2015) presented a further 22 new eclipse observations obtained between 2011 and 2014. The new observations showed deviations of 60−120 s from the previous ephemeris which required a complete re-analysis. Their results indicate that the hypothesis for a third and fourth body in HU Aqr is uncertain, however, their dynamical stability criterion and a particular geometry of orbits rule out coplanar orbits for the proposed two planets. In addition, they found examples of three-planet models for HU Aqr which require the middle planet to orbit in a retrograde motion, which are stable for at least 10^9 years and consistent with the observations.

NN Ser is one of the few post common-envelope binaries that has been suspected to host planets and has been extensively studied (e.g. Beuermann et al. 2011). Initially, Brinkworth et al. (2006) showed that NN Ser was losing angular momentum at a rate predicted by Rappaport et al. (1983) but only if they assume that magnetic braking was not cut off as the secondary reaches 0.3 $M_{\odot}$. NN Ser was later shown to host two planets around its orbit by Qian et al. (2009b) and Beuermann et al. (2010; 2011). The two-planet model, derived to explain the eclipse time variation for NN Ser, has been shown to be dynamically stable and survived follow-up eclipse time measurements (Horner et al. 2012a, Beuermann et al. 2013, Marsh et al. 2014). In addition, a recent study conducted by Bours et al. (2016), on WD binaries, showed that the long-period quadratic term in the model of NN Ser is in the direction of increasing period and this is unlikely caused by natural processes that lead to angular momentum loss. Therefore, this suggests that circumbinary planets are needed to explain the variations observed for NN Ser. Recently, Hardy et al. (2016) detected a circumbinary disc around NN Ser and this further supports the planetary system hypothesis.

Other systems found to show orbital period variations include: a WD and a main-sequence star binary e.g. QS Vir (e.g. Parsons et al. 2010, Almeida & Jablonski 2011) and V471 Tau (e.g. Kundra & Hric 2011); systems with a hot subdwarf primary and a main-sequence or a brown dwarf companion e.g. HW Vir (e.g. Lee et al. 2009, Beuermann et al. 2012), NY Vir (e.g. Qian et al. 2012, Lee et al. 2014, Song et al. 2019, Er et al.

2021) and HS 0705+6700 (V470 Cam) (e.g. Qian et al. 2009a; 2013, Bogensberger et al. 2017); low-mass X-ray binaries e.g. EXO 0748−676 (Wolff et al. 2009, Raman & Paul 2017) and MXB 1658−298 (Jain et al. 2017, Iaria et al. 2018); millisecond binary pulsars e.g. PSR J2051−0827 (Lazaridis et al. 2011) and PSR J2339−0533 (Pletsch & Clark 2015). The majority of the planetary systems proposed for these systems had been found to be dynamically unstable on time scales $< 10^4$ years e.g. HW Vir (Horner et al. 2012b), QS Vir (Horner et al. 2013); while some are dynamically stable for 10^8 years e.g. NY Vir (Song et al. 2019). Recently, the eclipse times of HW Vir were revisited by different authors (e.g. Esmer et al. 2021, Brown-Sevilla et al. 2021, Mai & Mutel 2022) and reanalyzed with new data added and still show continuation of eclipse time variations but none of these studies found stable solutions for the suspected planetary systems on time scale of 10^5 years. For QS Vir, Parsons et al. (2016) recently found evidence of prominences passing in front of both the companion star and the WD and also noted that the M star was heavily spotted suggesting a high level of magnetic activity on the companion. Recently, Latković et al. (2019) analysed photometric light curves of QS Vir and noted that a dark spot is responsible for the light curve distortions. For V471 Tau, the presence of circumbinary planets were later disproved by Hardy et al. (2015) and they suggest that the variation in this system is consistent with the Applegate mechanism. Recently, Vanderbosch et al. (2017) used two clocks: the spin period and orbital period, and came to the same conclusion ruling out possibility of circumbinary planets and rather they attributed this to magnetic activities in the dwarf K-star companion. Further studies conducted recently on V471 Tau by different authors (e.g. Zaire et al. 2021, Kővári et al. 2021) continue to favour magnetic cycle activities of the secondary star. For V470 Cam, Mai & Mutel (2022) found dynamically stable solutions with two and three circumbinary planets on time scale of 10^8 years, however, they noted that their solutions had reduced χ^2 values ranging from 10 to 15 and attributed this to underestimated uncertainties in previously published timing measurements.

2.2 Historical mid-eclipse times of UZ For

The first eclipses of UZ For were obtained with the EXOSAT satellite in 1983 and 1986 and reported in Osborne et al. (1988). A total of two eclipses were derived from the X-ray data. The first ephemeris of UZ For was derived by Beuermann et al. (1988) based on six mid-eclipse times determined from photometric, spectroscopic and polarimetric light curves of this system. These were combined with the mid-eclipse times from Osborne et al. (1988) to derive an improved linear ephemeris, see Eq. 2 of Beuermann et al. (1988). However, Beuermann et al. (1988) noted that there was no significant orbital period change over the four-year interval of the above observations. Therefore, their ephemeris was adequate to assign the cycle number for all the eight available eclipse times. They used a quadratic fit to derive the orbital period change for UZ For and found this to be on the time scale greater than 4×10^6 years. They concluded that the stability of UZ For's spin−orbit coupling was as good as that of another AM Her system, DP Leo (e.g. Biermann et al. 1985). Further four

mid-eclipse times of UZ For were obtained by Berriman & Smith (1988) and these were used to refine the orbital period of the binary. In another study, Ferrario et al. (1989) presented a further four mid-eclipse times of UZ For and these were combined the mid-eclipse times from Osborne et al. (1988) to improve the ephemeris. No further analysis was pursued. Allen et al. (1989) obtained another mid-eclipse time of UZ For and this was combined with all the other mid-eclipse times from the literature (e.g. Osborne et al. 1988, Beuermann et al. 1988, Berriman & Smith 1988, Ferrario et al. 1989) to bring the total to 17 and these were used to improve the ephemeris. Similar to Beuermann et al. (1988), Allen et al. (1989) reported that there was no evidence for a significant departure from linear ephemeris in the timing residuals of UZ For.

Bailey & Cropper (1991) obtained a further six mid-eclipse times of UZ For in 1989 October and these were combined with the 17 mid-eclipse times used in the ephemeris of Allen et al. (1989) in order to improve and update the ephemeris. Their results showed that significant residuals remained with after subtracting the linear ephemeris from the observed mid-eclipse times of UZ For (see Figure 3 Bailey & Cropper 1991). They noted that the mid-eclipse times of UZ For could not be fitted with a linear ephemeris but required a quadratic term. Ramsay (1994) presented a further five mid-eclipse times of UZ For and these were combined with the timings from the literature (e.g. Osborne et al. 1988, Beuermann et al. 1988, Ferrario et al. 1989, Allen et al. 1989, Bailey & Cropper 1991), excluding those from Berriman & Smith (1988) to bring the total to 23 eclipse times, in order to improve the ephemeris. They fitted a linear and a quadratic fit to the eclipse times of UZ For and noted that the quadratic fit (which gave reduced chi-square value of 1.23) was a better fit to the data compared to the linear fit (reduced chi-square of 3.07). Furthermore, their F-test revealed that the quadratic fit was a better fit compared to the linear fit with confidence level of 97.7%. Although no conclusion was given, Ramsay (1994) noted that the quadratic term of UZ For was in the direction of increasing period on a time scale of $\sim 10^8$ years. Period changes in CVs at that time had already been detected in other systems such as EX Hya (Bond & Freeth 1988) and DQ Her (Warner 1988). The period changes in these systems were all in the direction of decreasing orbital period and the opposite of what was seen on UZ For. However, Warner (1988) attributed the period changes in these binaries to solar-type magnetic cycles in the secondary star.

Warren et al. (1995) derived two further mid-eclipse times from EUVE observations. These were combined with the eclipse times from the literature mentioned above, however they first offset the mid-eclipse times obtained before Bailey & Cropper (1991) by 9 s in order bring them to the centre of the WD eclipse rather than the centre of eclipse of the bright spot and constructed a residual diagram by fitting a linear function to the timings of UZ For. In a follow-up study, Imamura & Steiman-Cameron (1998) obtained eight mid-eclipses of UZ For, as usual these were also combined with those from the literature and corrected for the offset as mentioned above prior to fitting a quadratic function to the timings. Their quadratic term pointed at an increasing orbital period of UZ For, consistent with that of Ramsay (1994). In addition, Perryman et al. (2001) derived a linear ephemeris using their three eclipses

combined with earlier six timings presented by Bailey & Cropper (1991). They (Perryman et al. 2001) excluded the other existing mid-eclipse times from Ramsay (1994), Imamura & Steiman-Cameron (1998) due to that they give residuals of ±50 s. The large residuals were attributed to the motion of the accretion spot on the surface of the WD (∼40 s but this was unlikely since the emission does not originate far above the WD's surface. In addition, the uncertainties in correcting the mid-eclipse times to the centre of the WD also pose a threat to earlier data which were of low resolution. Their new ephemeris was used to produce a residual diagram which showed less than 1 s residuals when compared to their mid-eclipse times (Perryman et al.'s data) and less than 4 and 5 s residuals when compared with the eclipse times of Bailey & Cropper (1991) and Ramsay (1994), respectively. They attributed the residuals of the order of ±50 s to timing errors or other untraceable inconsistencies. A further eclipse light curve of UZ For is presented in de Bruijne et al. (2002).

Over a decade ago, Dai et al. (2010) presented 44 mid-eclipses of UZ For and noticed a deviation from linear and quadratic trends in the O−C diagram of UZ For. They explained the deviations by adding a sinusoidal term to the ephemeris and attributed the cyclic variation as due to a planet with the period of ∼23(5) years. Potter et al. (2011) presented new mid-eclipse times, including those from literature and included in Dai et al. (2010), over the 28 year baseline and noticed a deviation from linear and quadratic trends with amplitudes of 60 s. They interpreted this as the result of two cyclic variations due to two extrasolar planets in orbit around the binary with periods of ∼16 ± 3 years and ∼5.25 ± 0.25 years. However, they did not rule out the possible effect of a magnetic cycle mechanism. This chapter presents a further long-term (∼8 years) photometric monitoring of UZ For, extending the baseline of observations to 35 years, in order to test the two planet-model previously proposed to explain the variations in the eclipse times of UZ For spanning over 27 years.

2.3 Observations and data reductions

Photometric observations were made between 2011 March and 2018 February on the 1.0-m and 1.9-m telescopes (see Figure 2.1) located at the site of the South African Astronomical Observatory (SAAO) in Sutherland using either the HIgh-speed Photo-Polarimeter (HIPPO; Potter et al. 2010) or the Sutherland High-speed Optical Camera (SHOC; Gulbis et al. 2011a, Coppejans et al. 2013). The former (HIPPO) was built in order to replace the ageing and successful single-channel University of Cape Town photo-polarimeter (Cropper 1985). The latter came into use to replace the University of Cape Town Photometer (O'Donoghue 1995). The details of each of these instruments are given in Sections 2.3.1 and 2.3.2, respectively.

2.3.1 Photometry with HIPPO

Photo-polarimetric observations of UZ For were obtained by Dr Stephen Potter using the HIPPO instrument that is mounted on the Cassegrain focus of the SAAO 1.9-m telescope from 2011 March 08 to 2018 October 04 as part of the on-going photo-polarimetric monitor-

Table 2.1: Observational log of UZ For. All observations were made with the HIPPO and SHOC instruments on the SAAO 1.0-m and 1.9-m telescopes.

Date of observation	Start time UT	End time UT	SAAO telescope used	Instrument used	Length of observations (hours)	Binning used	Number of eclipses
2011-03-08	18:12	18:34	1.9-m	HIPPO	0.37	-	1
2011-10-27	23:52	02:28	1.9-m	HIPPO	2.60	-	1
2011-10-31	21:28	22:22	1.9-m	HIPPO	0.90	-	1
2011-11-01	00:58	02:14	1.9-m	HIPPO	1.26	-	1
2012-02-26	18:40	20:18	1.9-m	HIPPO	1.63	-	1
2012-07-17	03:18	04:11	1.9-m	HIPPO	0.88	-	1
2012-12-17	20:43	21:18	1.0-m	SHOC	0.59	16 × 16	1
2013-02-08	20:01	21:03	1.9-m	SHOC	1.02	8 × 8	1
2013-03-13	18:16	19:42	1.9-m	HIPPO	1.43	-	1
2013-03-16	18:46	19:33	1.9-m	HIPPO	0.79	-	1
2013-03-17	18:04	19:10	1.9-m	HIPPO	1.11	-	1
2013-10-03	02:02	02:33	1.0-m	SHOC	0.52	16 × 16	1
2013-11-28	19:50	21:31	1.9-m	HIPPO	1.68	-	1
2014-01-12	20:40	21:48	1.9-m	SHOC	1.13	8 × 8	1
2014-03-02	18:17	19:56	1.9-m	HIPPO	1.65	-	1
2014-10-22	20:45	21:45	1.9-m	SHOC	1.00	16 × 16	1
2014-10-23	21:45	22:55	1.9-m	SHOC	1.17	16 × 16	1
2014-10-24	21:22	22:08	1.9-m	SHOC	0.77	16 × 16	1
2014-10-26	21:59	22:35	1.9-m	SHOC	0.62	16 × 16	1
2014-10-28	20:30	23:12	1.9-m	SHOC	2.70	16 × 16	2
2015-02-18	19:11	21:15	1.0-m	SHOC	2.06	16 × 16	1
2015-02-23	18:35	19:26	1.0-m	SHOC	0.85	16 × 16	1
2015-03-21	17:52	19:13	1.9-m	HIPPO	1.35	-	1
2015-07-31	02:20	03:20	1.9-m	SHOC	1.00	8 × 8	1
2015-09-04	01:30	02:30	1.9-m	SHOC	1.00	8 × 8	1
2016-11-11	19:25	21:29	1.0-m	SHOC	2.08	8 × 8	1
2016-11-14	19:30	21:31	1.0-m	SHOC	2.03	8 × 8	1
2017-10-26	20:35	22:50	1.0-m	SHOC	2.25	8 × 8	1
2017-11-16	20:24	01:31	1.9-m	HIPPO	5.12	-	3
2018-02-21	18:54	19:53	1.9-m	HIPPO	1.00	-	1
2018-10-04	22:42	00:14	1.9-m	HIPPO	1.54	-	1*
2018-11-06	20:10	22:29	1.9-m	SHOC	2.30	4 × 4	1*
2019-10-13	22:46	01:00	1.0-m	SHOC	2.23	4 × 4	1*
2021-01-20	00:45	02:47	1.0-m	SHOC	1.73	4 × 4	1*

Notes: * – marks the observations that were not included in the analysis of this chapter.

Figure 2.1: Picture showing some of the telescopes at the SAAO site in Sutherland used in this PhD study. (Picture adopted from www.saao.ac.za and edited for the purpose of this work.)

ing campaign of mCVs. The log of observations is shown in Table 2.1. All the observations were made in good seeing conditions. The schematic of the HIPPO instrument is shown in Figure 2.2. The HIPPO has superachromatic half- and quarter-wave plates and uses a Thompson beam-splitter. HIPPO uses two photo-multiplier tubes that act as detectors. Therefore, HIPPO is a photon counting instrument capable of obtaining simultaneous measurement in both channels at a resolution of 1 ms and this is ideal for studying variability in mCVs. The dual counter-rotating half- and quarter-wave plates modulate the signal at 10 Hz and allow simultaneous determination of all four Stokes parameters.

The HIPPO instrument was operated in its photo-polarimetry mode (all-Stokes) and the observations were clear filtered (white light, 3500–9000 Å) and were defined by the response of the two RCA31034A GaAs photo-multiplier tubes. However, this study uses the photometric mode of the HIPPO instrument. Background sky measurements were taken at frequent intervals (i.e. every 30 min) during the observations. All the observations were synchronized to the Global Positioning System (GPS) to better than a millisecond. Data reduction was performed by Dr Stephen Potter following the procedures described in Potter et al. (2010). Both the 1 ms photometric data streams from the target and the background obtained were sorted into channel 1 and channel 2 counts, then co-added and binned into 1 s bins. The binned background sky measurements were subtracted from the binned target measurements. A total of 16 eclipses were obtained in photometric conditions. An example of a light curve taken by HIPPO is shown in Figure 2.3. Note that HIPPO is a photon-counting device, therefore, the typical error on the points shown are given as the square root of the total counts.

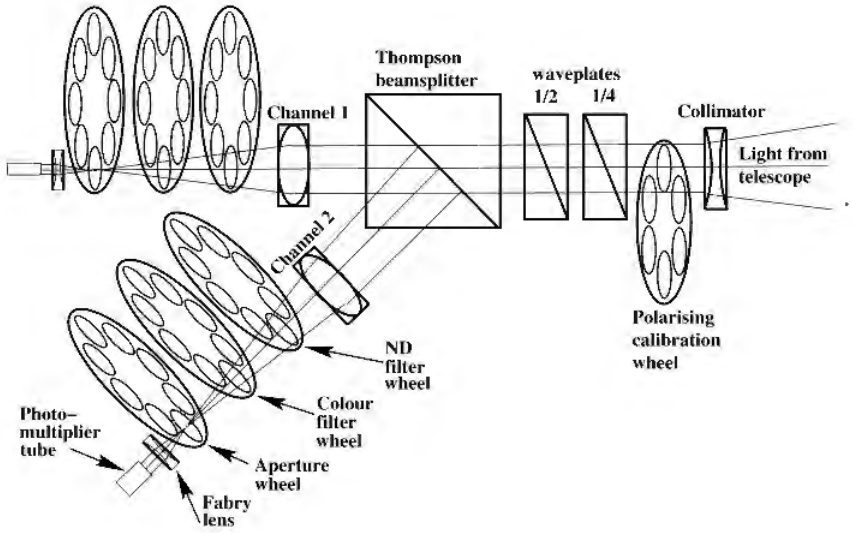

Figure 2.2: The optical layout of the HIPPO instrument. Adopted from Figure 1 of Potter et al. (2010).

2.3.2 Photometry with SHOC

High-speed photometric observations of UZ For were obtained by several people (Dr Stephen Potter, Dr Enrico Kotze, Mr Hannes Breytenbach and Dr Andrey Semena) with the SHOC instrument mounted on Cassegrain focus of either the SAAO 1.0- or 1.9-m telescope between 2012 December 17 and 2018 November 6. The SHOC cameras (see Figure 2.4) are two nearly identical instruments that are available to use on either the SAAO 1.0-m or 1.9-m telescopes. The log of observations is shown in Table 2.1. All the observations were made in good seeing conditions. The SHOC design is based on two other existing instruments Portable Occultation, Eclipse, and Transit Systems (POETS; Souza et al. 2006) and Massachusetts Institute of Technology Optical Rapid Imaging System (MORIS; Gulbis et al. 2011b). POETS was developed by a collaboration between groups from Massachusetts Institute of Technology (MIT) and Williams College and MORIS at 3-m NASA Infrared Telescope Facility (NASA-IRTF) on Mauna Kea, Hawaii. The SHOC 1 and 2 instruments are high-speed, visible wavelength systems, which employ an Andor iXon 888 EM CCD cameras with physical size of 2048 × 1024, 13 μm pixels CCD (and an imaging area of 1024 × 1024, 13 μm pixels), that are mounted using the existing filter wheels employed by the SAAO CCDs. They have high quantum efficiency (>90% from 4800–7000 Å) and have an electron multiplying capability. The SHOC cameras use intelligent reference TM-4 GPS receivers and two filter wheels. The SHOC cameras have a field of view (FoV) of 2.85 × 2.85 and 2.79 × 2.79 arcmin for the SAAO 1.0-m and 1.9-m telescopes, respectively. These cameras have a selection of amplifiers each having multiple electron to ADU gain settings. For more details on these cameras, see Coppejans et al. (2013).

All the observations were made with the SHOC detector in frame-transfer mode with

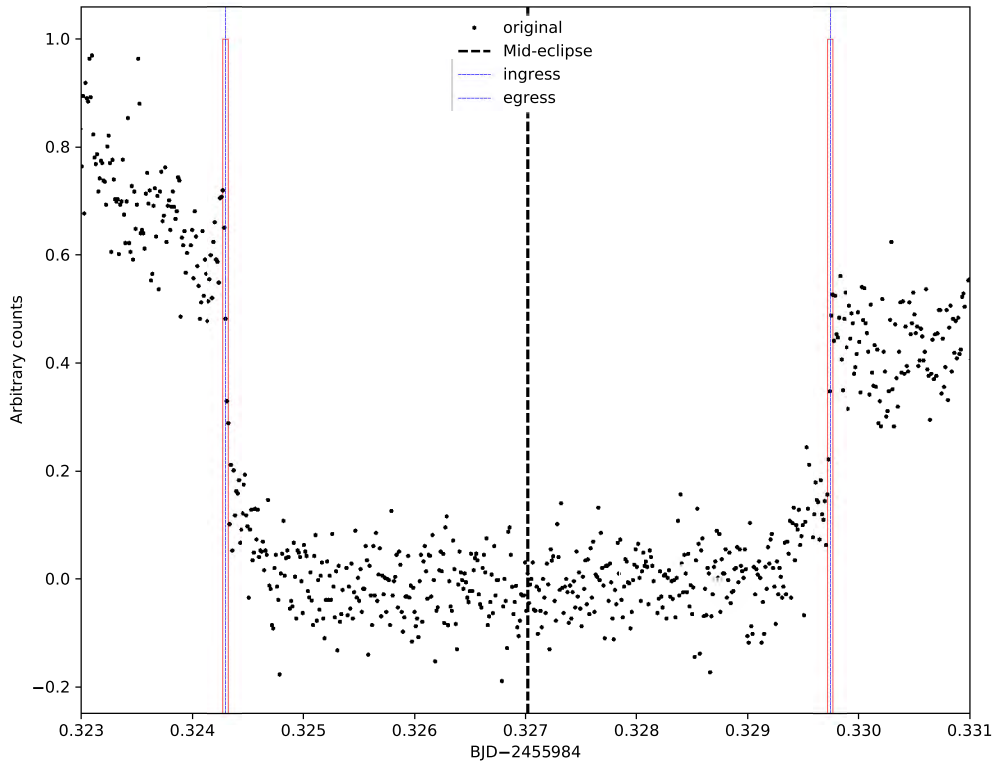

Figure 2.3: An example eclipse of UZ For obtained with the HIPPO instrument on 2012 February 26 during the faint state. The vertical blue dashed lines represent the times of ingress and egress of the main accretion spot, whereas the vertical black dashed line marks the time of mid-eclipse. The red box around the ingress and egress mark the standard error associated with their measurement.

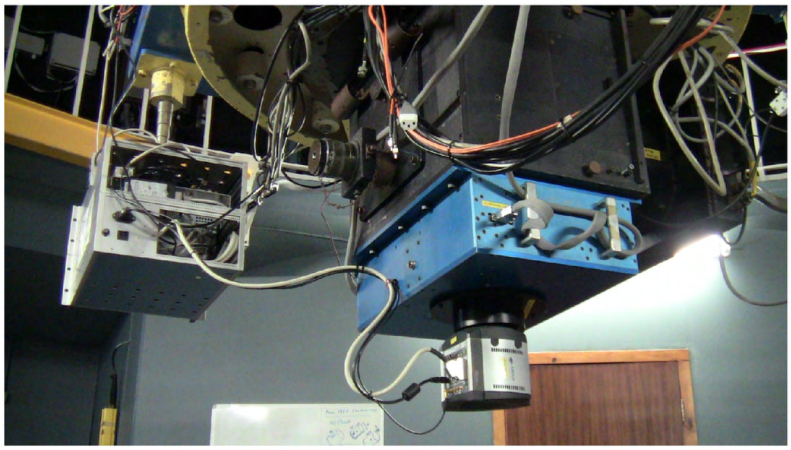

Figure 2.4: The SHOC instrument mounted below the Cassegrain focus of the SAAO 1.0-m telescope. Adopted from Figure 2 of van Gend et al. (2016).

a clear filter (white light mode). The binning of data ranged from 4 × 4 to 16 × 16 (see Table 2.1) and the exposure times of one second were used. Differential photometry was performed on the resulting data cubes by the observers (Dr Stephen Potter, Dr Enrico Kotze, Mr Hannes Breytenbach, Dr Andrey Semena) using the SHOC-pipeline described in Coppejans et al. (2013). A total of 17 high-time resolution and high signal-to-noise ratio eclipses of the target were obtained. An example of a light curve taken by SHOC is shown in Figure 2.5. The larger scatter in Figure 2.3 compared to that in Figure 2.5 is due to different states of mass accretion between the two observations. These two figures will be discussed in detail in Section 2.4.1. These eclipse profiles are discussed in Section 2.4.1. The eclipses of UZ For from the two instruments, HIPPO and SHOC, were combined to give a total of 33.

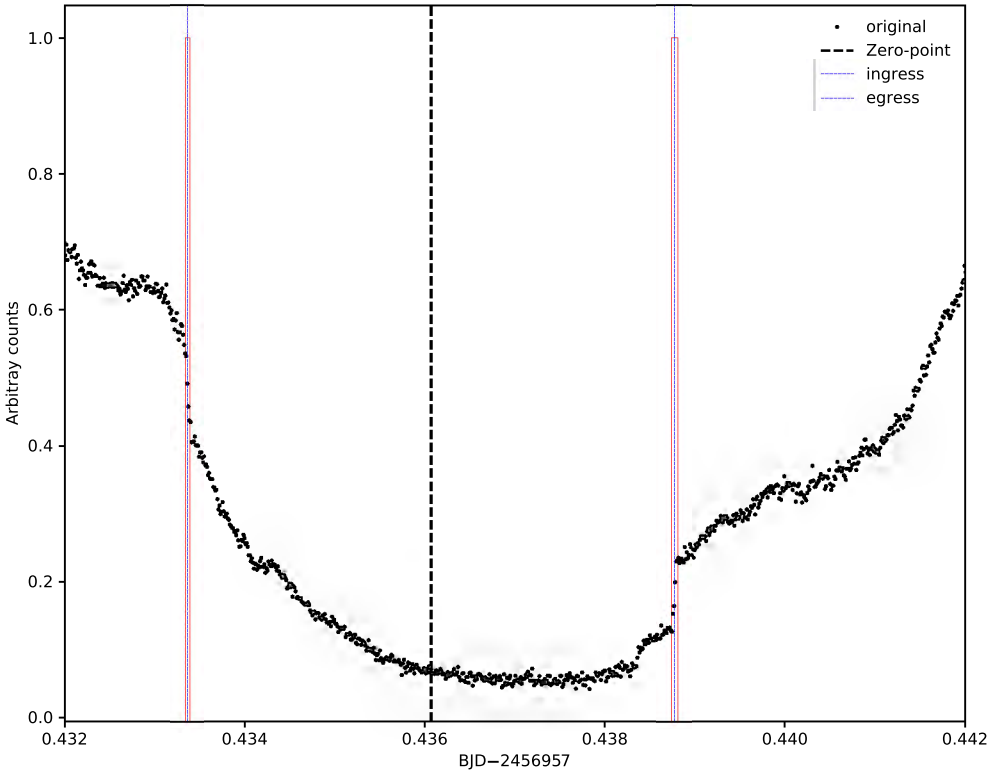

Figure 2.5: An example eclipse of UZ For obtained with the SHOC instrument on 26 October 2014 during the high state. The vertical blue dashed lines represent the times of ingress and egress of the main accretion spot, whereas the vertical black dashed line marks the time of mid-eclipse. The red box around the ingress and egress mark the standard error associated with their measurement.

2.3.3 Measurement of the times of mid-eclipse

The shapes of the eclipse profiles of some eclipsing CVs, specifically AM Her systems, allow us to determine, with precision, the time of mid-eclipse. UZ For is such an example and its

eclipse profiles have clearly defined ingress and egress of the main accretion spot as shown in Figure 2.5. For this thesis, the ingress time is defined as the midpoint between the start and end times of the steep drop to minimum, lasting ∼3 seconds, when the main accretion spot is eclipsed as shown in both Figures 2.3 and 2.5. On the other hand, the egress time is defined as the midpoint between the start and end times of the steep rise from minimum, lasting ∼3 seconds, of the main accretion spot as shown in Figures 2.3 and 2.5. The ingress and egress points used in this thesis are consistent with those used in Paper I.

Before any measurements could be made, all the times were corrected for the light travel-time to the barycentre of the solar system, converted from Julian Date (JD) to Barycentric Dynamical Time (TDB) system as Barycentric Julian Date (BJD, Eastman et al. 2010) using an Interactive Data Language (IDL*) script written by Dr Stephen Potter. In other cases, the resulting ingress and egress times were converted to BJD using the online-version† of the IDL scripts which utilize the coordinates of UZ For (right ascension (RA) and declination (Dec)) and the observatory where the observations were made. Both methods give BJD's to an accuracy of 20 ms or less and this is sufficient for the science that is undertaken. The conversion to BJD was done in order to remove any timing systematic, particularly due to the accumulation of leap seconds with Coordinated Universal Time (UTC) and the effects due to the influence of Jupiter and Saturn when heliocentric corrections only are applied.

In order to accurately determine the times of mid-eclipse, measurements of the start and end times of the ingress and egress of the main accretion spot were made by eye on a python window. In some cases where the ingress and egress are not clear, the light curve were smoothed using Savitzky-Golay filter (Savitzky & Golay 1964) as implemented in python. The times of ingress or egress were then determined by averaging the two times (i.e. the start and end times of the ingress or egress) to get the midpoint time. The standard error in the times of ingress and egress are defined as the width (or duration) of the steep ingress and egress times as shown in Figures 2.3 and 2.5. The ingress and egress times are presented in column 5 and 6 of Table 2.3 (at the end of this Chapter) and the number in brackets are the standard error associated with each measurement.

Similar to the times of ingress and egress, the time of mid-eclipse were determined as the midpoint between the ingress and the egress of the main accretion spot (see e.g. Figure 2.5). The calculated values of the times of mid-eclipse are shown in column 2 of Table 2.3 and given in BJD. The standard error in the determined time of mid-eclipse were propagated using equation 2.1 below:

$$\Delta \mathrm{BJD_{TDB}} = \sqrt{(\Delta \mathrm{T_{ingress}})^2 + (\Delta \mathrm{T_{egress}})^2}, \tag{2.1}$$

where $(\Delta \mathrm{T_{ingress}})$ and $(\Delta \mathrm{T_{egress}})$ are the estimated error in the measurements of the times of ingress and egress, respectively. The standard errors in the mid-eclipse times are shown in column 3 of Table 2.3 in units of days. The difference between the times of ingress and

*IDL is a trademark of ITT and/or exelis Visual Information Solutions. For further details see http://www.exelisvis.com/ProductsServices/IDL.aspx.

†More details can be found at http://astroutils.astronomy.ohio-state.edu/time/utc2bjd.html.

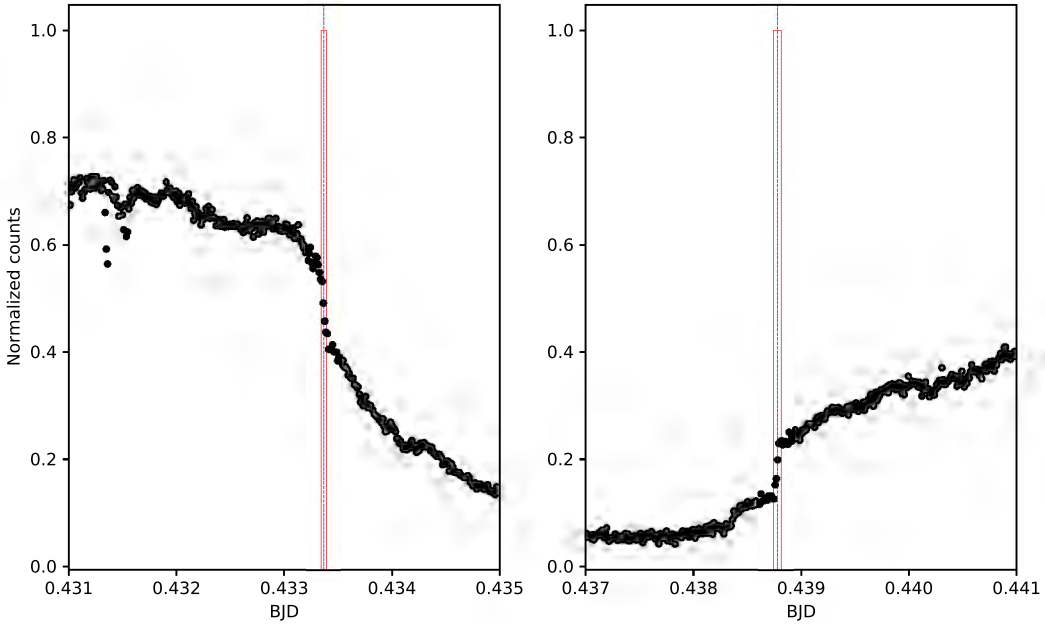

Figure 2.6: A zoom-in around the time of ingress (left) and egress (right) of the main accretion spot of UZ For. The vertical dashed blue lines show the time of ingress or egress and the red box enclosing the vertical blue dashed lines represent the margin of errors associated with the measurement of the ingress and egress.

egress gives the width or duration of the eclipse in seconds and these values are shown in column 4 of Table 2.3 and the numbers in parenthesis are the one σ errors in the times of mid-eclipse given in units of seconds. The new mid-eclipse times were combined with the 42 mid-eclipse times (and their standard errors) presented in Paper I to give a new total of 75 and these are presented in Table 2.3. Note that the standard errors from the literature (i.e. Paper I) were calculated depending on the signal-to-noise ratio (S/N) and time resolution at the time of the spot ingress and egress.

2.4 Results

2.4.1 Eclipse profiles

Figures 2.3 and 2.5 show two examples of the eclipse profiles of UZ For. The former was obtained during a faint state whereas the latter was obtained during a bright state. This is reflected by large scatters in the former compared to the latter figure. The rest of the eclipse light curves obtained for this study, from 2011 to 2018, are shown in Figures 2.7 and 2.8. The large scatter in counts in some panels of these two figures (Figures 2.7 and 2.8) are due to flickering and other factors such as reduced state of accretion and consequently the system is fainter. The observation dates and the instrument used are included in the top right corner of each panel. It is evident from the two figures that the ingresses and egresses

of the main accretion spot are clearly defined and lasts a few seconds. However, there was no flux calibration performed to all the light curves and therefore, the relative signal-to-noise of the datasets presented is indicative of the relative brightness. The eclipse profiles of UZ For are understood in the framework of the standard model of an AM Her system (Beuermann et al. 1988, Ferrario et al. 1989, Bailey & Cropper 1991). Depending on accretion state, UZ For shows either one-pole (Bailey & Cropper 1991, Imamura & Steiman-Cameron 1998) or two-pole (Perryman et al. 2001) accretion spots.

The faint state eclipse profile appears flatter and noisier than the brighter state eclipse profile (most seen in Figure 2.7, top and second rows). It is apparent that there are two clear stages in both the ingress and egress. The ingress is defined by a fast drop in counts which lasts approximately 3 s. This is followed by a more gradual decline to a minimum (∼50 s). After this the eclipse or counts remain flat/constant for (∼380 s). The egress begins with a slow initial rise in counts which lasts ∼30 s and this is followed by a rapid rise (∼3 s). The shapes of the faint-state eclipse profile is similar to those of the low-state of UZ For presented in Bailey & Cropper (1991).

The bright-state eclipse profile also shows different stages in both the ingress and egress (see examples in Figure 2.8, top and second rows). The ingress is characterized by a fast drop in counts lasting ∼3 s. This is followed by a brighter and longer gradual decline to a minimum lasting ∼260 s, compared to the faint-state eclipse profile, resulting in a shorter time for the flat minima (∼169 s). The flatter minima is not entirely flat in shape. The egress begins with a two-step increase in counts (∼34 s), possibly indicating accretion at the second pole, followed by a rapid increase (∼3 s) as the main pole egresses. The various stages are consistent with bright-state accretion with two accretion spots and a brighter magnetic accretion stream contributing to the overall brightness of the system. The bright-state eclipses presented here are similar to those presented by Imamura & Steiman-Cameron (1998). In both cases, the faint and bright states, the eclipse width remained the same at ∼472 s, consistent with the eclipse of the main accretion spot. It is possible to derive the size of the accretion spot using the duration of the ingress/egress, the semi-major axis of the binary, the inclination angle of the binary. Noteworthy, O'Donoghue et al. (2006) used models the eclipse ingress and/or egress to constrain the size of the accreting region for SDSS J015543.40+002807.2.

2.4.2 The new mid-eclipse times

2.4.2.1 Assigning Cycle Numbers

In order to assign cycle numbers to the new mid-eclipse times, Eq. 2.2 below was used:

$$N = \frac{T_i - T_0}{P_{\rm orb}} \tag{2.2}$$

where N is the cycle number, T_i is the individual measured time of mid-eclipse, T_0 is the time of epoch (T_0 = 2453405.30066303) and $P_{\rm orb}$ is the orbital period of the binary ($P_{\rm orb}$

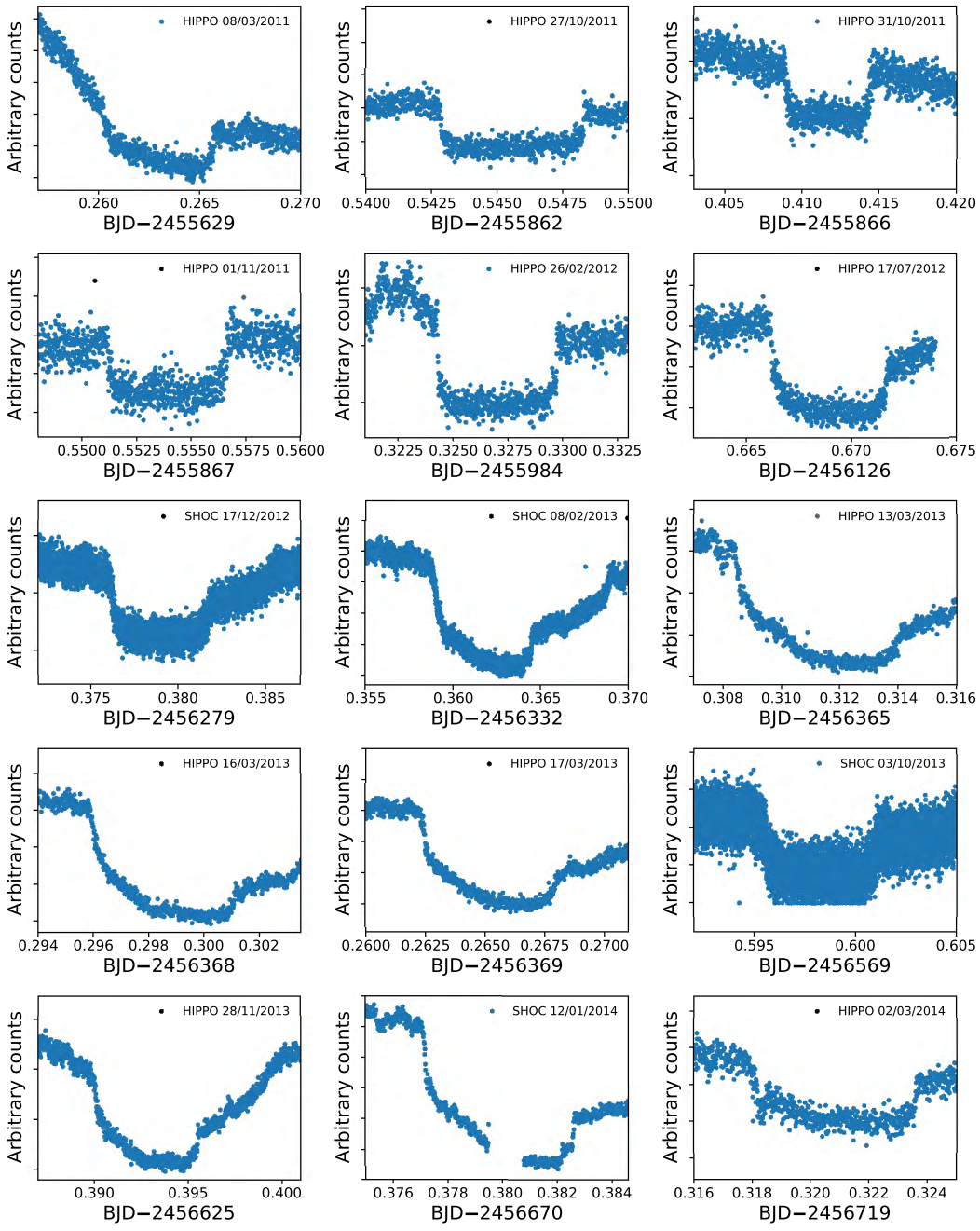

Figure 2.7: A sample of the new eclipse observations of UZ For. The legend in each panel shows the name of the instrument used as well as the date of the observations.

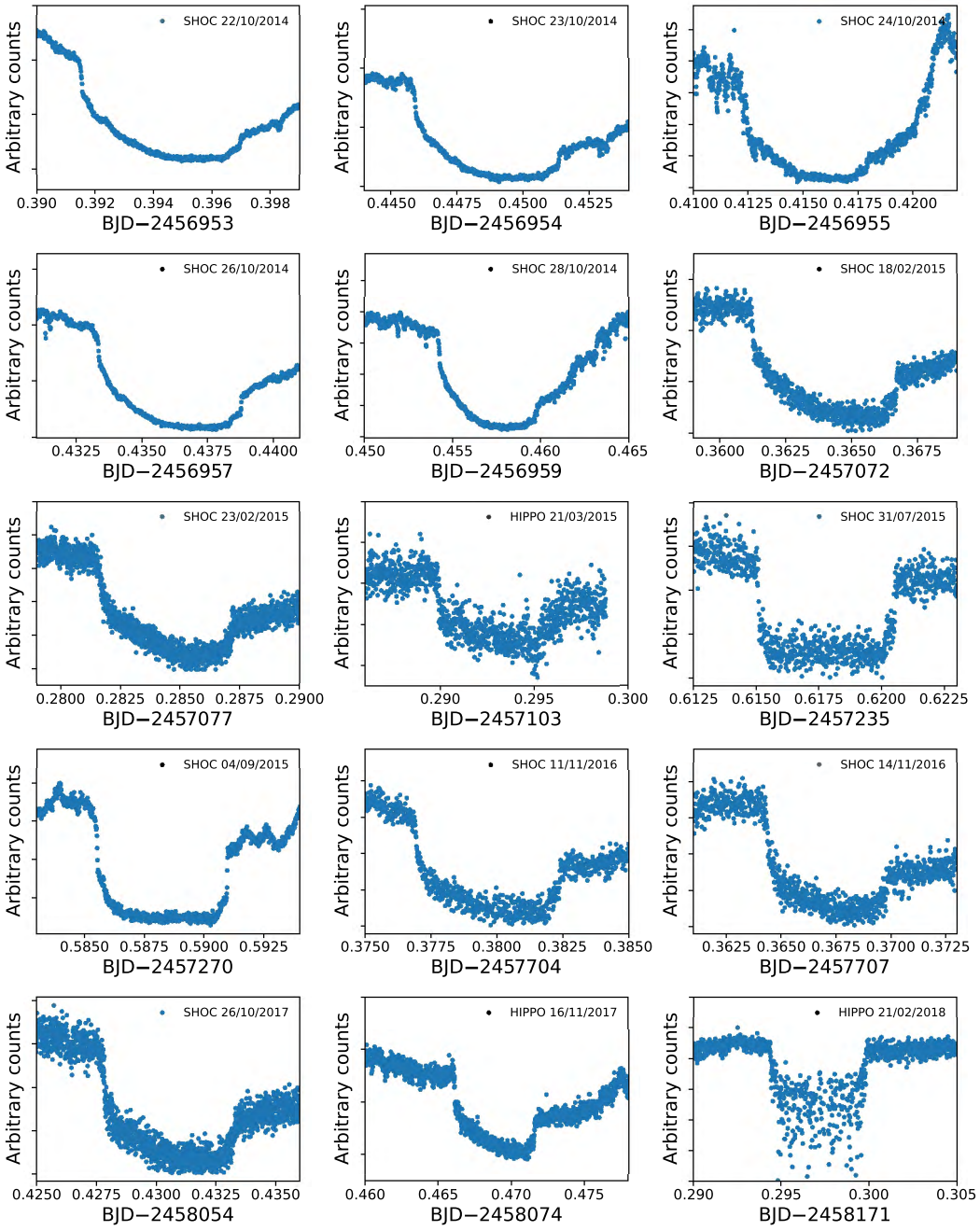

Figure 2.8: A sample of the new eclipse observations of UZ For. The legend in each panel shows the name of the instrument used as well as the date of the observations.

= 0.087865425 day). Both the epoch and the orbital period are those from Paper I. The orbital period is accurate enough to assign cycle numbers to the entire 35 years of eclipses. These values are shown in column 1 of Table 2.3 (at the end of this Chapter).

2.4.2.2 The old O−C diagram

As already mentioned in Section 2.2, departures from a linear and quadratic ephemeris from UZ For were noted by Dai et al. (2010) and Potter et al. (2011). In both these studies, the general approach was to model the residuals T using an equation of the form:

$$T(\mathrm{BJD_{TDB}}) = T_0 + P_{\mathrm{bin}}E + AE^2 + \sum_p \tau_p(E) \tag{2.3}$$

where T_0 is the time of the epoch, P_{bin} is the orbital period of binary in days, A is the quadratic parameter and $\tau_p(E)$ is a cyclic term for the residuals deviations induced by gravitational perturbation of the centre of mass by the extrasolar companions (p=3,4, ...). For the case of a third and/or forth body in elliptical orbit, the $\tau_p(E)$ term is given by the formulation of equation 3 of Irwin (1952) shown below:

$$\tau_p(E) = K_{\mathrm{bin},(p)}\left[\frac{\sin(\upsilon_p - \varpi_p)(1-e_p^2)}{1+e_p\cos(\upsilon_{\mathrm{p}})}\right]$$

where $K_{\mathrm{bin,p}}$ is semi-amplitude of the eclipse time variation of body p, υ_p is the true anomaly, ϖ_p is the argument of periastron and e_p is the eccentricity of the orbit. The other parameters such as the time of periapsis (T_p) and the orbital period (P_p) of body p are introduced indirectly through the eccentric anomaly $E_p(t(E))$. The time-dependent variable, $E_p(t(E))$, is given by Kepler's equation (e.g. Eq. 2.35 of Hilditch 2001):

$$E_p(t(E)) = \frac{2\pi}{P_p}(t(E) - T_p) + e_p\sin E_p(t(E)) \tag{2.4}$$

where the term $\frac{2\pi}{P_p}(t(E)-T_p)$ is the mean anomaly (M). The term $2\pi/P_p$ denotes the mean motion of the combined binary in its light travel-time orbit. Computing the true anomaly as a function of time (or cycle number) requires the solution of Kepler's equation above (Eq. 2.4). This can be done as outlined in Hinse et al. (2012) by solving for E from Eq. 2.4 using Newton-Raphson algorithm to iterate towards a solution for E with an initial starting guess of E=M. The true anomaly, υ_p is given by the following expression:

$$\tan\left(\frac{\upsilon_p}{2}\right) = \sqrt{\frac{1+e_p}{1-e_p}}\tan\left(\frac{E_p(t(E))}{2}\right). \tag{2.5}$$

The authors of Paper I derived an underlying quadratic ephemeris of the binary by

fitting a model with two elliptical terms (τ_p, described above), as follows:

$$T(\mathrm{BJD_{TDB}}) = 2453405.30086(3) \; + \; 0.087865425(2)E \; - \; 7(2) \times 10^{-14}E^2. \tag{2.6}$$

These authors noted that models consisting of either a quadratic term only or a quadratic term plus an elliptical term gave a best reduced χ^2 values of >95 and 6.2, respectively. These models were insufficient to explain the O−C diagrams of UZ For since significant residuals remained after their subtraction. They conducted an F-test between models with a quadratic term only and a quadratic plus an elliptical term and their results gave > 99.99% confidence in the latter method although residuals with amplitude of ∼10 s remained. In order to test the two-companion model, we plot the O−C residuals diagram using both the literature data and our new eclipse timings, utilizing the solution presented in Table 2 of Paper I and Eq. 2.7, in Figure 2.9. The O–C diagram of UZ For is constructed by successive subtracting of each term from the eclipse ephemeris and spans over 35 years. The vertical green line in Figure 2.9 separates recent data (to the right of the green line) and those from Paper I up to 2010 (to the left of the green line). The new data stretch an additional eight years (from 2011 to 2018) extending the baseline to 35 years. The model invoked to explain the O−C residuals from Paper I consists of a combination of a quadratic and two elliptical terms, Eq. 2.7, shown below:

$$\begin{aligned} T(\mathrm{BJD_{TDB}}) &= T_0 + P_{\mathrm{bin}}E + AE^2 \\ &+ K_{\mathrm{bin},(3)}\sin(\upsilon_3 - \varpi_3)\frac{[1-e_3^2]}{[1+e_3\cos(\upsilon_3)]} \\ &+ K_{\mathrm{bin},(4)}\sin(\upsilon_4 - \varpi_4)\frac{[1-e_4^2]}{[1+e_4\cos(\upsilon_4)]}, \end{aligned} \tag{2.7}$$

where T_0 is the time of epoch, P_{bin} is the orbital period of the binary in days, A is the quadratic parameter which is related to the rate of period decrease $\dot{P} = \frac{2A}{P_{\mathrm{bin}}}$ and E is the binary cycle number which comprises the quadratic term of the ephemeris. As described in Paper I and Khangale et al. (2019b), the remaining ten parameters were introduced in the context that the variations in the eclipse times are due to the light travel-time effect caused by the gravitational influence of a third and fourth body orbiting the central binary system. $K_{\mathrm{bin},(3,4)}$ are the amplitudes of the eclipse time variations as a result of the light travel-time effect of the two bodies. $\upsilon_{(3,4)}$ are the true anomalies of the two bodies, here we assume that $\upsilon_{(3,4)} \approx (E + T_{(3,4)})f_{(3,4)}$ (the mean anomaly), which progress through 2π over the orbital periods $[P_{(3,4)}]$ and are functions of E. $T_{(3,4)}$ are the times of periastron passages and $\varpi_{(3,4)}$ are the longitudes of periastron passage measured from the ascending node in the plane of the sky. Lastly, $e_{(3,4)}$ and $f_{(3,4)}$ are the eccentricities and orbital frequencies (in radians per binary cycles) of the two bodies.

The best-fit solution from Paper I (red curves) is overplotted in the second and third panel. The top panel of Figure 2.9 shows the O−C diagram after subtraction of the linear ephemeris. It is clear from the figure that a linear fit does not give a valid description of

the data. Also, the residuals on the top panel appears periodic and this suggests that more terms, in addition to the linear and quadratic, are required in order to describe the O−C diagram.

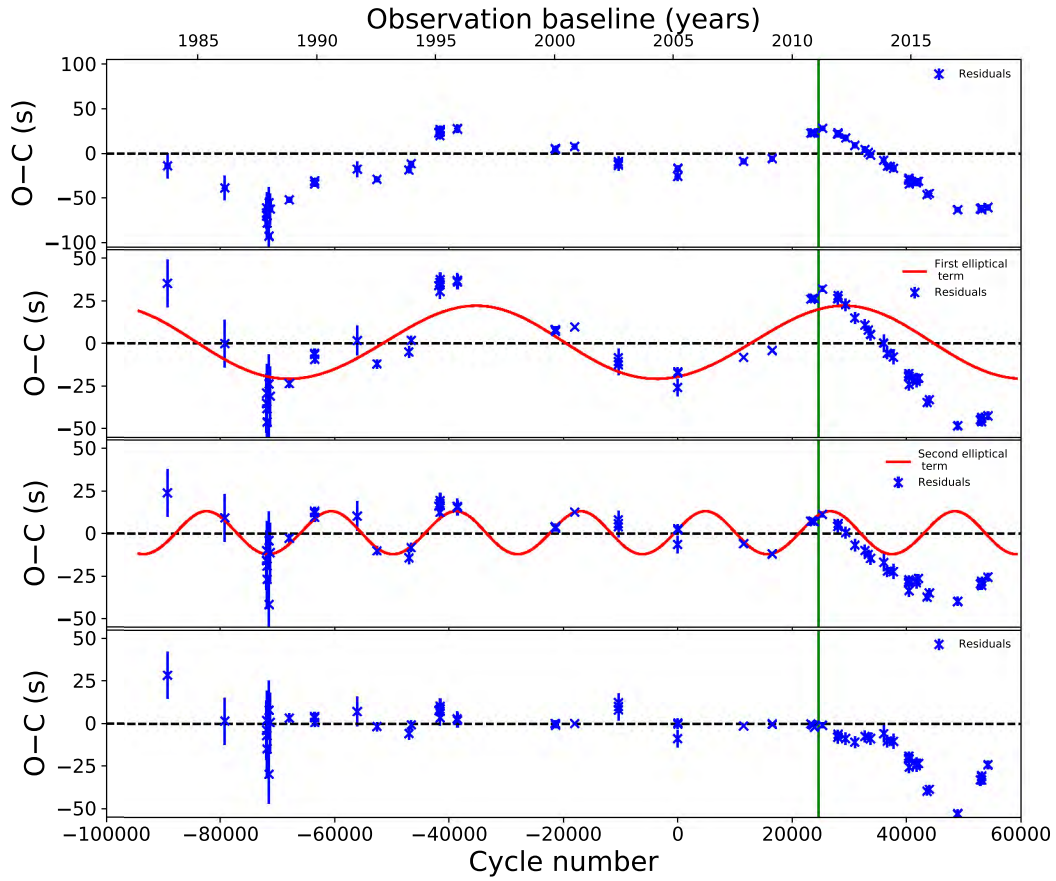

Figure 2.9: The O−C diagram of UZ For from Paper I but with new eclipses added. The vertical green line in each panel separates the eclipse times from literature (to the left) and the recent eclipse times obtained for this study (to the right). See text for more details.

The second panel shows the O−C diagram after subtraction of the quadratic term with the first elliptical term overplotted (red curve). It is clear from the second panel that the red curve does not go through most of the data points but follows the general trend of the residuals. Therefore, a second elliptical term might be required in order to reduce the residuals. The third panel shows the O−C residuals after subtraction of the first elliptical term with the second elliptical term (red curve) overplotted. The bottom panel shows the final O−C residuals after subtraction of the second elliptical term. The residuals are close to zero with no obvious periodic variation seen in the bottom panel. Therefore, no further additional elliptical term is required. As stated in Khangale et al. (2019b), the new mid-eclipse times were not included in the fit. The original fit presented in Paper I was not the formal best solution but instead included the constraint that the eccentricities of the

elliptical terms were ≤0.1 in order to be consistent with a stable two-planet model.

The mathematical function fitted to the old data (the blue crosses to the left of the green lines) predicted a maximum in the O−C residuals around ∼2010−2011 and a minimum in the O−C residuals between 2016 and 2018. The maximum is followed by a gradual decline in the O−C residuals (Figure 2.9, second and third panels) followed by a minimum in the O−C residuals. The new mid-eclipse times obtained in this study (the crosses to the right of the green lines in Figure 2.9, second and third panels) agree with the predictions in the sense that a maximum in the O−C residuals is observed around ∼2011−2012 and a minimum in the residuals is also seen between 2016 and 2018. However, we note that the maximum followed by a gradual decline in the residuals which appears steeper than predicted and occurs earlier and continues to diverge after ∼2013 until the minimum in the residuals is reached between 2016 and 2017. Since the proposed model is sinusoidal, the minimum in the residuals is followed by an upturn in the O−C residuals and this is in agreement with predictions. It is immediately obvious that with the new mid-eclipse times added, the fitting parameters from Paper I need to be revised. This is discussed in the next section (Section 2.4.3).

2.4.3 Calculating a new O−C diagram

In Paper I, the authors first fitted a quadratic fit to the mid-eclipse times using least-square fitting − with appropriate weightings given by the mid-eclipse times error. They noted that the deviations were periodic with amplitudes ranging between 60−80 s with a reduced chi-square >95. They then preceded by considering solutions with a quadratic fit plus one elliptical term to the eclipse times. Their reduced chi-square value was still greater than 6.2. Also, residuals with an amplitude as big as 10 s still remained in the O−C diagram. An F-test comparison between the above two models showed that the model with a quadratic fit and an elliptical term was a better fit. In order to reduce the residuals and get a much better fit, they adopted a model with a quadratic term and two elliptical terms to describe the O−C diagram. This gave reasonable values of the reduced chi-square. The inclusion of the quadratic term in the ephemeris of UZ For (Eq. 2.7) is to account for any effects due to other mechanisms, such as Applegate mechanism, in addition to the circumbinary planets that are probably causing the mid-eclipse time variations. A quick look at Figure 2.9 (top panel), the residuals after subtraction of the linear term, appears sinusoidal but also there an underlying slope which is longer than the two dominant periods. This feature is consistent with a downward parabola of the mid-eclipse variations, orbital period decay or can be a third sinusoidal variation with longer period. We interpret this as a secular change and to avoid overfitting the data, we decided to only consider a maximum of two cyclic terms in modelling the mid-eclipse time variations of UZ For.

This study adopted the approach from Paper I but instead of fitting the quadratic term first and then fitting a quadratic and one elliptical term, etc. and comparing the reduced chi-square value, simultaneous least square fitting of all the three terms was carried out. We note that a model including a quadratic term and two elliptical terms will undoubtedly give

lower values of reduced χ^2 compared to a model with a quadratic term and one elliptical term. The steps and procedure taken is discussed in the next paragraph.

As already mentioned above, the model invoked explain the O−C residuals from Paper I consists of a combination of a quadratic and two elliptical terms, Eq. 2.7, and can be re-written by substituting $\upsilon_{(3,4)} = (E + T_{(3,4)})f_{(3,4)}$ as mentioned in the previous section to the following equation:

$$\begin{aligned} T(\mathrm{BJD_{TDB}}) &= T_0 + P_{\mathrm{bin}}E + AE^2 \\ +K_{\mathrm{bin},(3)}\sin((E+T_3)f_3 - \varpi_3)&\frac{[1-e_3^2]}{[1+e_3\cos((E+T_3)f_3)]} \\ +K_{\mathrm{bin},(4)}\sin((E+T_4)f_4 - \varpi_4)&\frac{[1-e_4^2]}{[1+e_4\cos((E+T_4)f_4)]}. \end{aligned} \tag{2.8}$$

The parameters, T_0, P_{bin}, A, E and the remaining ten parameters from the two cyclic terms are the same as described in Eq. 2.7. It is clear that equation 2.8 has thirteen free parameters, three from the quadratic term and five each from the first and second elliptical term. The program written in IDL and used in Paper I was used with a few modifications. This code takes a set of inputs, performs minimization using CURVEFIT and returns a reduced chi-square value. In order to perform the minimization, a grid of starting parameters was required in order to investigate the parameter space. The generated grid had 10360 starting points for the two elliptical frequencies with the following characteristics:

- evenly spaced with f_3 (between 0.0000552 and 0.000138) and f_4 (between 0.0001794 and 0.0004555) cycles per binary cycle,
- first three parameters (T_0, P_{bin} and A) associated with the quadratic term were fixed at the values given in Paper I,
- the remaining eight of the ten elliptical parameters were randomized to within reasonable values of the solution given in Paper I e.g. the eccentricities took random values between 0 and 1.

Simultaneous least-square fitting was then performed for each starting set of parameters. During minimization all the parameters were allowed to vary. As already mentioned in Khangale et al. (2019b), all the minimization did not converge to a single solution but instead gave a range of solutions with final reduced chi-squared (χ^2) values between 2.06 and 717.13 with eccentricities ranging from zero to 14707 and 6820 for e_3 and e_4, respectively. The wide ranges in the values of eccentricities and the reduced χ^2 includes parabolic and hyperbolic solutions. The minimization was done several times with a new grid of random values for the parameters and each time the results were similar. These solutions are explored in the next two sections.

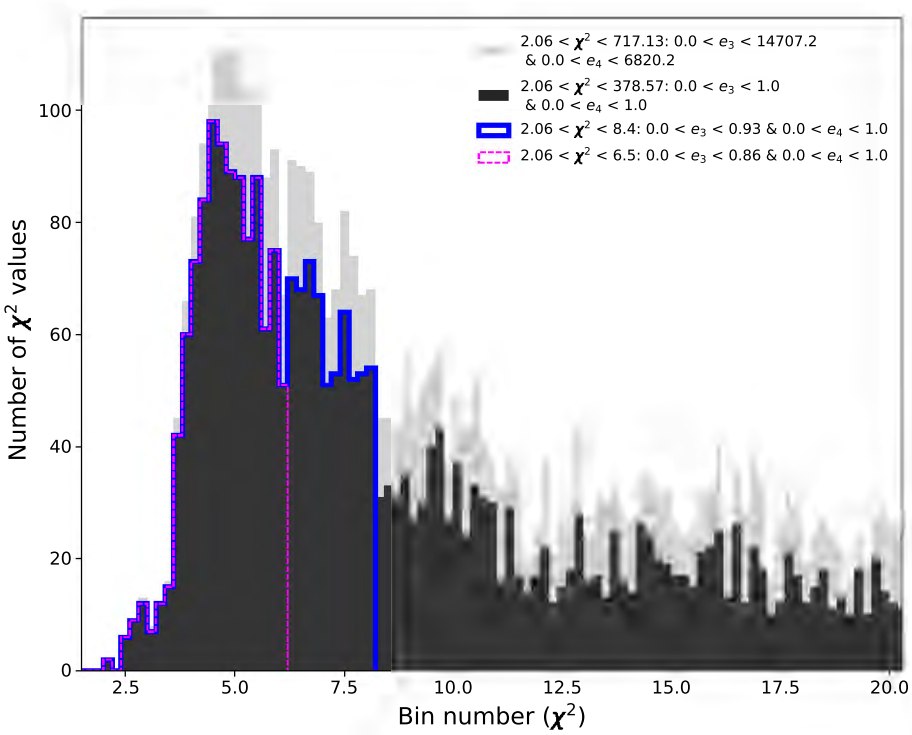

Figure 2.10: The distribution of the reduced χ^2 parameter space. The ranges of the reduced χ^2 values and eccentricities are given for each colour in the legends. (See text for details).

2.4.4 Distribution of the elliptical frequencies

The distribution of the reduced χ^2 of the 10360 solutions is shown in Figure 2.10 (light grey colour) and is typical of a reduced χ^2 with 13 degrees of freedom. The histogram peaks at the reduced χ^2 ≈5. The figure is an expanded view around the reduced χ^2 of less than 22. The distribution of the reduced χ^2 values peaks rapidly from a reduced χ^2 of ∼3.5 to 4.5 reaching a maximum of ∼110 solutions per bin and declines gradually reaching a minimum of ∼40 at the reduced χ^2 of 6.4. The distribution of the reduced χ^2 values peak up again reaching a maximum of ∼70 at the reduced χ^2 of 7.0. The second maximum is followed by a decline before flattening out beyond the reduced χ^2 of ten. In order to reduce the size of the solutions, a constraint in the eccentricity was added to exclude the parabolic and/or hyperbolic solutions, i.e. solutions where either e_3 and/or e_4 are ≥ 1.0. About 4414 solutions remained after excluding solutions with $e_{3,4} > 1.0$ and their distribution is shown as black in Figure 2.10. The reduced sample of solutions had a size of 4414 and is shown with a black colour in Figure 2.10. This translates to 42.6% and implies that ∼57.4% of all the solutions that were obtained from the minimization had unrealistic eccentricities in the context of the two-planets model. The peak of the distribution of the reduced χ^2 values

show some kind of bi-modality, with the first peak centred on the reduced χ^2 value of 5 and the second peak centered at the reduced χ^2 value of 7 and a cut-off just above the reduced χ^2 value of 8.4. Therefore, these solutions were then separated into three criteria based on the distribution of reduced χ^2, that is, separated according to solutions around the peaks defining low-, mid- and high chi-squared values. There were no motivations to make more cuts than that. The total number of solutions with low- and mid-reduced χ^2 values (i.e. $<$8.4 and $e<$1.0) is 1679 and their distribution is indicated as a blue line in the figure – this is ∼16.2% of the original. The first peak contains ∼1151 solutions whereas the second peak contains ∼528 solutions. The former represents 11% of all the minimized solutions whereas the latter contains about 5% of all the minimized solutions. For this work and the remainder of the analysis, only the solutions with reduced χ^2 of less than 6.5 (≈11% of all solutions) – marked with a magenta dotted line in Figure 2.10 – were considered and their elliptical frequencies are discussed in the next paragraph.

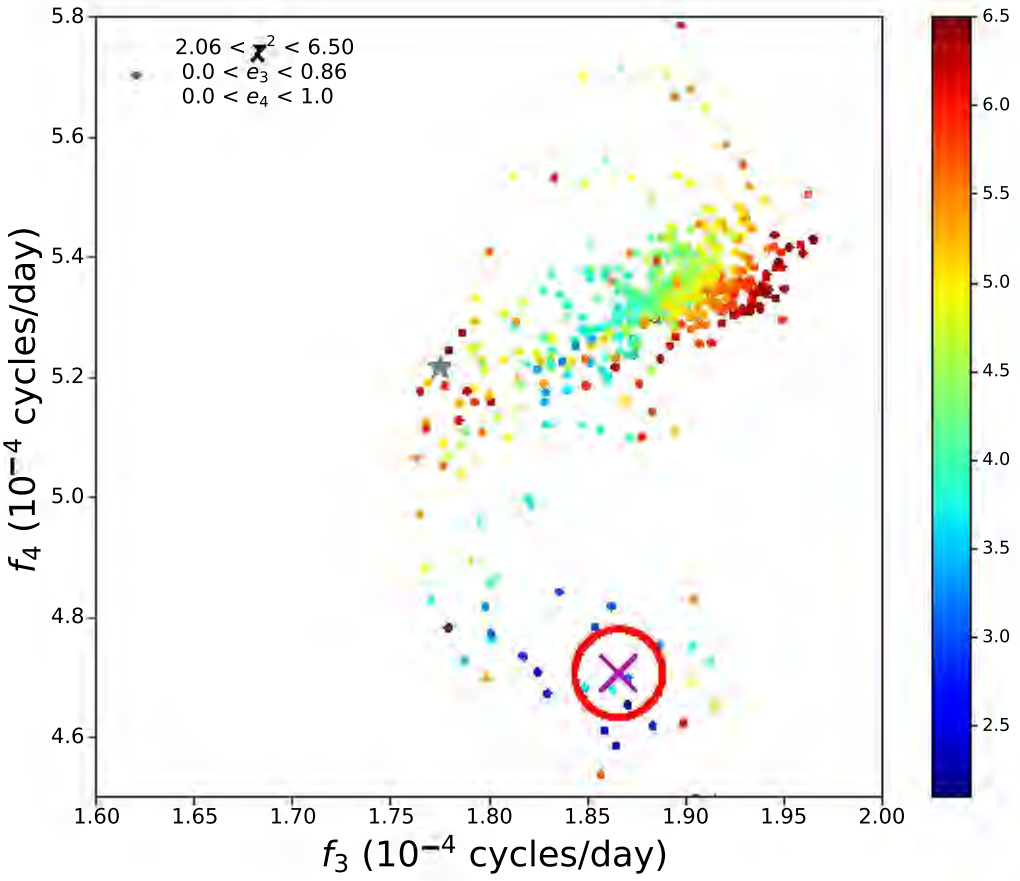

Figure 2.11: The reduced χ^2 parameter space for the two elliptical frequencies. The points have been colour-coded to show increasing values of the reduced χ^2 from blue to red. The solutions with $e \geq 1.0$ were excluded since their solutions will give parabolic and hyperbolic orbits. The grey star marks the location of the solution adopted in Paper I, whereas the red circle and magenta cross mark the solution with the lowest reduced χ^2 adopted as the best-fit in this study.

Figure 2.11 shows the distribution of the solutions with reduced χ^2 of less than 6.5 as the function of the two elliptical frequencies, where f_3 and f_4 are frequencies of the first and second elliptical terms, respectively. These solutions have been colour-coded to show increasing values of the reduced χ^2 from blue to red. Note that the figure is an expanded view of the parameter space focused on the region where most of the solutions were concentrated. The overall distribution of the reduced χ^2 as a function of the two elliptical frequencies form an arc with the reduced χ^2 values increasing from the lower right through the centre to the upper right regions of Figure 2.11. The grey star, towards the centre of Figure 2.11, marks the location of the solution presented in PAPER I and lies in the region where the intermediate solutions are found. It is clear from the figure that there is a scarcity of solutions with frequencies (f_3) values below 1.75×10^{-4} and above 1.95×10^{-4} cycles per day. The solutions around these two regions are generally associated with higher values of the reduced χ^2. On the other hand, the f_4 frequencies takes a wide range of values, some of which are much smaller or larger than those shown in Figure 2.11.

2.4.5 Distribution of the eccentricities

Figure 2.12 shows the range of two elliptical eccentricities for the solutions presented in Figure 2.11, i.e. $\chi^2 < 6.5$ and $0 < e < 1$. Here e_3 and e_4 are the eccentricities of the first and second elliptical terms according to Eq. 2.8 . These solutions have been colour-coded to show increasing values of the reduced χ^2 from blue to red. The distribution of the eccentricities forms two vertical ridges on e_3 (named in descending order of e_3 values from right to left), the first vertical ridge is centred on e_3 between 0.5 to 0.7 and the second vertical ridge is centred on $e_3 \approx 0.4$. The first vertical ridge contains solutions with the lowest reduced χ^2 values (dark blue circles) and takes a wide range of e_4 eccentricities ranging from 0 to approximately 0.9. The second vertical ridge, centred on e_3 ≈0.4 and spanning from 0 to 1 for e_4, is associated with the large concentration of light blue and orange to dark red solutions shown in the top right region of Figure 2.11. The scattered solutions between the two vertical ridges correspond to the lower density of blue and red circles towards the centre of Figure 2.11. The solutions to the upper left of the second vertical ridge ($e_3 < 0.3$ and $e_4 > 0.2$) are associated with the solutions with lower f_4 frequencies and not shown in Figure 2.11. Immediately obvious is the absence of solutions in the lower left quadrant corresponding to low values of e_3 and e_4. The solutions where both values of the eccentricities are lower will give circular orbits and generally tends to have higher values of the reduced χ^2. There is also a cut-off in the e_3 eccentricities at 0.86 in Figure 2.11. Solutions with $e_3 > 0.86$ will require e_4 of zero and such solutions were excluded from this study due to them having higher reduced χ^2 values. Also, the solutions with e_3 below 0.4 are rare in the upper right part of the figure (above e_4 >0.8).

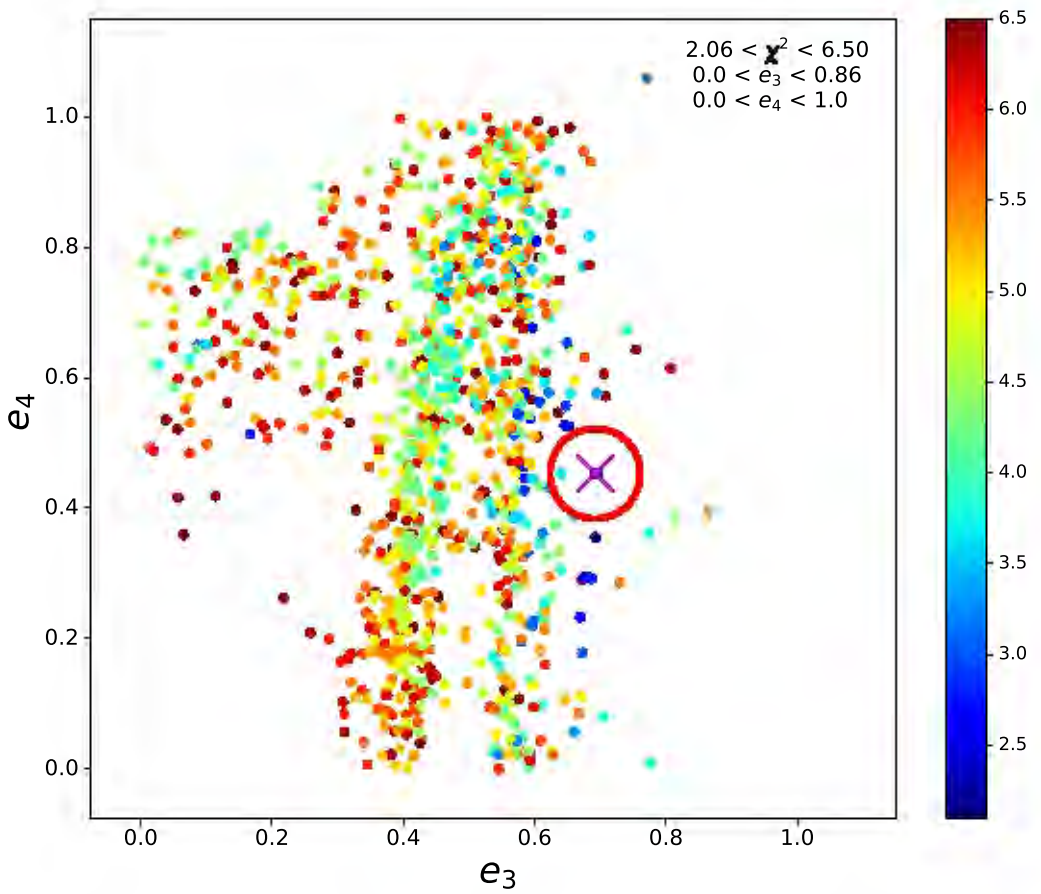

Figure 2.12: The reduced χ^2 parameter space for the two elliptical eccentricities. The points have been colour-coded to show increasing values of the reduced χ^2 from blue to red. The solutions with $e \geq 1.0$ were excluded since their solutions will give parabolic and hyperbolic orbits. The red circle and magenta cross mark the solution adopted as the best-fit for this chapter.

2.4.6 The updated O−C diagram

In order to create an updated O−C diagram, the formal best-fit solution with the lowest value of the reduced χ^2 (2.06) was chosen and is marked by a magenta cross enclosed with a red circle in both Figures 2.11 and 2.12. This particular solution has the e_4 eccentricity of ∼0.45. Similar to the other best solutions, it has an eccentricity of e_3 ∼0.69. The formal best fit O−C diagram using the indicated solution is shown in Figure 2.13 and is discussed below.

The top panel shows the residuals after subtraction of the linear term of Eq. 2.8. As already mentioned in Paper I, with the linear term removed, the residuals show a periodic variation. The second panel shows the residuals after subtraction of the quadratic term. This leaves residuals with amplitudes of ∼60 s and the residuals are best described using an elliptical term as shown by the red line in the second panel of Figure 2.13. Similarly,

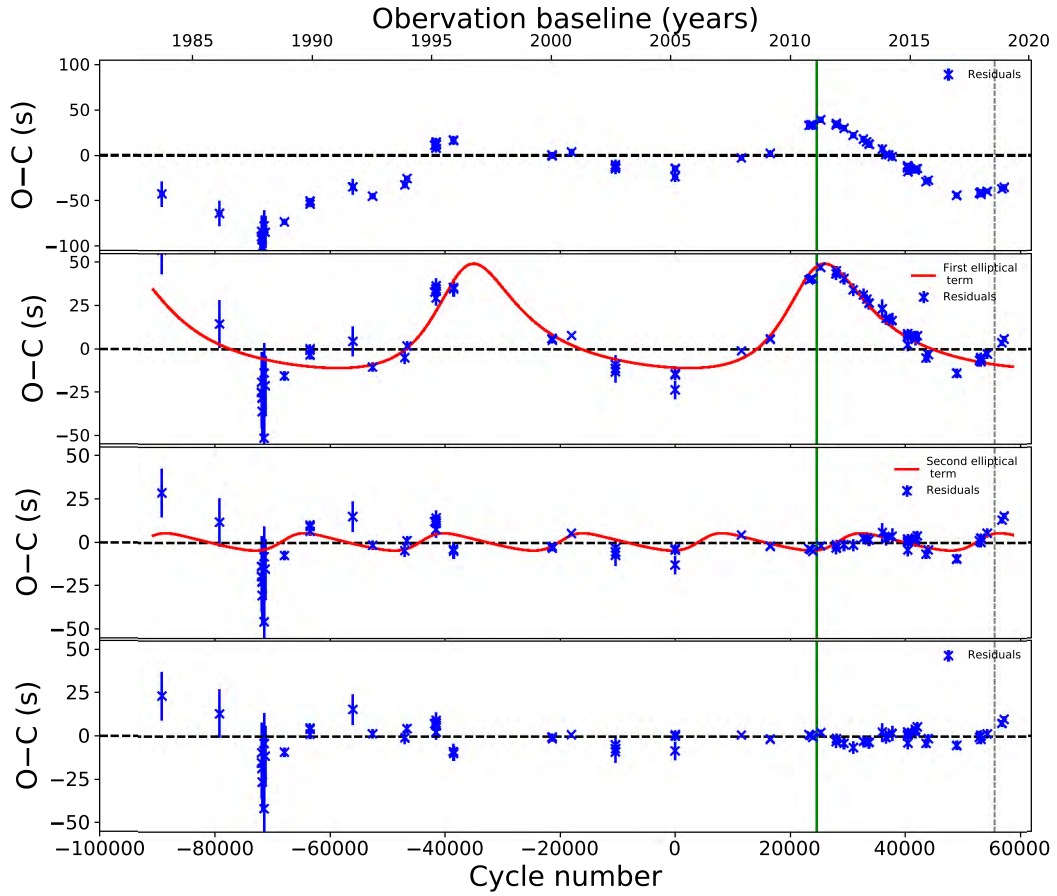

Figure 2.13: The formal best O−C diagram of UZ For, based on new parameters shown in Table 2.2, after successive subtraction of the three terms comprising the new eclipse ephemeris. Top panel: O−C after subtraction of the linear term. Second panel: O−C after subtraction of the quadratic term with the first elliptical term overplotted (red line). Third panel: O−C after subtraction of the first elliptical term with the second elliptical term overplotted (red line). The bottom panel shows the final O−C residuals after subtraction of the second elliptical term. The vertical green line in each panel separates the eclipse times from literature (to the left) and the new eclipse times (to the right). The grey dashed line in each panel separates the data used in the fitting (left) and those not included in the fit (to the right).

the third panel shows the residuals after subtraction of first elliptical term with the second elliptical term (red line) overplotted. Even after subtraction of the first elliptical term, residuals with an amplitude as large as 10 s still remain. The red line in the third panel shows the second elliptical term overplotted to the residuals. The bottom panel shows the final residuals after subtraction of the second elliptical term. Some residuals still remain in the bottom panel but there is no obvious periodic variations seen. However, adding a third elliptical term will reduce the residuals further. Note that there are other solutions of similar reduced χ^2 to the formal best solution as can be seen from the other blue points in

Figures 2.11 and 2.12. The parameter values of the best solution are listed in Table 2.2.

In conclusion, the baseline of the current observation is not consistent with low eccentricities for the two elliptical terms and that the best solutions at minimum require the e_3 eccentricity to be ∼0.7. The residuals in the bottom panel of Figure 2.13 are suggestive that adding a third or fourth elliptical term would reduce the χ^2 value further. However, the current dataset is insufficiently constrained to warrant an additional elliptical term(s). Such an additional term will probably be of period less than two-three years. Note that in Paper I, it was also concluded that the best mathematical solution require high eccentricities.

The recently obtained mid-eclipse times, not included in the fit, are shown to the right of the grey dotted line in Figure 2.13 and still agree with the current trends of a quadratic and two elliptical terms as the explanation for the cyclic variations in the O−C diagram of UZ For.

2.5 Discussion

This chapter presents new observations in order to further explore the departures from a simple quadratic fit to the eclipse times of the UZ For system. As already mentioned in Paper I using the old data (42 mid-eclipse times), these departures were suggestive of the presence of two elliptical terms with periodicities of ∼16(3) and ∼5.25(25) years. Similarly, the results obtained in this study using the new data (75 mid-eclipse times) reveal that the deviations in the eclipse O−C (shown in Figure 2.13) continue to be best described with a combination of a quadratic and two elliptical terms with periodicities of ∼14.67(1) and ∼5.82(3) years, respectively. The deviations are suggestive/reminiscent of both secular and/or periodic variations operating in UZ For. It is generally understood that period changes in binary systems result from one of the following mechanisms: gravitational radiation (Faulkner 1971, Paczynski & Sienkiewicz 1981), magnetic braking (Verbunt & Zwaan 1981, Rappaport et al. 1983), the Applegate mechanism (Applegate 1992) due to magnetic cycle activity of the secondary star or the presence of circumbinary planets in orbit around the binary (e.g., Bours et al. 2016). Magnetic braking is understood to operate above the orbital period gap whereas gravitational radiation operates below the orbital period. However, recent studies show that there is no evidence that magnetic braking turns off completely when the binary system evolves from longer to shorter periods (Schreiber et al. 2010).

In the case of UZ For, Paper I concluded that the two favoured mechanisms to derive the periodicities are either two giant extrasolar planets as companions to the binary or the Applegate mechanism (Applegate 1992). They further argued that the Applegate mechanism is the least likely of the two since it would require the entire radiant energy output of the secondary – and recommended a revision such as those described by Lanza et al. (1998). They noted that the two-planet model proposed to explain the residuals provided realistic solutions even though the model did not capture all the eclipse measurements. They argued that the best solutions, for the two-planet model, require a high eccentric orbit for the outer planet. However, such a two-planet configuration is unlikely to be stable with high

eccentricities. In conclusion, they further suggested that it is possible to have both the Applegate mechanism and circumbinary planets driving the periodicities. The next two sections discuss the two favoured mechanisms taking into account the results obtained in this study and recent work published by various authors (e.g. Bours et al. 2016).

2.5.1 Circumbinary planets

The parameters listed in the left panel of Table 2.2 were used to derive the orbital and physical properties of the two planets listed in the right panel of the same Table. Firstly, the amplitudes of oscillations ($K_{\mathrm{bin},(3,4)}$) were used to calculate the projected distances $a\sin(i)$ from the centre of mass of the binary to the centre of mass of each of the triple systems using Eq. 2.9 below:

$$a_{jk} = a\sin i = \mathrm{K}_{\mathrm{bin},(k)} \tag{2.9}$$

where $j = 1$ and denote the central binary system, and $k = 3$ or 4 is the subscript denoting the inner or outer planet. The calculated centre of mass of each of the triple system, $a_{1,3}$ and $a_{1,4}$ are 0.064(1) and 0.011(1) AU for the outer and inner planet, respectively. The numbers in brackets are 1σ errors propagated based on one solution presented and excludes the range in periods shown in Figure 2.11.

In order to calculate the mass function ($f(m_{(3,4)})$), first the orbital frequencies ($\omega_{(3,4)}$) for the inner and outer companion were calculated using the following equation, (Eq. 2.10):

$$\omega_{(3,4)} = \frac{2\pi}{P_{(3,4)}} \tag{2.10}$$

where $P_{(3,4)}$ are the orbital periods of the outer and inner planets respectively. The orbital frequencies were then used to calculate the mass function using the following equation:

$$f(m_{(3,4)}) = \frac{\omega^2_{(3,4)} a^3_{jk}}{G}\sin^3 i. \tag{2.11}$$

These give the corresponding mass functions for the outer, $f(m_3) = 1.2116(3)\ \times 10^{-6}\ M_{\odot}$, and inner planet, $f(m_4) = 4.045(7)\ \times 10^{-8}\ M_{\odot}$, respectively. The above mentioned mass functions were used to calculate the individual masses of each planet, $M_{(3,4)}$ using the following equation:

$$f(m_{(3,4)}) = \frac{M^3_{(3,4)}}{(M_{(3,4)} + M_1)^2}\sin^3 i, \tag{2.12}$$

where M_1 is the combined mass of the central binary $M_1 = 0.84\ M_{\odot}$ (i.e. the mass of the WD, $M_{WD} = 0.7\ M_{\odot}$, combined with the mass of the red dwarf, $M_{RD} = 0.14\ M_{\odot}$). The total mass in denominator, $M_{\mathrm{tot}} = M_1 + M_{(3,4)} \simeq M_1$, since $M_1 >> M_{(3,4)}$. Therefore, Eq. 2.12 is simplified to the following relation:

$$f(m_{(3,4)}) = \frac{M^3_{(3,4)}}{M^2_{\rm tot}} \sin^3 i \tag{2.13}$$

where i is the binary inclination. The binary inclination (i) of 81° was used for this study and the respective minimum masses of the third and fourth body were found to be 0.00307(5) and 0.00955(2) $M_{\odot}$ and would therefore qualify as extrasolar giant planets [3.22(5) and 10.01(2) Jupiter masses (M_J)]. The quoted errors are 1σ errors propagated based on the one solution presented and excludes the range in periods shown in Figure 2.11. These parameters are summarized in right column of Table 2.2. The two-planet parameters derived above are specific to this one best-fitting solution. As already mentioned in Section 2.4.4, there are other solutions with similar reduced χ^2 to the best-fitting solution presented here. These solutions give similar values for the quadratic parameter and this gives the rate of period decrease to be $\dot{P}_{\rm bin} = \frac{2A}{P_{\rm bin}} = -3.29(3) \times 10^{-12}$ s s^{-1} $= -1.21 \times 10^{-9}$ day/year. This is equivalent to the rate of period decrease ($P_{\rm bin}/\dot{P}$) on the time scale of 72.9 million years. The value of $\dot{P}_{\rm bin}$ from Paper I is $-1.56(5) \times 10^{-12}$ s s^{-1} (or -5.8×10^{-10} day/year). The new value is two times bigger compared to that reported in Paper I. This is an equivalent of the rate of change on the time scale of 150 million years. Recently, Esmer et al. (2021) estimated the period change of $\sim$9.16 $\times$ 10^{-09} day/year for HW Vir*. This is an equivalent of the rate of period change on the time scales of 12.7 million years. The rate of period increase or decrease in mCVs is small compared to some novae. For example, Patterson et al. (2017) found that the orbital period of T Pyx was increasing at a rate of 3 $\times$ 10^5 years.

According to equation 5 of Brinkworth et al. (2006) reproduced below (Eq. 2.14):

$$\dot{\rm J} = \frac{2}{3}\frac{A}{P^2_{\rm bin}}{\rm J}, \tag{2.14}$$

where A is the quadratic parameter, $P_{\rm bin}$ is the orbital period of the binary system and J is the total angular momentum of the system which is given by following expression:

$$\rm J = \left(\frac{Ga}{M_{tot}}\right)^{1/2} M_{WD} M_{RD},$$

where a is the binary separation and is assumed to be $\sim$5.5 $\times$ 10^{10} cm and, M_{WD} and M_{RD} are the mass of the WD and RD, respectively. This gives the rate of angular momentum loss of $\sim -8.3 \times 10^{34}$ erg.

However, the expected theoretical rate of angular momentum loss due to gravitational radiation (Eq. (12) of Brinkworth et al. 2006, corrected from Eq. (2) of Andronov et al.

*HW Vir is an Algol-type eclipsing binary with an orbital period of 0.1167 d and is a prototype of binary systems consisting of subdwarf-B primary (Berger & Fringant 1980) and a main-sequence M-type secondary (dM).

Table 2.2: The mid-eclipse ephemeris of the main accretion spot of UZ For and corresponding planet model parameters. The uncertainty in the ephemeris were rounded off to the 1σ errors. The planet parameter errors are 1σ errors and were propagated from the one fitting solution and may underestimate true errors of range in parameter space of possible solutions. The minimum planet masses are listed assuming coplanarity and $f(m_{(3,4)})$ is the mass function. The combined mass of the primary and secondary stars is assumed to be $0.84 M_{\odot}$. (Table reproduced from–Potter et al. 2011).

Quadratic term	$T_0 = 2453405.300833(5)$ d	
	$P_{bin} = 0.087865421(1)$ d	Planet
	$A = -14.5(2)\times10^{-14}$	Parameters
1st elliptical term	$\upsilon_3 = (E + T_3)f_3$	$f(m_3) = 1.326(7)10^{-6} M_{\odot}$
	$T_3 = 67198(145)$ (binary cycle)	$M_3 = 10.00(2)\ M_J$
	$f_3 = 0.0001030(1)$ (radians per binary cycle)	$P_3 = 14.67(1)$ years
	$\varpi_3 = 2.10(1)$ radians	$a_3 = 5.7(1)$ AU
	$K_{bin,(3)} = 0.000371(3)$ d	$a_{1,3} = 0.064(1)$ AU
	$e_3 = 0.69(1)$	
2nd elliptical term	$\upsilon_4 = (E + T_4)f_4$	$f(m_4) = 3.43(9)10^{-8} M_{\odot}$
	$T_4 = 7444(219)$ (binary cycle)	$M_4 = 3.22(5)\ M_J$
	$f_4 = 0.000260(1)$ (radians per binary cycle)	$P_4 = 5.82(3)$ years
	$\varpi_4 = -0.22(5)$ radians	$a_4 = 3.0(2)$ AU
	$K_{bin,(4)} = -0.000065(3)$ d	$a_{1,4} = 0.011(1)$ AU
	$e_4 = 0.45(6)$	

2003) shown in Eq. 2.15 below:

$$\dot{\mathrm{J}}_{\mathrm{grav}} = -\frac{32}{5}\frac{G^{7/2}}{c^5}a^{-7/2}M_{WD}^2 M_{RD}^2 M_{tot}^{1/2}, \tag{2.15}$$

where $a = (GM/\omega_{orb}^2)^{1/3} = \sim 5.5 \times 10^{10}$ cm, is the binary separation and the remaining parameters are as described above. This gives the value of the angular momentum loss of $\dot{\mathrm{J}}_{\mathrm{grav}} = -3.2 \times 10^{33}$ erg.

Angular momentum loss due to magnetic braking is given by (Eq. (A6) of Knigge et al. 2011 (based on the magnetic braking law by Verbunt & Zwaan 1981)) shown below:

$$\dot{\mathrm{J}}_{\mathrm{mb}} = -5 \times 10^{-29} k_2^2 f^{-2} M_{RD} R_{RD}^4 \Omega^3 \tag{2.16}$$

where f is the optimal scaling factor and it is = 1.78 according to Smith (1979), k_2 is the radius of gyration and $\sim$0.1 for low-mass stars, $\Omega = 2\pi/P_{\mathrm{bin}}$ is the angular velocity. The other parameters are those of the RD. This gives the angular momentum loss due to magnetic braking to be $\sim -5.7 \times 10^{33}$ erg. Esmer et al. (2021) found that for HW Vir, the value of the rate of angular momentum loss due to magnetic braking was within the range from -5.48×10^{36} to -4.16×10^{33} erg. This is consistent with the value found for UZ For above. The combined angular momentum loss from both gravitational radiation and

magnetic braking is $\sim 8.9 \times 10^{33}$ erg. Therefore, the implied rate of angular momentum loss using the $\dot{P}_{\rm bin}$ term only, is ten times larger than the combined angular momentum loss rates predicted by gravitational radiation and magnetic braking.

The angular momentum loss rates derived above suggest that the departures in the residuals of UZ For can not be explained by one mechanism. As already discussed in Khangale et al. (2019b), the periodic variations of the formal best solution is possibly consistent with two planets locked in a 3:1 resonance with orbital periods of 14.67(1) and 5.82(3) years, respectively. However the high eccentricity for both planets implies that such a two-planet solution would not be stable. There are solutions of similar reduced χ^2 in which the inner planet has a low eccentricity. Figure 2.14 shows the elliptical periods calculated from the the elliptical frequencies shown in Figure 2.11. It is clear from the figure that P_3 takes values between 14 and 15.5 years whereas P_4 takes a wide range of values centred at $\sim$5 years. A vast amounts of blue solutions are clustered between $5.6 < P_4 < 6.1$ whereas P_3 is within errors of 15 years. As already mentioned in Section2.4.5, all the best solutions require a high eccentricity for the outer planet.

There is a need for an independent observational approach to shed some light on the existence of planets around UZ For. One such technique may be astrometric monitoring of the precession of the UZ For binary as it wobbles back and forth due to extrasolar companions. The ongoing Global Astrometric Interferometer for Astrophysics (GAIA; Gaia Collaboration 2018) mission provides micro arc-second parallaxes to thousands of objects and places UZ For at a distance of $\sim$240 pc and it might be possible to detect its companion after five years of observations. A simulation by Goździewski et al. (2015) suggests that it should be possible to detect $\sim$30 micro arc-second for a 7 M_J planet in a 5 AU orbit. They argued that for HU Aqr, an AM Her type system which shows variations in its O$-$C diagram and lies at a distance of $\sim$200 pc, it should be possible to detect the outermost companion using parallaxes.

2.5.2 Revised Applegate mechanism

It was shown in Section 2.4.6 that significant residuals remain in the O$-$C of UZ For that points to something in addition to the presence of two companions to the binary system. As already described in Paper I, the Applegate mechanism would require more than the radiant energy output of the secondary to drive the period changes observed in this study. In light of this, the authors of Paper I argued that Applegate mechanism is unlikely to be causing the period changes in UZ For. Recently, Völschow et al. (2016) presented a revision of Applegate's mechanism which was constructed by including angular momentum exchange between the finite shell and the core of the secondary star. The revised Applegate's mechanism places UZ For amongst four systems that could be explained by magnetic activity of the secondary star. Furthermore, the calculations performed by Navarrete et al. (2018) for the necessary energy required considering different shells, as a fraction of the available energy, to drive the change in the quadrupole moment to give raise to the observed period revealed that applegate mechanism is potentially feasible on at least five systems (HU Aqr, QS Vir,

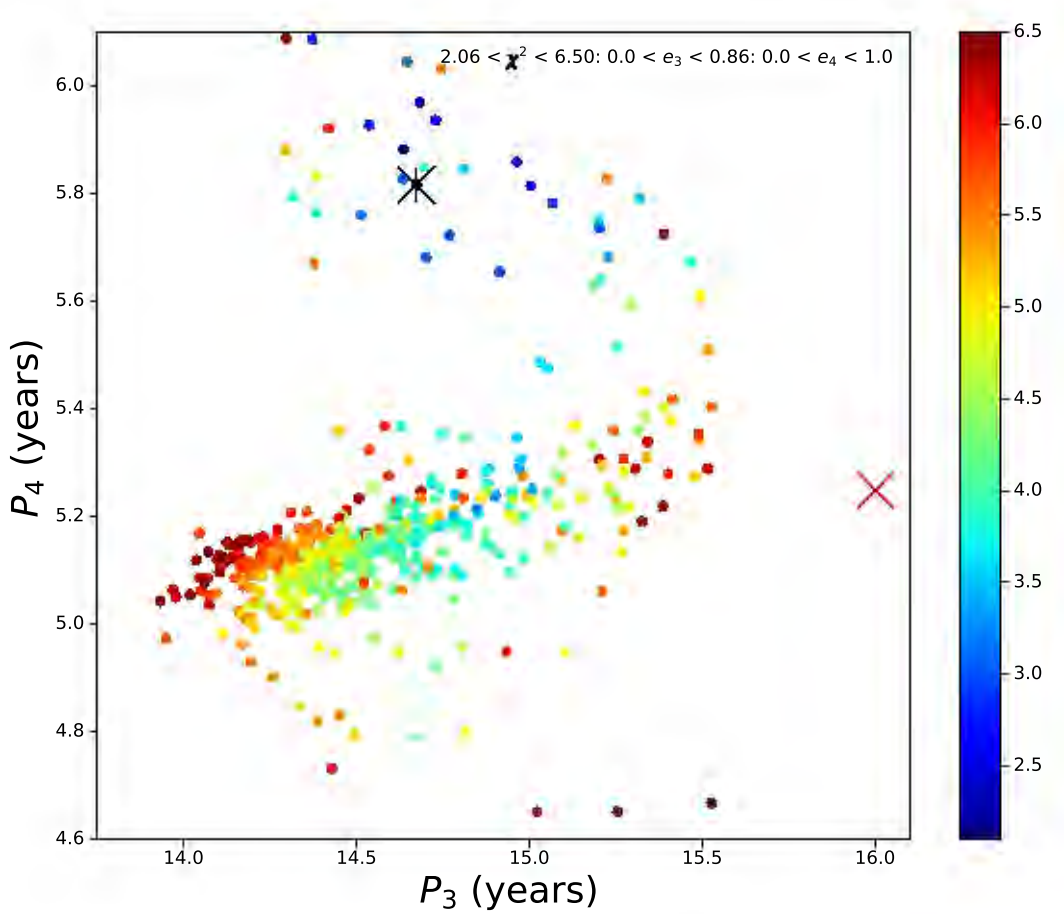

Figure 2.14: The reduced χ^2 parameter space for the two orbital periods. The points have been colour-coded to show increasing values of the reduced χ^2 from blue to red. The black cross marks the solution adopted as the best-fit for this thesis whereas the red cross marks the solution presented in Paper I.

UZ For, DP Leo and V471 Tau). In conclusion, the results obtained in this study strongly suggest that both extrasolar planets and some form of Applegate's mechanism should be considered when explaining the O−C diagram of UZ For. For example, small-amplitude residuals remain after subtraction of the the quadratic and first elliptical term. Esmer et al. (2021) found that for HW Vir circumbinary planets alone were not able to explain the eclipse time variations periodicities. However, they ruled out magnetic activity of the secondary star since the period change derived was inconsistent with Applegate mechanism. Völschow et al. (2018) identified short-period post-common envelope binaries with active component masses between 0.3–0.36 $M_{\odot}$ as the strongest candidates for the Applegate mechanism. They suggest that the planetary hypothesis should be excluded as a possible explanation for cyclic period variations.

Recently, Lanza (2020) proposed a new model to explain the observed orbital period variations in close binary systems. According to the new model, the variations arise from

the angular momentum exchange between the spin of the active component and the orbital motion. In the new model, the spin-orbit coupling is not induced by tides, but is created by a non-axisymmetric component of the gravitational quadrupole moment of the active star due to a persistent non-axisymmetric internal magnetic field. While this model easily satisfies all the energy constraints and explains the variations observed in HR 1099* and V471 Tau, its application on NN Ser revealed that the luminosity time-scale of this system is much longer than the modulation cycle. These results imply that the period change in NN Ser is likely due to circumbinary planets or other yet unknown mechanisms. It will be worth to explore the models Lanza (2020) on UZ For.

2.5.3 Other eclipsing mCVs

UZ For is one of the few mCVs which presumably hosts single or multiple planetary systems, e.g. HU Aqr (Qian et al. 2011, Horner et al. 2011, Wittenmyer et al. 2012, Goździewski et al. 2015) and DP Leo (Qian et al. 2010, Beuermann et al. 2011). The two-planet model initially proposed by Qian et al. (2011) for HU Aqr required that the outer planet have higher eccentricity $\sim$0.5 and they assumed a circular orbit for the inner planet (i.e. lower eccentricity $<$0.1) in order to have stable orbits for the planetary system. However recent results presented by Goździewski et al. (2015) suggest eccentricities ranging from 0.1-0.3 for both the inner and the outer planet in HU Aqr. They also suggest that for stable orbits to exist in the HU Aqr system there must be a third companion orbiting with a very long orbital period and with the middle planet orbiting in retrograde orbit. Furthermore, they concluded that the HU Aqr planetary system may be more complex, e.g. highly non-coplanar and that the residuals may also be driven by some form of the Applegate mechanism e.g. Lanza et al. (1998). Recently, Schwope & Thinius (2018) presented a further 26 new eclipse times of HU Aqr obtained between 2014 and 2018. Their results show that the steep and continuous decrease of the orbital period observed in between 2010−2013 has slowed down some times before mid 2016. In the case of DP Leo, the proposed extrasolar planet was found to be nonexistent by Beuermann et al. (2014) after additional data were added. Instead, they found evidence that the magnetic axis of DP Leo has shifted by 50° in azimuth implying a small asynchronism between the rotational and orbital periods of the WD. Their observations suggests an oscillation period of $\sim$60 years and an amplitude of about 25° and these were explained in terms of the variation of the magnetic moments of the WD and the secondary star.

It is worth mentioning that NN Ser, a non-magnetic CV binary system that had been studied extensively like HU Aqr, shows eclipse time residuals that are consistent with two extrasolar planets, see e.g. Bours et al. (2016). Apart from that, the planetary model of NN Ser had survived rigorous dynamical stability analysis (Marsh et al. 2014). Furthermore, the analysis of the secondary eclipses of NN Ser also follow the same proposed model and

*HR 1099 is an RS CVn-type binary which show orbital period modulation of 36 years and this could not be explained by a light-time effect as confirmed by the constant radial velocity measurements (Donati 1999).

this rules out apsidal precession (Parsons et al. 2014). Recently, Lanza (2020) introduced a model which is based on angular momentum exchange between the spin of the active component and the orbital motion and found this to be insufficient to explain the angular momentum loss in NN Ser. They recommend that the circumbinary planets should not be completely ignored in the case of NN Ser.

2.6 Summary

This chapter presented new photometric observations of UZ For together with historical observations collected from literature. The new observations were used to test the two-planet model proposed in Paper I to explain the variations in its eclipse times. This study had revealed that the new mid-eclipse times initially follow the general trend predicted in Paper I (Figure 2.9) but continues to diverge. In light of new eclipse times, the fitting parameters were recalculated in the similar manner as in Paper I. The solution with the lowest reduced χ^2 value was adopted as the best-fit solution. The parameters for this solution are shown in Table 2.2 and overplotted in the middle panels of Figure 2.13. The proposed model of the two planets requires the outer planet to have a relatively high eccentric orbit, i.e. $e_3 = 0.69$. Within errors, the departures in the O−C diagram (Figure 2.13) are still consistent with the two cyclic variations (14.67(1) and 5.82(3) years) reported in Paper I. However, significant residuals remain as indicated in the bottom panel of Figure 2.13. Thus adding more elliptical terms (effectively adding more planets) would obviously lower the reduced χ^2 value, however the data is of insufficient quantity to warrant this. This suggests that either the circumbinary planet solution is incorrect or requires extra planets, or some form of cyclic magnetic activity is contributing an extra quasi-periodic term to the O−C variations. Overall, the results presented in this chapter makes UZ For the third post common-envelope and/or CV binary system, after HU Aqr and NN Ser, in which new eclipse times are still consistent with circumbinary planets. There are other binary systems (e.g. HW Vir Esmer et al. 2021) and whose new eclipse time variations were found to be consistent with previous observations however none of the planetary solutions were found to be dynamically stable on time scales of 10^5 years. Further monitoring of the eclipse times is recommended. In the the next 5 to 10 years, the GAIA space mission may be able to detect parallax variations that would be consistent with circumbinary planet solutions as also been suggested by Goździewski et al. (2015) for HU Aqr.

Table 2.3: The mid-eclipse times of the main accretion spot of UZ For. BJD_{TDB} is the BJD in the TDB system and ΔBJD_{TDB} is the uncertainty associated with the precise determination of the time of mid-eclipse. The ingress and egress times have the integer of BJD subtracted. All the times have been barycentrically corrected.

Cycle	BJD_{TDB}	ΔBJD_{TDB}	Width(s)	$T_{ingress}$	T_{egress}	Ref.
-89206	2445567.17759700	0.00016				*a*
-79193	2446446.97380900	0.00016				*a*
-71889	2447088.74254900	0.0002				*b*
-71868	2447090.58778900	0.0002				*b*
-71857	2447091.55423900	0.0002				*b*
-71821	2447094.71735900	0.0002				*b*
-71786	2447097.79255900	0.0002				*b*
-71452	2447127.13943900	0.0002				*c*
-71451	2447127.22773900	0.0002				*c*
-71248	2447145.06433900	0.0002				*c*
-67915	2447437.91992000	0.00003	466.5(2.5)			*d,f*
-63476	2447827.95478000	0.00003				*e*
-63474	2447828.13052000	0.00003				*e*
-63462	2447829.18486375	0.00003				*e*
-56024	2448482.72808573	0.0001	477(5)			*f*
-52587	2448784.72141928	0.00003	463(4)			*k*
-46988	2449276.68005500	0.00004				*g*
-46605	2449310.33259382	0.00003	471(4)			*k*
-41790	2449733.40501704	0.00004	467(4)			*k*
-41571	2449752.64756800	0.00005				*h*
-41560	2449753.61402800	0.00005				*h*
-41538	2449755.54714800	0.00005				*h*
-41537	2449755.63497800	0.00005				*h*
-38543	2450018.70410800	0.00005				*h*
-38508	2450021.77938800	0.00005				*h*
-21429	2451522.43272958	0.00002	468(2)			*i*
-21361	2451528.40757990	0.00002	468(2)			*i*
-21360	2451528.49543399	0.00002	468(2)			*i*
-18023	2451821.70239393	0.00001	467(2)			*j*
-10376	2452493.60905802	0.00007	469(6)			*k*
-10365	2452494.57562568	0.000035	469(3)			*k*
-10362	2452494.83919610	0.000087	479(8)			*k*
-11	2453404.33404192	0.00006	467(4)			*k*
0	2453405.30066303	0.000035	469(3)			*k*

Continued on next page

Table 2.3 – *Continued from previous page*

Cycle	BJD_{TDB}	ΔBJD_{TDB}	Width(s)	$T_{ingress}$	T_{egress}	Ref.
23	2453407.32157438	0.00001	469(2)			*k*
34	2453408.28808581	0.0000086	469(1)			*k*
11518	2454417.33472170	0.0000086	468(1)			*k*
16526	2454857.36480517	0.0000086	469(1)			*k*
16526	2454857.36480850	0.00001	469(2)			*k*
23277	2455450.54462082	0.00001	467(2)			*k*
23595	2455478.48583116	0.00001	468(2)			*k*
23913	2455506.42703435	0.00001	468(2)			*k*
25311	2455629.26295762	0.00002	470(1)	0.260238(20)	0.265677(30)	*znk*
27966	2455862.54558562	0.00004	469(3)	0.542871(60)	0.548301(60)	*znk*
28010	2455866.41166271	0.00002	471(2)	0.408936(40)	0.414390(30)	*znk*
28023	2455867.55393431	0.00003	472(2)	0.551204(50)	0.556664(40)	*znk*
29352	2455984.32701723	0.00004	470(1)	0.324295(40)	0.329740(20)	*znk*
30972	2456126.66890920	0.00004	470(2)	0.666182(60)	0.671642(50)	*znk*
32710	2456279.37896176	0.00004	472(3)	0.376250(30)	0.381696(30)	*znk*
33313	2456332.36177629	0.00003	470(2)	0.359056(20)	0.364497(20)	*znk*
33688	2456365.31135803	0.00004	471(2)	0.308634(60)	0.314082(40)	*znk*
33722	2456368.29859146	0.00004	471(1)	0.295865(20)	0.301318(30)	*znk*
33733	2456369.26522176	0.00004	472(3)	0.262493(50)	0.267951(60)	*znk*
36013	2456569.59832086	0.00006	475(5)	0.595571(40)	0.601070(40)	*znk*
36648	2456625.39279285	0.00004	471(3)	0.390068(30)	0.395518(30)	*znk*
37160	2456670.37988451	0.00002	471(1)	0.377161(20)	0.382608(40)	*znk*
37717	2456719.32090166	0.00006	470(3)	0.317920(80)	0.323621(30)	*znk*
40381	2456953.39425098	0.00002	471(1)	0.391527(40)	0.396975(20)	*znk*
40393	2456954.44862704	0.00002	472(1)	0.445895(20)	0.451359(30)	*znk*
40404	2456955.41517125	0.00003	472(2)	0.412439(30)	0.417903(40)	*znk*
40427	2456957.43605536	0.00002	471(1)	0.433331(30)	0.438779(30)	*znk*
40449	2456959.36909531	0.00002	471(1)	0.366371(20)	0.371819(30)	*znk*
40450	2456959.45690562	0.00004	470(3)	0.454187(50)	0.459624(80)	*znk*
41735	2457072.36399146	0.00004	472(3)	0.361262(30)	0.366721(30)	*znk*
41791	2457077.28447068	0.00004	472(4)	0.281738(30)	0.287203(30)	*znk*
42087	2457103.29264038	0.00003	472(3)	0.289908(30)	0.295372(20)	*znk*
43593	2457235.61779679	0.00004	470(3)	0.615071(30)	0.620522(20)	*znk*
43991	2457270.58825176	0.00003	471(3)	0.585528(20)	0.590976(20)	*znk*
48928	2457704.37964299	0.00002	472(2)	0.376910(10)	0.382376(10)	*znk*
48962	2457707.36706944	0.00003	471(2)	0.364344(20)	0.369795(20)	*znk*
52912	2458054.43550982	0.00004	471(4)	0.432808(50)	0.438234(60)	*znk*
53139	2458074.38097010	0.00002	471(2)	0.378244(10)	0.383696(10)	*znk*

Continued on next page

Table 2.3 – *Continued from previous page*

Cycle	BJD_{TDB}	ΔBJD_{TDB}	Width(s)	$T_{ingress}$	T_{egress}	Ref.
53140	2458074.46884132	0.00003	472(2)	0.466109(20)	0.471574(20)	^{znk}
53141	2458074.55667742	0.00003	471(3)	0.553950(20)	0.559405(20)	^{znk}
54242	2458171.29654185	0.00003	472(3)	0.293811(20)	0.299227(20)	^{znk}
56805	2458396.49564811	0.00002	472(2)	0.492916(10)	0.498381(10)	^{znk}
57179	2458429.35725846	0.00002	470(2)	0.354538(10)	0.359979(10)	^{znk}
61062	2458770.53872780	0.00003	472(3)	0.535998(30)	0.541458(20)	^{znk*}
66352	2459235.34652124	0.00002	472(2)	0.343790(10)	0.349252(10)	^{znk*}

Notes: Ref – is the reference where the times of eclipses first appeared.
[a]Osborne et al. (1988); [b]Beuermann et al. (1988); [c]Ferrario et al. (1989); [d]Allen et al. (1989); [e]Bailey & Cropper (1991); [f]Ramsay (1994); [g]Warren et al. (1995); [h]Imamura & Steiman-Cameron (1998); [i]Perryman et al. (2001); [j]de Bruijne et al. (2002); [k]Potter et al. (2011); [znk]Khangale et al. (2019b).

Chapter 3

Phase-resolved spectroscopy and Doppler tomography of UZ Fornacis

This chapter presents a detailed spectroscopic analysis of the eclipsing AM Her system UZ For. Some parts of this work has been published in the form of a paper in the **Monthly Notices of the Royal Astronomical Society Journal** in 2020 titled *"A spectroscopic, photometric, polarimetric and radio study of the eclipsing polar UZ Fornacis: the first simultaneous SALT and MeerKAT observations"* – see Khangale et al. (2020) for more details.

This chapter focuses mainly on applying the standard and inside-out Doppler tomography techniques of Kotze et al. (2015), together with flux modulation mapping from Kotze et al. (2016), to phase-resolved spectra of the eclipsing AM Her system UZ For obtained with the Southern African Large Telescope (SALT[†]; see e.g., Buckley et al. 2006b). The inside-out and flux modulation Doppler tomography techniques have been shown to be complementary to the established standard Doppler tomography when interpreting phase-resolved spectroscopic observations of interacting binary systems. The inside-out projection coupled with the flux modulation mapping forms a useful addition for unravelling the different emission line components in the observed spectra of mCVs.

The main objectives of this chapter are as follows:

- to reduce and analyze phase-resolved spectroscopy of UZ For obtained with SALT,
- to perform Doppler tomography of the strongest emission lines (e.g. Balmer, HeII 4686 and CaII lines) using the inside-out technique of Kotze et al. (2015) to unravel the contributions of the different emission components which add to the complex emission structure seen in the trailed phase-resolved spectra,

[†]More details on SALT can be found at http://www.salt.ac.za

- to use the flux modulation Doppler tomography technique of Kotze et al. (2016) to study the phase-resolved spectra of UZ For − in order to investigate the emission that varies with the orbital period, and,
- to investigate and improve the understanding of the geometry and accretion dynamics on UZ For.

This chapter is organized as follows. Section 3.1 contains a literature review of Doppler tomography (standard and inside-out projections) as well as examples were these methods were used. Section 3.2 contains a literature review of the work previously done on UZ For. This is followed by the description of the Robert Stobie Spectrograph(RSS; Burgh et al. 2003, Kobulnicky et al. 2003) instrument used in Section 3.3. Section 3.4 outlines the observations and reductions carried out for this project. The mean orbital spectrum as well as phase-binned spectra of UZ For are presented in Section 3.5. Section 3.6 discusses the average standard and inside-out Doppler tomography obtained for this target. Section 3.7 discusses the standard and inside-out modulation amplitude Doppler maps as well as phase of maximum flux maps. Section 3.8 contains the discussion and the conclusion.

3.1 Doppler tomography

As already mentioned in Chapter 1, Doppler tomography is an indirect imaging technique that was developed by Marsh & Horne (1988) which uses orbital phase-resolved spectra to construct a two-dimensional image of astrophysical objects (e.g. CVs) in velocity space. The five axioms that governs Doppler tomography outlined in Marsh (2001) has already been mentioned in Section 1.4 and are repeated below, to aid the development of this chapter and are as as follows:

1. all points in the system are equally visible at all times;
2. the flux from each point in the frame of rotation is constant;
3. all motion is parallel to the orbital plane and is mapped accordingly;
4. all velocity vectors co-rotate with the system; and
5. the intrinsic line profile width is negligible.

The Doppler maps produced by violating any of the axioms listed above does not necessarily mean that maps are “useless”. For example, the first and second axioms are easily violated since the exact geometry of CVs is unknown. In addition, axioms 1 and 2 are also violated in high-inclination and eclipsing systems. The third is violated in AM Her systems since not all the motion is confined in the orbital plane of the binary. Sections 3.1.1 and 3.1.2 contains reviews and application of both the standard and inside-out projections method of which this chapter is based on.

3.1.1 Standard Doppler tomography

Doppler tomography was developed by Marsh & Horne (1988), has been reviewed by Marsh (2001; 2005) and most recently by Marsh & Schwope (2016). Therefore, we refer the readers to these articles for detailed review. This chapter focuses on its application to mCVs with specific focus on AM Her systems. Probably a good example of the application of standard Doppler tomography, in non-magnetic CVs, is the discovery of two-arm spiral shocks in the accretion disc of dwarf novae during outbursts e.g. IP Peg (Steeghs et al. 1997) and in nova-likes e.g. V3885 Sgr (Hartley et al. 2005). Doppler tomography has revolutionized the interpretation of complex line profiles in the phase-resolved spectroscopic observations of interacting binary systems. This technique has also found usage in a wide range of other astrophysical objects, including Algols (Richards et al. 1994) and black-hole binary systems (González Hernández & Casares 2010).

The first Doppler map of an AM Her system was performed by Diaz & Steiner (1994) for VV Pup using the Hα line. Their results showed a tomogram with a large blob near the L_1 point – no obvious emission components or structures were seen except that these results showed a clear distinction between the Doppler map of a disc and discless accretors. A number of follow-up studies by various authors followed from this but no further useful results were obtained. For example, Shafter et al. (1995) presented Doppler maps of HeII and Hβ for the long orbital AM Her system RS Cae (RX J0151.6+0105), however, their tomograms showed a blob-like feature centred at the origin. The Doppler map of BL Hyi presented by Schwope et al. (1999) also showed a blob centred at the origin – no obvious structures were visible. Hastings et al. (1999) presented Doppler maps constructed using different lines of V884 Her, they show a blob towards the centre of the tomograms. Gänsicke et al. (1998) constructed Doppler maps of AM Her from the ultraviolet spectra using three emission lines, CIII, SiIV and NV. The tomograms of CIII revealed emission from the magnetic stream whereas those of the SiIV and NV showed two components; a narrow component close to the origin (centre of the velocity coordinate where both velocities are zero) which they attributed to emission from or close to the secondary star and a fan-like feature associated with the magnetic stream. In another example, Schwarz et al. (2005) found that the Doppler maps of BY Cam were different from other AM Her systems. The bulk of the emission showed evidence of accretion through the accretion curtain.

In all the AM Her systems studied in the past three decades, there were a few systems where the application of Doppler tomography techniques yielded good results. For example, HU Aqr was the first target in which well-resolved Doppler maps of a AM Her system were presented (Schwope et al. 1997a). Its Doppler maps were found to be dominated by emission from three regions: the irradiated face of the secondary, the cometary tail-like feature which they associate with the accretion stream and the third component from the magnetically confined accretion stream. They also reported on evidence for the existence of a transition region between the magnetic stream and ballistic stream. In another example, Potter et al. (2004) presented the Doppler maps of V834 Cen and they showed three emission components, namely: emission from the irradiated face of the secondary star, the ballistic

and the magnetically confined accretion stream. These were achieved by constructing maps with spectra from consecutive half-orbits. Other examples of AM Her systems whose Doppler maps are presented in the literature include, e.g. QQ Vul, BL Hyi and V1309 Ori (see Schwope et al. 1999) and further examples are listed in Marsh & Schwope (2016).

3.1.2 Inside-out Doppler tomography

The Doppler maps discussed in Chapter 1 (i.e. Sections 1.4 and 1.8) and Section 3.1.1 were all projected in cartesian coordinates (i.e. V_x, V_y) in velocity space and centred in the binary's centre of mass. In this configuration, the zero velocity is placed at the origin whereas the maximum velocities are on the edge of the coordinate frame. Recently, Kotze et al. (2015; 2016), presented a new Doppler tomography inversion method called the inside-out velocity projection technique or simply "inside-out technique", see Kotze (2017) for the full thesis*, which uses polar coordinates. This technique was applied to the observations of three mCVs (HU Aqr, V834 Cen and PQ Gem) already presented in literature (Schwope et al. 1997a, Potter et al. 2004, Hellier 1997). The results show that the blended emission is separated into various components which makes the Doppler maps easier to interpret (Kotze et al. 2016). The inside-out Doppler tomography method has been used to construct the maps of the following AM Her systems: MASTER OT J132104.04+560957.8 (Littlefield et al. 2018a), IPHAS J052832.69+283837.6 (Gabdeev et al. 2019) and RX J0502.8+1624 (Tau 4) (Littlefield et al. 2020) including two asynchronous AM Her systems IGR J19552+0044 (Tovmassian et al. 2017) and CD Ind (Littlefield et al. 2019). This method has also been used on two DQ Her systems: EX Hya (Echevarría et al. 2016) and FO Aqr (Kennedy et al. 2020). Other usages of this method include non-magnetic CVs, e.g. SU UMa dwarf novae CRTS J035905.9+175034 (Littlefield et al. 2018b) and period bouncers CVs, e.g EZ Lyn Amantayeva et al. (2021). The inside-out technique made it possible to distinguish between the various emission components present in the tomograms of CVs (Kotze et al. 2015) and is reviewed below.

3.1.2.1 Spatial polar coordinates

Figure 3.1 shows a model of an mCV in spatial polar coordinates. The model mCV has a ballistic stream and the magnetically confined accretion flows along the magnetic dipole field lines. The radial component r is the distance measured from the binary's centre of mass and is normalised by the binary separation a. The angular component θ_s (or the polar angle) is measured in an anticlockwise direction from the line between the centres of mass of the binary and the secondary. The radial components of the centres of mass of the primary and secondary are functions of the mass ratio q, i.e., $r = q/(1+q)$ for the primary's centre of mass and $r = 1/(1+q)$ for the secondary's centre of mass. The modelled single-particle ballistic trajectory includes gravitational and centrifugal effects as well as a magnetic drag force (similar to that employed by Schwope et al. (1997a). The drag force

*See https://open.uct.ac.za/handle/11427/25356 for more details.

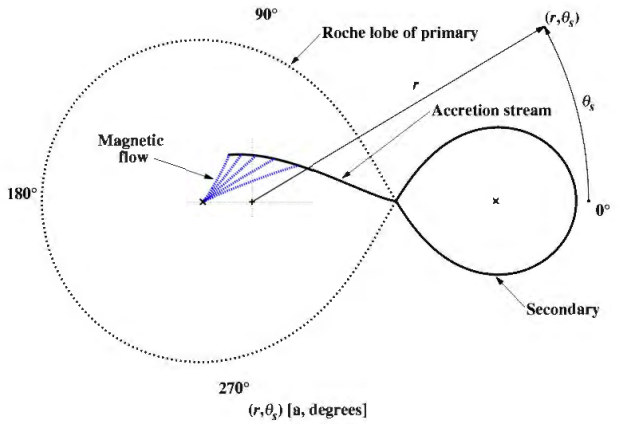

Figure 3.1: Co-rotating spatial polar coordinates for a model mCV. Adopted from Figure 1 of Kotze et al. (2016).

decreases exponentially as a function of the distance from the primary's centre of mass and is included in order to account for the pull of the primary's magnetic field on the partly ionised ballistic stream. The structure of the primary's magnetic field is taken to be a dipole with undefined magnetic strength.

3.1.2.2 Velocity polar coordinates

As described in Kotze (2017), every spatial point (r, θ_s) in the system has a two-dimensional velocity polar coordinate (u, θ) in the co-rotating spatial coordinate frame. Note that the angular component θ_s in the spatial coordinate frame is not the same as the the angular component θ in the velocity coordinate frame. The projection of all the (u, θ)-coordinates onto the rotating frame forms the velocity polar coordinate frame with (v, θ)-coordinates. The inclination angle i is taken into account in the projection, i.e., $v = u\sin i$.

Figure 3.2 shows the velocity polar coordinates for a model mCV based on the co-rotating spatial polar coordinates defined in Figure 3.1. The binary's centre of mass is indicated by the plus sign (+) at the origin whereas the centre of mass of the secondary and primary are marked with a cross signs (×) on the 90° and 270° lines. The red circles along the ballistic accretion stream indicate the points where the magnetic dipole field lines connect whereas the red dotted lines are non-physical tracers for the change in the line-of-sight velocity as the magnetically confined accretion flows leave the orbital plane of the binary along the magnetic dipole field lines. The blue dotted lines mark the magnetic dipole field lines as they diverge to higher velocities.

The inclination angle of the system is assumed to be 87° and the radial component v (the velocity magnitude) increases as a linear function of the origin. The velocity direction or angular component θ is measured in an anticlockwise direction from the line drawn from the binary's centre of mass horizontally to the right. The advantage of using velocity polar coordinates is that a coordinate (v, θ) directly describes its magnitude v and direction θ. The velocity cartesian coordinates must be converted to get its magnitude v and direction θ.

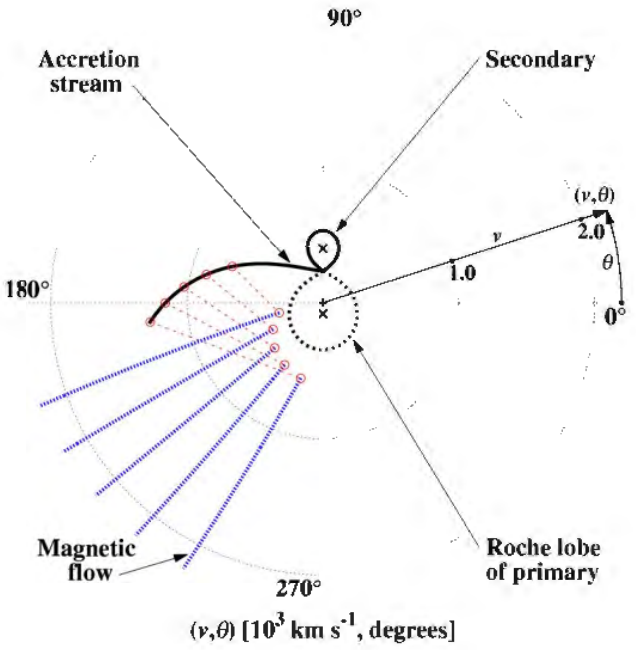

Figure 3.2: The velocity polar coordinates for a model mCV with ballistic and magnetic accretion flows. See text for more details. Adopted from Figure 1 of Kotze et al. (2016).

Kotze (2017) argue that "it is more intuitive to describe velocity in terms of its magnitude and direction than to describe it in terms of its x- and y-axial components."

The first dipole connection on the ballistic stream is at (283 km/s, 131°), whereas the first dipole trajectory starts at (126 km/s, 166°). The consecutive connections and trajectories are at locations with progressively higher velocities and polar angles. These velocities include the effect of the simulated magnetic drag force mentioned above. The profiles of the dipole trajectories radiate outwards from lower velocities where they leave the orbital plane towards higher velocities as they approach the primary. That is, the dipole profiles diverge towards higher velocities.

3.1.2.3 Inside-out velocity polar coordinates

The standard velocity polar coordinate frame discussed in Section 3.1.2.2 forms the basis for the inside-out velocity polar coordinate frame. The angular velocity θ of a point mentioned in the previous section remains unchanged and is measured in an anticlockwise direction from the line drawn from the binary's centre of mass horizontally to the right as shown in Figure 3.3. But in the inside-out velocity polar coordinate, the radial component v increases as a linear function of distance from zero velocity on the outer circumference towards the centre of the coordinate frame with the same direction θ.

The default centre of the inside-out coordinate frame is set to the maximum radial velocity used to construct the standard coordinate frame. But a small arbitrary element velocity δv is added to the maximum radial velocity. Essentially, this maximum radial

velocity is the same maximum velocity v_{max} extracted from an emission (or absorption) line from the edge of the observed phase-resolved spectra and projected onto the coordinate frame to construct a tomogram. Therefore, the centre and the outer circumference of the inside-out coordinate frame are the transposition of the zero velocity origin and the maximum outer velocities, plus small arbitrary velocity element δv, of the standard coordinate frame.

The set of maximum velocities at the small arbitrary velocity element δv from the centre of the inside-out coordinate frame is given by Eq. 3.1 below

$$(v, \theta) = (v_{max}, \theta) \tag{3.1}$$

for all values of θ. This means that the edge of the data is projected around the centre of the inside-out coordinate frame. The centre of the inside-out coordinate frame represents a discontinuity and the inner four velocity bins (pixels) around it are not used in the inside-out projection, i.e, shaded in black colour. Placing zero velocity at the edge of the inside-out coordinate frame means that where it used to be only one point in the standard coordinate frame, it now becomes a set of zero values described by

$$(v, \theta) = (0, \theta) \tag{3.2}$$

for all values of θ.

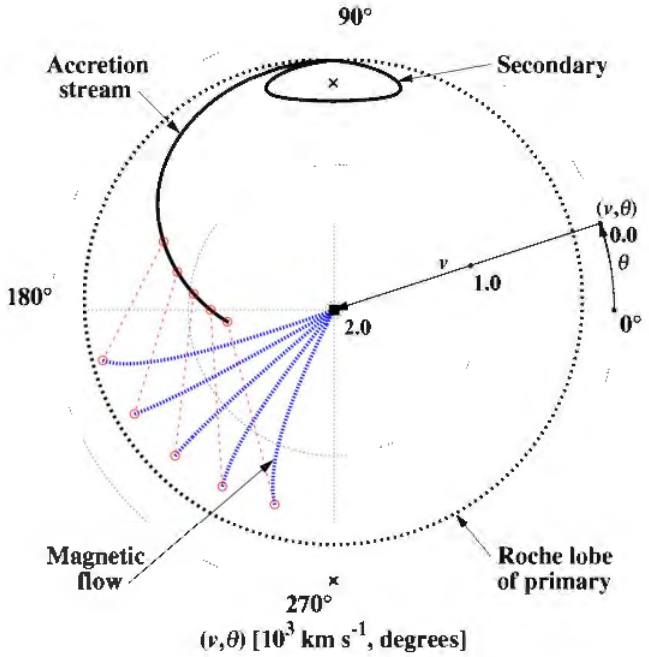

Figure 3.3: A schematic of the inside-out velocity polar coordinates for a model mCV with a ballistic and magnetic accretion flows. See text for more details. Adopted from Figure 1 of Kotze et al. (2016).

Figure 3.3 shows the equivalent inside-out velocity map of the standard velocity map

shown in Figure 3.2. The inside-out velocity map is centred on the rest frame of the binary. The binary's centre of mass for the inside-out coordinate frame is the zero velocity outer circumference. The centre of mass of the primary and secondary are marked with crosses ($\times$) on 270°- and 90°- lines. The secondary star is orientated upside down because it orbits as a solid body and the side of the secondary furthest to the binary's centre of mass moves faster than the side closest to the binary's centre of mass. The Roche lobe of the primary is now the outer bounded area between zero velocity and the dashed line that contains the primary's centre of mass which is marked by a cross ($\times$) at 270°. The ballistic stream leaves the secondary at an angle of 90° and curves inwards as it accelerates towards the threading region and the primary. The red circles, red and blue dotted lines are as described in Section 3.1.2.2. However, the profiles of the dipole trajectories now radiate inwards from lower velocities when they leave the orbital plane towards higher velocities as they approach the primary. The dipole fields simply converge towards higher velocities.

The previous sections discussed the change from cartesian coordinates to spatial polar coordinates and to the inside-out velocity polar coordinate frame. In cartesian coordinates, the velocity coordinate frame is divided into discrete square velocity bins each of which is centred on a unique velocity coordinate (v_x, v_y). Each velocity coordinate frame describes a velocity vector that has both a magnitude v and direction θ. In both the standard and inside-out polar coordinate frames, each velocity pixel is centred on a velocity coordinate (v, θ) which describes the magnitude v and angle θ of the corresponding centre velocity vector $\vec{v} = (v, \theta)$. Therefore, each pixel represents a square velocity bin which has sides of magnitudes dv_p.

The sinusoidal radial velocity in the cartesian coordinate frame, Eq. 3 of Marsh 2001, is now given in polar coordinates by Eq. 3.3 of Kotze (2017) as follows:

$$v_r = \gamma - v\cos(\theta + 2\pi\phi) \tag{3.3}$$

where γ is the systemic velocity, v is the velocity magnitude and θ is the velocity angle of the velocity vector described by the velocity coordinate. Note that the radial velocity (v_r) are inferred from the spectral wavelength profile of the emission line using the relativistic Doppler shift (Einstein 1905) in its wavelength form given by the following relation:

$$\frac{\lambda}{\lambda_0} = \sqrt{\frac{1 + v_r/c}{1 - v_r/c}},$$

which can be re-written (see equation 2.1 of Kotze 2017) as follows :

$$v_r = \left(\frac{\lambda^2 - \lambda_0^2}{\lambda^2 + \lambda_0^2}\right) \times c,$$

where λ is the observed wavelength containing the Doppler shift, λ_0 is the rest wavelength of the emission line as measured in the laboratory and c is the speed of light. The standard and inside-out tomograms were reconstructed using 4048 (23×176) discrete velocity bins

(pixels). More details on this method can be found in the form of journal articles (Kotze et al. 2015; 2016) or the PhD Thesis (Kotze 2017).

3.1.3 Flux modulation Doppler tomography

The violation of any of the Doppler tomography axioms listed in Section 3.1 does not mean that the Doppler maps produced thereafter are meaningless. For example, Steeghs (2003) extended the standard Doppler tomography technique by violating the second axiom which state "the flux of each element is constant" in order to isolate the emission components that vary harmonically as a function of the spin or orbital period. The modulation method introduced by Steeghs (2003) treats the image as a Fourier series in orbital phase using the following expression from Marsh & Schwope (2016) as

$$I(V_x, V_y) = I_0(V_x, V_y) + A(V_x, V_y)\cos 2\pi\phi + B(V_x, V_y)\sin 2\pi\phi. \tag{3.4}$$

The above expression implies that one needs three parameters to describe the line flux from a specific velocity vector, i.e., the average flux I_0 and the cosine and sine components of A and B. The latter two terms are often given in terms of the amplitude and phase of modulation. Thus one ends up with three Doppler maps with one being the average map plus the cosine and sine of the average flux maps. This method was applied to different objects, e.g. dwarf novae IP Peg (Steeghs 2003) and a neutron star EXO 0748−676 (Bassa et al. 2009). In another study, Potter et al. (2004) violated the first axiom, which states that "all points in the binary system being mapped are equally visible at all times". This implies that it is possible to construct a Doppler map using trailed spectra covering half the orbit. Therefore, Potter et al. (2004) took advantage of this when they applied the Doppler tomography technique to the spectra of V834 Cen since they used data covering consecutive half of the orbital phase.

The inside-out Doppler tomography, discussed in Section 3.1.2, also included some form of modulation techniques discussed in detail in Kotze et al. (2016) and chapter 5 of Kotze (2017). The modulation technique takes advantage of the first axiom, since it is already violated in most CVs and e.g. in Potter et al. (2004), was used to isolate the various emission components from the tomogram by using spectra covering half of the orbital phase. The third axiom that assumes that the observed flux from any point in the binary system is constant is also violated while using this method. This is because in CVs, especially mCVs, the flux from any typical emission component does modulate. Therefore, when using standard Doppler tomography, any phase-dependent flux modulation is not recovered in the reconstructed spectra. Recognising this and the recipes from Steeghs (2003) and Potter et al. (2004), Kotze et al. (2016) introduced a variant form of modulation Doppler tomography called the "flux modulation technique" which produces the Doppler maps that represent the average, amplitude and phase of the modulated emission. Any phased modulation in the observed flux is extracted from a series of consecutive half-phase tomograms and used to map how the flux from a specific emission component modulates over a complete phase. For

this method, it is assumed that the flux from an emission component varies harmonically over the observed phases and it is possible to extract the average (B_j), amplitude (A_j), phase-offset (φ) of the flux modulation in the j-th pixel from a simple sinusoid fit (Eq. 2 of Kotze et al. (2016)) of the form

$$F_{i,j} = A_j \sin[2\pi(\Phi_i - \varphi_j)] + B_j \tag{3.5}$$

where $F_{i,j}$ is the flux in the j-th pixel and Φ_i is the mid-phase value of the i-th half-phase tomogram. The average for each pixel (B_j) is effectively the normal tomogram in both the standard and inside-out projections. The amplitude map, obtained from the fitted amplitude for each pixel (A_j), helps identify which pixel emission component(s) are modulated and is presented in the same colour scheme as the normal tomogram. The phase of maximum flux map is obtained by adding 0.25 to the fitted phase-offset (φ_j) and this shows at which phase an emission component appears brightest to an observer and is colour coded according to phase: 0.0 – black; 0.25 – red, 0.5 – green and 0.75 – blue. Section 3.7 is based on an application of the modulation method on UZ For.

3.2 Historical spectroscopy of UZ For

The discovery of UZ For was reported in an IAU circular by Giommi et al. (1987) and the first optical spectroscopy of the X-ray counterpart in the field of view of this source was obtained in 1987 October 20−26 and presented by Beuermann et al. (1987; 1988). The optical spectra of UZ For was characterized by a variable blue continuum with weak emission from the Balmer lines in the blue and very strong molecular bands (TiO) in the red associated with the secondary star (see Figure 2 of Beuermann et al. 1988). During these first observations, UZ For was in its low state of accretion and its spectral characteristics confirmed it to be an AM Her type system. The spectra taken a month later, 1987 November 27, by Ferrario et al. (1988; 1989) showed strong emission from the Balmer lines and HeII 4686 Å on a continuum that rises in the red. For these observations, UZ For was "caught" in its high state of accretion, i.e. strong emission from the Balmer lines and HeII 4686 Å in optical spectra are signatures of a high state of accretion.

A few weeks later, UZ For was observed by Allen et al. (1989) on 1987 December 9 and their spectrum appeared flat with strong emission from the Balmer lines and HeII 4686 Å. Their average spectrum shows a steep Balmer decrement and the strength of the emission lines (Balmer and HeII lines) indicate that UZ For was in an intermediate state of accretion. Additional spectroscopic observations obtained on 1988 March 20 by Ferrario et al. (1989) revealed similar spectra with a steep Balmer decrement. However, UZ For was fainter (i.e. in its low state accretion) for these observations compared to the 1987 November observations. In addition, Schwope et al. (1997b) obtained high signal-to-noise ratio low-resolution optical spectroscopy of UZ For in 1989 November 21−22 covering wavelengths from 5800−10000 Å. Their spectra were dominated by emission from the secondary star with weak emission from

Hα and absorption from NaI at 8200 Å. Their radial velocity analysis of the Hα suggests that the WD in UZ For is $\sim$1 $M_{\odot}$ whereas that of the NaI doublets place the mass of the WD at 0.44 $\pm$ 0.15 $M_{\odot}$. In addition, their results agree with the inclination of the binary being $<$83° (see e.g. Ferrario et al. 1989). During these observations, UZ For was in its low state similar to those reported in Beuermann et al. (1988) and Schwope et al. (1990).

In this chapter, medium-resolution phase-resolved spectroscopy of UZ For from a 10-m class telescope is presented with the purpose of investigating and improving the understanding of the geometry and accretion dynamics on UZ For using the inside-out Doppler tomography code of Kotze et al. (2015) and utilizing the physical parameters from various authors.

3.3 Southern African Large Telescope

Figure 3.4: Picture of the SALT telescope. Adopted from www.salt.ac.za.

SALT, shown in Figure 3.4, is a 10-m class optical-infrared telescope located at the observing station of the SAAO in Sutherland. The design of SALT is similar to that of Hobby Eberly Telescope (HET; Sebring & Ramsey 1997), however there are differences that came about to either improve the performance or capability of the telescope. Some of the improvements include a redesigned reflective spherical aberration corrector, a redesigned primary mirror support and actuation system to allow more control of the segments, etc, (see e.g. Buckley 2005). The telescope is made up of 91 identical 1-m wide hexagonal segments tilted at a constant zenith distance of 37 degrees, with azimuthal rotation only for target acquisition. The mirror segments, Figure 3.5, are arranged to form a primary mirror of dimensions 11-m to 10-m (Buckley et al. 2006a). The fixed elevation primary mirror directs incoming light to a moving tracker at the prime focus which is equipped with a spherical aberration corrector

(Buckley 2005). The declination range of the telescope is restricted to $+10° < \delta < -75°$, setting the track time of the object of interest to the time it takes to transit the annulus illustrated in Figure 3.6 (Buckley et al. 2003).

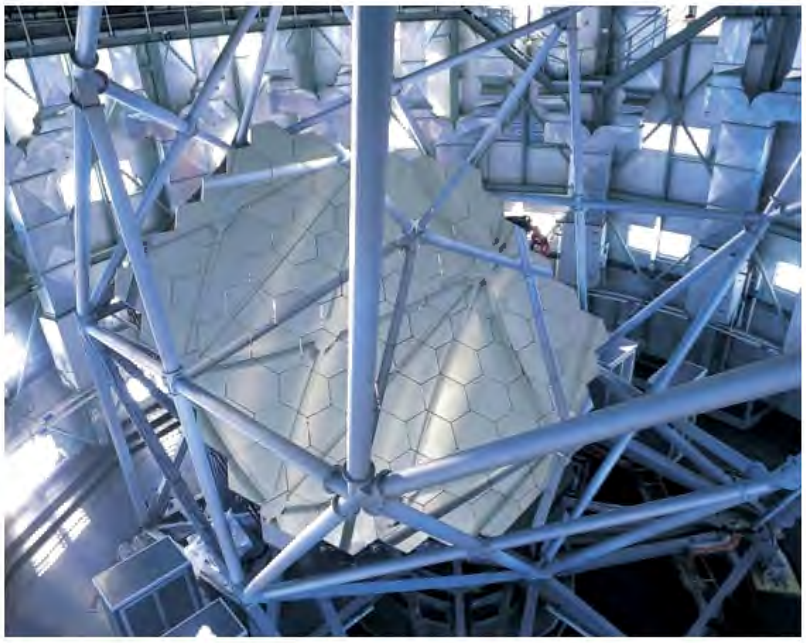

Figure 3.5: The SALT primary mirror array which consists of 91 hexagonal 1-m segments, with an accuracy of 15.7 nm RMS and a master sphere radius of curvature of 26.165m. Adopted from figure 1 of Buckley et al. (2006a).

The SALT telescope has a variety of instruments namely: RSS, SALT Imaging Camera (SALTICAM), High-Resolution Spectrograph (HRS) – installed in 2013 and a visiting instrument, the Berkeley Visible Image Tube (BVIT) camera. These instruments are described below:

- The RSS instrument is an imaging spectrograph that has been the main workhorse for SALT. It has a wavelength coverage from 3200–9000 Å and is upgradable to include an infrared-arm (up to 1.7 microns). RSS has a wide range of capabilities and operates in different modes including: long-slit spectroscopy, narrow-band imaging, Fabry-Perot imaging spectroscopy, high time-resolution spectroscopy and long-slit all-Stokes spectropolarimetry and imaging polarimetry (Buckley 2005).

- SALTICAM is a multi-purpose optical imager that is used as both a scientific imaging photometer and an acquisition camera (O'Donoghue et al. 2003). It operates from ultraviolet to visible wavelengths (3200–9000 Å) and can be used in several modes, e.g. frame transfer, normal imaging and slot mode (O'Donoghue et al. 2006). It is equipped with a mosaic pair of E2V Technologies 44-82 CCDs: 2048 × 4102 × 15 micron, each with an imaging area of ∼60 × 30 mm^2. The SALTICAM has a field

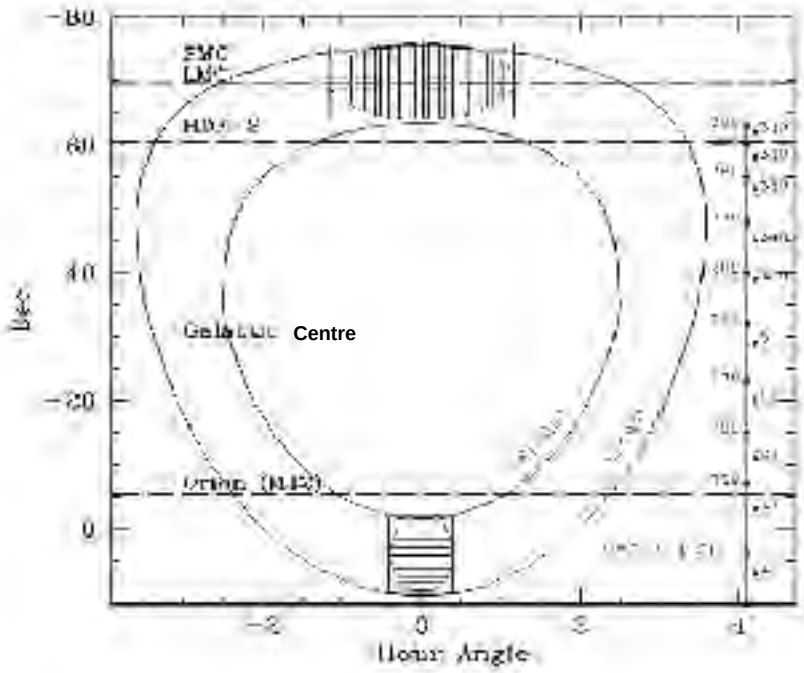

Figure 3.6: The visibility annulus of objects observable by SALT. Adopted from Figure 4 of Buckley et al. (2003).

of view of 8 and 10 arcmin for the science and guide star, respectively. It has a focal reduction ranging from f/4.2 to f/2 and uses eight filters: U, B, V, R, I, ND, clear filters, etc.

- HRS is a fibre-fed Échelle spectrograph designed for high-resolution and high efficiency seeing-limited spectroscopy on SALT. It has a dual-beam with the blue and red arms operating at wavelength ranges, 3700–5500 Å and 5500–8900 Å, respectively. The HRS instrument can be operated in three different modes at different resolutions: low resolution (R∼14000), medium resolution (R ∼40000) and high resolution (R∼65000), (Barnes et al. 2008, Bramall et al. 2012).

- BVIT is a visiting instrument that is mounted on prime focus of SALT – is an imaging, photon-counting camera with multi-colour (B,V, R, and H-α) capability, originally designed to perform high time-resolution astronomy of variable objects in the visible and near-ultraviolet bands (McPhate et al. 2012). It is currently not able to achieve high-precision absolute photometry, but can obtain a flux intensity relative precision of 5% by observing nearby standard stars.

One of the science objectives of SALT is to characterise and study transients across a wide range of classes, including CVs and other associated eruptive variables from all-sky large surveys such as the Mobile Astronomical System of Telescope-Robots (MASTER; Lipunov et al. 2010, Kornilov et al. 2012), CRTS (Drake et al. 2009), the All-Sky Automated Survey

for SuperNovae (ASAS-SN; Shappee et al. 2014), the Optical Gravitational Lensing Experiment (OGLE; Paczynski 1986, Udalski et al. 1994) and GAIA (Gaia Collaboration 2018) transient surveys. With its three primary instruments available and operating in different modes and coupled with queue scheduling, SALT makes it possible to observe mCVs over one or two visits depending on the orbital period and the visibility of the target as shown in Figure 3.6. For this study, UZ For was observed with SALT using the RSS instrument in long-slit spectroscopy mode. The details are discussed in Section 3.4.

3.4 Observations and data reduction

3.4.1 Observations

Table 3.1: The spectroscopic observation log of UZ For. All the spectra were taken with the RSS instrument on SALT.

Date of observation	Start time (UTC)	End time (UTC)	Number of Spectra	Exposure time (s)	Spectral Resolution (mm)	Wavelength Range (Å)
2013/01/03	21:35:11	22:12:24	7	360	4000	7550-8650
2013/01/06	21:24:21	22:13:14	7	360	2300	4050-5100
2013/01/07	21:19:59	22:08:23	8	360	2300	4050-5100
2013/01/08	21:44:18	22:28:42	8	360	2300	4050-5100
2014/01/30	19:59:56	20:49:54	7	360	4000	7550-8650

Spectroscopic observations of UZ For were obtained over five nights between 2013 January 3 and 2014 January 30 under programs 2012-2-RSA-008 and 2013-2-RSA-006 (PI: Dr Stephen Potter). The observations were made using the RSS instrument that is mounted on the prime focus of SALT (see e.g. Buckley et al. 2006b). The log of the observations is provided in Table 3.1. A long-slit of width 1.5″ was used and a total of seven or eight medium-resolution spectra, with 360 s exposure, were obtained per night. This exposure time was chosen in order to avoid velocity smearing, i.e. for AM Her systems a radial velocity study requires a phase resolution of $\Delta\phi \approx 0.05$ (Mukai 1988). For a binary like UZ For with an orbital period of 126.5 min, that is an equivalent to ∼360 s exposure. Two of the five nights were taken at longer (red) wavelengths and the remaining three nights were taken at shorter (blue) wavelengths. The PG2300 grating was used for the blue spectra at a grating angle of 32° and a camera station angle of 84°. This grating angle gives a central wavelength of 4600 Å and a coverage of ∼4050–5100 Å at a spectral resolution R≈2300 – allowing for sufficient coverage of the emission lines (HeII and Balmer lines) that are being investigated. For the red spectra, the PG1800 grating was used at a grating angle of 48° and a camera station angle of 124°. This grating angle gives a central wavelength of 8600 Å and a coverage of ∼ 7550–8650 Å at a spectral resolution of R≈4000. This setting allows for coverage of the single ionized calcium lines in the red. The order blocking was done with the PC00000 and PC04600 filters for the blue and red exposures, respectively. These observations were

taken in such a way that they cover one orbital phase of the binary. Careful planning, using the Principal Investigator Proposal Tool (PIPT, Hettlage et al. 2010), was required in order to avoid repeated observations of the same orbital phases. In total, a complete orbital cycle of the binary was covered in blue wavelengths with some spectra from different nights overlapping in phases whereas in the red, only ∼0.66 of the orbital cycle was covered. Also, the first set of red spectra observations were taken on 2013 January 3 and the second set was taken on 2014 January 31. Spectra of the ThAr arc lamps were taken at the end of each observation for the purpose of wavelength calibrations. In addition, the spectra of LTT 4364 and EG21, taken at blue and red wavelengths, respectively, were taken on the night of observation and these were used for relative flux correction.

3.4.2 Data reductions

The CCD pre-processing of the RSS observations were carried out using the SALT PYSALT package* (Crawford et al. 2010). The pre-reduction included overscan correction, bias subtraction and gain correction. The spectroscopic data of UZ For were reduced using the standard IRAF† (see e.g. Tody 1986) and/or PYSALT reduction procedures. As a first step, the science part of the CCD were copied from the processed multi-extension fits formats using IMCOMPY task in IRAF. This ensured that the final copied image had only one extension. To remove cosmic rays, the PYSALT task SALTCRCLEAN was used. The next step was to perform arc-line identification, this was based on the ThAr arc lines. The IRAF task, IDENTIFY and RE-IDENTIFY under onedspec in IRAF was used. To get low RMS∼0.04, a fifth-order Chebyshev function was used until the reasonable RMS was attained. The IRAF tasks under twodspec: FITCOORDS was used to fit the wavelength solution to the respective arc files and thereafter, another IRAF task, TRANSFORM was then used to apply the final wavelength solution to the science fits files. This ensures that the wavelength calibration is applied to both the arc and science fits files.

The next step was to extract the spectra from each of the science fits files, but before this could be done, background subtraction was carried out using the IRAF onedspec task BACKGROUND. The object's spectra were then extracted using IRAF task APALL under KPNOSLIT. Relative flux correction of the blue and red spectra was based on the sensitivity function of the spectrophotometric standard star LTT 4364 and EG21 (Baldwin & Stone 1984), respectively. Extinction correction was applied to the resulting spectra of UZ For based on an extinction file provided by the SAAO site. Doppler corrections due to the motion of the earth around the sun was applied following IRAF'S tasks RVCORRECT and DOPCOR. The average blue and red spectra of UZ For are presented in Figure 3.7. The two gaps in the spectra are due to the RSS detector consisting of a mosaic of three chips which in turn results in two small gaps (gap width of ∼10 Å) in the wavelength dispersion direction.

*http://pysalt.salt.ac.za/

†IRAF is distributed by the National Optical Astronomy Observatories, which are operated by the Association of Universities for Research in Astronomy, Inc., under cooperative agreement with the NSF.

3.5 Spectral analysis

3.5.1 Mean orbital spectrum

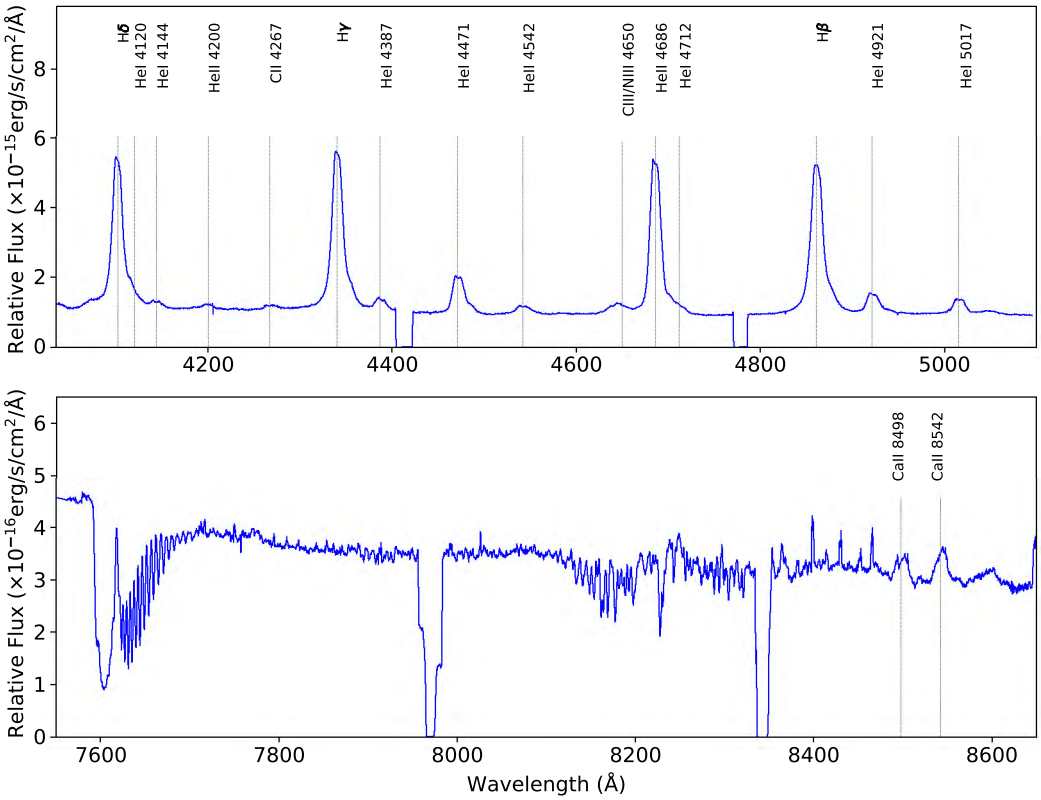

Figure 3.7: The average wavelength calibrated blue (top) and red (bottom) spectra of UZ For obtained with SALT. Prominent emission features have been labeled.

Figure 3.7 (top panel) shows the average blue spectrum of UZ For from the three nights. The blue spectrum/continuum is dominated by asymmetric single- and/or double-peaked emission from the Balmer lines ($H\beta$, $H\gamma$ and Hδ), singly ionized Helium (HeII) lines (at 4200, 4542, 4686 Å) and neutral Helium (HeI) lines (at 4120, 4144, 4387, 4471, 4712, 4921 and 5017 Å). Some HeI appears to have a flat top and probably double-peaked. However, the broadening of HeI 4471 Å is a result of blending with MgII at 4481 Å. While HeI 4712 Å is blended with HeII 4686 Å in the average spectrum in this case and at some orbital phases these two lines are separated (see Figure 3.8). These emission lines (the Balmer lines, HeII and some HeI lines) have a broad base component and a narrow component that is present throughout the orbital phase. The broad base component is thought to be associated with high-velocity gas falling towards the accretion region(s) on the surface of the WD (Warner 1995a). The narrow component is associated with emission from various parts of the accretion flow including the accretion stream and the secondary star. Normally, the optical spectrum of AM Her systems show two components in their emission lines, that

is, a strong broad base component and a narrow component whose velocity variations lag behind those of the broad components in phase. According to Liebert & Stockman (1985), the narrow emission line component is produced in the chromosphere of the red dwarf (i.e. in the region between the L_1 point and the red dwarf). This was confirmed by Mukai & Charles (1986) through the radial velocity observations of the CaII triplet in the spectra of ST LMi, MR Ser and QQ Vul. HeII 4686 Å and the Balmer lines dominate the spectrum but the former is the strongest feature. In addition, the strength of HeII 4686 Å is comparable to that of Hβ and this is typical for AM Her systems in a high state of accretion (Mukai 1988, Warner 1995a). The Balmer decrement ($H\gamma/H\beta \simeq 1$) is flat in the case of UZ For. This, according to Williams (1991), is indicative of a temperature of ∼10000 K. Notably, the work of Williams (1991) focused on emission regions in accretion discs and Gerke et al. (2006) argued that the same temperature-density relations should hold for the emission regions in the accretion flow of AM Her systems. Furthermore, the ratio of $H\gamma/H\beta$ for an optically thin gas is $\simeq 0.5$ (Brocklehurst 1971), and therefore the Balmer emission lines of UZ For are interpreted to be optically thick, that is, a region of high optical depth in the lines (Williams 1983). The other lines: the Bowen blend (CIII/NIII at 4650 Å) commonly seen in AM Her systems (e.g. Schachter et al. 1991) and CII 4267 Å, all appear in weak emission. The Bowen blend arises due to the de-excitation of CIII and NIII ions in the surrounding gas to the ground state emitting a series of photons including a group at 4640–4650 Å and OIII seen as emission lines. This mechanism is called Bowen fluorescence (Bowen 1934; 1935) and was linked to emission in X-ray binaries by McClintock et al. (1975). Note that the NIII and CIII ions in the gas are first excited by extreme-ultraviolet photons emitted from HeII 3040 Å (temperature $\geq$ 30000 K) since these ions have a transition very close to this wavelength.

The red spectrum of UZ For, Figure 3.7 (bottom panel), shows a continuum dominated by absorption lines with most features clustered around $\lambda \sim 7600$ Å and 8250 Å. The features at 7600 Å are due to absorption by the earth's atmosphere. There is strong emission from the CaII lines at 8498 Å and 8542 Å, members of the Paschen series. The emission of CaII is thought to originate from the irradiated face of the secondary star facing the WD which is due to heating by ultraviolet and X-ray photons from the WD and the accretion stream. In addition, there is possibly weak absorption from NaI at 8183 Å and 8194 Å (not labelled). Their weakness might be due to simply averaging the red spectra together, see e.g. QQ Vul (Catalán et al. 1999).

The wide range of ionization mentioned above shows that there is more than one region where these lines are formed. The source of the emission seen in AM Her stars is well understood and include the following: the accretion region(s) on the surface of the WD, the ballistic stream and the magnetically confined accretion stream and irradiated face of the secondary star. The latter two are bombarded by ultraviolet and X-ray photons from the accreting region(s) and the threading region. The vicinity of the threading region sometimes contribute to the overall emission of the binary, e.g HU Aqr (Vrielmann & Schwope 2001). The accretion stream in UZ For contributes about 55% of the total emission during the high state (Bailey 1995). Other systems that also show significant accretion stream contribution

during high states include HU Aqr (e.g. Harrop-Allin et al. 1999) and V2301 Oph (Barwig et al. 1994).

The excitation mechanisms that operate along the accretion stream are photoionization by high energy photons (such as X-rays) from the accretion region on the surface of the WD and collisional heating within the stream. Other heating mechanisms in magnetized flows of AM Her systems include compression of threaded blobs by the converging field lines and shock heating of any surviving unthreaded blobs by the threaded materials. Also, if the red dwarf is strongly irradiated by the WD, the radiation from the red dwarf can ionize the stream at L_1 (Schwope et al. 1997a). The low-excitation lines such as the Balmer and HeI lines are believed to originate primarily from low-density regions at the ballistic and magnetically confined accretion stream, threading region, accretion region(s) and irradiated face of the secondary star (e.g. Williams 1991). The Balmer emission lines arise from the de-excitation of an electron in a positive Hydrogen ion from a higher energy level (n = 6) to a lower energy level (n = 2) resulting in the emission of photons whose energy is equivalent to that of the energy difference between the two energy levels in a process called recombination. The high-excitation lines in AM Her systems: HeII and CII are believed to be emissions from the gas closer to the WD or an ionizing source such as the accretion stream, the threading region where the ballistic stream begins to couple to the magnetic field or irradiated face of the secondary star (Sarty & Wu 2006). HeII 4686 Å emission line is formed through a recombination process of Helium ions and free electrons transitioning from a higher energy level (n = 4) to a lower energy level (n = 3) resulting in the emission of photons with equivalent energy to the two energy levels (e.g. Woods & Gilfanov 2013). Note that HeII (1640 Å and 4686 Å) lines are not capable of ionizing hydrogen and therefore are not strongly absorbed in the interstellar medium.

The lines from shock heated gases and photoionized gases have different properties. For example, simple photoionization-recombination models generally predict the ratios of Hα/Hβ of 3.5 but the observations show ratios that deviate significantly from these model predictions (Osterbrock 1989). The deviation implies that the line formation process is more complex than simple photoionization and recombination. Phase-resolved spectroscopy of CVs can be used to study the emission line distribution within these systems (Horne & Marsh 1986, Marsh & Horne 1988). The strongest features from both the blue and red spectra were used to compute Doppler maps of emission lines for further investigation, see Section 3.6.

3.5.2 Phase-binned spectra

All 23 spectra obtained in the blue part of the spectrum were binned into 10 bins each with the bin-width of 0.1 of the orbital phase. The orbital phases here were calculated with respect to the photometric ephemeris of Khangale et al. (2019b) and reproduced in Chapter 2 (Table 2.2). The spectra were binned such that a bin centred at 0.1 contains all the spectra from $0.05<\phi<0.15$ and the bin centred at 0.2 contains all the spectra from $0.15<\phi<0.25$, etc. The results are shown in Figure 3.8. The individual spectra were shifted by an increment

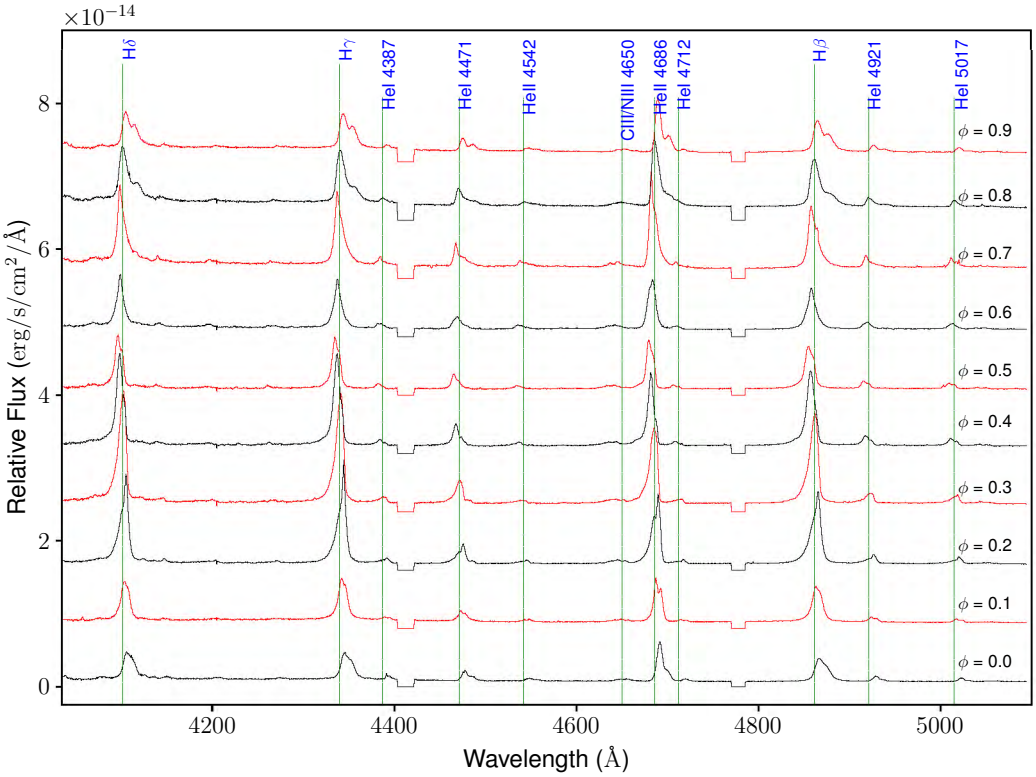

Figure 3.8: Phase-binned spectra of UZ For. The individual spectra have been shifted by an increment of 0.8×10^{-14} from bottom to top. The numbers above the spectra indicate the respective orbital phases.

of 0.8×10^{-14} from bottom to top and their respective orbital phases are shown in the right above each spectrum. The prominent emission lines are also labelled. It is clear from the figure that both the Balmer lines and HeII 4686 Å lines are double-peaked at certain orbital phases, however, this is more pronounced at phase 0.9. HeI 4471 Å shows similar behaviour to that of the Balmer and HeII 4686 Å emission lines. Even though the flux presented is relative, it is clear from the figure that the strength of the emission lines increases from phase 0.1, when the binary system is out of eclipse, and reaches a maximum at phase 0.3, with the emission lines becoming more single-peaked. This is followed by a steady decline from phase 0.4 to 0.6. The line profiles remains flat between phase 0.5 and 0.6, probably due to partial eclipse of the emitting region by the accretion stream. A slight increase is seen at phase 0.7 followed by a decline leading to the primary eclipse after phase 0.9, with the emission lines changing from single-peaked (phase 0.6–0.8) to double-peaked profiles (phase 0.9). The slight-increase at phase 0.7 is explained as a result cyclotron emission from the main-accretion region which becomes visible from phase 0.65. The variation in line profiles were first noted in the phase-binned spectra presented by Allen et al. (1989) and can be explained in terms of the geometry of UZ For proposed by Ferrario et al. (1989) and shown in Figure 1.26. It is clear from Figure 3.8 that the blue-shifted peak of the double peak is

the strongest of the two peaks in most phases whereas the red-shifted component is only dominant between phase 0.2 and 0.3.

3.6 Standard and inside-out Doppler tomography

As already mentioned in Section 1.8.3 (and shown in Figure 1.27), the first Doppler map and trailed spectra of UZ For was presented in Figure 3 of Schwope et al. (1999) and subsequently reproduced in Figure 7 of Schwope (2001) and Figure 11.13 of Marsh & Schwope (2016) and were constructed using the HeII 4686 Å emission line. The trailed spectra from these authors showed the presence of "several line components displaying pronounced radial velocity and intensity variations" similar to those seen for HU Aqr (Schwope et al. 1997a). These components were associated with emission from the donor star, ballistic and magnetic confined stream (see Section 1.8.3). The Doppler map of UZ For show emission from the irradiated face of the secondary star, the ballistic and a cometary tail-like feature associated with the magnetically confined accretion stream. These features were identified by overlaying models with different mass ratios, inclinations, ballistic and magnetically confined stream trajectories to the Doppler map of UZ For. However, these features were difficult to differentiate from the Doppler map prior to the radial velocities studies of HU Aqr conducted by Schwope (1995) and the successful maps of the same system presented in Schwope et al. (1997a).

Preliminary Doppler tomography results of UZ For, based on the observations reported in this chapter, were presented in Figure 3 of Potter et al. (2015) and Figure 3 of Khangale et al. (2019a) as conference proceedings. In these articles, only the Doppler map of HeII 4686 Å were presented, similar to the study of Schwope et al. (1999). This chapter extends the scope of the Doppler maps of the strongest emission lines, to the red part of the spectrum utilizing the Doppler tomography code* described in Kotze et al. (2015; 2016) as part of the PhD† study of Kotze (2017), to include the Balmer lines in the blue and CaII lines in the red. This Doppler tomography code is freely available (i.e. open source) and can be used with minor modifications where necessary as in this thesis. As already mentioned in Section 3.1.2, this code has already been used in several AM Her systems (see e.g. Littlefield et al. 2018a, Gabdeev et al. 2019, Littlefield et al. 2020). However none of these studies employed the full extent of this code but rather they focused on producing either the inside-out maps or both the standard and the inside-out maps. This is because when dealing with the standard Doppler tomography, the maps that are produced are sometimes difficult to interpret and this code, with its ability to project various emission components on different parts of the tomograms, makes it complementary to understanding these systems. The only time where the both the inside-out maps and flux modulation amplitude maps based on this code were presented was by Kotze et al. (2016) and Kotze (2017). The former, Kotze et al. (2016), reanalysed the high-state observations of HU Aqr, V834 Cen and PQ Gem.

*See http://www.saao.ac.za/~ejk/doptomog/main.html for more details.
†See https://open.uct.ac.za/handle/11427/25356 for more details.

While in the latter, Kotze (2017), in addition to these three systems, the results from the CTCV J1928−5001 while in an intermediate high-state were presented. In this thesis I have explored the full capabilities of this code as will be seen later on in this section (Section 3.6) and Section 3.7. The Doppler maps and trailed spectra produced in this thesis are shown in Figures 3.9 to 3.11 and were normalized by the maximum flux of the input spectra for each spectrum. Note that the inside-out map is computed independently of the standard map, however, the maximum velocity at the centre of the inside-out maps is set to the maximum velocity from the standard maps.

The model overlay has the WD mass, $M_1 = 0.71\ M_\odot$, mass ratio ($q = \frac{M_2}{M_1}$) of 0.2 and inclination, $i = 81°$ has been overplotted to aid with their interpretation of the tomograms (Bailey & Cropper 1991). The Doppler maps are centred on the rest frame of the binary. In the standard projection Doppler maps, the binary's centre of mass is marked with a plus (+) sign. The plus sign is also the centre of the map. In the inside-out projection Doppler maps, the centre of mass of the binary is the zero velocity outer circumference of the map. The centre of mass of both the primary and secondary are marked with a cross (×) in all the Doppler maps, i.e. in both the standard and inside-out projections. The Roche lobe of the WD is shown with a dashed line whereas that of the secondary is shown with a solid line in both the standard and inside-out Doppler maps. The ballistic stream is marked with a single-particle trajectory (solid black line) from L_1 up to 45° in azimuth around the primary. The magnetic dipole trajectories are marked with thin dotted blue lines and are calculated at 10° intervals in azimuth from 15° up to 45° around the primary. The magnetic axis azimuth (ψ) of 30° and magnetic co-latitude (β) of 20° were used. The colour-bars in all figures, to the right of the tomograms, show the scale with which the Doppler maps and trailed spectra were produced.

3.6.1 Observed and reconstructed trailed spectra

Before proceeding, it is important to define an observed and reconstructed trailed spectra since these are widely used in this chapter and thesis. An observed trailed spectra is a two-dimensional intensity map of the observed flux density of an emission or absorption profile as a function of radial velocity (or wavelength) and orbital phase. On the other hand, a reconstructed trailed spectra is a two-dimensional intensity map of the observed flux as a function of radial velocity (or wavelength) and orbital phase reconstructed by summing up the S-wave components from all pixels in the Doppler tomogram. The reconstructed trailed spectra is used to check the validity of the Doppler tomography technique, that is, the reconstructed trailed spectra needs to look very similar to the observed trailed spectra in order to give confidence that the technique has worked properly.

The middle row of Figures 3.9 to 3.11 show the observed (centre) and reconstructed trailed spectra, based on the standard (left) and inside-out (right) projections, from the Hβ, HeII 4686 Å and CaII 8542 Å emission lines, respectively. The bottom row of these figures show the trailed absolute residuals spectra for the standard (left) and inside-out (right) projection, calculated as the difference between the observed minus reconstructed

trailed spectra. The observed trailed spectra of Hβ and HeII 4686 Å emission lines are similar to each other and show the presence of three distinct emission components. The first is a relatively narrow component (red colour) which has a low-velocity amplitude and is understood to be associated with the accretion stream – vicinity of the threading region. The narrow component has a maximum blue-shift at phase 0.5 and maximum red-shift at phase 0.95 and crosses the zero-velocity from red to blue and blue to red at phases 0.3 and 0.8, respectively. This component is brightest from phase ∼0.2 to 0.5 and again from phase ∼0.55 to 0.75 for the Hβ line. The narrow component is seen in most orbital phases in the case of HeII 4686 Å line and is brightest at phases 0.15 to 0.5, 0.55 to 0.75 and 0.85 to 1.0. There is little evidence that this component is seen at phases below 0.15 and this might not be associated with the rest of the narrow component – implying two bright-spot regions. We attribute the absence of the narrow component at phases 0.5 to 0.55 to partial or total obscuration by either the WD, the stream itself or the magnetically confined accretion stream. In addition, at this orbital phase we are looking directly into the incoming accretion stream which now is aligned with the line of sight of the observer and this region now lies between the red dwarf and the WD. The narrow component also suffers from partial obscuration by the accretion stream as it leaves the orbital plane at phase 0.75 to 0.85 and this is normally seen as an absorption dip in X-ray and optical/infrared light curves of these systems. The second is a broad component (blue colour) which has a mid-velocity amplitude and crosses zero-velocity from red to blue around phase 0.3 and then from blue to red at phases around 0.8. This component has a maximum red-shift at phase 0.95 and a maximum blue-shift at phase 0.5 and appears to consist of two peaks at certain orbital phases (see Section 3.5.2). In short, this component switches from double-peaked to single-peaked at phase ∼0.3 and from single-peaked to double-peaked at phase ∼0.5 and back to single-peaked after phase 0.8. However the resolution of the observations does not allow for further resolving these two components. The third component is a relatively broad feature (yellow colour) which is visible throughout the orbital phase has a maximum blue-shift around phase 0.4–0.5 and a maximum red-shift at phase 0.85. The two broad components (blue and yellow) are associated with emission produced in different parts of the accretion flow such as the ballistic and magnetically confined accretion stream as well as the emission from the irradiated side of the secondary star. As already mentioned above, the trailed of Hβ and HeII 4686 Å emission lines are similar except for the narrow-component which is more pronounced in the latter.

The observed trailed spectra from the CaII 8542 Å line shows the presence of at least two emission components. The first is a narrow component (blue and red colour) which has a mid-velocity amplitude and is understood to be associated with the emission from the irradiated face of the secondary star. Therefore, CaII lines are tracers of the motion of the secondary star. This component is prominent from phase ∼0.3–0.7 and possibly at phases leading to the primary eclipse. The second is a broad component (yellow) which is seen throughout the coverage of the trailed spectra. The broad component is associated with the emission produced in various parts of the accretion flow. The trailed spectra of CaII 8542 Å

emission line is simple compared to those of Hβ and HeII 4686 Å emission lines. However, the spectra taken in the red wavelengths did not cover the whole orbital phase of the binary, so any conclusions arrived here may not be robust.

The reconstructed trailed spectra of Hβ and HeII 4686 Å emission lines, based on both the standard and inside-out projections, reproduce the basic structure of the observed trailed spectra. The low-velocity component (red colour) is absent in both the reconstructed trailed spectra. The observed flux distribution is not reproduced in all the reconstructed trailed spectra. However, the reconstructed trailed spectra based on the inside-out method does show traces of the narrow component at phases 0.3 and 0.8, respectively. The trailed absolute residuals spectra of these two lines show that some residual structures remain when subtracting the reconstructed trailed spectra from the observed trailed spectra. However, there was no significant difference between residuals spectra of the two methods used. The residuals of the Hβ line has a root mean square (rms) value of 0.223 and 0.221 in normalized flux for the standard and inside-out projections, respectively. Similarly, the residuals of HeII 4686Å emission line has an rms value of 0.205 and 0.187 in normalized flux for the standard and inside-out projections, respectively. The rms values of Hβ and HeII 4686Å lines imply that the inside-out projections method reproduce the input spectra well compared to the standard projection. It is worth mentioning that Kotze et al. (2015; 2016) arrived at the same conclusion when comparing the standard and inside-out residuals spectra of HU Aqr, V834 Cen, etc.

The reconstructed trailed spectra of the CaII 8542 Å line based on both the standard and inside-out projection reproduce the basic structure of the observed trailed spectra. However, the mid-velocity component (red and blue) is absent in both the reconstructed trailed spectra. As with the Hβ and HeII 4686 Å emission lines, the observed flux distribution is not reproduced in both the reconstructed trailed spectra. Both the reconstructed trailed spectra seems to be introducing additional features and this is due to the partial coverage of the orbit. The mismatch between the observed and reconstructed trailed spectra serves a measure of reliability of the Doppler maps and in this case the results should be explained with extreme care. The trailed absolute residuals spectra of CaII 8542 Å show that significant residual structures remain, especially in the trailed absolute spectra based on the standard projection. The residuals has an rms value of 0.366 and 0.328 in normalized flux for the standard and inside-out projections, respectively. As with the Hβ and HeII 4686 Å emission lines, the rms value of CaII 8542 Å suggest that the inside-out projection reproduce the observed spectra better than the standard projection. It is worth mentioning that the flux of the emission lines of AM Her systems, especially eclipsing systems, vary significantly over the orbital period of which the normal Doppler tomography technique is not designed to model. This is addressed in Section 3.7.

3.6.2 Standard and inside-out tomograms

The top row of Figures 3.9 to 3.11 show the standard (left) and inside-out (right) Doppler tomogram of the Hβ, HeII 4686 Å and CaII 8542 Å emission lines. The tomograms of other

Balmer lines (Hγ and Hδ) are similar to those of the Hβ line whereas the tomograms of other HeII (and HeI) line(s) are similar to those of HeII 4686 Å line. Similarly, the tomograms of CaII 8498 Å line are similar to those of CaII 8542 Å line. The tomograms of these three emission lines are discussed in detail below starting with the standard Doppler maps.

Standard tomograms:

The standard tomograms of Hβ and HeII 4686 Å emission lines are very similar and show a "blob-like" feature of blended emission concentrated in the top left region (second quadrant*) of the Doppler map and stretching into the bottom left region (third quadrant) of the tomogram. The blended emission is asymmetrical and compacted. The bulk of the emission (red colour) originates from the vicinity of the ballistic stream and the threading region, and is centred at velocities of (∼500 km/s, 160°). This is further indicated by the overlaid Doppler model with the ballistic stream and threading region (vicinity of the dipole connections) intersecting the bulk of the emission shown in red and blue colours. Some of the emission in this region originates from the low-velocity material of the magnetically confined accretion flow as the ballistic stream is redirected to move along the field lines. There is evidence of emission forming a curtain-like structure associated with emission from the magnetically confined accretion stream in the bottom left region (third quadrant) of the tomograms. Due to the complexity of the tomogram, there is little to no evidence of emission from the vicinity of the secondary star. This is because the emission from the threading region and the ballistic stream dominates the tomogram – the other components such as the secondary star are blurred out. In addition to this, the ballistic stream and the threading region are blended together in the Doppler map since they are projected into fewer pixels in velocity space. This is the main issue with the standard projection – the low-velocity components are projected onto fewer pixels and the high-velocity components are projected onto many pixels.

Comparison between the Doppler map of HeII 4686 Å emission line presented in this thesis and that presented in Figure 3 of Schwope et al. (1999) (and Figure 7 of Schwope (2001)) reveal that two maps are slightly different. The main difference between the two maps is the absence of strong emission from the irradiated face of secondary star in our tomograms which is present and strong in the Doppler map from Schwope et al. (1999). As already mentioned in Section 3.5, UZ For was observed while in a higher state of accretion whereas the observations of Schwope et al. (1999) were taken during a low state. Therefore, these maps are highlighting the different states of mass transfer from the red dwarf to the WD. According to (Bailey 1995), the ballistic and magnetically confined accretion stream contribute over 50% of the entire emission in UZ For during the high state and therefore dominating emission from the secondary star. Furthermore, Kube et al. (1999) had noted that UZ For shows a bright threading region from the modelling of the ultraviolet observations obtained

*The two perpendicular bisectors divide the Doppler map into four quadrants. Here the first quadrant is between 0° and 90°, and the second quadrant is between 90° and 180°, the third quadrant is between 180° and 270° and fourth quadrant is between 270° and 360°.

during the high state and presented by Stockman & Schmidt (1996).

The standard Doppler tomogram of CaII 8542 Å emission line appears different from that of Hβ and HeII 4686 Å emission lines in the sense that its map is dominated by emission from the irradiated face of the secondary star as opposed to the threading region and the ballistic stream seen in the tomograms of the Hβ and HeII 4686 Å emission lines. This is supported by the bulk of the emission in red and blue overlaid in the vicinity of the Roche lobe of the secondary star. As already mentioned in Section 3.6.1, CaII 8542 Å line is a good tracer of the motion of the secondary star. There is little to no evidence of emission from the ballistic and magnetically confined accretion stream in the top left and bottom left regions of the standard tomogram. This may be due in part to the data coverage with phases between 0.2–0.3 and 0.7–0.8 not covered by our observations. The other low-level emission seen in the Doppler map are due to additional features added by the Doppler tomography code and are mostly seen in the reconstructed trailed spectra based on the standard projection.

Inside-out tomograms

The inside-out Doppler tomograms of Hβ and HeII 4686 Å emission lines are similar to each other and reveal the presence of emission from three distinct regions: 1) the irradiated face of the secondary star, 2) the ballistic stream and the threading region, and 3) the magnetically confined accretion stream. The emission from the secondary star is seen as a diffuse feature overlaid in yellow and covering the Roche lobe at (250 km/s, 90°). This is due to that in the inside-out projection, the emission from the secondary is projected onto many pixels than in the standard projection. Note that the secondary star is orientated upside down in the inside-out tomograms because it orbits as a solid body and the side of the secondary furthest to the binary's centre of mass moves faster than the side closest to the binary's centre of mass. The ballistic stream is a "faint arc of emission" overlaid in yellow and is traced by a single-particle trajectory (solid black line) from L_1 (Roche lobe of the secondary star) up to 45° in azimuth. The stream starts faint (yellow) from L_1 and increases in brightness to the maximum at ($\geq$300 km/s, 145°) as shown by an extended feature overlaid in blue and red which extends up to ($\geq$600 km/s, 170°) at the vicinity of the threading region. The faint part of the ballistic stream is more pronounced in the inside-out tomograms of the Hβ line. This is because the photoionization and recombination of the Balmer lines occur at lower temperatures than that required to excite HeII (4686 Å) line, that is, the Balmer lines are easily excited in the ballistic stream than HeII lines. Other possible explanation for faint ballistic stream is that this result from increased mass transfer from the secondary star resulting in the increase in the density in the partially ionized gas and therefore the stream becoming optically thick to singly ionized helium which is emitted and re-absorbed in the stream or perhaps the stream is made of blobs-like materials and there is less ionization.

The vicinity of the threading region, indicated in red and blue colour and centred at (500 km/s, 155°), dominates the emission in the inside-out Doppler maps of both the Hβ and HeII 4686 Å emission lines. The reason we see strong emission from the threading region in the Doppler tomograms of these two lines is due to the increased mass transfer

from the secondary star to the WD. Such high mass transfer rate will result in a strong shock being formed at the vicinity of the threading region as the ballistic stream impacts the magnetosphere of the WD. The shock further ionizes the already partially ionized gas of all sizes (ranging from fine grains to huge blobs) in the threading region, heating it up to high temperatures due to increased collision within the gas and magnetic heating, etc, and emitting strong radiation in a wide range of wavelengths including optical. The threading region appears more extended in the Hβ line but a close inspection shows that this region is brighter in HeII 4686 Å line. The ionized gas is threaded further by the field lines and the surviving materials couples onto the field lines and is deflected to move perpendicularly to the motion of the binary along the magnetic field lines. This motion is indicated by the red dotted lines in the inside-out Doppler tomograms.

The various parts of the magnetically confined accretion stream is evident for both the Hβ and HeII 4686 Å lines starting in the upper left region and stretching to the lower left region of the tomograms (500–1500 km/s, 180–270°) as the materials are forced to move along the field lines, resulting in the formation of an accretion curtain, before being funnelled close to the magnetic poles of the WD. The curtain-like feature is evident in the third quadrant (180–270°) with diffuse-level of emission in the inside-out tomograms of both lines. The funnelling of materials onto the WD is evident at (1000–1500 km/s, ∼225°) and is clear in the inside-out Doppler tomogram of the Hβ line with concentrated emission shown in blue colour falling towards the WD. The high-velocity component of the magnetically confined accretion stream is less pronounced in the HeII 4686 Å line than in the Hβ line. This is due to that the Balmer lines have the ability to ionizes the gas upstream as it falls towards the WD. The tomograms of Hβ and HeII 4686Å appear different and this is expected because these two lines have different excitation levels as already mentioned in Section 3.5.

The inside-out Doppler tomogram of CaII 8542 Å emission line are different from those of Hβ and HeII 4686 Å emission lines. This is expected since CaII lines originates solely from the irradiated face of the secondary star. The tomogram of CaII 8542 Å reveals the presence of emission from two distinct regions, namely: the irradiated face of the secondary star and part of the ballistic stream around the threading region. The irradiated face of the secondary star dominates the emission in the inside-out Doppler tomogram of CaII 8542 Å. There is no evidence of emission from the magnetically confined accretion stream in the top and bottom left regions of the inside-out tomogram.

This section presented the average Doppler maps based on standard Doppler tomography techniques using both the standard and inside-out projections. Overall, the various emission components contained in emission lines are more clearly distinguished in the inside-out tomogram than in the standard Doppler tomogram especially the high-velocity magnetically confined accretion stream. The maps of UZ For demonstrate the clear distinction between the tomograms based on the emission lines in the blue and red wavelengths.

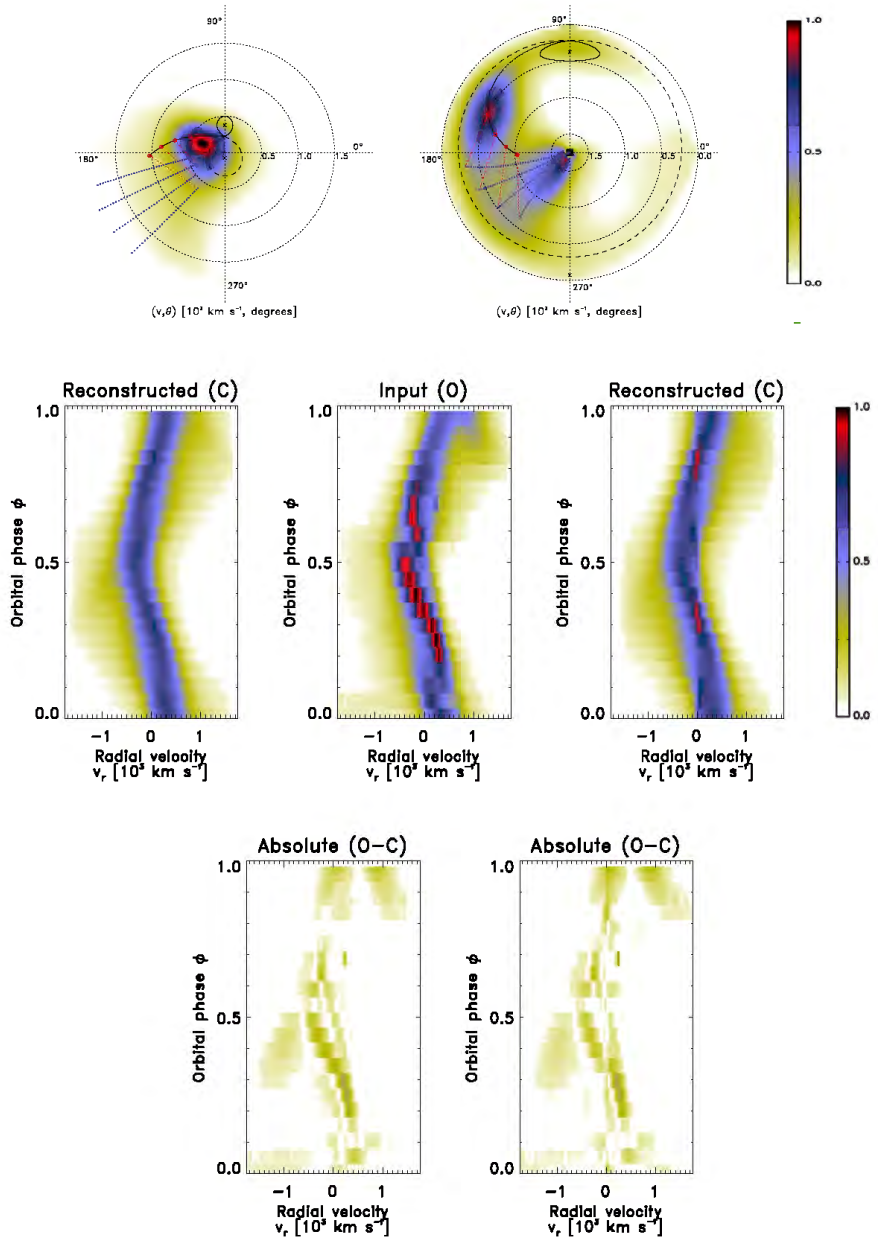

Figure 3.9: Standard and inside-out Doppler maps and trailed observed and reconstructed spectra of UZ For using the Hβ line. Top row: the average standard (left) and inside-out (right) Doppler tomograms. Second row: the input trailed spectra (centre) with the reconstructed trailed spectra for the standard (left) and inside-out (right) tomograms, respectively. The bottom row shows the corresponding trailed residual spectra.

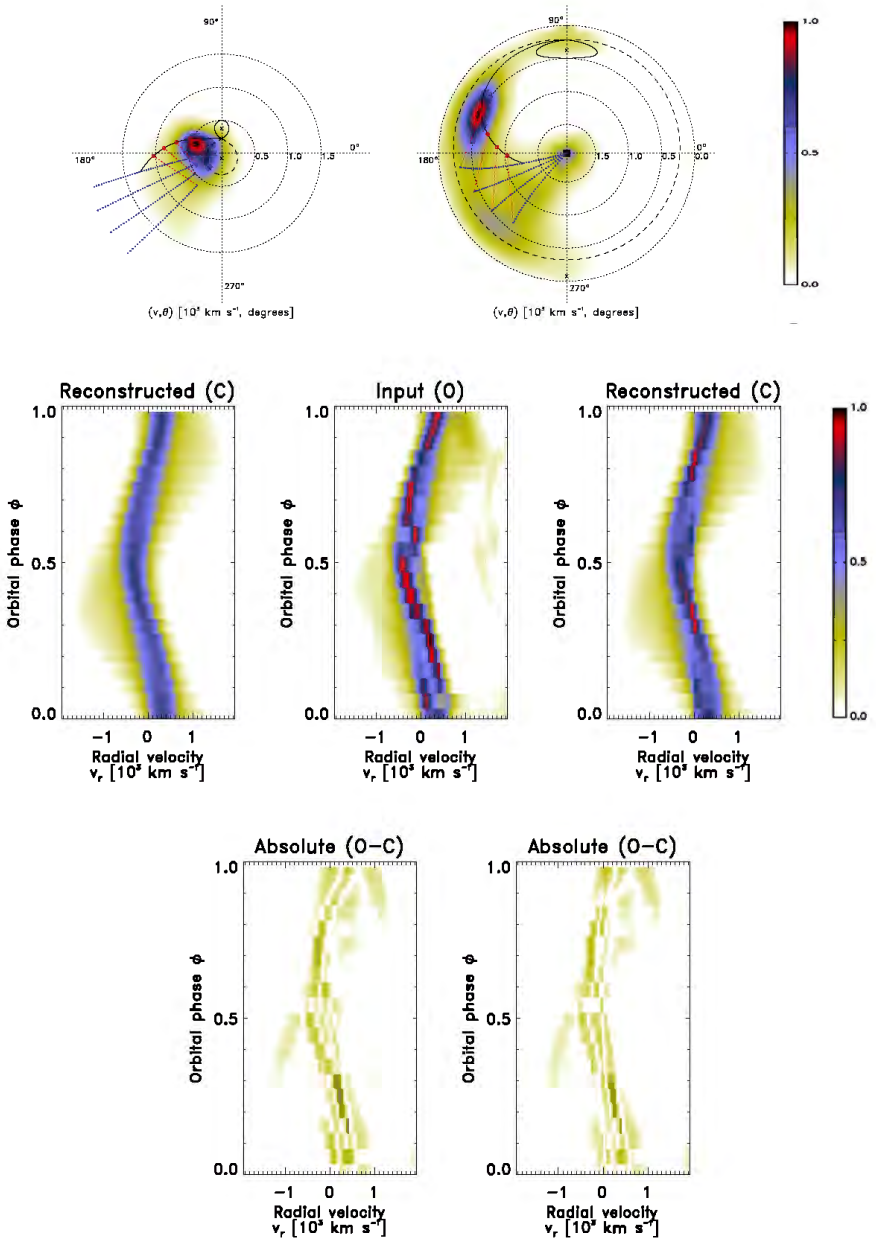

Figure 3.10: Same as Figure 3.9, but using the HeII 4686 Å line.

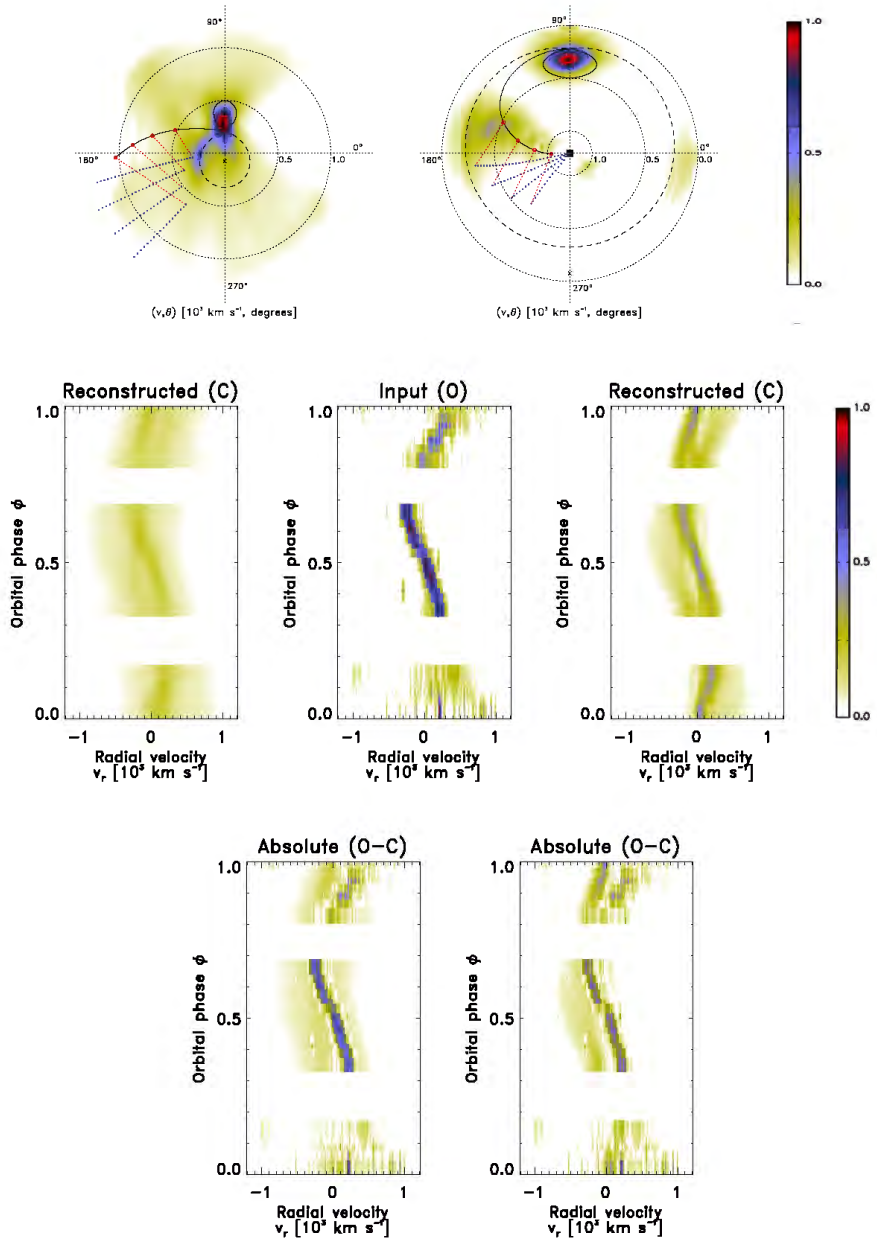

Figure 3.11: Same as Figure 3.9, but using CaII 8542 Å line.

3.7 Flux modulation mapping

This section presents Doppler maps based on the flux modulation mapping technique described in Kotze et al. (2016) and Kotze (2017) and reviewed in Section 3.1.3. The modulation mapping technique produces Doppler maps that represent the average, amplitude and phase of the modulated emission. This is achieved by extracting any phased modulation in the observed flux from a series of consecutive half-phase tomograms. The maps presented here and shown in Figures 3.12 to 3.14 are based on ten consecutive half-phases (i.e. 0.0–0.5, 0.1–0.6, ..., 0.7–0.2,..., etc) of the Hβ, HeII 4686 Å and CaII 8542 Å emission lines shown in Appendix A (Figures A.1 to A.30). The reconstructed trailed spectra as well as the trailed absolute residuals spectra based on this method are also presented for each emission line. The results from this method are discussed in the next sections (i.e. Sections 3.7.1 to 3.7.3).

3.7.1 Reconstructed trailed spectra

The third row of Figures 3.12 to 3.14 show the observed (centre) and flux modulation reconstructed trailed spectra based on the standard (left) and inside-out (right) projections for the Hβ, HeII 4686 Å and CaII 8542 Å emission lines. The observed trailed trailed spectra for each line has already been discussed in Section 3.6.1, the discussion here will only focus on the reconstructed trailed spectra. It is clear from the figures that the reconstructed trailed spectra based on the flux modulation mapping reproduces the basic structure of observed trailed spectra. Similar to the standard Doppler tomography techniques discussed in Section 3.6, the low-velocity (red colour) is not reproduced in the reconstructed trailed spectra based on flux modulation mapping. Therefore, the observed flux distribution is not reproduced in the reconstructed trailed spectra of these lines. However, the reconstructed trailed spectra of the Hβ and HeII 4686 Å emission lines do show traces of the low-velocity component at phases 0.3 to 0.5. Comparisons between the two reconstructed trailed spectra for each line reveals that the reconstructed trailed spectra based on the inside-out projection reproduce the observed trailed spectra better compared to the one based on the standard projection. This is evident in the reproduced flux distribution which is more pronounced in the reconstructed trailed spectra based on inside-out projection. In addition, the low-velocity component is more pronounced in the trailed reconstructed spectra based on the inside-out projection.

The bottom row of Figures 3.12 to 3.14 show the trailed absolute residuals spectra of the Hβ, HeII 4686 Å and CaII 8542 Å emission lines based on the standard (left) and inside-out(right) projections. The residuals spectra show that some structure still remains after subtracting the reconstructed spectra from the observed spectra. However, there is no clear discernible features between the trailed absolute spectra of the Hβ, HeII 4686 Å and CaII 8542 Å lines based on flux modulation mapping and those presented in Section 3.6.1. The only significant improvement is seen in the rms values obtained from flux modulation mapping. For example, the flux modulation residual spectra of the Hβ line gave the rms values of 0.155 and 0.161 for both the standard and inside-out projections, respectively.

This is a significant improvement compared to the rms values of 0.223 and 0.221 obtained for the same line reported in Section 3.6.1. The others lines showed similar improvements in the rms values (and results), that is, HeII 4686 Å gave the rms values of 0.185 and 0.168 whereas CaII 8542 Å gave the rms values of 0.280 and 0.239 for the standard and inside-out projections, respectively. The improvement is due to that in standard Doppler tomography techniques, of Marsh & Horne (1988), the flux from each point in the frame of rotation of the binary is assumed to be constant. But this is not the case for eclipsing and high-inclination CVs, that is, the flux from the typical emission features modulate with the orbital phase and this information is lost when spectral features are mapped in Doppler tomography. These variations can now be recovered with modulation mapping.

3.7.2 Flux modulation amplitude maps

The top row of Figures 3.12 to 3.14 show the standard (left) and inside-out (right) flux-modulated amplitude Doppler maps for the Hβ, HeII 4686 Å and CaII 8542 Å emission lines.

Standard modulation amplitude maps

The standard projection flux modulation amplitude maps of the Hβ and HeII 4686 Å emission lines show that the following components are modulated with the orbital phase: the irradiated face of the secondary star, the ballistic stream and the threading region, and the magnetically confined accretion stream. The ballistic stream and the threading region are the most flux-modulated components in the case of the Hβ line whereas the irradiated face of the secondary star is the most flux-modulated component in the case of HeII 4686 Å line. These modulation are shown by the red and blue colours overlaid in the vicinity of the threading region (for the Hβ line) and the Roche lobe of the secondary star (for the HeII 4686 Å line). The reason for seeing strong modulation from different components for the Hβ and HeII 4686 Å lines suggest that these two lines are emitted from different regions and also the fact that they are excited at different temperatures. For the Hβ line, the Roche lobe of the secondary star is overlaid with the mixture of blue and yellow colours, however, the blue colour might just be an extension of the modulation of the ballistic stream at it leaves the L_1 point. The strong modulation of the ballistic and threading region makes it difficult to detect the modulation from the irradiated secondary star due to the compactness of the tomogram. The vicinity of the ballistic stream and the threading region in the modulation map of the HeII 4686 Å line is overlaid with yellow colour with little to no evidence of blue colour. Therefore, the ballistic stream in the HeII 4686 Å line shows low-level of modulation and this is attributed to that this line suffers less absorption compared to the Balmer lines.

Both the Hβ and HeII 4686 Å emission lines show flux modulation from the magnetically confined accretion stream and what used to be one feature in the lower left region of the standard map is now split into two components: a low-velocity component associated with the accretion curtain when the ballistic stream is coupled to the magnetic field lines and

the high-velocity component, also associated with the accretion curtain, which traces the trajectory of the magnetic stream as it falls towards the accretion region on the surface of the WD. Kotze et al. (2016) has shown that it is possible for the inside-out projection to separate the low- and high-velocity parts of the magnetically confined accretion stream since emission is re-binned in a larger area with more pixels. In our case this is seen in the standard tomograms in addition to the inside-out tomograms (see the discussion below). The modulation mapping has made it possible to distinguish between these two components (i.e. the low- and high-velocity components) as the stream leaves the orbital plane and also when it accelerates towards the surface of the WD. This will be discussed in Section 3.7.3.

The standard flux modulation maps of the CaII 8542 Å emission line shows modulation from the irradiated face of the secondary star (i.e. the most flux-modulated component) and the vicinity of the threading region in the ballistic stream. The modulation from the secondary star is expected since the irradiated side moves in and out of view depending on the orbital phase. CaII 8542 Å shows little to no evidence of modulation from the magnetically confined accretion stream largely due to the coverage of the observations.

Inside-out modulation amplitude maps

The flux modulation amplitude maps of Hβ and HeII 4686 Å lines based on the inside-out projection show modulation from the same components as those of the standard modulation maps, namely: the irradiated face of the secondary star, the ballistic stream and the threading region, and the magnetically confined accretion stream. However the strong modulation mentioned above for the standard projection (blue and red colours) is replaced by the blue colour in the inside-out modulation maps. The reason being that in the inside-out projection, the various emission components contained in the trailed spectra are projected in different parts of the tomogram (see e.g. Kotze et al. 2015; 2016). In addition, the low-velocity emission which is projected onto fewer pixels in the standard tomogram is re-binned onto many pixels whereas the high-velocity which is projected onto many pixels in the standard map is now re-binned into fewer pixels. The inside-out flux modulation map of the Hβ line shows that the vicinity of the threading region in the ballistic stream and magnetically confined accretion stream are the most flux-modulated components. On the other hand, the flux modulation maps of the HeII 4686 Å line shows that the irradiated face of the secondary star and the magnetically confined accretion stream are the most flux-modulated components.

The flux modulation of the secondary star is more clear in the inside-out tomograms for both the Hβ and HeII 4686 lines and this is shown in yellow colour overlaid in the Roche lobe of the secondary star. What used to be strong modulation from the irradiated face of the secondary star in the standard tomogram of the for HeII 4686 Å line is now just moderate (yellow colour) flux modulation due to that in the inside-out projection, the emission from the secondary star is now projected onto an extended region. As already mentioned above, the flux modulation of the ballistic stream and the threading region is pronounced in the Hβ line and this is shown by the yellow and blue colours in these regions. On the other

hand, the tomograms of the HeII 4686 Å line show relatively low flux-modulation from the ballistic stream and the threading region.

The magnetically confined accretion stream shows strong and moderate flux modulation for Hβ and HeII 4686 Å emission lines, respectively. There is also evidence of funnelling as the gas falls towards the surface of the WD for both lines. However, the modulation of the magnetically confined accretion stream as well as the funnelling of the gas is more pronounced in the tomograms of the Hβ line. Similar to the standard flux modulation maps, the magnetically confined accretion stream is separated into two components (i.e. the low-velocity and high-velocity components) in the flux modulation maps of both lines. As already mentioned above, the low-velocity component is associated with the motion of the magnetic stream (or curtain) as it leaves the orbital plane and the high-velocity component of the magnetically confined accretion stream traces the motion of the gas when accelerating towards the WD. There is also evidence of strong modulation of materials with velocity exceeding 1500 km/s in both the standard and inside-out tomograms of the Hβ and HeII 4686 Å lines. But this is more clear in the inside-out maps and might be due to that the emission in the inside-out projection is projected onto fewer pixels and therefore tends to appear brighter. The inside-out flux modulation map of CaII 8542 Å line shows strong modulation from the irradiated face of the secondary star – which is expected due to changing viewing angles as seen by the observer with increasing orbital phase. There is also evidence of flux modulation from the vicinity of the threading region or ballistic stream.

Our results show modulation from the secondary star and various parts of the accretion flow. This is expected since UZ For is an high-inclination eclipsing system and the flux from the irradiated side of the secondary star, the ballistic and magnetically confined accretion stream will modulate over the orbital phase of the binary due to changing viewing angles. Overall, while the modulation of the ballistic and magnetically confined accretion stream are easily identified in the standard and inside-out flux modulation maps, the modulation of the secondary star is only clearly visible in the inside-out modulation maps.

3.7.3 Phase of maximum flux maps

The second row of Figures 3.12 to 3.14 show the standard (left) and inside-out (right) phase of maximum flux maps based on the Hβ, HeII 4686 Å and CaII 8542 Å emission lines. These maps show the orbital phase at which a specific emission component appears brightest to an observer. Here the pixels where the corresponding modulation amplitude is at least 10% of the maximum amplitude are displayed and they are colour-coded according to phase as follows: 0.0 – black, 0.25 – red, 0.5 – green and 0.75 – blue. The phase of maximum flux maps of UZ For are easily understood using the schematic of UZ For shown in Figure 3.15. This figure is based on an original schematic by Ferrario et al. (1989) (their Figure 8 and reproduced in Figure 1.26) which is constructed based on the polarization, eclipsing and radial velocity properties of this system. The new figure now presents geometries that are based on measurements made by the modeling and fitting of actual observations. Note that the polarization properties of Berriman & Smith (1988) and Bailey & Cropper (1991)

are reserved for Chapter 4 since it includes recent linear and circular polarization. The schematic consist of the scaled binary system based on the model overlaid in the Doppler maps (see Section 3.6) with the red dwarf (bloated star shown with red lines), the ballistic stream (orange line), the magnetic field lines (or curtain) and the WD (grey lines) towards the centre of the figure. Note that the size of the WD is exaggerated five times for display purpose. Also marked in the figure is the location of the accretion region with a red arc-like feature (not to scale) where the field lines connects with the WD surface. The model of the binary is that seen by the observer at phase 0.0 (viewed along the plane of the paper from the bottom) or 0.5 (viewed along the plane of the paper from the top). The orbital phases in the schematic increases counterclockwise and are also colour-coded in the similar manner as the phase of the maximum flux maps. The motion of the binary is clockwise around the center of mass. As already mentioned in Section 3.5, the orbital phases here were calculated with respect to the photometric ephemeris of Khangale et al. (2019b) and reproduced in Chapter 2 (Table 2.2).

The phase of maximum flux maps based on the standard and inside-out projections show that the irradiated face of the secondary star appear brightest to the observer around phase 0.5 for all three lines: the Hβ, HeII 4686 Å and CaII 8542 Å emission lines. This is indicated by the green colour covering the Roche lobe of the secondary star in all the phase of maximum flux maps of all the three lines under consideration. This is expected since phase zero of UZ For is defined as the time of mid-eclipse when the WD is eclipsed by the secondary star. Therefore, half of the orbital cycle later (i.e. at phase 0.5), the irradiated face of the secondary star is expected to be pointing towards the observer as shown in Figure 3.15. Thus the observer will have a full view of the illuminated side of the red dwarf – assuming that there is no significant obscuring from the ballistic stream and accretion curtain. It is expected that the trailing and leading side of the secondary would appear brightest to the observer at orbital phases 0.25 (red colour) and 0.75 (blue colour), respectively. However, there is little evidence for this in the phase of maximum flux tomograms of UZ For probably due to that only moderate emission was observed from the irradiated face of the secondary star in the flux modulation maps.

The ballistic stream appears brightest to the observer around phase 0.25 for both the Hβ and HeII 4686 Å lines. The ballistic stream is shown by the red colour tracing the single-trajectory of the stream leaving the secondary star to the threading region. This is due to that at phase 0.25, the observer has the full view of the irradiated inside facing side of the ballistic stream as shown in Figure 3.15. Also seen are green colours at lower- and higher-velocity parts of the ballistic stream. The green colour of the ballistic stream is associated with parts of the ballistic stream that are visible to the observer around phase 0.5 – when the stream is flowing towards the observer. As already mentioned in the previous section (Section 3.7.2), the ballistic stream is more pronounced in the case of the Hβ line. On the other hand, the ballistic stream in the case of HeII 4686 Å can be explained as due to that HeII 4686 Å line is formed in regions where there is high-level of ionization (e.g. threading and accretion region). In addition, HeII 4686 Å line shows a high-velocity component of the

ballistic stream (blue and black colours) visible to the observer from phase 0.75 to 1.0. The reason for this is that at phase 0.75, the observer has a full view of the leading outside facing side of the ballistic stream whereas around phase 0.0 the ballistic stream is flowing away from the observer. The CaII 8542 Å line shows a mismatch between the expected position of the ballistic stream modulation and red feature shown in the Figure 3.14. Therefore, the red feature that appears in both the standard and inside-out phase of maximum flux maps is not associated with the ballistic stream due to its position in the two maps. The vicinity of the threading region, where the ballistic stream first interacts with the magnetic field lines (after first dipole connection), is a mixture of red, blue and black colours which implies that this region is visible at phases 0.25, 0.75 and 1.0 to the observer and hence brightest around these phases. The absence of the threading region around phase 0.5 is expected since this region is eclipsed by the WD at this orbital phase. The threading region is mostly visible in the phase of maximum flux maps of the Hβ and CaII 8542 Å lines. There is little evidence that this feature is seen in the maps of HeII 4686 Å emission line.

The phase of maximum flux maps show that the magnetically confined accretion stream region is visible in the tomograms of Hβ and HeII 4686 Å emission lines as revealed earlier by the modulation amplitude maps. This region is divided into two components: the low-velocity and a high-velocity components. The low-velocity component is covered in green colour in the case of the Hβ line whereas the same feature is covered in red colour in the case of the HeII 4686 Å line. This suggest that parts of the magnetically confined accretion stream or accretion curtain are seen around phase 0.5 for the Hβ line where it appears brightest to the observer. For HeII 4686 Å line, this imply that this part of the magnetically confined accretion stream or accretion curtain is seen around phase 0.25 where it is brightest to the observer. The different phases arises due that that these two lines are produced in different parts of the accretion flow. The high-velocity component is covered in blue for both lines (i.e. Hβ and HeII 4686 Å) and this imply that this part of the magnetically confined accretion stream or curtain appear brightest to the observer at phase 0.75. This is expected since the larger area of the magnetically confined accretion stream is visible to the observer around this phase and therefore will appear brightest (see Figure 3.15). There is also evidence of emission from materials with velocity $>$1500 km/s in both the tomograms of the Hβ and HeII 4686 Å lines. Some of this emission is attributed to the high-velocity materials in the curtain, that is, the funnelling of materials onto the WD. There are also some artefacts that arises from the edge of the tomograms seen in the standard tomograms (e.g. red and green features in the tomograms of Hβ line). These features also appears in the centre of the inside-out amplitude maps and phase of maximum flux maps.

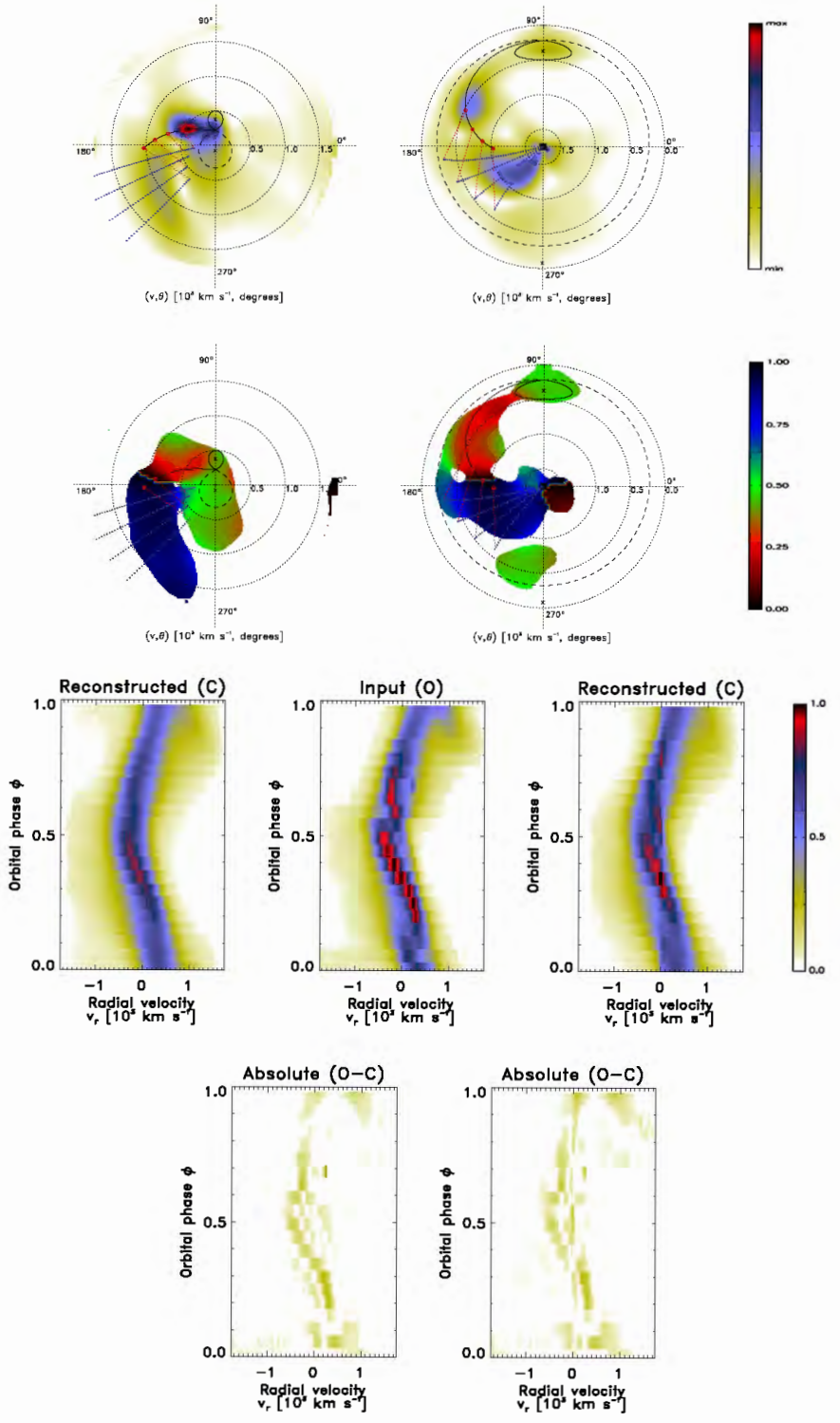

Figure 3.12: Standard and inside-out Doppler maps and trailed observed and reconstructed spectra of UZ For using the Hβ line. Top row: the standard and inside-out modulation amplitude flux Doppler maps. Second row: the standard and inside-out phase of maximum flux Doppler maps. Third row: the input trailed spectra (centre) with the summed reconstructed trailed spectra for the ten consecutive half-phases for standard (left) and inside-out (right), respectively. The bottom row shows the corresponding trailed summed absolute residual spectra.

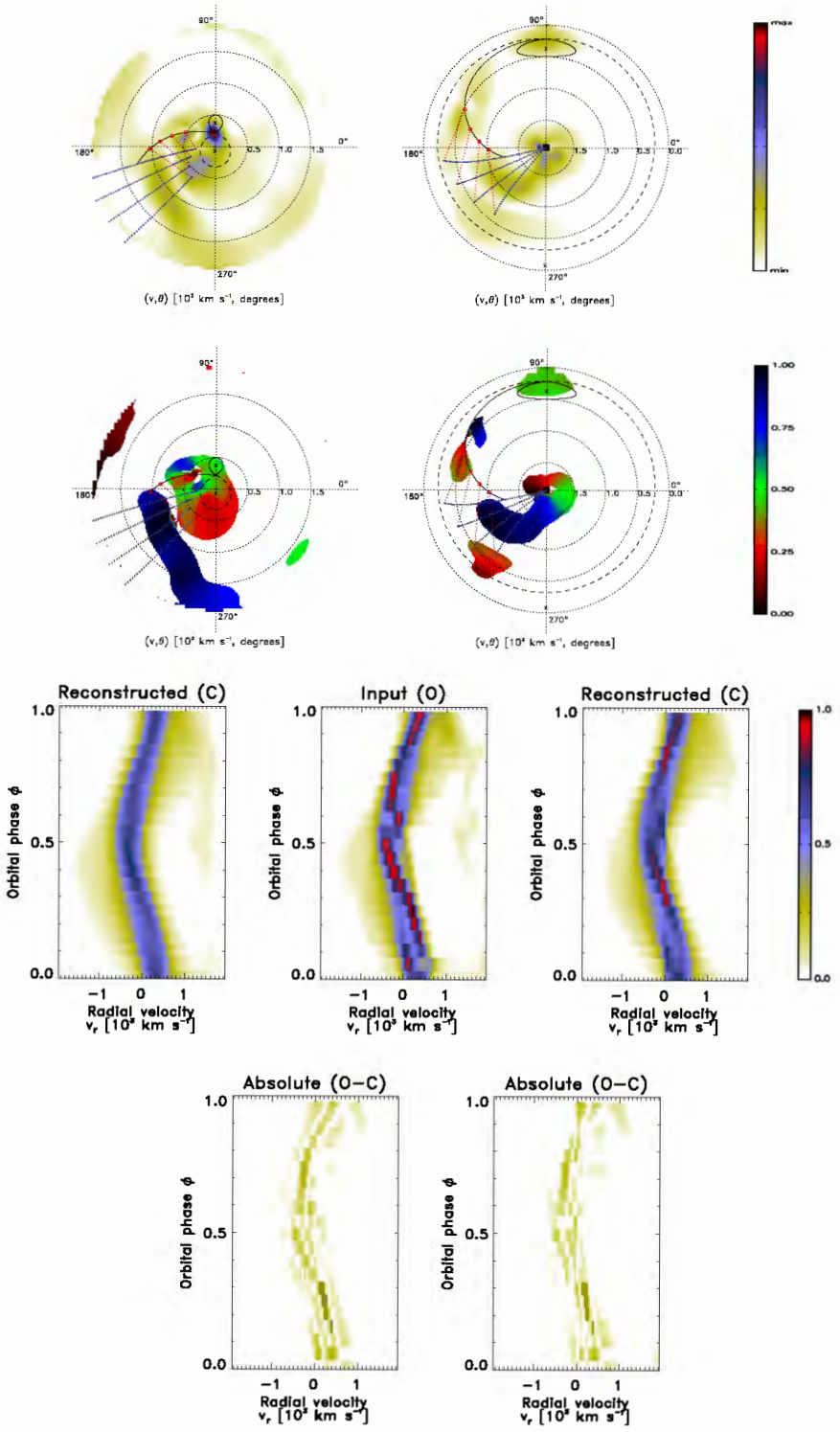

Figure 3.13: Same as Figure 3.12, but using the HeII 4686 Å emission line.

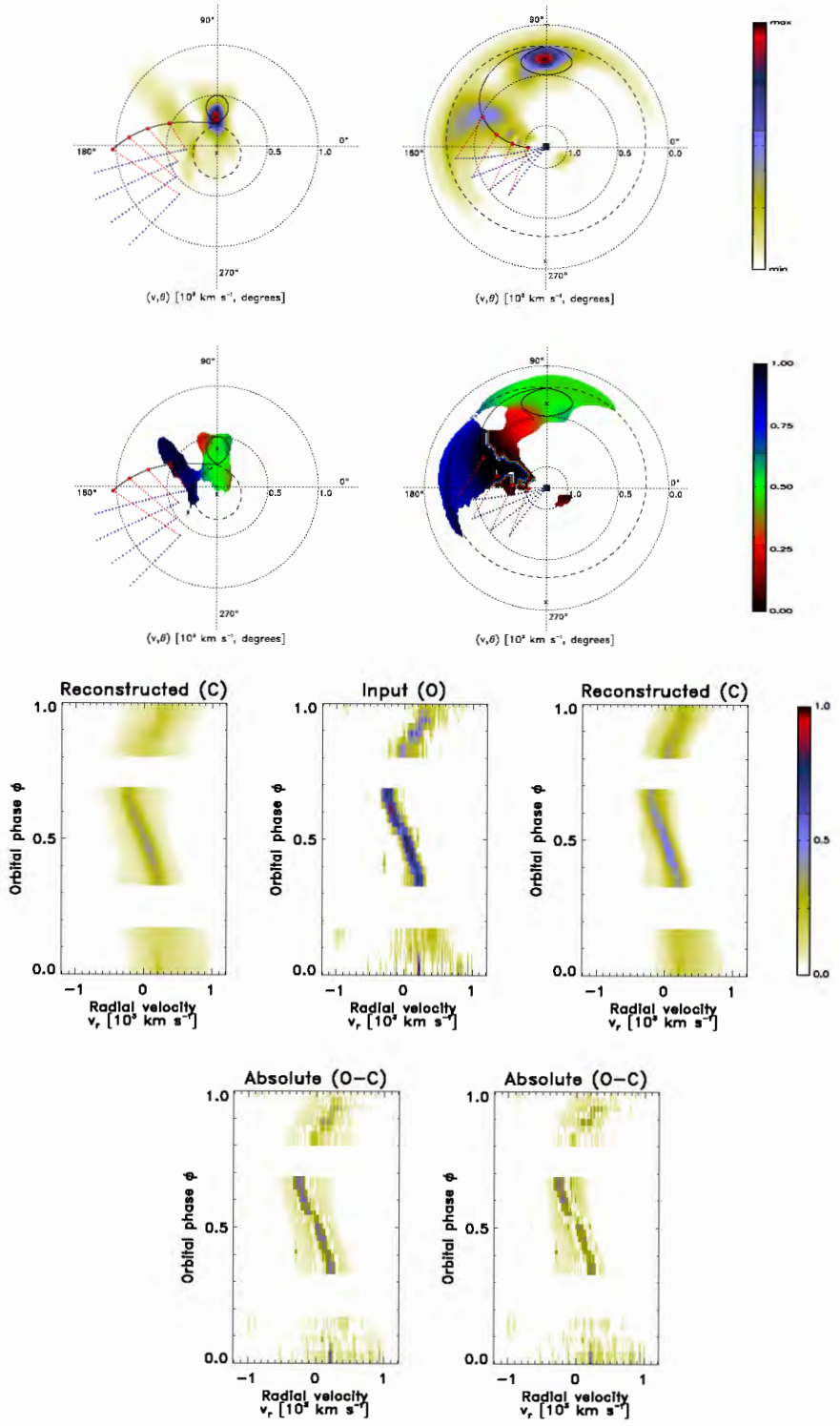

Figure 3.14: Same as Figure 3.12, but using the CaII 8542 Å emission line.

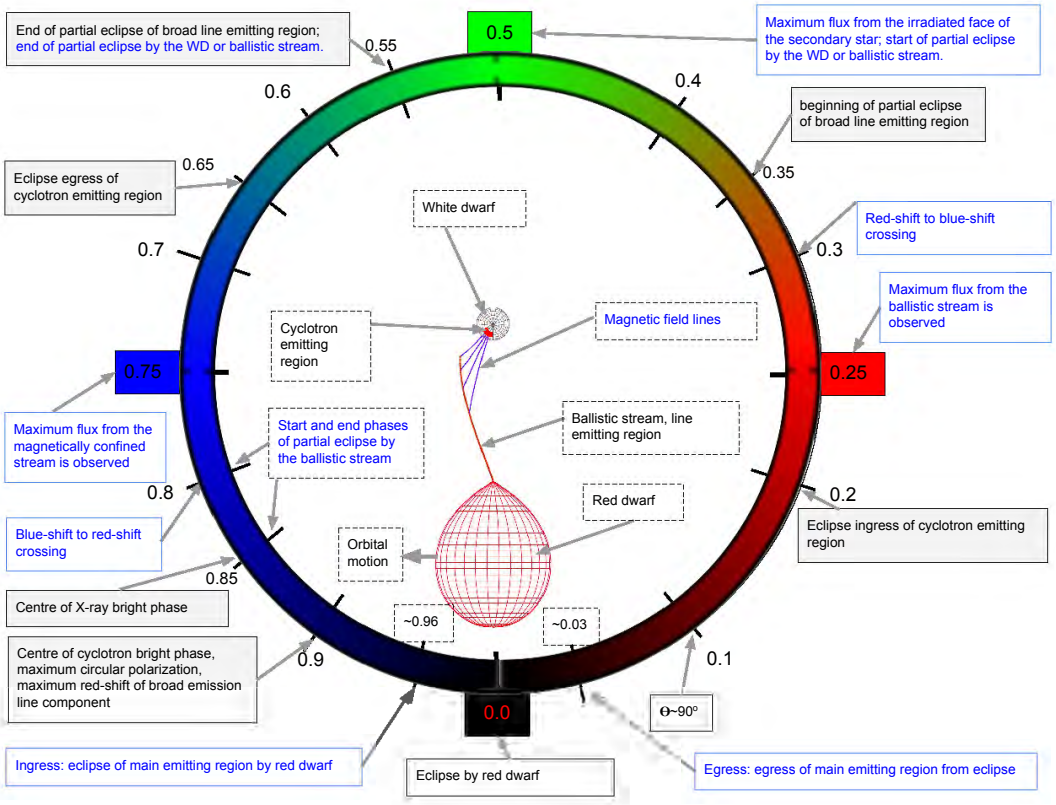

Figure 3.15: A schematic illustration of the model of the UZ For as viewed from the top. The four phase colours black, red, green and blue of the ring correspond to the phases of maximum flux 0.0, 0.25, 0.5 and 0.75 mentioned in Section 3.7.3. The system parameters are the same as in Section 3.6. The physical size and geometry of the red dwarf, ballistic stream and magnetic field lines are physically correct, except for radius of the WD which has been exaggerated to five times the calculated radius, and are based on the assumed system parameters. The physical size of the cyclotron emitting region is arbitrary. Different orbital phases has been labelled and mark the various observational properties shown in text-boxes. The text in black is from Ferrario et al. (1989) whereas the text in blue is for this work.

3.8 Discussion and conclusions

This chapter presented results from the recent phase-resolved spectroscopic observations of the eclipsing AM Her type system UZ For obtained with SALT.

3.8.1 Spectroscopy/spectral properties

The blue mean orbital spectrum presented in Section 3.5 is dominated by emission from Balmer (Hβ, Hγ and Hδ) and HeII 4686 Å emission lines. The other lines, HeII and HeI as well as the Bowen fluorescence complex at 4640–4650 Å (commonly seen in polars) are seen in weak emission. Based on the strength of the emission lines (i.e. the ratio of Hβ to HeII 4686 Å is almost unity), I conclude that the spectrum of UZ For presented in Figure 3.7 was obtained during a high state of accretion when mass transfer from the secondary star is increased. This is supported by strong emission lines from the Balmer and HeII 4686 Å with a broad base and superposed on a continuum that rises in the ultraviolet (see Figure 3.7). Similar high-state spectra of UZ For were presented by Ferrario et al. (1989) and showed strong emission from the Balmer and HeII 4686 Å lines. However, their continuum seems to rise in the red which is the opposite of what is reported in this thesis. As already mentioned in Section 1.5.2, the continuum of an AM Her system in a high-state can either rise in the blue or red wavelengths due to increased thermal emission and/or cyclotron emission. Therefore, our results are consistent with high-state. The ratio of Hβ to Hγ or Hδ is close to unity, signifying that these lines are emitted in an optically thick region.

Another spectrum of UZ For showing strong emission from the Balmer lines and HeII 4686 Å, albeit obtained during an intermediate state, were presented by Allen et al. (1989). Their mean spectrum show steep Balmer decrement* while our mean spectrum show flat Balmer decrement. Therefore, our results are not consistent with those reported by Allen et al. (1989). The spectrum of UZ For presented here differ from that obtained during the low state presented by Beuermann et al. (1988) – covering wavelengths from 4000–9000 Å – which showed weak emission from the Balmer lines in the blue and strong molecular bands in the red which are associated with the secondary star. During the low state, the strength of the emission lines (Balmer and HeII 4686 Å) from the AM Her systems is significantly reduced and emission from the WD's photosphere and the secondary star dominate the continuum. The mean orbital red spectrum was also presented (see Section 3.5) and shows weak emission from CaII lines at 8498 and 8542 Å. These lines are understood as being emitted from the the irradiated face of the secondary star.

It is generally understood that AM Her systems undergo various states of mass transfer on a time scale ranging from months to years. The mean orbital spectrum of UZ For presented in this thesis highlight this characteristics when compared with those from the literature. There are other AM Her systems which show this kind of behaviour, e.g. BL Hyi (Gerke et al. 2006), RX J1007−2017 (Thomas et al. 2012) and CSS 080228: 081210+0403

*The spectrum in question here was averaged from phase 0.2 to 0.6 – to exclude contribution from the magnetic pole.

(Thorstensen et al. 2020).

3.8.2 Doppler tomography

The first detailed standard and inside-out Doppler tomography analysis of the eclipsing AM Her type system UZ For using the Hβ, HeII 4686 Å and CaII 8542 Å emission lines is presented. As already mentioned in Sections 1.8.3 and 3.6 this is not the first time a Doppler map of UZ For is presented. Earlier work by Schwope et al. (1999) (and reproduced in Schwope 2001 and Marsh & Schwope 2016) from the observations taken during the low state focused on analyzing the tomogram of the HeII 4686 Å emission line and the Doppler map of this line revealed three emission regions: the irradiated face of the secondary star, the ballistic part of the accretion stream and the magnetically dominated part of the accretion stream. In this chapter, two Doppler tomography projections, the standard and inside-out methods, were used to unravel the various emission components contained in the observed trailed spectra of UZ For while in a different state (i.e. high state).

3.8.2.1 Observed and reconstructed trailed spectra

The observed trailed spectra in the blue and red are discussed in detail in Section 3.6.1 for the three emission lines studied in this thesis (i.e. Hβ, HeII 4686 Å and CaII 8542 Å). It is worth mentioning that this is the first time a trailed spectra of Hβ and CaII 8542 Å lines is presented for this system. Since UZ For is an high-inclination AM Her systems, one would expect its trailed spectra to be similar to that of HU Aqr (Schwope et al. 1997a, Kotze et al. 2016) with an inclination of 84° but this is not the case. The overall structure of the trailed spectra of UZ For resembles that of the Balmer lines from CTCV J1928−5001 (Kotze 2017) with an inclination of 78° but without the red-shifted narrow component from the secondary star. As already mentioned in Kotze (2017), the idea of inclination as a driver for the observed emission structure of AM Her systems is discarded. But instead, it serves to highlight the intrinsic differences in the accretion geometries of these AM Her systems. The observed trailed spectra of both the Hβ and HeII 4686 Å emission lines are similar since they are produced in the accretion flow and show the presence of three distinct emission components associated with emission from the ballistic stream and the threading region, from the magnetically confined accretion stream and from the irradiated face of the secondary star.

The trailed spectra of HeII 4686 Å line presented here is different from that of the same line presented by Schwope et al. (1999) but they both contain three components which are associated with various parts of the accretion flow including the irradiated face of the secondary star. The main difference between our results and those of Schwope et al. (1999) is the narrow component which we associate with the threading region and the ballistic stream and not the irradiated face of the secondary star as discussed in Schwope et al. 1999. The difference in the two observed trailed spectra is attributed to the fact that the observations presented in this thesis were taken during a high-state whereas those of Schwope

et al. (1999) were obtained during the low state. Therefore, one would expect the emission from the ballistic and magnetically confined parts of the accretion stream to dominate over emission from the secondary star during high state. UZ For is not the only AM Her system to not show the narrow component in its trailed spectra during a high state. In fact, AM Her was reported to show a narrow component by Staude et al. (2004) while a trailed spectra presented recently by Schwope et al. (2020b) did not show the narrow component. The absence of the narrow emission line was explained as a result of shielding of the secondary star by the accretion curtain which gives rise to the prominent soft X-ray absorption prior to phase zero.

The observed trailed spectra of CaII 8542 Å emission line differs from that of the Hβ and HeII 4686 Å lines and shows the presence of two components, that is, a narrow component (red and blue) which is associated with the emission from the irradiated secondary star and a broad component (yellow) which is associated with emission from the threading region and/or the ballistic stream. As already mentioned earlier, CaII lines is produced from the illuminated side of the secondary star. The trailed spectra of CaII 8542 Å is similar to that of HU Aqr obtained during an intermediate state and presented by Schwope et al. (2011). Our reconstructed tailed spectrum – based on both the standard and inside-out projections – show the basic structures of the observed trailed spectra. This is because in normal Doppler tomography techniques, the emission distribution is averaged over the entire orbital phase and the variations from one orbital phase to another is not accounted for and therefore not reproduced in the reconstructed trailed spectra.

3.8.2.2 Standard and inside-out maps

One of the objective of this thesis was to use the standard and inside-out projections techniques to produce detailed Doppler maps of the strongest emission lines of UZ For. Both the standard and inside-out maps (Figures 3.9 to 3.11, top rows) of the emission lines in the blue part of the spectra (Hβ and HeII 4686 Å lines) show tomograms dominated by emission from the ballistic stream, that is, the vicinity of the threading region, and the magnetically confined accretion stream. These maps also show low-level emission from the irradiated face of the secondary star. But the emission from the secondary star is only discernible in the inside-out tomograms for both lines. That is to say, when using the standard projection, it is difficult to distinguish the various emission components seen in the observed trailed spectra because one or two component(s) are projected close to each other. For example, the vicinity of the ballistic stream and the threading region dominates the emission in the standard Doppler maps of both the Hβ and HeII 4686 Å emission lines and as such, emission from the secondary star is barely visible to the eye. As already mentioned in Kotze et al. (2015; 2016), the standard Doppler tomography projection tends to concentrate and enhance lower velocity features while the higher velocity features are more separated and smeared out. In the case of the inside-out projection, the various emission components present in the observed trailed spectra are now projected onto different parts of the tomogram and the overall emission is redistributed amongst the components. For example, the inside-out

Doppler map of the Hβ line shows strong emission from the vicinity of the threading region and the magnetically confined accretion stream close to the WD. As already mentioned in Kotze et al. (2015; 2016), the inside-out projection redistributes the relative contrast levels in and amongst the emission components thereby exposing the low-velocity emission details which are overly compacted in the standard projection and enhancing the high-velocity emission details which are blurred out in the standard projection.

The standard Doppler maps of the Hβ and HeII 4686 Å emission lines are similar to those presented by Schwope et al. (1999) for UZ For using the HeII 4686 Å line in the sense that they both show significant emission from the ballistic stream and the threading region as well as the emission from the magnetically confined accretion stream. However, our results show deviations in the expected emission from the irradiated face of the secondary star which dominates emission in the low-state Doppler maps of HeII 4686 Å line presented by Schwope et al. (1999) and is fainter or nonexistent in our high-state Doppler maps. The inside-out maps also show similar results to the standard projection, but in this case, the Roche lobe of the secondary star is overlaid in yellow and clearly visible since in the inside-out projection the emission is redistributed amongst the different components. As already mentioned in Section 3.8.2.1, Schwope et al. (2020b) attributed the absence of the narrow emission component in the recent high-state trailed spectra of the Hα line and subsequently the absence of strong emission from the location of the secondary star in the Doppler map of AM Her to shielding by the accretion curtain. This can also result due to the emission from ballistic and magnetically confined accretion stream outshining that from the donor star in the blue or spectral resolution of the observations. The absence of bright spot from the secondary star can be explained by any of the following: 1) the emission from ballistic and magnetically confined accretion stream outshone that from the donor star in the blue, 2) the formation of an accretion curtain that is shielding the emission from the secondary star and 3) spectral resolution of the observations. Therefore, the absence of significant emission from the irradiated face of the secondary star in the high-state Doppler maps of UZ For is due to obscuration by the enhanced magnetic accretion curtain. This is supported by moderate to strong emission in the vicinity of the magnetically confined accretion stream in both the standard and inside-out maps and the presence of an extended accretion curtain-like feature for both lines. In addition to this, the short-period AM Her systems are harbouring smaller and cooler companion than the long-period AM Her systems (Marsh & Schwope 2016). Also, the secondaries in short-period AM Her systems are only observed during the low-state with the exception of HU Aqr (see e.g. Schwope et al. 2011).

The standard and inside-out Doppler maps of the CaII 8542 Å show strong emission from the irradiated face of the secondary star. This is expected since CaII lines are emitted from the upper hemisphere of the red dwarf facing the primary star. This is significant results given that this is the first time the Doppler maps of CaII 8542 Å is presented for UZ For, and putting aside the fact that the spectra used, specifically those from phase 0.36 to 0.65, were obtained more than a year after the blue spectra were taken. The Doppler maps of CaII 8542 Å presented in this thesis are consistent with those of HU Aqr constructed

using the observations obtained during an intermediate state of accretion and presented by Schwope et al. (2011). This reaffirms the results presented here.

There are several AM Her systems that has Doppler tomography records in the literature while they were in high-state and the list include AM Her (Staude et al. 2004, Schwope et al. 2020b), QQ Vul (Schwope et al. 2000a, Staude et al. 2004), HU Aqr (Schwope et al. 1997a), V834 Cen (Potter et al. 2004), etc. The Doppler maps from these authors revealed emission from several components including the emission from the irradiated face of the secondary star, from the ballistic and the magnetically confined accretion stream. In most of these studies, the emission from either the secondary star or the ballistic stream dominated the emission distribution in the Doppler maps. For example, the Doppler maps of AM Her using the HeII 4686 Å and Hβ lines presented by Staude et al. (2004) show a bright spot at the location of the secondary star whereas the tomogram of the same system using the Hα line presented by Schwope et al. (2020b) shows an extended emission in all quadrants with non-existent emission from the location of the secondary star. In another example, the multi-epoch (1986, 1991 and 1993) Doppler maps of QQ Vul presented by Schwope et al. (2000a) using HeII 4686 Å line show the bright spot at the location of the secondary star and a second bright spot at the location of the ballistic stream. They noted that the location of the bright spot in the ballistic stream was variable from one epoch to another with the tomograms from two epochs (1991 and 1993) placing the bright spot near L_1 and the the remaining epoch (1986) placing the spot in the lower-velocity region of the magnetically confined accretion stream. Schwope et al. (2000a) attributed the absence of the brighter ballistic stream from the 1986 high-state observations of QQ Vul to the resolution of the observations and the brightness of the other components. A follow-up study of QQ Vul conducted by Staude et al. (2004) revealed prominent emission from the location of the secondary star and the ballistic stream in the Doppler maps of HeI 4921 Å and Hβ lines. They noted that the tomogram of HeII 4686 Å line only showed prominent emission from the ballistic stream. This was explained as due to blocked X-ray emission from the accretion region not reaching the secondary star to ionize the HeII line. The high-state standard and inside-out maps of HU Aqr (Schwope et al. 1997a, Kotze et al. 2016) based on HeII 4686 Å showed strong emission from the irradiated face of the secondary star and the ballistic stream. On the other hand, the high-state maps of V834 Cen presented by Potter et al. (2004) showed strong emission from the ballistic and magnetically confined accretion stream.

Overall, the tomograms of UZ For presented in this PhD study show variation in the emission distribution of this system from one epoch to another. This is demonstrated by Doppler maps showing strong emission from the vicinity of the threading region and/or ballistic stream as well as the magnetically confined accretion stream. These components dominate the emission distribution in the Doppler maps of UZ For for both HeII 4686 Å and Hβ lines. Therefore, UZ For is now amongst several other systems whose emission distribution in the Doppler maps vary from one epoch to another, e.g AM Her (Staude et al. 2004, Schwope et al. 2020b), QQ Vul (Schwope et al. 2000a, Staude et al. 2004). The absence of bright spot from the secondary star can be explained as due to the formation

of an accretion curtain that is shielding the emission from the secondary star. It is worth mentioning that the standard and inside-out Doppler maps of CTCV J1928−5001 using the Hβ emission line show strong emission from the ballistic and magnetically confined accretion stream as well as some emission from the irradiated face of the secondary star (see Chapter 6 of Kotze 2017). However, this system was observed in an intermediate-state of accretion.

3.8.2.3 Flux-modulation mapping

The flux modulation amplitude maps (Figures 3.12 and 3.13, top panels) of UZ For using the Hβ and HeII 4686 Å lines discussed in Section 3.7.2 show that at least two emission components are flux-modulated, that is, the ballistic stream and the threading region, and the magnetically confined accretion stream. This is expected since UZ For is an high-inclination system and the flux from various emitting components will be modulated with the orbital phase due to their changing viewing angles with respect to an observer. The reason we see strong modulation from the vicinity of the threading region and the high-velocity component of the magnetically confined accretion stream close to the WD is due to that these regions are characterized by high density materials – especially the shocks in both regions. As already mentioned in Section 3.7.2, the modulation of the ballistic and the magnetically confined accretion stream is more pronounced for the Hβ line in both the standard and inside-out modulation maps. The low-level flux modulation of the ballistic and magnetically confined accretion stream in the tomograms of HeII 4686 Å line is attributed to that the excitation and recombination of this line occurs at high temperatures than the Balmer lines and also suffer less absorption by the medium. On the other hand, the threading region is capable of reaching higher temperatures due to strong shock but the modulation from this line is still less pronounced than that of Hβ line. This could be explained by the presence of big blobs of materials that are difficult to ionize as opposed to fine grains of gas.

The Hβ and HeII 4686 Å lines also show flux modulation from the irradiated face of the secondary star, but this is mostly clear in the inside-out maps. This is also expected since the irradiated face of the secondary star is only visible to an observer at certain orbital phases. In the case of CaII 8542 Å line, the irradiated face of the secondary star is the most flux-modulated component. This line (CaII 8542 Å) also shows evidence of flux modulation from the ballistic stream. Similar to Hβ and HeII 4686 Å lines, the modulation of the CaII 8542 Å line is expected since the irradiated face of the secondary star and the ballistic stream are only visible to an observer at certain orbital phases.

Overall, the flux modulation amplitude maps of UZ For are different from those of HeII 4686 Å line presented by Kotze et al. (2016) for HU Aqr and V834 Cen while they were in high-state. As already mentioned above, HU Aqr show strong emission from the irradiated face of the secondary star, the ballistic and magnetically confined accretion stream. But its standard and inside-out modulation amplitude maps show low-level modulation from the magnetically confined accretion stream. On the other hand, V834 Cen showed strong emission from ballistic and magnetically confined accretion stream with low-level of emission from the irradiated face of the secondary star. The flux modulation amplitude maps of this

system show strong modulation from ballistic and magnetically confined accretion stream also with low-level modulation from the secondary star. CTCV J1928−5001 is another AM Her system whose standard and inside-out flux modulation amplitudes maps, using the Hβ emission line, were presented by Kotze (2017). However, this system was observed in an intermediate high-state – either rising to or descending from the high-state. The flux modulation maps of CTCV J1928−5001 show strong emission from the irradiated face of the secondary –most flux-modulated component, the ballistic and magnetically confined accretion stream. The results of the Hβ line presented in this thesis share some similarities with that of CTCV J1928−5001 in sense that the extended curtain is seen in both systems and also seen is evidence of funnelling as the gas free-fall towards the WD. The deviations are seen in the vicinity of the threading region which is brighter in the case of UZ For and fainter for CTCV J1928−5001. These results reveal that each system is different from the other irrespective of the inclination.

3.8.2.4 Phase of maximum flux maps

The phase of maximum flux maps (Figures 3.12 to 3.14, second rows) were presented for the Hβ, HeII 4686 Å and CaII 8542 Å lines using both the standard and inside-out projections in order to highlight the orbital phase at which an emission component appears brightest to an observer. These results were explained in great detail in Section 3.7.3 and led to the construction of the geometry of UZ For shown in Figure 3.15. As expected, the maximum flux from the ballistic and magnetically confined accretion stream for both Hβ and HeII 4686 Å lines is observed around phases 0.25 and 0.75, respectively. But some parts of the ballistic and magnetically confined accretion stream are visible at phase 0.5 (green) when the stream is flowing in the direction of the observer. This is also expected since various parts of these two components are seen at different orbital phases. The threading region is a mixture of blue, red and black for Hβ and HeII 4686 Å lines and this is expected since this region is visible in most all phases except at phase 0.5 since its eclipsed by the WD at this phase. All three lines show that maximum flux from the irradiated face of the secondary star is seen around phase 0.5 and this is expected since the observer will have a full view of the illuminated face of the red dwarf at this phase. The phase of maximum flux results are consistent with what an observer, viewing the binary on the plane of the paper of the schematic shown in Figure 3.15, would see at different orbital phases. This coupled with the fact that UZ For is an high-inclination system.

The phase of maximum flux of UZ For share some similarities with those of HU Aqr and V834 Cen (Kotze et al. 2016) and CTCV J1928−5001 (Kotze 2017). For example, the phase at which the maximum flux from the magnetically confined accretion stream is observed is the same, that is 0.75 and overlaid in blue, for all these four systems (including UZ For). The expected phase at which the maximum flux from the irradiated face of the secondary star is 0.5 and this is consistent throughout these systems and is shown in green colour. The ballistic stream, however, is overlaid in more than one colour for most of these systems implying that parts of the stream are seen at different orbital phases. For example, the

ballistic stream is overlaid in blue colours for HU Aqr whereas in the case of V834 Cen the ballistic stream is overlaid in blue and red colours implying that these regions are visible to the observer at phase 0.25 and 0.75, respectively. In the case of CTCV J1928−5001, the ballistic stream is overlaid in red and green colours. One also expect to see the trailing and leading face of the secondary star at phase 0.25 (red) and phase 0.75 (blue), respectively. This has been seen in phase of maximum flux maps of HU Aqr and V834 Cen (Kotze et al. 2016). Their absence in our maps is probably due to that we only see low-level emission from the secondary star. Furthermore, we note that the mean orbital spectrum of HU Aqr presented by Schwope et al. (1997a) showed a prominent narrow emission line superposed on a broad component and in this study this narrow component is not observed.

3.9 Summary

This chapter presented results from the recent phase-resolved spectroscopic observations of the eclipsing AM Her system UZ For. The mean blue orbital spectrum (discussed in detail in Section 3.5.1) is dominated by strong emission from the Balmer and HeII 4686 Å lines. Also present in the spectra were weak emission from other species of HeII and HeI lines as well as the CIII/NIII Bowen fluorescence blend at 4650 Å and CII line. The emission lines in AM Her systems are understood to originate from the various parts of the accretion flow including the ballistic and magnetically confined accretion streams as well as the irradiated face of the secondary star. The strength of HeII 4686 Å is comparable to that of the Hβ line and this is typical of AM Her systems during a high state of accretion. UZ For show flat Balmer decrement (i.e. the ratio of Hγ/H$\beta \simeq 1$) and this implies that these lines were emitted from an optically thick regions. These spectral characteristics, that is, emission line strengths and their orbital variations (discussed in Section 3.5.2), are consistent with a high state of accretion. The mean spectrum in the red showed emission from CaII lines at 8498 and 8542 Å and these lines are produced in the irradiated face of the secondary star.

The strongest features from the blue and red parts of the spectra were used to construct both the standard and inside-out Doppler tomograms specifically using the Hβ, HeII 4686 Å and CaII 8542 Å emission lines. These maps were discussed in full detail in Section 3.6 and show emission from various components of the binary, that is, the ballistic stream and the threading region, the "curtain-like" magnetically confined accretion stream and the irradiated phase of the secondary star. The various emission components are clearly distinguishable in the inside-out maps. As already mentioned in Kotze et al. (2015; 2016), the inside-out projection exposes low-velocity emission details that are overly compacted and enhances high-velocity emission details that are overly tenuous in the standard projection. The extra information revealed by the inside-out projection is extremely valuable to get a more complete picture of the emission components not only in UZ For but also in other AM Her systems.

Flux modulation mapping, in both the standard and inside-out projections, was also used to map emission components that vary with the orbital phase using the ten consecutive

half-phase tomograms. The results presented in Section 3.7.2 show modulation from the irradiated face of the secondary star, from the ballistic stream and the threading region, and from the magnetically confined accretion stream. The secondary star show strong modulation for CaII 8542 Å and HeII 4686 Å lines but the latter also show strong modulation from the magnetically confined accretion stream. Hβ line show strong modulation from the ballistic stream and the threading region as well as from the magnetically confined accretion stream and emphasizes the funnelling of the gas as it falls towards the WD. These results are expected given that UZ For is an high-inclination system and therefore, emission from different components of the binary will modulate with the orbital phase due to eclipsing amongst other factors.

Finally, the phase of maximum flux maps for both the standard and inside-out projections were also presented in this chapter. The phase of maximum observed flux maps agree with the expected modulation based on the model-schematic of UZ For shown in Figure 3.15. In both the standard and inside-out maps, the phasing of the high-velocity emission is preserved but it is more structured in the inside-out tomograms. Furthermore, the inside-out projection preserved the modulation of the low-velocity emission. As already mentioned in Section 3.7.3, Figure 3.15 is an improved version of figure 8 of Ferrario et al. (1989) (see e.g. Figure 1.26) and is based on the polarization, eclipsing and radial velocity characteristics observed at certain orbital phases. Now I have added the properties of this system from what was uncovered from the Doppler tomography studies. These properties are summarized below:

- Secondary star: the maximum flux is observed at phase 0.5, that is, when the observer is viewing the binary at an angle bisected by the green colour (i.e. from the top of Figure 3.15). Other parts of the secondary star such as the trailing side should be seen at phase 0.25 (red) whereas the leading side should be seen at phase 0.75 (blue).

- Ballistic stream: maximum flux from the trailing side of the stream is observed at phase 0.25 when the observer is viewing the binary through an angle bisected by the red colour. However, some parts ballistic stream are still visible to an observer at phase 0.5 (phase colour green) for both lines and 0.75 (phase colour blue) for HeII 4686 Å.

- The magnetically confined accretion stream: the maximum flux from the curtain is observed around phase 0.75, when the observer is viewing the binary through the blue colour.

- Radial velocity crossing from red-shift to blue-shift occurs at phase 0.3 (boundary of red and green colour) and the crossing from blue-shift to red-shift occurs at phase 0.8 (mixture of blue and black).

Overall, the results presented here establishes that the inside-out projection provides extra emission information that is mostly missed when the standard projection is used and is essential to get a more completed picture of the emission components in UZ For.

Chapter 4

Optical and radio observations of UZ Fornacis

This chapter presents circular spectropolarimetry, photometry, polarimetry and radio observations of the eclipsing AM Her system UZ For. As with Chapter 3, some parts of this chapter have been published as a main article in the **Monthly Notices of the Royal Astronomical Society** journal in 2020 titled "*A spectroscopic, photometric, polarimetric and radio study of the eclipsing polar UZ Fornacis: the first simultaneous SALT and MeerKAT observations*" by Khangale et al. (2020). Some parts were reproduced in a conference proceeding titled "Multi-wavelength study of the eclipsing polar UZ Fornacis" by Khangale et al. (2021).

This chapter focuses mainly on the analysis of simultaneous circular spectropolarimetry and radio observations of UZ For obtained with both SALT and MeerKAT[†] (Karoo Array Telescopes; Jonas & MeerKAT Team 2016). This is the first time these two telescopes have been used in this manner. The observations with SALT were taken as part of the commissioning of the spectropolarimetry mode of the RSS instrument. It is worth mentioning that this is the first circular spectropolarimetry from SALT to ever be published. To aid with the interpretation of the circular spectropolarimetry, photometric and photopolarimetric observations of UZ For taken either simultaneously or within weeks of the SALT circular spectropolarimetry observations are also analysed here.

The main objectives of this chapter are as follows:

- to present the reductions and analysis of the first circular spectropolarimetry observations of UZ For as part of the commissioning of the polarimetry mode of the RSS instrument,
- to model cyclotron spectra and polarized flux of UZ For by utilizing the models of the stratified accretion shocks of Potter (1998) in order to determine the magnetic field strength of the main accreting pole in UZ For,

[†]The word "meer" is Afrikaans for "more". This simply to More Karoo Array Telescopse.

- to use photopolarimetry from HIPPO to aid the interpretation of the circular spectropolarimetry, and,
- to use MeerKAT radio telescope to investigate or understand the nature of radio emission from UZ For.

This chapter is structured as follows: Section 4.1 gives a literature review of UZ For. The details of two major telescopes and/or instruments used in this chapter are given in Section 4.2. The observations and reductions are described in Section 4.3. The photometric results are briefly explained in Section 4.4.1. The linear and circular photopolarimetric results are discussed in Section 4.4.2. The circular spectropolarimetry results are discussed in detail in Section 4.4.3 including modeling of the polarized flux. The MeerKAT radio results obtained from the MeerKAT observations are described in Section 4.4.4. Section 4.5 gives discussion and conclusion based on the results.

4.1 Multi-wavelength study of UZ For

UZ For was first discovered by the EXOSAT satellite as an X-ray source (Giommi et al. 1987, Osborne et al. 1988). Its orbital period of 126.5 min affords us an opportunity to study it at conceivable timescales. UZ For had been studied extensively in a wide range of wavelengths including optical (e.g. Beuermann et al. 1988, Bailey & Cropper 1991, Imamura & Steiman-Cameron 1998, Perryman et al. 2001, de Bruijne et al. 2002), X-rays (e.g. Osborne et al. 1988, Ramsay et al. 1993, Still & Mukai 2001), ultraviolet (Stockman & Schmidt 1996) and extreme ultraviolet (e.g. Warren et al. 1995), and radio (Barrett et al. 2017). Photometric properties of UZ For has been presented by various authors (see e.g. Bailey & Cropper 1991, Perryman et al. 2001) and is reviewed in Section 1.8.1. This section reviews some of the observational characteristics of UZ For that had been recorded over the years.

The first polarimetry studies of UZ For were obtained on 1987 November 28 and presented by Berriman & Smith (1988). Their results showed polarization reaching ∼10% in circular and ∼5% in linear and decreasing with increasing wavelength. The polarimetric results were explained in terms of a one-pole accretion model, with the accretion region emitting cyclotron radiation becoming visible to the observer before the primary eclipse and showing white-light polarization that reaches ∼10%. In addition, they also found evidence that the second pole was also emitting cyclotron radiation. In a separate study, Ferrario et al. (1989) detected strong circular polarization reaching 10% in the blue and ≤2% in the I band from the polarimetry observations taken on 1987 December 15. The circular polarization was seen during the bright phase and lasts 70 min of the orbital period − consistent with the results of Berriman & Smith (1988). Similar to Berriman & Smith (1988) and Ferrario et al. (1989), Bailey & Cropper (1991) reported detection of circular polarization during the bright phase reaching 10% in the blue and 3% in the red from the lower time resolution polarimetric observations of UZ For obtained on 1989 October 28 and 29. Strong positive polarization was seen in the blue and weakening with increasing wavelength during the bright phase. The

negative circular polarization was seen at phases 0.1−0.3, consistent with previous results (see e.g. Ferrario et al. 1989).

In another study, Imamura & Steiman-Cameron (1998) noted that the high-state light curves of UZ For appeared different in shape from those of the low state. During the high state, the accretion stream contributes a significant fraction of the overall luminosity of the system. The low-state light curves are dominated by emission from the accretion hot spot and the WD's magnetosphere. According to Imamura & Steiman-Cameron (1998) and Perryman et al. (2001), UZ For displays one or two accretion spots depending on the accretion state.

The optical spectra of UZ For were found to show strong cyclotron humps whose location vary with epochs and orbital phase and these were interpreted as due to cyclotron emission from the accretion region. The cyclotron spectra of UZ For have been modelled using a one-pole accretion model with the magnetic field strength of ∼51−55 MG (Beuermann et al. 1988, Ferrario et al. 1989, Allen et al. 1989). These authors noted that the harmonics were wavelength and phase-dependent and only seen during the bright phase. Allen et al. (1989) note that the cyclotron harmonics disappear at phase 0.15 and reappear at phase 0.65. However, detailed theoretical models suggest the presence of a second emission region with field strength 28 MG (Ferrario et al. 1988, Ferrario & Wickramasinghe 1989, Ferrario et al. 1989) also emitting cyclotron radiation.

In light of the two-pole accretion model suggested by Ferrario et al. (1989), Schwope et al. (1990) used the original spectroscopic data of Beuermann et al. (1988) obtained on 1987 October 21 during the low state to study the geometry and physical properties of the cyclotron sources on the accreting WD of UZ For. Their bright-phase spectrum showed optical continuum modulation by intense cyclotron emission line, when the main accretion region is in view. The bright-state spectra of UZ For were modelled assuming a homogenous plasma with a temperature of 5−10 keV in a field of 53 ± 1 MG for the main emitting region located below the orbital plane at a stellar colatitude of 155° and the second emitting region was suggested to be in the opposite hemisphere at a colatitude of 10° and with field strength of ∼57−75 MG. Rousseau et al. (1996) remodelled the observations from Beuermann et al. (1988) and Schwope et al. (1990) by considering a WD heated by a stream of free-falling electrons and they estimated a magnetic field strength of ∼53 MG and ∼48 MG for the two poles. In addition, they found that the total low-state accretion rate of UZ For was $\sim 3 \times 10^{13}$ gs^{-1} and the size of accretion spot was $\sim 4 \times 10^{15}$ cm^2. The spectra of UZ For obtained by Nogami et al. (2002) in ultraviolet regime show cyclotron harmonics in both the low state and high state of accretion. They determined magnetic field strengths of 51 and 74 MG for the high state and low state, respectively. The distance to UZ For was estimated to be ∼240 pc by Khangale et al. (2019b) based on GAIA parallax measurements.

In the radio regime, UZ For was included in the NSF's Karl G. Jansky VLA study at 5 GHz by Mason & Gray (2004); they estimated the upper limits of detection of flux density of 2.4 mJy. In another study, Barrett et al. (2017; 2020b) detected radio emission from 33 mCVs, including UZ For, from the survey of 122 mCVs observed with the VLA. As already

mentioned in Section 1.7.2, the observations of Barrett et al. (2017; 2020b) were conducted in four frequency bands and lasted a few minutes per frequency band and some sources were observed on at least two different epochs. UZ For was observed twice in 2015 across three bands (C-, X- and K-bands), the first observations were made on 2015 May 04 and the second on 2015 June 15. This source was detected at the C-band with flux density of 78 $\pm$ 9 μJy from the first observations and the other two bands and the second observations yielded non-detection of this source in radio. It is worth mentioning that contemporaneous with Barrett et al. (2017), Coppejans et al. (2015; 2016b) observed nine nearby dwarf novae and nova-like CVs and detected eight of them at a flux level of a few tens of μJy.

In this chapter, simultaneous optical and radio observations of UZ For are presented. The optical observations include circular spectropolarimetry taken around the eclipse as well as photometry taken with two other telescopes. The circular spectropolarimetry is used to improve our understanding of the behaviour of the cyclotron spectra of this source with the aid of the photopolarimetry taken leading up to the simultaneous observations. The radio observations of this source are also presented.

4.2 Telescopes and/or instruments used

This section contains background and specifications of the instruments or telescope used. The details on HIPPO and SHOC had already described in Sections 2.3.1 and 2.3.2, respectively. Different modes of the RSS instrument had already been introduced in Section 3.3, here the spectropolarimetry mode is described in more detail. Also described are the MeerKAT and MeerLICHT (Bloemen et al. 2016) telescopes.

4.2.1 Spectropolarimetry mode(s) of SALT

The RSS instrument is located in the prime focus of SALT and provides numerous capabilities including: long-slit, multi-object spectroscopy, high-speed spectroscopy, imaging and Fabry-perot imaging spectroscopy, and polarimetry − in combination with any of the above-mentioned modes of operation. All of the RSS modes potentially support linear, circular and all-Stokes polarimetry. The RSS instrument is permanently mounted on the prime focus so that all its modes are available at all times. The optical schematics of the RSS polarimetry are shown in Figure 4.1. The RSS instrument offers several polarimetric modes which can be broken down into three main groupings: spectropolarimetry with gratings, imaging and Fabry-Perot polarimetry. Each of these groupings can be operated with the half- and/or the quarter-waveplates, thus enabling linear, circular and all-Stokes polarimetry. That is, the quarter-wave and/or half-wave plates can be inserted into the collimator separately or together to provide linear, circular or all-Stokes polarimetry.

The splitting of the ordinary (O) and the extraordinary (E) beams is achieved by the insertable beamsplitter in the camera. The beamsplitter consists of a 3 $\times$ 3 mosaic of calcite Wollaston prisms. The RSS is the first instrument to use such a mosaic beamsplitter. The

initial polarimetric commissioning began in April 2012 and successful polarimetric observations were made with the long-slit, imaging and Fabry-Perot modes (Nordsieck 2012). Each of the mosaic elements consists of two prism wedges which were originally lens-fluid-coupled. However, after less than a year of polarimetric commissioning, the calcite beamsplitter developed a coupling fluid leak for a second time. Due to this, it was decided to redesign the beamsplitter to use a different optical couplant gel, Nye 451. Further details on the specifications and commissioning of the RSS spectropolarimetry mode, including all the repairs, calibration and science verification, are described in Potter et al. (2016). It is worth mentioning that none of the above articles featured circular spectropolarimetry and therefore, this thesis presents the first such observations.

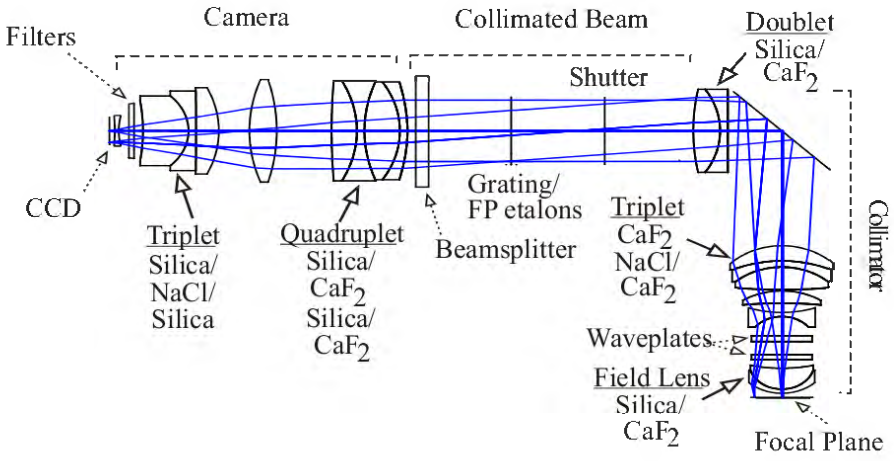

Figure 4.1: The optical schematic of the RSS instrument. Adopted from Figure 1 of Nordsieck (2012).

4.2.2 The MeerKAT radio telescope

The MeerKAT (Jonas 2009, Camilo et al. 2018, Jonas & MeerKAT Team 2016)) radio telescope is a precursor for the mid-frequency arrays for the Square Kilometre Array (SKA). MeerKAT is located in a radio-quiet zone in the Karoo desert at the site of the South African Radio Astronomy Observatory (SARAO) about 100 km from the small town of Carnavon in Northern Cape Province in South Africa. The initial goal specification of the MeerKAT was for an array of 80 symmetric centre-fed dishes, each with a diameter of 12-m and operating over continuous frequencies ranging from of 700 MHz to 10 GHz in order to match the mid-band dishes specification of the SKA (see e.g. Jonas & MeerKAT Team 2016, and references therein). The original design of the dishes were reviewed and the final design of MeerKAT array is shown in Figure 4.2 and the telescope now consists of 64 Gregorian-offset radio antennas, each with a diameter of 13.96 m and a maximum baseline of 8 km.

Figure 4.2: A picture of MeerKAT showing some of the radio dishes. Picture adopted from https://www.sarao.ac.za/gallery/meerkat/.

The change from centre-fed parabola dishes to offset-Gregorian optical configuration offers MeerKAT a high aperture efficiency and good sensitivity. The field of view of the MeerKAT telescope is 0.85 and 5 square degrees at 1.4 GHz and 580 MHz, respectively. The MeerKAT telescope currently allows two receivers covering frequencies ranging from 580 MHz to 1670 MHz in two overlapping bands, i.e. UHF-band (580−1015 MHz) and L-band (900−1670 MHz). Other bands that will be available on this telescope include the S-band (1750−3500 MHz) which is being provided by Max Planck Institute for Radio Astronomy and X-band (8−14.5 GHz). The 64 dishes of MeerKAT will be incorporated into the first phase of the larger project, the SKA, in 2022. The MeerKAT radio telescope is the most sensitive decimetre-wavelength radio interferometer array in the world at least until phase one of the SKA mid-band dishes start operating in 2022. See Jonas & MeerKAT Team (2016) for further details on the MeerKAT telescope. With a field of view of about one square degree at 1.4 GHz coupled with its sensitivity, MeerKAT is an excellent instrument to study radio emission from mCVs and the time resolution will allow for studying radio transient events in these systems, such as radio flares. The radio observations presented in this chapter were taken with the MeerKAT radio telescope and are discussed in Section 4.3.2.4.

4.2.3 The MeerLICHT robotic telescope

MeerLICHT* (Bloemen et al. 2016, Paterson 2019) is a fully robotic, wide-field optical telescope situated at the SAAO site in Sutherland and is a prototype for the BlackGEM

*See www.meerlicht.org for more details

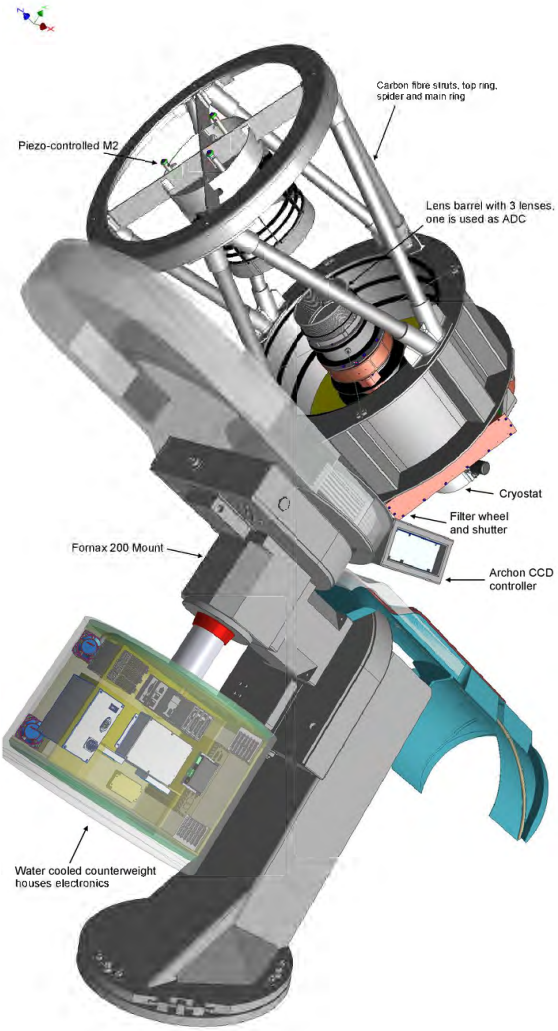

Figure 4.3: The model of the MeerLICHT/BlackGEM telescope adopted from Figure 1 of Bloemen et al. (2016).

array (Bloemen et al. 2015; 2016) of telescopes. The telescope design is shown in Figure 4.3 and consists of a carbon fibre frame housing optical systems on a FORNAX 200 equatorial mount. MeerLICHT's primary mirror has a diameter of 65 cm, with photometric aperture of 60 cm and focal length of 330 cm. The primary mirror is oversized to reduce vignetting. MeerLICHT has an instantaneous field of view matching that of MeerKAT and it "is the first fully dedicated telescope to follow another telescope in a different wavelength"−(Paterson 2019). Its main aim is to provide an instant optical view of the field being observed with MeerKAT during the night. It is equipped with an STA1600 detector − a 10k × 10k CCD − which provides a 2.7 square degree field of view at 0.56 arcsec/pixel at a seeing-limited resolution of 1″. It takes 60 s exposures across Sloan six filters, u, g, r, z, q and i (Gunn et al. 1998, Doi et al. 2010, e.g.). All data from MeerLICHT will be processed using a

pipeline and uploaded to a cloud environment in real-time for transient analysis. Bloemen et al. (2016) and a PhD thesis by Paterson (2019)* contains an in-depth description of the MeerLICHT telescope. The observations presented in Section 4.3.2.2 of this chapter were obtained with MeerLICHT.

4.3 Observations

4.3.1 Long-term light curve of UZ For

Figure 4.4 shows the long-term light curve of UZ For from photometric monitoring campaigns through various surveys. At the time of writing this thesis, the longest monitoring of this source (UZ For) was through the American Association of Variable Star Observers (AAVSO, Kafka 2020) monitoring programme from 2004 February 4 to 2020 February 22. The magnitudes from Catalina Real-time Transient Survey (CRTS; Drake et al. 2009) and All-Sky Automated Survey for SuperNovae (ASAS-SN†; Shappee et al. 2014) overlaps with those of the AAVSO monitoring campaign. The ASAS-SN monitoring of this source began on 2013 November 19 up until 2018 September 23 whereas the available magnitudes from CRTS‡ were taken between 2005 August 7 and 2013 March 14. Overall, the long-term light curve spanning 16 years shows at least four high states (V <16 mag). Low states (or faint state, V >16 mag) are not so clearly defined in the figure.

*See https://open.uct.ac.za/handle/11427/29987 for more details.

†More details here: https://asas-sn.osu.edu/variables

‡The CRTS routinely searches for optical transients in data from the Catalina Sky Survey from the 0.7-m Catalina Schmidt Telescope north of Tucson in Arizona state. More details here: http://nesssi.cacr.caltech.edu/DataRelease/

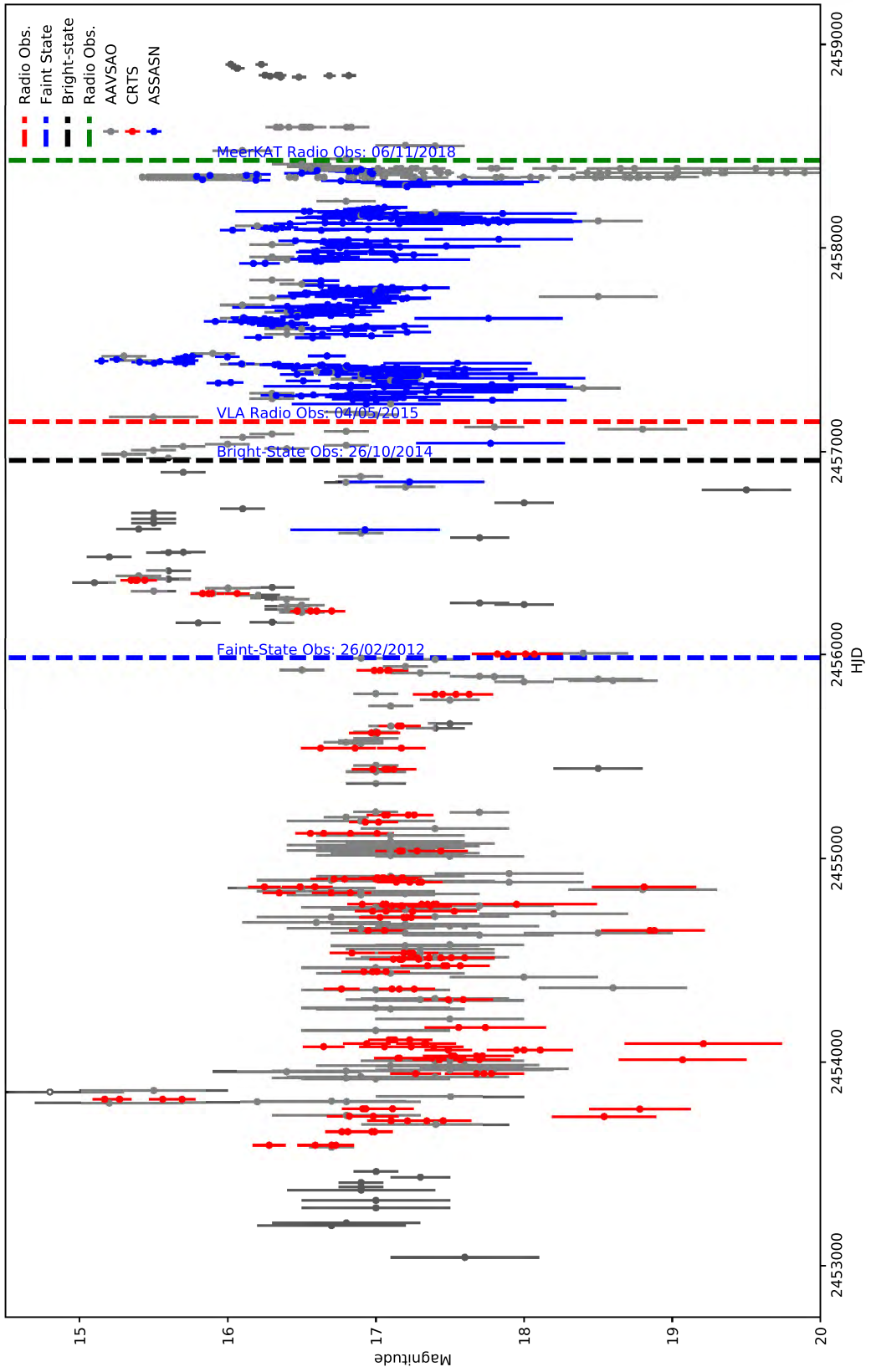

Figure 4.4: Long-term light curve of UZ For from various surveys. The grey dots show the AAVSO magnitudes, the red colour indicates CRTS monitors and the blue dots are from ASAS-SN survey. The red and green line marks the times of VLA and MeerKAT observations, respectively.

4.3.2 Simultaneous observations

This section contains photometry, circular spectropolarimetry and radio observations obtained simultaneously on the night of 2018 November 6. This section is structured as follows: Section 4.3.2.1 explains the photometry observations taken with the SAAO 1.9-m telescope using the SHOC instrument; Section 4.3.2.2 contains the observations made with the MeerLICHT telescope; Section 4.3.2.3 contains the spectropolarimetry data taken with SALT RSS instrument and the lastly, Section 4.3.2.4, contains the radio observations taken with the MeerKAT telescope.

4.3.2.1 SHOC photometry

High-speed photometric observations were obtained by Dr Andrey Semena (one of our collaborator) on the night of 2018 November 6 using the SAAO 1.9-m telescope equipped with the SHOC (Gulbis et al. 2011a, Coppejans et al. 2013) instrument described in Section 2.3.2. These observations were made during good photometric conditions. The SHOC detector was used in frame-transfer mode with a clear filter, 4×4 binning and exposure time of 1 s.

The resulting data cubes were reduced using the SHOC pipeline that is described in Coppejans et al. (2013). The white light counts were converted to magnitudes by comparing the measured magnitudes of UZ For with the B and R magnitudes of stars in the field around UZ For and listed on the United State Naval Observatory (USNO) catalogue (Monet et al. 2003). All the times were corrected for the light travel-time to the barycentre of the solar system (i.e. converted from JD to BJD; Eastman et al. 2010). The ephemeris from Table 2.2 (i.e. the orbital period and the epoch) was used to phase the light curve. The resulting light curve obtained after the data reduction is shown in Figure 4.5 and discussed in Section 4.4.1.

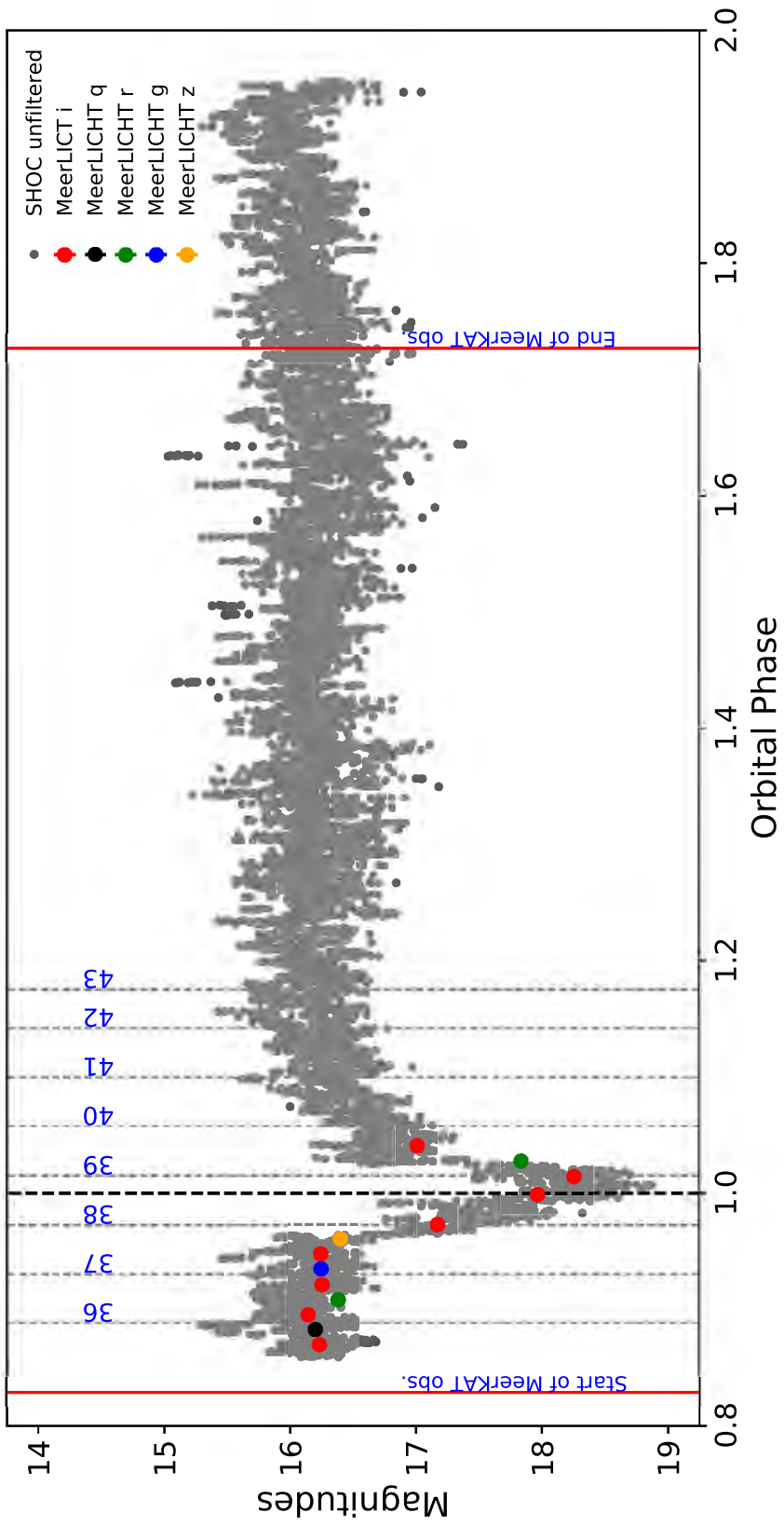

Figure 4.5: Simultaneous SHOC (grey dots) and MeerLICHT (filled circles) light curve of UZ For obtained on 2018 November 6, overlapping with SALT spectropolarimetric and MeerKAT radio observations. The vertical grey dashed lines mark the mid-exposure of the eight individual spectropolarimetry exposures taken with SALT whereas the black dashed line represents the time of mid-eclipse. The red vertical lines mark the start- and end-time of the MeerKAT observations.

4.3.2.2 MeerLICHT photometry

Simultaneous to the above SHOC observations, photometric observations of UZ For were obtained on the night 2018 November 6 using the MeerLICHT* telescope (Bloemen et al. 2016) described in Section 4.2.3. The observations started at 20:11 (UTC) and lasted for 22 minutes. Individual 60 s exposures in g, r, z, q filters were interleaved with 60 s exposures in the i filter. The MeerLICHT observations were taken during science commissioning of the telescope and covered most of the primary eclipse.

Data were processed using the MeerLICHT pipeline which is a combination of tools from the Terapix software suite (e.g. Bertin & Arnouts 1996) and the ZOGY image subtraction routines (Zackay et al. 2016), coded up by Vreeswijk & Paterson (2021) on behalf of the BlackGEM/MeerLICHT teams. Photometry for UZ For was extracted using the optimal photometry routines as outlined by Horne (1986) and Naylor (1998). The photometry was calibrated using a multi-mission, multi-wavelength all-sky photometric standard star databases: SDSS(DR14) (Abolfathi et al. 2018), PanSTARRS(PS1) (Chambers & et al. 2017), SkyMapper (Wolf et al. 2018), 2MASS (Cutri et al. 2003) and GALEX (Seibert et al. 2012). Further details on the calibration will be published in Vreeswijk et al. (in preparation). Both the processing as well as the photometric calibration will be fully discussed in a forthcoming paper by Groot et al. (in preparation). The times from MeerLICHT were given in modified julian dates and this was first converted to JD. As with SHOC data, the resulting times were then converted from JD to BJD. The times were then converted to orbital phases using the ephemeris (orbital period and epoch) presented in Table 2.2. The resulting light curve of UZ For is shown in Figure 4.5. Table 4.1 shows the resulting magnitudes from MeerLICHT.

4.3.2.3 SALT spectropolarimetry

UZ For was observed, simultaneously with the above SHOC and MeerLICHT observations, with SALT, under the Large Science Programme (Proposal ID: 2018-2-LSP-001; Buckley 2019), on the night of 2018 November 6. The RSS instrument was used in the circular spectropolarimetry mode as described in Section 4.2.1. A total of eight exposures of 300 s each, with phase resolution of about 0.05 of the orbital period and spectral resolution of 4 Å, containing the ordinary (O) and extraordinary (E) beams were obtained around the eclipse (see Figure 4.5). An exposure of an Argon lamp was taken after the science frames for wavelength calibration purposes. The PG0300 grating was used providing a resolving power of ∼2500 and a wavelength coverage of ∼3500−9500 Å. The observations of the spectrophotometric standard star (HILT600, unpolarized optical calibrator) were obtained on 2018 December 4 with the same setup as the science exposures.

The CCD pre-processing of the observations was performed using the polsalt-beta† software (Nordsieck 2012, Potter et al. 2016) based on the PYSALT package (Crawford et al.

*See www.meerlicht.org for more details

†See https://github.com/saltastro/polsalt/ for more details.

2010), this includes overscan correction, bias subtraction and gain correction. The wavelength calibration for both the O and E beams was performed using the Argon lamps taken with the same observation setup. The E and O beams of each spectra were extracted using the polsalt software and stored as two different extensions in a single output file. These extensions, containing the one dimensional extracted O and E beam spectra, were then split into two separate files via a script written in PYTHON.

The degree of circular polarization (V/I) was computed from every consecutive exposure, with the quarter wave retarder plate rotated by $\pm 45°$, using Eq. 4.1 below (see Euchner et al. 2005 and references therein):

$$\frac{V}{I} = \frac{1}{2}\left[\left(\frac{f^{\rm o} - f^{\rm e}}{f^{\rm o} + f^{\rm e}}\right)_{315°} - \left(\frac{f^{\rm o} - f^{\rm e}}{f^{\rm o} + f^{\rm e}}\right)_{45°}\right], \tag{4.1}$$

where 45° and 315° indicate the position angle of the quarter wave plate and $f^{\rm o}$ and $f^{\rm e}$ are the ordinary and extraordinary beams, respectively. The total relative intensity was obtained by adding the sum of the O and E beams. The spectrophotometric standard star HILT600 was used for relative flux calibration. The varying nature of pupil size of SALT does not allow for absolute flux calibration of the target spectra. The resulting total relative flux, percentage circular polarization and total polarized flux spectra are shown in Figures 4.7 to 4.10 and discussed in Section 4.4.3. The spectra were not corrected for telluric bands or contributions of other sources such as the WD photosphere, secondary star, accretion stream and the second pole.

4.3.2.4 MeerKAT radio observation

Observations of UZ For and the surrounding field were taken, simultaneously with the above SHOC, MeerLICHT and SALT, on 2018 November 6 using the MeerKAT radio telescope. These observations are part of The Hunt for Dynamic and Explosive Radio Transients with MeerKAT (ThunderKAT; Fender et al. 2017) large survey project. The observations were taken using 62 of the MeerKAT antennas, using the L-band (900−1670 MHz) receiver in imaging mode operating at a central frequency of 1.284 GHz, with a total bandwidth of 856 MHz split into 4096 channels. Observations started at 20:06:18 and finished at 21:59:59 (UTC), overlapping with both the photometric and spectropolarimetric observation taken in Sutherland. Visibilities were recorded every 8 seconds. The band-pass and flux calibrator, PKS J0408−6545, was observed for 10 minutes at the beginning of the observation. Thereafter the gain calibrator, PKS J0409−1757, and UZ For were observed, for approximately 1.5 minutes and 15 minutes, respectively, alternating between them repeatedly for the remainder of the observation. The total integration time on UZ For was approximately 100 minutes.

The data were initially processed using the SARAO MeerKAT* pipeline. The pipeline performs some initial flagging which includes the removal of data from shadowed antennas and as well as removal of automatic radio frequency interference (RFI) flagging and performs

*See https://meerkathi.readthedocs.io for more details.

delay and bandpass corrections. Data reduction was performed following some of the steps outlined in Driessen et al. (2020). These steps are part of the ThunderKAT pipeline which is still under development and at this stage, the data are reduced using PYTHON and Common Astronomy Software Applications (CASA* version 4.7.1, McMullin et al. 2007) based scripts. As a first step, all the data were unflagged using a CASA based python script. This is necessary since the data from MeerKAT comes flagged; it was realised that this pre-reduction script also flags useful frequencies and therefore there is a need to unflag all the data before any science can be done. The second step was to flag the data, this was carried out using AOFlagger† version 2.9.0 (Offringa 2010, Offringa et al. 2012). After flagging, the data were calibrated by following standard procedures in CASA. This included phase correction, antenna delays and band-pass corrections. The resulting data were averaged by a factor of 8 in frequency, resulting in 512 channels each with a bandwidth of 1.67 MHz.

Data reduction and first generation calibration were done by Mr Dante Hewitt‡ using standard procedures in CASA. The new wide-band, wide-field imager, facet-based radio-imaging package, DDFacet (Tasse et al. 2018), was used for imaging. DDFacet takes generic direction-dependent effects into account and this is important as MeerKAT has a very wide field of view (∼1 square degree). The imaging was performed by deconvolving over four frequency subbands implementing the SSDClean deconvolution algorithm and Briggs weighting (Briggs 1995) with a robust parameter (R) of 0.0. The scaling of R is such that R = 0 gives a good trade-off between resolution and sensitivity. The R takes value between −2 (close to uniform weighting) and 2 (close to natural). No self-calibration was implemented. The flux density (and its uncertainty) of UZ For was estimated by fitting one (or more) Gaussian using the CASA task IMFIT. The noise levels were measured in the vicinity of the expected position of the source. It is worth mentioning that re-reduction of this dataset using a more advanced OXKAT§ pipeline (Heywood 2020) yielded similar values of flux density. The results from MeerKAT are presented in Section 4.4.4.

4.3.3 Polarimetry observations with HIPPO

Photopolarimetry observations of UZ For were made by Dr Stephen Potter on 2018 October 4 with the SAAO 1.9-m telescope using the HIPPO (Potter et al. 2010) instrument. HIPPO was operated in its simultaneous linear and circular polarimetry and photopolarimetry mode (all-Stokes). The observations were clear filtered using the RCA31034A GaAs photomultiplier tubes which give a wavelength coverage from 3500−9000Å. Polarized and non-polarized standard stars (Hsu & Breger 1982, Bastien et al. 1988) were observed on the night in order to calculate the waveplate position angle offsets, instrumental polarization, and efficiency factors. Background sky measurements were taken at frequent intervals during the observations. Data reduction was performed by Dr Stephen Potter following the procedures

*See https://casa.nrao.edu/ for more details on CASA.
†See https://sourceforge.net/projects/aoflagger/ for more details.
‡Dante Hewitt was a Masters student of Dr Retha Pretorius and Prof Patrick Woudt.
§See https://github.com/IanHeywood/oxkat for more details.

described in Potter et al. (2010). No photometric calibrations were carried out; photometry is given as the total counts minus the background-sky counts. The observations were synchronized to a GPS to better than a millisecond.

As with the SHOC observations, all the times were corrected to the barycentre of the solar system (i.e. from JD to BJD). Data reduction was carried out following the procedures described in Potter et al. (2010). The resulting photometry light curve, percentage circular and linear polarization are shown in Figure 4.6 and discussed in Section 4.4.2. As with the other observations, all the times were converted from BJD to orbital phases using the ephemeris (orbital period and epoch) listed in Table 2.2.

4.4 Results

4.4.1 Photometry with SHOC and MeerLICHT

Figure 4.5 shows the light curve of UZ For obtained with the SHOC instrument. Overlaid on the plot are MeerLICHT data (listed in Table 4.1) taken with i, q, r, g and z filters around the eclipse. The variation in magnitudes from the MeerLICHT traces the primary eclipse of the binary system and the pre-eclipse dip arising from the eclipse of the emitting region by the accretion stream. The approximated calibration magnitudes from SHOC, calculated based on the stars from the USNO catalogue and in the field around UZ For, agree with those from MeerLICHT telescope. According to the long-term light curve, Figure 4.4 discussed in Section 4.3.1, the simultaneous observations were taken when UZ For was in the intermediate state with magnitudes ranging between 16−17 mag. The photometric observations were taken simultaneously with the SALT spectropolarimetric and MeerKAT radio observations. The vertical dotted grey lines mark the position of the mid-exposure of the spectropolarimetric observations labeled with the numbers 36 to 43. The vertical black dashed line indicates the position of mid-eclipse of the WD as determined from the ephemerides listed in Table 2.2. The light curve of UZ For shows lots of flickering when the system is out of eclipse. The shape of the eclipse is similar to those recorded in the literature (e.g. Bailey & Cropper 1991, Khangale et al. 2019b) and the out-of-eclipse shape of the light curve is similar to that of Perryman et al. (2001).

4.4.2 Photopolarimetry

The top panel of Figure 4.6 shows the phased light curve obtained with the HIPPO instrument. The duration of the light curve is 1.53 hours and covers the primary eclipse. The shape of the eclipse is similar to that shown in Figure 4.5 with clear defined ingress and egress of the main accretion spot. The out-of-eclipse variability is consistent with low amplitude flickering similar to Figure 4.5.

The middle panel of Figure 4.6 shows the clear-filtered circular polarimetric observations obtained simultaneously with the photometry discussed above. The percentage of circular polarimetry shows variability between 0 and −5%. The out-of-eclipse circular polarization

Table 4.1: Multi-filter photometric magnitudes from MeerLICHT.

Time in UTC	Magnitude	Magnitude error	Filter used	BJD-OBS
20:11:31	16.233	0.016	i	2458429.346314
20:13:09	16.201	0.006	q	2458429.347446
20:14:45	16.146	0.015	i	2458429.348555
20:16:22	16.379	0.012	r	2458429.349684
20:18:00	16.254	0.016	i	2458429.350815
20:19:43	16.246	0.008	g	2458429.352008
20:21:21	16.243	0.016	i	2458429.353140
20:22:58	16.397	0.039	z	2458429.354262
20:24:37	17.170	0.032	i	2458429.355409
20:26:15	–	–	u	2458429.356546
20:27:53	17.965	0.058	i	2458429.357676
20:29:50	18.253	0.076	i	2458429.359027
20:31:30	17.835	0.033	r	2458429.360189
20:33:09	17.008	0.026	i	2458429.361340

Notes: UTC – universal time central and BJD-OBS – Barycentric Julian Date of the observations. The u filter yielded no measurement.

between phases 0.5 and 0.7 is consistent with zero. Before the eclipse, from phase 0.7−0.95, the polarization increases to −5%. This is because the region emitting cyclotron radiation is visible to the observer around these phases. During the eclipse, the total flux decreases resulting in large error bars for polarization. After the eclipse, from phases 1.03−1.07, the emission is still negatively polarized with polarization ranging from 0 to −5%. Around phase 1.1, there is evidence of positive circular polarization which we associate with the reversal of polarization mentioned by Ferrario et al. (1989) at this phases. This is attributed to emission from the secondary region which also emit polarized radiation. After phase 1.1, UZ For shows a mixture of polarization which is consistent with zero.

The bottom panel of Figure 4.6 shows the clear-filtered linear polarimetry results. The percentage of linear polarization shows variability ranging between 0 and 10%. The out-of-eclipse linear polarization, from phase 0.5−0.7, is less than 5%. Before the eclipse, phases 0.7−0.95, the level of polarization increases by a few percent (<10%) – consistent with the circular polarization. During the eclipse, the total flux decreases resulting in large error bars for polarization. After the eclipse, there is a pulse of linear polarization reaching about 10% and decreasing gradually before flattening out between phase 1.1−1.2 and beyond. The pulse of linear polarization is naturally interpreted as due to viewing the emitting region from a direction perpendicular to the magnetic field (Stockman 1977, Chanmugam & Wagner 1978). This implies that the angle between the line of sight of the observer and the magnetic field will at the accreting region will be close to 90°. There are several AM Her systems that show one or two linear polarization pulse(s) in their polarimetric observations. A single pulse of linear polarization had reported for several AM Her systems e.g. AN UMa (Krzeminski & Serkowski 1977), VV Pup (Tapia 1977b) and HU Aqr (Glenn et al. 1994). On the other

hand, Buckley et al. (1998) reported detection of two linear polarization pulses from the polarimetric observations of MN Hya.

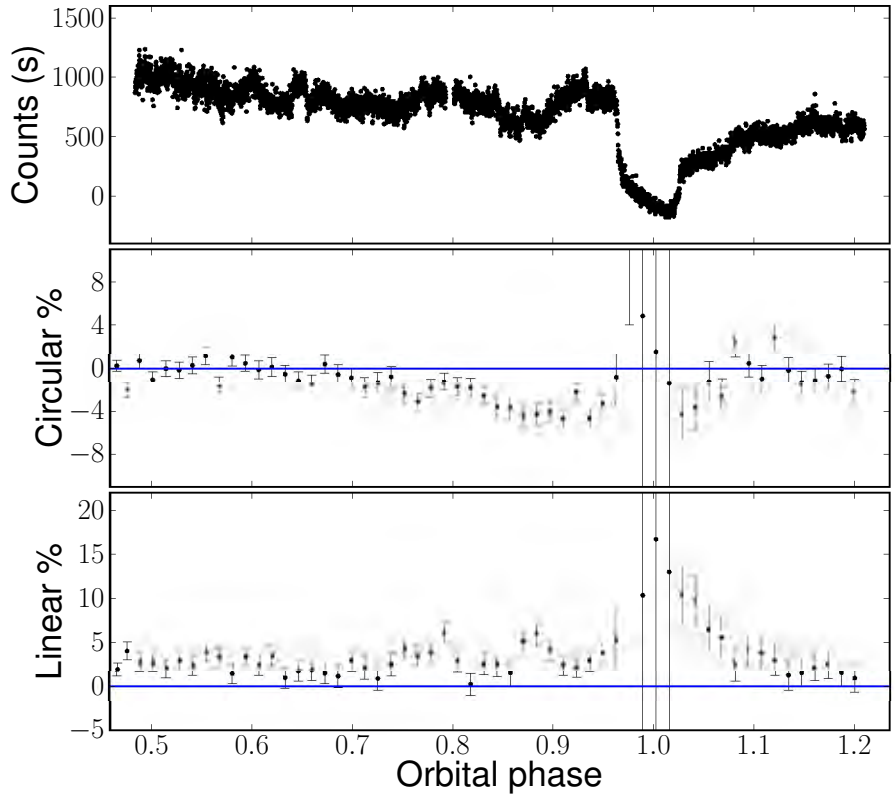

Figure 4.6: Photopolarimetry from 2018 October 4 made with the HIPPO instrument. Top to bottom panels correspond to photometry, percentage circular and linear polarization.

4.4.3 Circular spectropolarimetry

Figures 4.7 to 4.10 show the time sequence of circular spectropolarimetry obtained before the eclipse (Figure 4.7, phase 0.89−0.93), during the eclipse (Figure 4.8, phase 0.97−1.02), emerging out of the eclipse (Figure 4.9, phase 1.06−1.10) and after the eclipse (Figure 4.10, phase 1.14−1.18), respectively. For each figure, the top panel shows the total relative flux spectra, the middle panel shows the percentage of circular polarization and the bottom panel shows the total circularly polarized flux.

The total relative flux spectra show a continuum which rises in the blue and is dominated by broad emission features covering the entire waveband, e.g. broad hump around 5500 Å. As is expected, the total relative flux is higher before the eclipse and lower during the eclipse when the WD is eclipsed. The total relative flux again increases when emerging out of eclipse and remains high after the eclipse. The spectral features shown are similar to

those presented in Section 3.5 and the strength of the emission lines vary throughout the orbital phase.

4.4.3.1 Percentage circularly polarized spectra

The middle panels of Figures 4.7 to 4.10 show the time sequence of the percentage of circularly polarized spectra of UZ For. This compares well with the detection of negative circular polarization shown in Figure 4.6 (middle panel) during similar phase interval. The percentage of circularly polarized spectra show strong negative circular polarization (up to -8%) in the blue and decreasing gradually towards the red. The grey dashed vertical lines mark the location of the emission lines (as seen in the top panels) and it is clear that there are excursions towards 0% at their locations since emission lines are not polarized. The circular polarization spectra show the presence of three clearly resolvable negative polarized humps, centred at ∼4500 Å, 6000 Å and 7800 Å, that are understood as cyclotron harmonics due to cyclotron emission from the hot plasma in the shock. The harmonics are more visible in the spectra taken before the eclipse, i.e. Figure 4.7 (middle panel). During the eclipse, Figure 4.8 middle panel, the strength of the harmonics are significantly reduced, especially at longer wavelengths. Some indication of the harmonics are seen during the eclipse and is because the first exposure (marked 38 in Figure 4.5) started before the eclipse ingress and the second exposure (marked 39 in Figure 4.5) was taken during mid-eclipse. The spectra taken when the system was emerging out of the eclipse, Figure 4.9, show some polarization in the blue part of the spectra. The circularly polarized spectra taken after the eclipse (Figure 4.10) is consistent with 0% circular polarization over most of the observed wavelength. But between 7000 Å and 9000 Å, there is a marginal detection of positive polarization.

The percentage of circularly polarized spectra is consistent with the photopolarimetry described in Section 4.4.2 and is consistent with our understanding of Figure 4.6 in that from phases $0.7-0.95$ the accretion spot emitting cyclotron radiation is visible to the observer around these phases. The spot is eclipsed between phases $0.95-1.03$ and therefore no polarization is observed. According to Figure 4.6, there should be negative circular polarization when the WD emerges from the primary eclipse, but it is not clear whether this is seen in Figures 4.9 and 4.10. However, Figure 4.9 shows evidence of a hump in the blue at 4500 Å. Furthermore, there is a marginal detection of positive polarization in Figure 4.10 towards the red.

4.4.3.2 Total circularly polarized flux

The total relative flux spectra was multiplied by the percentage of circularly polarized spectra to get the total circularly polarized flux. The total polarized flux is of pure cyclotron origin and is free of contamination, e.g., emission from the secondary star. The results are shown in the bottom panels of Figures 4.7 to 4.10. As expected, much of the circularly polarized flux is seen in the blue in Figure 4.7 (bottom panel) just before the eclipse and where the percentage of polarization reaches $\sim -8\%$. During the eclipse (Figure 4.8, bottom panel),

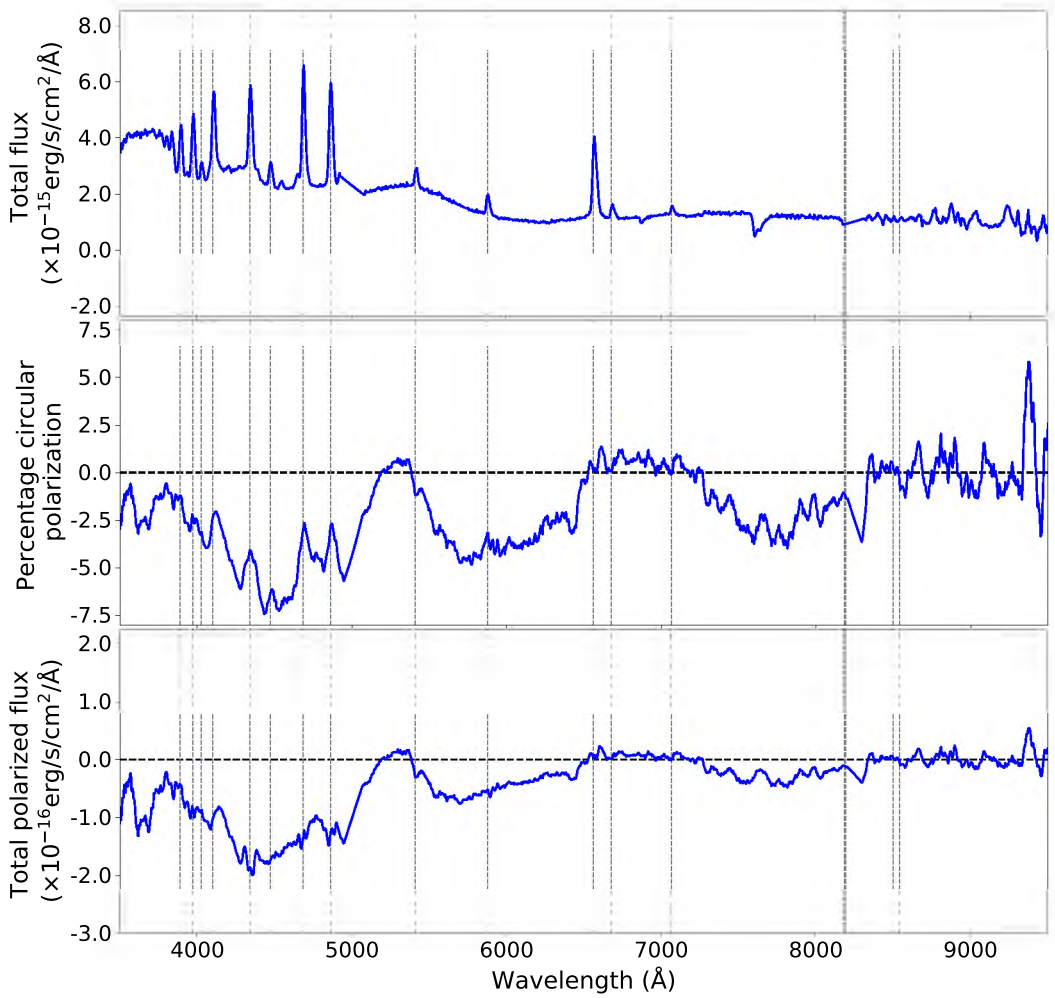

Figure 4.7: The spectra of UZ For taken before the eclipse ($\phi = 0.89-0.93$) showing the cyclotron spectrum in total relative flux (top panel), percentage circular polarization (middle panel) and the total polarized flux (bottom panel).

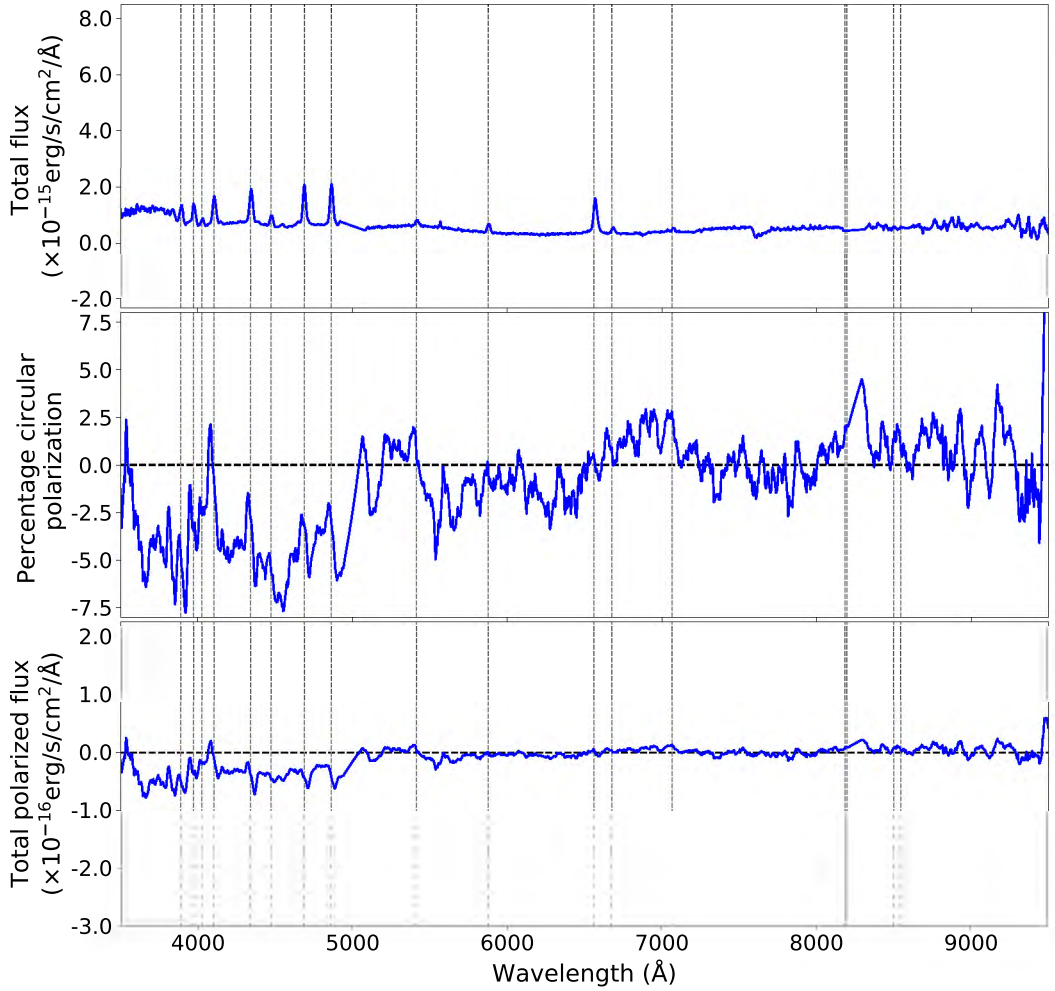

Figure 4.8: The spectra of UZ For taken during the eclipse ($\phi = 0.97-1.02$) showing the cyclotron spectrum in total relative flux (top panel), percentage circular polarization (middle panel) and the total polarized flux (bottom panel).

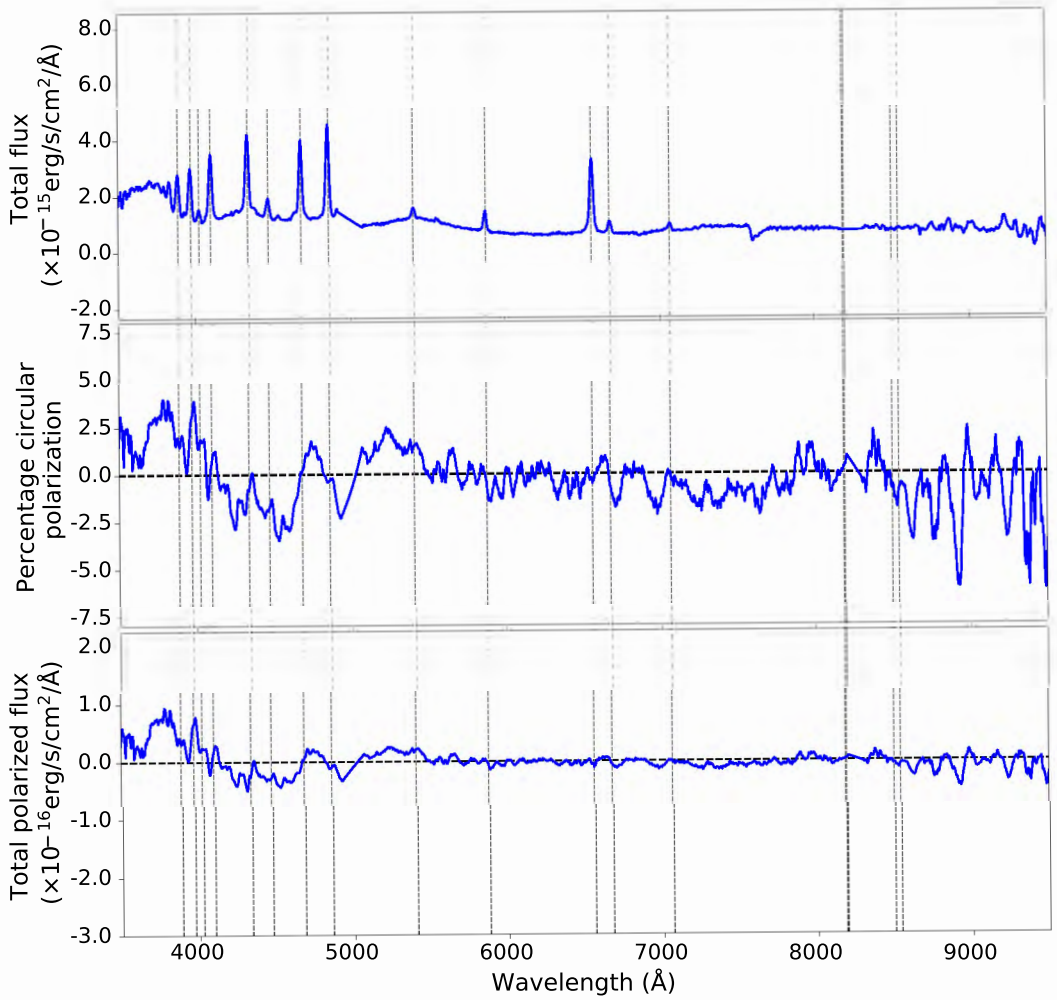

Figure 4.9: The spectra of UZ For taken while emerging out of eclipse ($\phi = 1.06-1.10$) showing the cyclotron spectrum in total relative flux (top panel), percentage circular polarization (middle panel) and the total polarized flux (bottom panel).

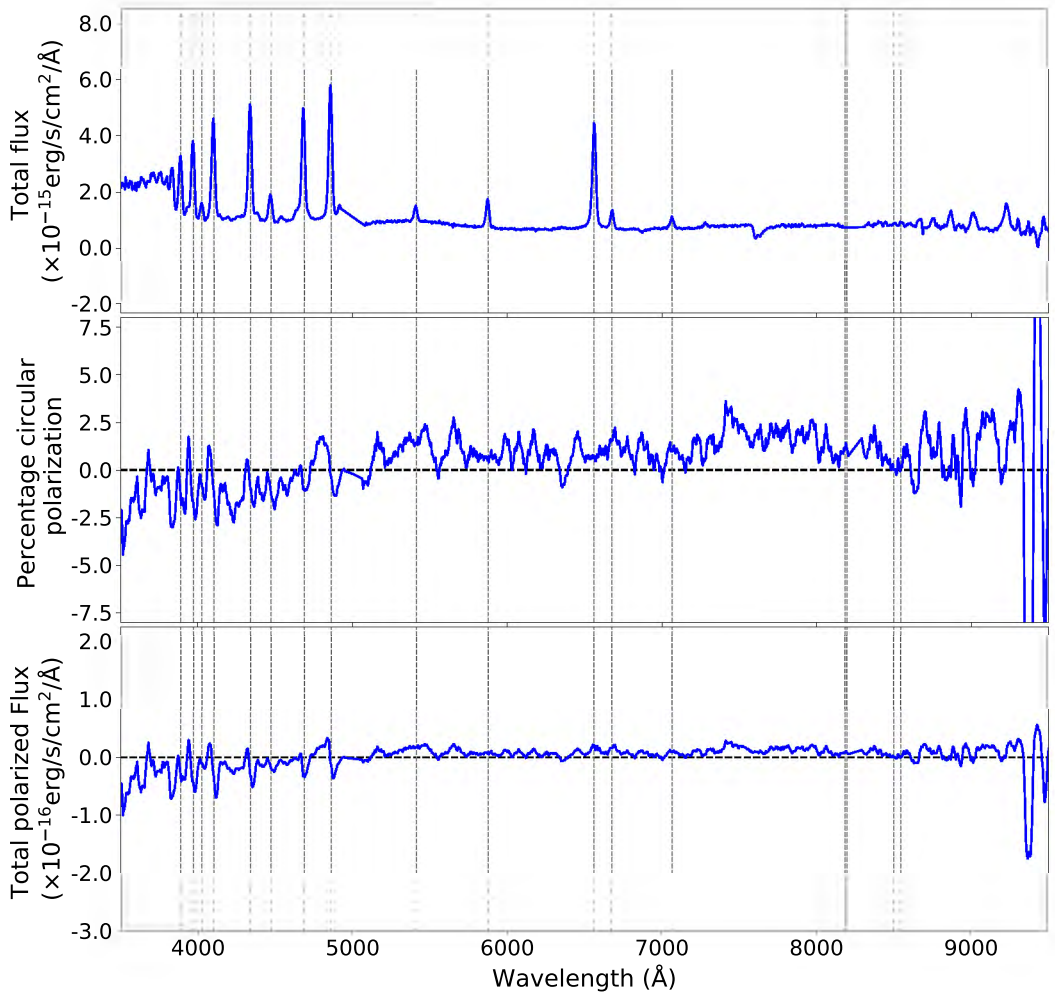

Figure 4.10: The spectra of UZ For taken after the eclipse ($\phi = 1.14-1.18$) showing the cyclotron spectrum in total relative flux (top panel), percentage circular polarization (middle panel) and the total polarized flux (bottom panel).

some polarized flux is still seen in the blue end of the spectra as explained in the above Section 4.4.3.1. The other explanation might be that either the accretion spot emitting cyclotron radiation is not completely eclipsed during the primary eclipse or there is a second region also emitting cyclotron radiation. After the eclipse, Figures 4.9 and 4.10, little or zero polarized flux is seen and the continuum is much flatter implying that the accretion spot emitting cyclotron radiation has moved away from the line of sight of the observer. The marginal positive polarization seen (in Figure 4.10) after the eclipse could be coming from the second pole that might also be emitting cyclotron radiation.

4.4.3.3 Modelling the circularly polarized flux

As mentioned in Section 1.6, there are several ways in which the magnetic field on the surface of the WD can be determined. The spacing between any two adjacent harmonics in the spectrum also provides a direct measurement of the field strength in the accretion region. Other techniques involve modelling of cyclotron harmonic features (i.e. humps) found in the spectra of these systems. The circularly polarized flux centered at phase 0.91* (Figure 4.7, bottom panel) shows broad features which peak at approximately 4500 Å, 6000 Å and 7800 Å. These features display the characteristic properties predicted by the theory for cyclotron emission from a hot plasma (e.g. Wickramasinghe & Meggitt 1982, Barrett & Chanmugam 1985).

Field strength from spacing of harmonics

While the fundamental frequency or the first harmonic usually falls into the infrared, the higher harmonics modulate the spectra in the visible region. Therefore, if more than one harmonic is identified in the spectra (as is the case in Figure 4.11), then one can infer the intensity of the magnetic field (B) in the accretion region near the magnetic pole using equation 4.2 (e.g. equation 1 of Kalomeni et al. (2005)) below:

$$w_o = \frac{eB}{m_e c} = 2\pi c \left(\frac{1}{\lambda_{n+1}} - \frac{1}{\lambda_n} \right) \tag{4.2}$$

where w_o is the fundamental frequency, c is the speed of light, m_e is the mass of the electron, e is the charge of the electron, λ is the wavelength of the harmonic and n is the integer giving the harmonic number. From using Eq. 4.2, we determined the magnetic field strength of ∼59 MG for the harmonics centred at 4500 Å and 6000 Å and the magnetic field strength of ∼41 MG for the harmonics centred at 6000 Å and 7800 Å, respectively. This implies the mean magnetic field of ∼50 MG. It is well understood that at low temperatures the positions of the nth harmonic for a given magnetic field (B) and viewing angle ($\theta = 90°$) is given by equation 54 of Wickramasinghe & Ferrario (2000b) (equation 1 of Ferrario et al. 1989) given below:

*The bright phase of UZ For start from phase 0.65 and lasts until phase 1.1, therefore the centre of the bright is at phase 0.88.

$$\lambda_n = g_n(T_e)\frac{10710}{n}\left(\frac{10^8\mathrm{G}}{B}\right), \tag{4.3}$$

where $g_n(T_e)$ is a slowly varying function of n at a given temperature and has been tabulated by Wickramasinghe (1988). For $T_e \lesssim 10$ keV, one can assume that $g_n(T_e) \sim 1$ as a first approximation. Then Eq. 4.3 becomes

$$\lambda_n = \frac{10710}{n}\left(\frac{10^8\mathrm{G}}{B}\right), \tag{4.4}$$

where λ_n is the wavelength of the peak of the harmonic and n is the harmonic number. Equation 4.4 was used to determine the harmonic number (n) of each cyclotron peak given the strength of the magnetic field determined from Eq. 4.2 and the wavelength positions of each harmonic. For $B \simeq 59$ MG, the three cyclotron features at ∼4500 Å, 6000 Å and 7800 Å are identified with harmonic numbers 4, 3 and 2, respectively. On the other hand, the three cyclotron features at 4500 Å, 6000 Å and 7800 Å may also be identified with harmonic numbers 5, 4 and 3, using the mean field strength of 50 MG. It is worth mentioning that Schwope et al. (1990) and Rousseau et al. (1996) identified these cyclotron features from the low state spectra of this system with harmonic numbers 5, 4 and 3, respectively. As mentioned in e.g. Ferrario et al. (1989), the positions and shapes of the harmonics depends on other parameters such as electron temperatures, optical depth and viewing angle. Therefore, more detailed cyclotron modelling requires more detailed phase-resolved spectropolarimetric observations to investigate this further.

Modelling of cyclotron flux

In order to determine the strength of the magnetic field of UZ For during our observations, comparisons between the observed circularly polarized flux with the theoretical flux from pure cyclotron models was required. The total circularly polarized flux was modelled following the cyclotron emission models from the stratified accretion shocks, described in Potter (1998) and Potter et al. (2002) and reviewed in Section 1.6.2, calculated based on mass flow rates in the shock ($\dot{M}_s$) of 1 g/cm^2/s and 10 g/cm^2/s for cyclotron model 1 and 2, respectively. The results from modelling, for phase = 0.91 (i.e. before the eclipse), are shown in Figure 4.11 with model 1 overplotted in black colour and model 2 overplotted in red colour. Model 1 suggests that the cyclotron spectra of UZ For is best fitted with the magnetic field of 57 MG and the viewing angle of 70° with respect to the line of sight. Note that the viewing angle is the angle between the line of sight of the observer and the direction of the magnetic field lines in the accretion region. The three cyclotron features at ∼4500 Å, 6000 Å and 7800 Å may be identified with harmonic numbers 4, 3 and 2, respectively. On the other hand, model 2 suggests that the cyclotron spectra of UZ For is best fitted with the magnetic field of ∼44 MG and the viewing angle of 67° with respect to the line of sight, According to model 2, the three cyclotron features mentioned above could be identified with harmonic numbers 5, 4 and 3, respectively. As already mentioned above, Schwope et al. (1990) and

Rousseau et al. (1996) identified these cyclotron features from the low state spectra of this system with harmonic numbers 5, 4 and 3, respectively. This is consistent with the results obtained from model 2 mentioned above but this requires a lower value of the magnetic field.

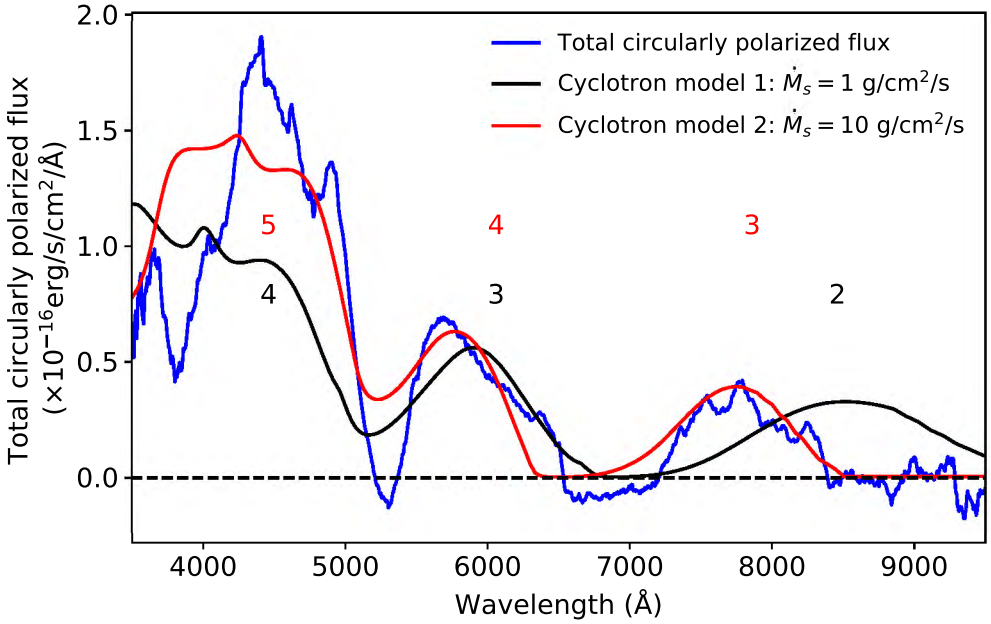

Figure 4.11: Total circularly polarized flux (blue) of UZ For centred at phase 0.91 (see Figure 4.7) and overlaid are the two pure cyclotron models: model 1 (black) with the magnetic field strength of ∼57 MG and viewing angle of 70°, and model 2 (red) with the magnetic field strength of ∼44 MG and viewing angle of 67°, based on cyclotron emission models calculated from the stratified shock with mass flow rates in the shock ($\dot{M}_s$) of 1 g/cm^2/s for model 1 and 10 g/cm^2/s for model 2. The numbers 4, 3 and 2 in black and 5, 4 and 3 in red mark the theoretical positions of the three cyclotron harmonics for each model used.

As is evident from Figure 4.11, not all the spectral features are described by the two cyclotron models. Noticeably, model 2 in red fits the cyclotron features better compared with model 1 (black) and correctly predicts the positions of the third and fourth harmonics at ∼7800 Å and 6000 Å but underestimates the polarized flux of the fifth harmonic. This is due to the fact that the cyclotron model in which the modelling is based depends on several other parameters such as the electron temperature, optical depth and the viewing angle θ. Even though the cyclotron spectra of UZ For is of pure cyclotron origin (e.g. free of thermal emission spectrum), the available data is of insufficient quality and limited phase coverage to allow for further exploration of the parameter space. Some attempts were made to vary the parameter space and the fits presented in Figure 4.11 was the best fit given the quality of the data. Also, it is not possible to fit all the harmonics seen with the single value of the magnetic field. In this study, the viewing angle θ and magnetic field strength were varied. In addition to the above, Schwope et al. (1990) noted that the flux emitted in the 5th harmonic exceeded that of the 4th harmonic. This is suggestive that the harmonics with the number $n \leq 4$ become optically thick whereas those with $n \geq 5$ are optically thin. This was also

confirmed from the models presented by Kalomeni et al. (2005) for UZ For. However, this behaviour has also been reported in the spectra of V405 Aur (Tutar & Rennan Pekünlü 2013). According to Wickramasinghe & Meggitt (1982), the lower harmonics generally have higher opacity and become optically thick first. An example of cyclotron spectra of the highly polarized RX J1313.2−3259 is shown in Section 5.3.1 (Figures 5.1 and 5.2) and this shows the importance of having multiple viewing angles when fitting models. The results presented here are discussed in Section 4.5.

4.4.4 MeerKAT radio detection

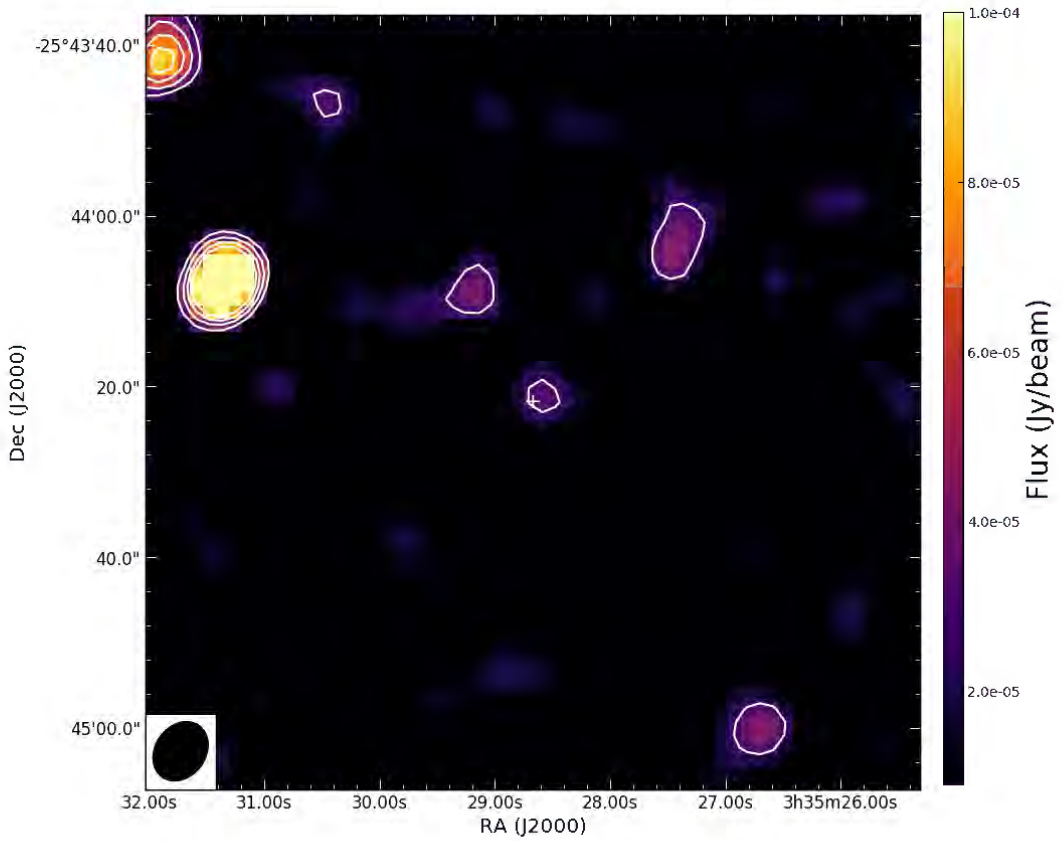

Figure 4.12: Colour map with contours overlayed of the field surrounding UZ For. The contours are at 3σ, 5σ, 7σ and 9σ levels of flux/beam. The beam on the lower left corner has dimensions of $7.45'' \times 5.91''$ and a position angle of $-35.81°$. The plus (+) sign at the centre of the image marks the position of the optical coordinates of UZ For. The colour bar on the right shows the colour scale with which the map was produced.

Figure 4.12 shows a colour map with contours overlayed of the field surrounding UZ For at radio wavelengths obtained with MeerKAT. The position of the optical coordinates for UZ For is indicated with a plus (+) sign at the centre of the image with one contour around the vicinity of the radio source. There are some noticeable radio sources in the field of view with the strongest radio emitters to the left of UZ For. These are background galaxies in

the field since all MeerKAT images are full of background galaxies with multi-wavelength counterparts. The brightest source to the left of UZ For has been identified in GAIA data release whereas the source at the top left corner is yet to be identified. Our observations taken with MeerKAT telescope in imaging mode show a faint source, with a peak flux of 30.7 ± 5.4 μJy/beam (3.4σ detection), located at (epoch J2000) RA: 03:35:28.596 $\pm$ 0.024 and Dec: $-$25:44:21.33 $\pm$ 0.34. The sigma (σ) of detection is calculated by dividing the signal with the background noise which is estimated to be 9 μJy/beam. The uncertainty in the flux density was calculated using CASA following the method of Condon (1997). The synthesized beam size is 7.45×5.91 arsec^2 at a position angle of $-35.81°$. The position of this source coincides, within the uncertainty given, with the optical coordinates of UZ For $-$ RA: 03:35:28.652 $\pm$ 0.048 and Dec: $-$25:44:21.766 $\pm$ 0.057 (epoch J2000, Gaia Collaboration 2018).

The results presented here makes UZ For the first AM Her system to be detected in radio at 1.28 GHz. This study demonstrate that it is possible to detect AM Her systems, in the L-band centred at 1.28 GHz with MeerKAT. However, the current dataset is of insufficient quality* and phase coverage to allow for further spectral and/or orbital phase dependency investigation of this source since the flux reported in this study is below a 5σ of detection. Further details on this measurements and results is discussed in Section 4.5.3.

4.5 Discussion and conclusions

This chapter presented the first simultaneous circular spectropolarimetry obtained with SALT RSS instrument and radio observations obtained with MeerKAT. Two other telescopes, the SAAO 1.9-m telescope and the MeerLICHT, were used during these observations in photometric mode. To aid with the interpretation of the SALT circular spectropolarimetry results, photopolarimetry observations obtained with the HIPPO instrument on the SAAO 1.9-m a few weeks before the simultaneous observations are also presented.

4.5.1 Photometry and polarimetry

Section 4.4.1 presented photometric results from the simultaneous observations obtained with the SAAO 1.9-m telescope utilizing SHOC and MeerLICHT. The results from these two telescopes, shown in Figure 4.5, agree with each other since the MeerLICHT magnitudes trace the shape of the eclipse produced with SHOC. Comparisons between the light curve obtained with SHOC and HIPPO (Figure 4.6) instruments show that the former is dominated by higher amplitude flickering than the latter. This is expected since UZ For changes between low and high state in timescales ranging from a few weeks to months.

The results from both unfiltered circular and linear photopolarimetric observations of UZ For obtained with HIPPO were presented in Section 4.4.2. The circular polarimetry shows negative polarization from phases $\sim$0.7$-$1.1 with polarization reaching $\sim -5\%$ before

*The observations from MeerKAT lasted $\sim$100 minutes and this is a single epoch.

the eclipse. As mentioned in Section 4.4.2, there is evidence of the reversal in the sign of circular polarization around phase 1.1. The circular photopolarimetric results obtained in this study are not consistent with those reported in literature (see e.g. Berriman & Smith 1988, Ferrario et al. 1989, Bailey & Cropper 1991). These authors reported positive circular polarization at phases beginning at 0.65 and lasting until phase 1.2. However, the orbital phases in which circular polarization is observed is similar to those those reported by Ferrario et al. (1989). According to e.g. Katajainen et al. (2003), a single accreting pole can only give brief sign reversal when the accreting region is near the limb of the WD and also if the geometry is such that the angle between the line of sight and the magnetic field can go through 90°. Some AM Her systems are known to show reversal in the sign of circular polarization and this is interpreted as viewing emission from the second accreting pole e.g. SDSS J015543.40+002807.2 (Wiehahn et al. 2004). This kind of behaviour is seen from one cycle to another, that is, the sign-reversal is stable or persistent for a long time. In this study, the negative circular polarization increases from phases greater than 0.6 leading to the eclipse. The reversal in the sign of polarization seen in our results suggest that during our observations the second pole (in the opposite hemisphere) is responsible for the polarized radiation. There are other AM Her systems that show negative polarization, e.g. VV Pup (Liebert & Stockman 1979) and UW Pic (Romero-Colmenero et al. 2003). In the former (or rather both), the reversal in the sign of polarization was interpreted as evidence that the additional radiation is due to accretion onto a second region of the WD, where the longitudinal component of the magnetic field is of the opposite sign with respect to that at the primary accreting pole.

The unfiltered linear polarimetry shows polarization reaching ∼5% when out of eclipse. A pulse of linear polarization is seen during the eclipse reaching ∼10% and decreasing gradually before phase 1.1. After that (phase 1.1), the polarization is consistent with 5%. The percentage of linear polarization as well as the orbital phases in which is observed is consistent with the results presented by Berriman & Smith (1988) with the pulse in linear polarization occurring around the eclipse. However, the observations reported by Berriman & Smith (1988) were of low resolution, this thesis presents an improved phase resolution and now reveals more troughs and humps which coincide with the increase and/or decrease of the photometric light curve.

4.5.2 Spectropolarimetry

The total relative flux shows a continuum that rises in the blue with a broad hump around 5500 Å. The slope of the continuum is consistent with those recorded in the literature when UZ For was in a low state (Beuermann et al. 1988, Schwope et al. 1990). However, the spectra presented in this study were taken during an intermediate or high state and this is supported by strong emission from the HeII 4686 Å and Balmer lines whereas those of Beuermann et al. (1988) and Schwope et al. (1990) were taken during a low state.

The percentage of circularly polarized spectra shows negative circular polarization reaching $\sim -8\%$ in the blue before the eclipse and decreasing with increasing wavelength. In

addition to negative polarization, the circularly polarized spectra showed three cyclotron features (at ∼4500 Å, 6000 Å and 7800 Å) associated with harmonic numbers 4, 3 and 2, respectively. Our recent modelling results using cyclotron emission models based on an accretion shock with a higher mass flow rates suggest that there three features could also be identified with harmonic numbers 5, 4 and 3, respectively. These three features weaken going into the eclipse. When the WD and the accretion spot(s) are emerging from the eclipse, only the strongest hump (∼4500 Å) is still visible and there is a possibility of an additional hump below 4000 Å but this shows positive polarization. The additional hump is present in the spectra presented by Ferrario et al. (1989). After the eclipse, the spectrum appears flat and exhibits nonzero polarization in the red.

The resulting polarized flux from this cyclotron spectra was modelled using pure cyclotron models with the magnetic field strength of ∼57 MG and 44 MG for model 1 and 2, respectively. Noticeably, the overlayed cyclotron model 1 (black) does not fit all the cyclotron harmonics well especially in the red part of the spectrum. On the other hand, the second cyclotron model fits the 3rd and 4th harmonics well but fail to reproduce the flux level of the 5th harmonic in the blue. This is because the cyclotron models used are specific for a given magnetic field and depends on other parameters like the electron temperatures, optical depth, viewing angle, etc., therefore changing any of these parameters will give a slightly different fit to the polarized flux. In addition, the mismatch between the observations and the models could be attributed to the second spot (or pole) on the surface of the WD which is also emitting cyclotron radiation. As already mentioned in Section 4.4.3.3, the current dataset is underconstrained to allow for further investigation.

Previous studies of UZ For in low state (Beuermann et al. 1988, Allen et al. 1989, Schwope et al. 1990) and high state (Ferrario et al. 1989) revealed the presence of at least three resolvable cyclotron humps at different wavelengths and these were attributed to a field strength of 51−57 MG for the main accretion region with the possibility of the second accretion region with field strength of 33−75 MG also emitting cyclotron radiation. The three cyclotron features were identified with harmonic numbers 5, 4 and 3, respectively (Schwope et al. 1990, Rousseau et al. 1996). In this thesis two models with different mass flow rates were used to model the bright-phase cyclotron spectra of UZ For. Model 1 suggests that the cyclotron spectra of this system could be described with a field strength of 57 MG and the three cyclotron features could be identified with harmonic numbers 4, 3 and 2. On the other hand, model 2 suggests that the cyclotron spectra of this system could be fitted with a field strength of 44 MG and the three cyclotron features could be identified with harmonic numbers 5, 4 and 3. Thus the results of model 2 are more in agreement with the studies of Schwope et al. (1990) and Rousseau et al. (1996). The position of the harmonics presented in this work is not consistent with those of the other authors (e.g. Allen et al. 1989, Ferrario et al. 1989). This is expected since the position of the harmonics depends on the electron temperature, optical depth and viewing angle, among other properties. However, the strength of the magnetic field derived in this work is consistent with those determined during the bright phase by different authors (e.g Ferrario et al. 1989, Schwope et al. 1990).

4.5.3 Radio emission

This study presented evidence of radio emission at the expected position of UZ For using MeerKAT in the L-band centred at 1.28 GHz. The results show a source with a peak flux of 30.7 ± 5.4 μJy/beam at the position of UZ For. As already mentioned in Section 4.4.4, UZ For is the first AM Her system to be detected in the L-band in radio at 1.4 GHz and it is one of three mCVs to be detected at 1.28 GHz (or 1.4 GHz); the other two systems are AE Aqr (e.g. Bookbinder & Lamb 1987) and LAMOST J024048.51+195226 (Pretorius et al. 2021). The reported magnitude of UZ For by the AAVSO ranges between 16.5−16.1 around the time of MeerKAT observations. This is consistent with the out-of-eclipse i, q, r, g, z magnitudes obtained from the MeerLICHT observations. Barrett et al. (2017; 2020b) detected UZ For in the radio regime using the VLA at C-band (4−6 GHz). They found it to have a flux density of 78 ± 9 μJy* and showed circular polarization reaching a percentage of -100 ± 42. The other bands, X-band (8−10 GHz) and K-band (18−22 GHz), yielded non-detection of the source. The flux density obtained at 1.28 GHz in this study is factor of two lower than that recorded at 4–6 GHz by Barrett et al. (2020b), and demonstrates the sensitivity of MeerKAT telescope. These results suggest that UZ For is variable in radio wavelengths, but the timescales of this source's variability is not yet known. Barrett et al. (2020b) concluded that the most likely emission mechanism that produces highly circularly polarized radio emission of short duration in mCVs is electron cyclotron maser emission from coronal loops of the donor star where plasma density and frequency are low enough to allow cyclotron maser emission to escape. They were able to directly estimate the mean coronal magnetic field strengths of the donor stars in several mCVs to be ∼1–4 kG, assuming that the donor stars have a high magnetic filling factor (50%). The estimated coronal magnetic field strength of the donor star in UZ For is 1960 ± 365 G.

The majority of the mCVs detected in radio frequency by Barrett et al. (2017; 2020b) showed radio emission in no more than two frequency bands (except AM Her, AR UMa and AE Aqr) and more than one epoch (except AR UMa and AE Aqr). As shown in Table 1 of Barrett et al. (2020b), seven mCV systems were detected in more than one frequency band, four of these systems (e.g. VV Pup, MR Ser, AR UMa and WX LMi) show that the flux density decreases with the increasing frequency band – implying a negative spectral index. The remaining three systems (e.g. AM Her, V603 Aql and AE Aqr) show that the flux density increases with the increasing frequency band – implying a positive spectral index. However, these results are insufficient to warrant any robust conclusion regarding the spectral index, given the nature of the observations (i.e. few minutes exposures) from which this conclusion is based on. Recent studies conducted by Pretorius et al. (2021) and Barrett (2022) of the new AE Aqr-like system, LAMOST J024048.51+195226, using radio observations obtained with MeerKAT at 1.28 GHz and the VLA at 2–26 GHz reveal that this source has a negative spectral index (i.e. -0.60 ± 0.02) similar to that of V603 Aql.

*Barrett et al. (2017) earlier reported a flux density of 315 ± 101 μJy for UZ For and weak circular polarization's 13 ± 19 %. However, their results were based on low signal to noise ratio. Therefore, I will only quote the flux densities from Barrett et al. (2020b).

As mentioned in Barrett (2022), both LAMOST J024048.51+195226 and V603 Aql show strong, randomly varying, circular polarization. On the other hand, the radio observations of AE Aqr presented by Barrett (2022) show that this source has a positive spectral index. While LAMOST J024048.51+195226 shows strong circular polarization in radio, AE Aqr show unpolarized radio emission. However, the optical properties of these two systems are similar (see e.g. Thorstensen 2020b). These results show that radio emission in mCVs depend on both the accretion state and the spectral distribution. Therefore, further radio observations of different mCV systems covering multiple bands (and orbital phases) are required to further investigate their radio emission and spectral distribution.

UZ For lies in one of the MeerKAT International GHz Tiered Extragalactic Exploration (MIGHTEE, Jarvis et al. 2016) survey fields, its variability can be studied further through commensal access to the MIGHTEE data by the ThunderKAT projects. Therefore, it will continue to be monitored in both optical and radio wavelengths. Such radio observations will allow us to investigate any orbital variability and/or frequency dependence, assuming that this source is detected in the future, of the radio emission from UZ For. An example of a spectral dependence of an AM Her system had been presented recently for LW Cam by Barrett et al. (2020b). This was achieved by rebinning the ten minutes X-band observations of LW Cam into bins of 256 MHz. Their results show a rather flat spectral distribution which reveal short-lived narrowband emission feature around 10.295 GHz with a width of $<$300 MHz and they attributed this to a maser event.

4.6 Summary

One of the objectives of this chapter was to present and analyze multi-wavelength observations of UZ For. The first circular spectropolarimetry observations of an AM Her system from SALT were reduced and analyzed and found that the level and sign of circular polarization is consistent with that obtained from photopolarimetric observations obtained with HIPPO. However, the level of circular polarization from SALT spectropolarimetry is almost twice the value from HIPPO suggesting that the former observations were obtained during a different state than the latter. Earlier, Berriman & Smith (1988) had reported significant fluctuations in the level of circular polarization ranging from 5% to 10% from one night to another.

The circularly polarized spectropolarimetry of UZ For revealed three negative cyclotron features (cyclotron humps) at ∼4500 Å, 6000 Å and 7800 Å which were identified with harmonic numbers 4, 3 and 2 in a magnetic field of 57 MG from modelling. However changing the mass flow rate in the stratified shock to $\dot{M}_s = 10$ g/cm^2/s, the same cyclotron features at ∼4500 Å, 6000 Å and 7800 Å can be identified with harmonic numbers 5, 4 and 3 in a magnetic field of ∼44 MG with harmonic number 2 shifted in the infrared (i.e. beyond 10000 Å). The magnetic field strength of the main emitting region is consistent with the field strengths of this system reported in the literature (e.g. Ferrario et al. 1989, Schwope et al. 1990). As already mentioned in Section 1.6, previous observations of this kind such as those

presented in Ferrario et al. (1989) and Schwope et al. (1990) had to subtract contamination from the ballistic stream, magnetic confined stream and the secondary star in order to reveal the pure cyclotron spectra of this target. The circularly polarized spectropolarimetry observations presented in this thesis demonstrate that SALT can be used to study AM Her systems in circular spectropolarimetry mode without the need to remove extra contamination in order to reveal the pure cyclotron spectra of the target and such observations can be used to infer the magnetic field strengths, among other properties, through modelling of the cyclotron spectra.

UZ For was detected at 1.28 GHz in the radio observations made with MeerKAT although it was a factor of two fainter compared with previous observations at higher frequency of 4–6 GHz conducted with the VLA (Barrett et al. 2017; 2020b). This study demonstrates that it is possible to detect AM Her systems in the L-band. It is worth mentioning that UZ For is the first AM Her and one of three mCVs, which include AE Aqr (e.g Bookbinder & Lamb 1987) and LAMOST J024048.51+195226.9 (Pretorius et al. 2021), to be detected in the L-band in the radio.

The properties of UZ For presented in this chapter are summarized below and can best be understood with the aid of the model schematic and/or geometry of this binary system shown in Figure 4.13. This figure is based on an original figure (Figure 8 of Ferrario et al. 1989) but now presents geometries that are based on measurements made by the modeling and fitting of actual observations. Figure 4.13 combines Doppler tomography properties discussed in Chapter 3 and polarimetric properties discussed in Section 4.4.2 (including the works from Berriman & Smith 1988 and Bailey & Cropper 1991), and include the physical size and geometry of the binary (i.e. the primary, the red dwarf, the ballistic stream trajectory and the magnetic confined stream) based on modelling of data directly.

Circular polarization:

- negative circular polarization is observed starting around phase 0.65 and lasting until phase 1.1, and after this phase ($\phi = 1.1$) the polarization is consistent with zero,
- the maximum circular polarization is observed at phases ranging between 0.85–0.9 coinciding with the centre of the bright phase reported in the literature, and,
- a brief reversal in sign of circular polarization observed around phase 1.1 – consistent with the.

Linear polarization:

- linear polarization is observed throughout the coverage of the data (i.e. from phase 0.5 to 1.2), and,
- a pulse of linear polarization centred at phase 1.0 is observed around the eclipse with polarization reaching 15%.

Circular spectropolarimetry:

- phase 0.89–0.93: maximum circular polarization reaching -8% – with detection of the three cyclotron harmonics,
- phase 0.97–1.02: detection of negative circular polarization in the blue reaching -5% during the primary eclipse,
- phase 1.06–1.10: zero polarization and the continuum is flatter – implying that the spot emitting cyclotron radiation has moved from view, and,
- phase 1.14–1.18: detection of marginal positive polarization is seen around these phases and could be coming from the second emitting region.

Radio observations:

- UZ For was detected in radio at 1.28 GHz and was found to have a flux density of 30.7 $\pm$ 5.4 μJy/beam with the rms of 9 μJy/beam.

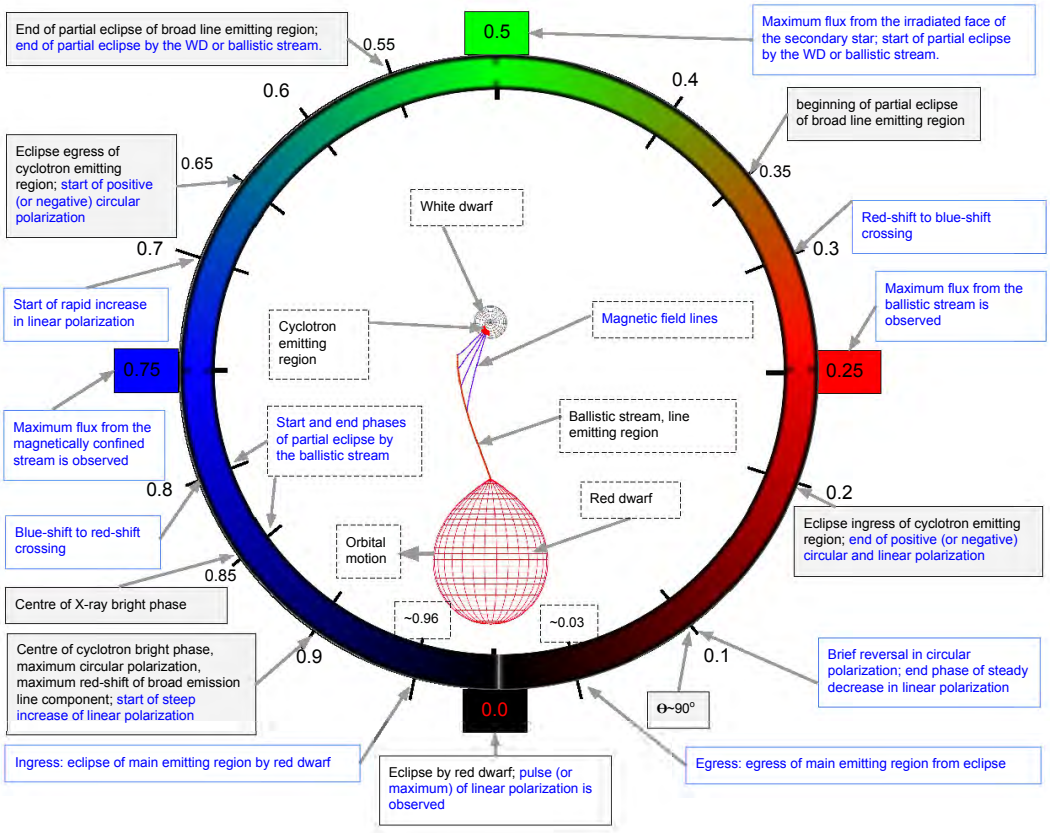

Figure 4.13: A schematic illustration of the model of the UZ For as viewed from the top. The four phase colours black, red, green and blue of the ring correspond to the phases of maximum flux 0.0, 0.25, 0.5 and 0.75 mentioned in Section 3.7.3. The system parameters are the same as in Section 3.6. The physical size and geometry of the red dwarf, ballistic stream and magnetic field lines are physically correct, except for radius of the WD which has been exaggerated to five times the calculated radius, and are based on the assumed system parameters. The physical size of the cyclotron emitting region is arbitrary. Different orbital phases has been labelled and mark the various observational properties shown in text-boxes. The text in black is from Ferrario et al. (1989) whereas the text in blue is for this work including Berriman & Smith (1988) and Bailey & Cropper (1991).

Chapter 5

Summary and future work

5.1 Summary

In this thesis, I have presented a detailed multi-wavelength study of the eclipsing AM Her system, UZ For. This work was done in collaboration with various people who provided some of the data and in some cases contributed to the analysis and discussion. These studies are summarized in the next three paragraphs.

Chapter 2 focused on high-speed photometry of UZ For and it was demonstrated through an updated O−C diagram that the ephemeris presented in Paper I continues to deviate from a linear and quadratic trends of ∼60 s. These deviations were explained as due to either the presence of two circumbinary planets in orbit around UZ For or some form of Applegate mechanism due to magnetic cycle activities on the surface of the red dwarf. As already mentioned in Chapter 2, some residuals remain after subtraction of the two elliptical terms. This implies that neither the two planetary model nor Applegate mechanism are sufficient to explain the O−C diagram of UZ For on their own. Therefore, it is proposed that both mechanisms, some form of Applegate mechanism and circumbinary planets, should be considered while explaining the O−C diagram of UZ For.

In Chapter 3, detailed normal Doppler maps, flux modulation maps and phase of maximum flux maps based on both the standard and inside-out Doppler projections of UZ For were presented using emission lines in the blue and red part of the spectrum, specifically the Hβ, HeII 4686 Å and CaII 8542 Å. Both the standard and inside-out Doppler maps based on emission lines from the blue wavelengths are dominated by emission from the ballistic stream and the threading region, the magnetically confined accretion stream as well as low-level emission from the irradiated face of the secondary star. The absence of strong emission from the irradiated face of the secondary star, in comparison with the low-state Doppler map of Schwope et al. (1999), is attributed to the shielding of the donor star by the enhanced accretion curtain during a high state. On the other hand, the standard and inside-out Doppler maps from the CaII 8542 Å line in the red wavelengths are dominated by emission from the irradiated face of the secondary star. This is expected since CaII lines

originate from the chromosphere of the secondary star which is illuminated by extreme ultraviolet and X-rays radiation from the accretion region(s) on the surface of the WD. The flux modulation amplitude maps from these three lines show that the ballistic stream and the threading region, the magnetically confined accretion stream and the irradiated face of the secondary star are flux-modulated. This is because UZ For is an high-inclination eclipsing system and we expect emission from various parts of the binary to modulate with the orbital phase. The phase of maximum flux maps show the orbital phase at which a specific emission component appears brightest to an observer. These maps are easily understood with the aid of the geometry of UZ For shown in Figure 3.15 constructed based on measurements made by the modeling and fitting of actual observations and correctly predicts the maximum flux from the three components identified in the Doppler maps.

Chapter 4 presented simultaneous optical and radio observations of UZ For. This was the first time SALT and MeerKAT were used in such a manner. The SALT circular spectropolarimetry results (discussed in detail in Section 4.4.3) show circular polarization reaching about -8% before the eclipse (phase 0.91) and the polarization is consistent with zero after the eclipse. This result is consistent with the simultaneous linear and circular photopolarimetry results obtained with HIPPO which shows circular polarization reaching about -5% during the bright phase. In addition to this, the phases at which the linear and circular polarization is observed in this thesis is in agreement with those from literature (e.g. Berriman & Smith 1988, Bailey & Cropper 1991). However, all these studies from literature reported positive polarization. The polarization behaviour of UZ For is best understood using the light curve of this system and the geometry of this system shown in Figure 4.13. The light curve of this system can be divided into two components: the faint phase (phase 0.2–0.65) and the bright phase (phase 0.65–1.2). The polarization seen before the eclipse (during the bright phase) is understood as due to the fact that the main region emitting cyclotron radiation is visible to the observer during these orbital phases (see Figure 4.13). The absence of detectable level of polarization is understood as due to the fact that the accretion region emitting cyclotron radiation is eclipsed during the faint phase. The cyclotron spectra (and circularly polarized flux) at phase 0.91 show the presence of three negative humps which are interpreted as cyclotron harmonics from the hot plasma and these were modelled using cyclotron emission models based on a stratified accretion shock with mass flow rates of 1 g/cm^2/s and 10 g/cm^2/s for model 1 and 2, respectively. According to model 1, the cyclotron spectra of UZ For is best fitted with the magnetic field strength of $\sim$57 MG and the three cyclotron features are identified with harmonic numbers 4, 3 and 2, respectively. On the other hand, model 2 suggest that the cyclotron spectra of UZ For is best fitted with the field strength of $\sim$44 MG and the three cyclotron features could be identified with harmonic numbers 5, 4 and 3, respectively. The result of model 2 is consistent with the results of Schwope et al. (1990) and Rousseau et al. (1996) who identified these three cyclotron features as harmonic numbers 5, 4 and 3, respectively. Even though the observations are of insufficient quality for detailed modelling, the magnetic field strength determined in this thesis is consistent with those from literature (e.g. Ferrario et al. 1989, Schwope et al.

1990). While this is the first observations of its kind (i.e. circular spectropolarimetry) to be carried out by SALT, this result demonstrates that other magnetic systems can now be studied with this telescope. Complementary photometry were obtained with the SAAO 1.9-m and MeerLICHT to aid with the interpretation of the spectropolarimetry observations. The MeerKAT radio observations show a faint source which has a peak flux density of 30.7 $\pm$ 5.4 μJy/beam at 1.28 GHz at the position of UZ For. As already mentioned in Chapter 4, this makes UZ For the first AM Her system to be detected in radio at 1.28 GHz and one of three mCVs (e.g. AE Aqr (Bookbinder & Lamb 1987) and LAMOST J024048.51+195226 Pretorius et al. (2021)) to detected in the L-band (1–2 GHz).

5.2 General conclusion and future work

These studies demonstrate that multi-wavelength follow-up of CVs is essential for better interpretation of their different emission processes, accretion mechanisms and understanding how these characteristics change with time. The following sections contain the general conclusion and potential future work for this study.

5.2.1 Variation in eclipse times

The high-speed photometry presented in this thesis was crucial not only in further confirming that mid-eclipse times are indeed variable, but also solidifying that there are two periodicities of 5.82(3) and 14.67(1) years, respectively. The new mid-eclipse times extended the baseline of observations by a further eight years (from 27 to 35 years) and covers at least half of the longest period of the outer planet showing a maximum and minimum in eclipse time residuals. However, the cause of variability can either be due to the presence of extrasolar planets around the binary or some form of Applegate mechanism due to magnetic cycle activities on the surface of the red dwarf, or the combination of both. Future photometric follow-up of this target will allow further investigation of the long-term behaviour of the mid-eclipse times. Furthermore, in order to perform analysis of the selected best-fitting solutions to the mid-eclipse times well, it is encouraged to use one of the more sophisticated methods such as Markov Chain Monte Carlo (MCMC), e.g. EMCEE* (Foreman-Mackey et al. 2013), to analyse the parameter correlation in detail.

UZ For is the third eclipsing CV after HU Aqr (Goździewski et al. 2015) and NN Ser (Bours et al. 2016) which shows consistent eclipse times variation from one observation to the next which could still be possibly explained by the presence of extrasolar planets. There are other AM Her systems that show variations in their mid-eclipse times, e.g. DP Leo (Beuermann et al. 2011) and most recently HY Eri (Beuermann et al. 2020). However, for the former, new eclipse times seem to dispute the extrasolar planets hypothesis whereas for the latter, HY Eri, the baseline is still too small to warrant any conclusion. It is worth mentioning that recent studies conducted on HW Vir (Esmer et al. 2021, Brown-Sevilla

*EMCEE is an open source Python implementation of the affine-invariant ensemble sampler for Markov Chain Monte Carlo (MCMC) proposed by Goodman & Weare (2010).

et al. 2021) and NY Vir (Er et al. 2021) revealed that the eclipse times variations of these two systems are also consistent with circumbinary planets. However, the planetary systems suggested were also unstable on short time scales.

We will continue to monitor UZ For in order to study the evolution of the said eclipse times variations. This work will be extended to other eclipsing CV binaries with Declination lower than $+10°$. Similar work has been carried out by Bours et al. (2016) in the northern hemisphere were they studied 67 eclipsing binaries. Their results showed that the probability of observing eclipse time variations increases significantly with observational baseline. They found that for binaries in which the observational baseline is greater than 10 years and spectral type of K2−M5.5, these systems show eclipse time variations of up to 2 minutes. However, they found no evidence of eclipse time variations for binary systems where the secondary is of an M6 spectral type or later and the observational baseline is less than 10 years. The range of orbital periods that are revealed by mid-eclipse timings range between a few years to decades. Therefore, an observational baseline of several decades is required in order to detect any cyclic variations.

5.2.2 Spectroscopy

We presented phase-resolved spectroscopy of UZ For covering one orbital phase obtained while the system was in a high state and used the spectra perform to Doppler tomography using the code described in Kotze et al. (2015; 2016). We note that the inside-out tomograms prove to be an invaluable complement to the standard maps. In particular, we find that the inside-out Doppler map of the Hβ emission line clearly defines and maps the high-velocity magnetically confined accretion stream being funnelled towards the position of the WD. The results presented here are outstanding and further phase-resolved spectra of this target through different accretion states would give us more insight into the changing accretion dynamics in different states.

For future studies, we will perform a detailed photometric and spectroscopic study of poorly studied mCVs and other AM Her candidates discovered in other surveys such as Mobile Astronomical System of Telescope-Robots (MASTER; Lipunov et al. 2010, Kornilov et al. 2012), CRTS (Drake et al. 2009), ASAS-SN (Shappee et al. 2014) and future ThunderKAT (Fender et al. 2017) and/or MeerKAT surveys and current and future X-ray surveys carried out by the following satellites: XMM-Newton (Jansen et al. 2001), *Chandra* (Weisskopf 1999, Weisskopf et al. 2000), INTEGRAL (Winkler et al. 2003), Swift/BAT (Gehrels et al. 2004, Barthelmy et al. 2005), MAXI (Matsuoka et al. 2009), NuSTAR (Harrison et al. 2013), ASTROSAT (Singh et al. 2014) and eROSITA (Predehl et al. 2010, Pillepich et al. 2012). Recently, Schwope et al. (2022) reported on the discovery of the first AM Her system, eRASSt J192932.9−560346, with the eROSITA during the ongoing all-sky survey by this satellite. eRASSt J192932.9−560346 is a bright source showing double-peaked light curves typically of two-pole accreting system and also it is an eclipsing system. This source is highly polarized with linear polarization reaching 15% and show strongly variable circular polarization ranging from -10% to $+10\%$. In addition, the optical spectra of eRASSt

J192932.9−560346 obtained with SALT show strong Balmer, HeII and HeI emission lines. This source offers great potential for photometric and Doppler tomography in order to constrain the physical parameters and accretion geometry of the system. Other future X-ray astronomy facilities include ASTRO-H (see e.g. Takahashi et al. 2010; 2012; 2014), International X-ray Observatory (IXO, Rando et al. 2010) and Gravity and Extreme Magnetism Small Explorer (GEMS, Swank & et al. 2010).

The photometric observations will be used to improve or determine orbital periods for those systems. The interesting targets, especially eclipsing AM Her systems, will then be studied in detail through spectroscopic and photometric observations to study their emission dynamics through Doppler tomography and determining system parameters through eclipse modelling. Doppler tomography is useful in constraining the physical parameters of the binary systems such as mass ratio, individual masses of the primary and secondary, etc. and therefore this technique can be used in other eclipsing CVs with unknown orbital parameters constrain their parameters. An example of such a study was carried out recently by Thorstensen et al. (2020) where they performed a detailed photometry and spectroscopic follow-up of eight AM Her candidates with the aim of determining or improving existing orbital periods for these systems. They found that the orbital periods of these systems range between 80 and 219 minutes and are typical of AM Her systems. Seven of their candidates, for which spectroscopic observations were available, show high-amplitude radial velocity curves, strong Balmer and HeII 4686 Å emission lines, and makes these systems ideal for Doppler tomographic investigations.

5.2.3 Multi-wavelength study

The first circular spectropolarimetry results from SALT revealed the presence of three negative cyclotron humps in the spectra of UZ For. The polarized flux was modelled with the magnetic field strength of 57 MG at a viewing angle of 70°. We were able to accurately determine the orbital phases at which the circular polarization emission was emitted with the aid of the SHOC photometry observations taken simultaneously with the SALT observations. However, we were not able to determine the field structure or the location of the magnetic poles due to the limited quality of the data. Therefore, more follow-up circular phase-resolved spectropolarimetry of this source is required. Section 5.3.1 shows an example of circular spectropolarimetry observations of a highly circularly polarized source, RXJ1313.2−3259, obtained with SALT. These observations showing resolvable cyclotron harmonics will be modelled in order to constrain the geometry and location of the magnetic poles. Such observations will also be used to investigate the effects of other parameters such as optical depth, temperature, size, etc., on circular polarization of these systems.

We detected UZ For at 1.28 GHz with the MeerKAT and obtained a flux density which is at least two times lower than that obtained with the VLA at 4−6 GHz (Barrett et al. 2017; 2020b). The radio observations presented in this thesis were obtained while MeerKAT was operating in imaging mode and lasted only 100 minutes and this is still less than the full orbit of UZ For. Future radio observations of this target, in imaging and polarization mode,

in different bands and covering multiple orbits are encouraged in order to investigate the orbital and long-term variability timescales of this system. Such observations will be used to determine whether the radio emission originates from closer to the WD or the secondary star or both. In addition, this object will be included in future radio surveys of mCVs (see Section 5.3), and falls in the footprint of the MeerKAT's MIGHTEE survey (Jarvis et al. 2016).

5.3 Other future prospects

In future, we will conduct an optical and radio study of mCVs southward of the +10° in declination to complement the work that is being done by Barrett et al. (2017; 2020b) in the northern hemisphere. In their study, Barrett et al. (2017; 2020b), presented observations of at least 122 mCVs obtained with the VLA over multiple semesters. They reported detection of 33 radio sources, 28 of which are new detections and subsequently increasing the number of known radio mCVs sources to over 40. Although their sample contains mCV targets in both the northern and southern hemisphere, we note that most of their targets were visited only twice and in general, only for a few minutes per frequency band. In our case, we will prioritize mCV candidates with known orbital periods and with parallax measurements given in the GAIA DR2 catalogue. We will use the distance as one of the criteria, i.e. distances < 700 pc. A similar study was recently carried out by Hewitt et al. (2020) using MeerKAT at 1.28 GHz for nova-likes with known orbital periods and with distances within 350 pc. Their final sample contained eleven nova-likes and they reported a 5σ detection of four of the systems while placing further upper limits constrain to one of the system's properties.

5.3.1 RXJ1313.2−3259

RXJ1313.2−3259 (hereafter RXJ1313−32, also known as V1043 Cen) was identified as one of the brightest X-ray source in the RASS programme (Voges et al. 1999). It was one of those source detected at high galactic latitudes (Thomas et al. 1998) and has an orbital period of 4.19 h (Thomas et al. 2000). Gänsicke et al. (2000) found this system to be a low-accretion rate AM Her systems which makes it ether a new CV or an old CV in a prolonged state of accretion. RXJ1313−32 is located at a distance of 200 pc and its magnetic field strength, determined from cyclotron modelling, is 56 MG. Thomas et al. (2000) give the following linear ephemeris for RXJ1313−32:

$$T(\mathrm{BJD_{TDB}}) = 2448632.4442(43) + 0.17459209(15)E.$$

Recently, Barrett et al. (2020b) presented radio observations of RXJ1313−32 with the VLA and was found to have a flux density of 20 ± 5 μJy. In addition, RXJ1313−32 show 100% circular polarization and this is consistent with electron cyclotron maser emission. They estimated the coronal field strength of the secondary star to be 3563 ± 730 G for this source.

RXJ1313−32 was observed with SALT, under proposal 2020-2-SCI-035 on 2021 April 16 and again on 2021 April 22 (four months after first submission of this thesis) utilizing the RSS instrument in circular spectropolarimetry mode. A total of two exposures were obtained per night each with an exposure time of 300 s containing the ordinary and extraordinary beams. An exposure of an Argon lamp was taken after the science frames for wavelength calibration purposes. The PG0300 grating was used providing a resolving power of ∼2500 and a wavelength coverage of 3500–9500 Å. The data was reduced following the procedure

described in Chapter 4 (Section 4.3.2.3) and the results are shown in Figures 5.1 and 5.2.

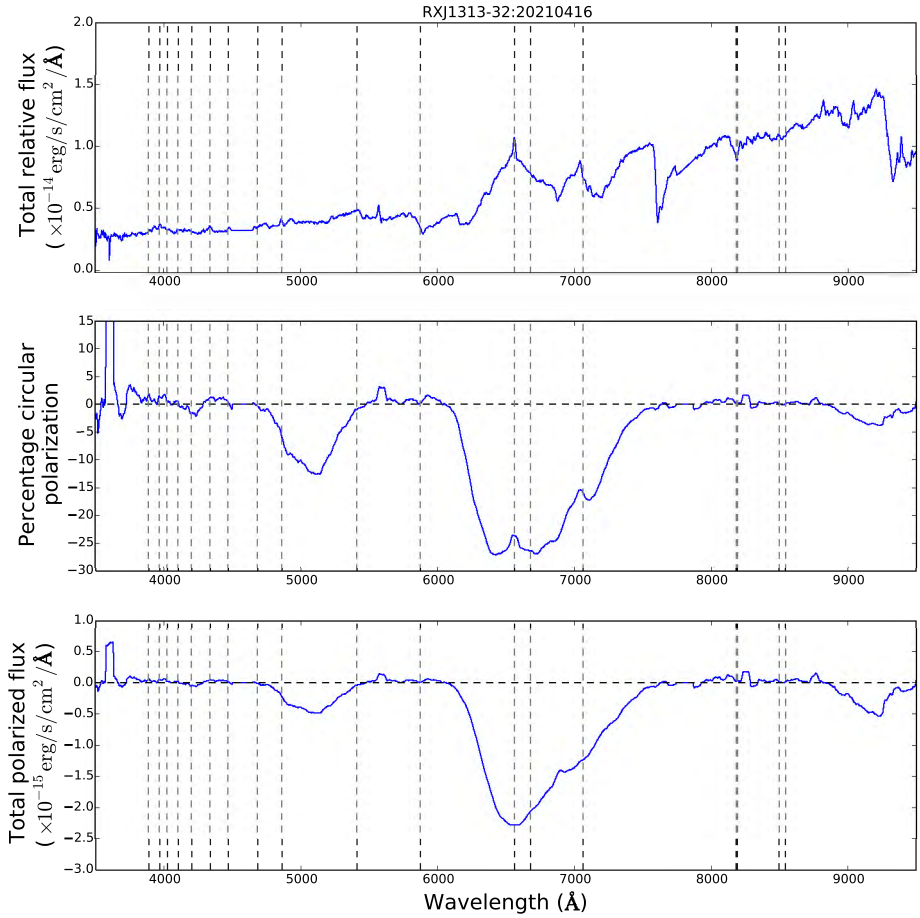

Figure 5.1: The total intensity spectra (top), percentage cyclotron spectra (middle) and percentage of circularly polarized intensity of RXJ1313−32 centred at $\phi = 0.88$. The vertical dotted lines marks the location of prominent emission lines.

The total intensity spectra of RXJ1313−32 (Figures 5.1 and 5.2, top panels) show typical spectra of an AM Her system during the low state with weak emission from the Balmer lines and strong atmospheric absorption lines towards the red part of the spectrum. Similar low-state spectrum of this source is presented by Thomas et al. (2000) and van der Heyden et al. (2002). The middle panels of Figures 5.1 and 5.2 show the percentage circularly polarized spectra of this source and reveal negative circular polarization reaching −25% and −15%, respectively. The percentage circularly polarized spectra show the presence of three negative polarized humps, centred at ∼5000 Å, 6600 Å and 9100 Å, that are understood as cyclotron harmonics due to cyclotron emission from the hot plasma. These cyclotron

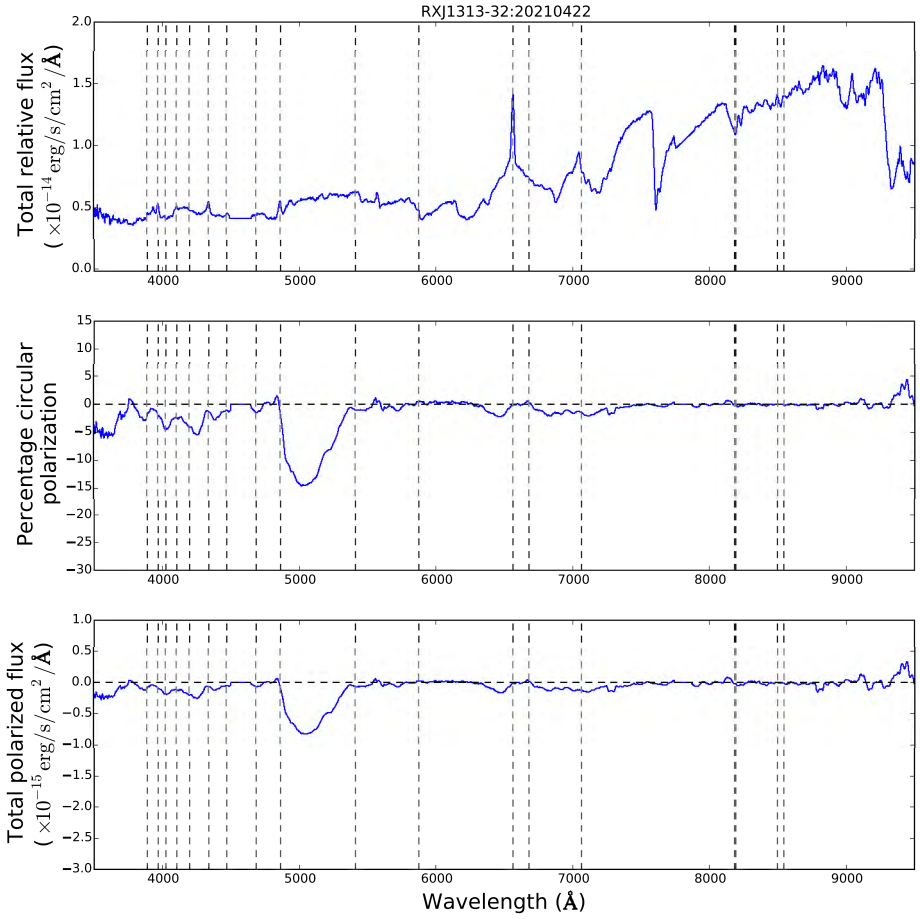

Figure 5.2: The total intensity spectra (top), percentage cyclotron spectra (middle) and percentage of circularly polarized intensity of RXJ1313−32 centred at $\phi = 0.69$. The vertical dotted lines marks the location of prominent emission lines.

features are mostly visible in the spectra obtained on 2021 April 16 (phase 0.88, Figure 5.1). As demonstrated in Figure 10 of Thomas et al. (2000), the strength (and position) of the three cyclotron features of RXJ1313−32 depend on the orbital phase and possibly the accretion state and this is shown in Figures 5.1 and 5.2. This could also be attributed to varying strength of the magnetic field of the WD between the two observations or the viewing angle since the two observations shown were taken five days apart and show different orbital phases. We determined the magnetic field strength of the main accreting region using Eq. 4.2, given the harmonic positions mentioned above, to be in the range of 44–51 MG. The value of the field strength is within the range of that determined by Thomas et al. (2000) from cyclotron spectra modelling. We also identified the harmonic numbers using

Eq. 4.3 and the three humps were identified with harmonic numbers 5, 4 and 3, respectively. Since RXJ1313−32 is highly polarized, it will be possible to investigate the effects of other parameters such as optical depth, temperature, size, etc. Therefore, detailed modelling of the circularly polarized spectra of RXJ1313−32 will reveal more information about the magnetic field strength of this system, among other properties.

Appendix A

Half-phase Doppler tomography

This appendix contains the complete half-phase Doppler tomography used in the flux modulation mapping presented in Chapter 3 (Section 3.7) for each emission line considered: Hβ, HeII 4686 Å and CaII 8542 Å emission lines. The figures are divided as follows: Figures A.1 to A.10 show the half-phase Doppler tomography using the Hβ line, Figures A.11 to A.20 show the hal-phase Doppler tomography using HeII 4686 Å line and Figures A.21 and A.30 show the half-phase Doppler tomography using CaII 8542 Å line. The corresponding orbital phase ranges for each tomograms are given in the caption of each figure. In all the figures, the standard and inside-out half-phase tomograms are shown in the top left and right panels, respectively. The middle rows show the observed or input trailed spectra (center) with the reconstructed trailed spectra for the corresponding half-phase tomogram to the left and right of it. The bottom panels show the trailed absolute residual spectra for the corresponding half-phase tomogram.

A.1 Hβ half-phase Doppler tomography

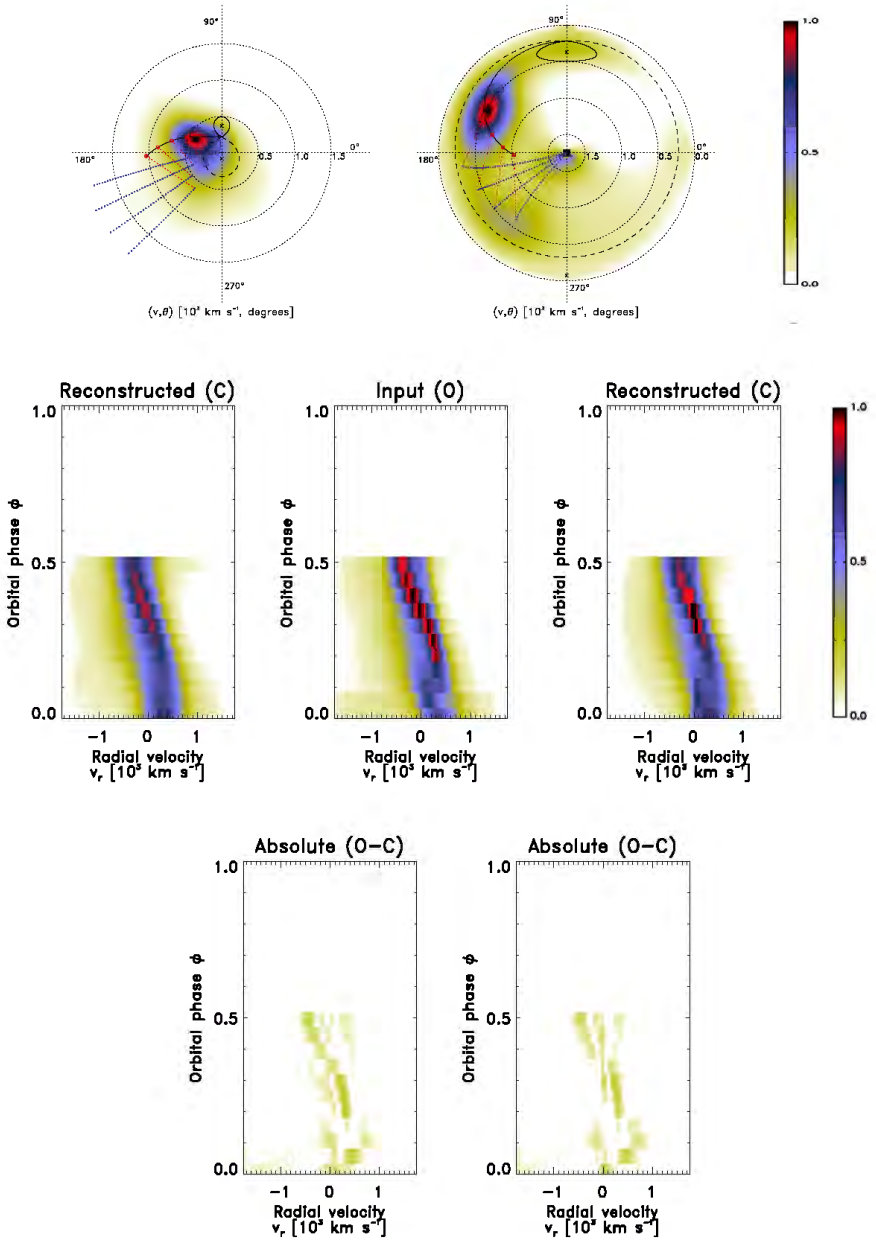

Figure A.1: Half-phase Doppler tomography of UZ For using the Hβ line taken for phases 0.0–0.5.

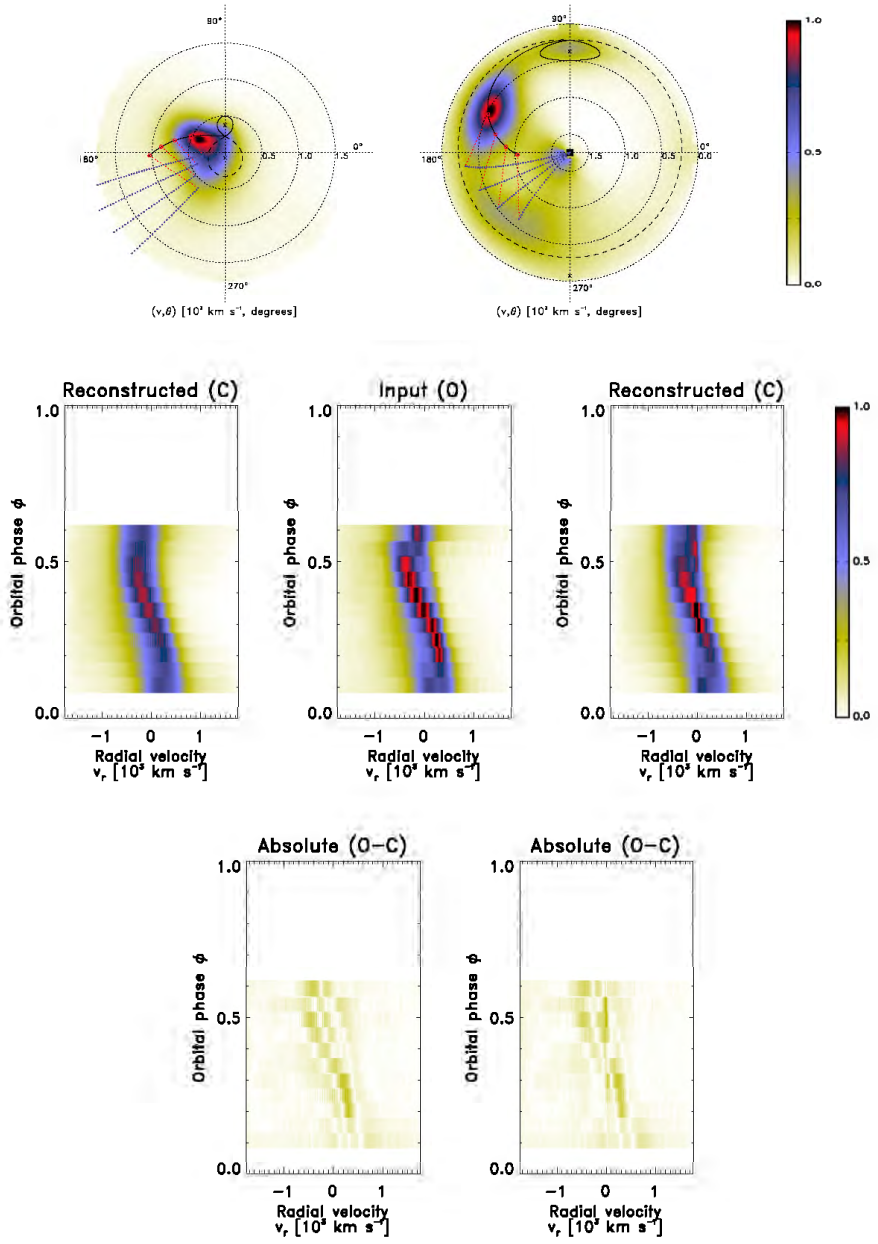

Figure A.2: Half-phase Doppler tomography of UZ For using the Hβ line taken for phases 0.1–0.6.

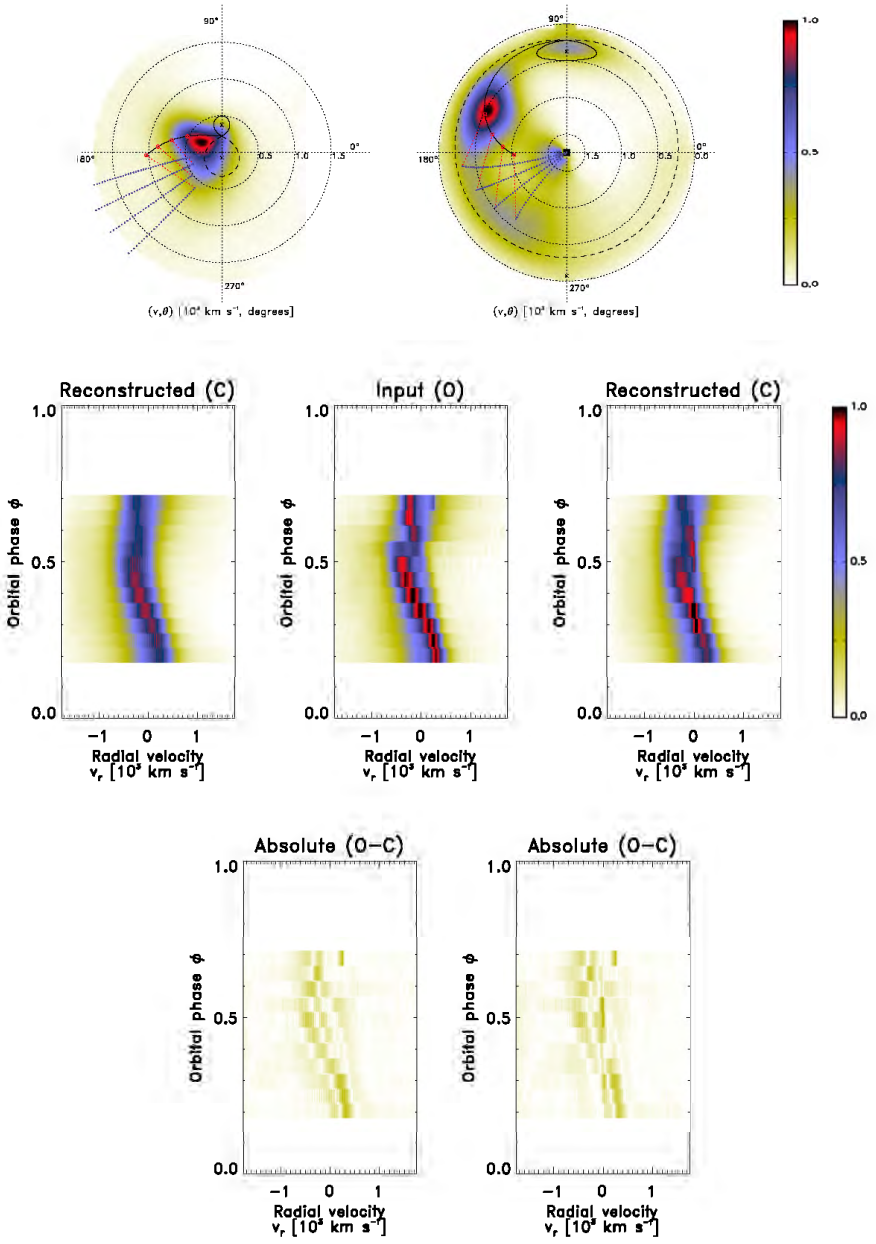

Figure A.3: Half-phase Doppler tomography of UZ For using the Hβ line taken for phases 0.2–0.7.

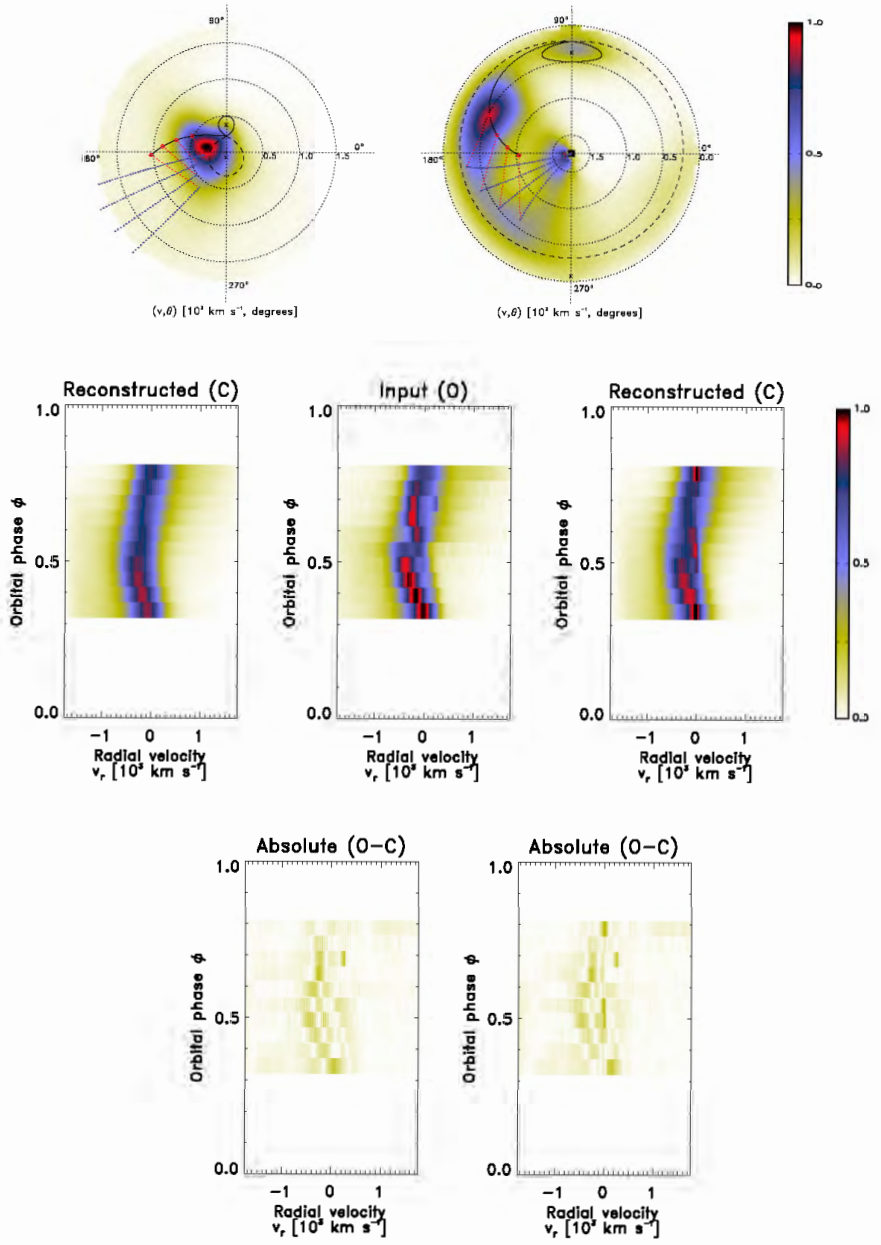

Figure A.4: Half-phase Doppler tomography of UZ For using the Hβ line taken for phases 0.3–0.8.

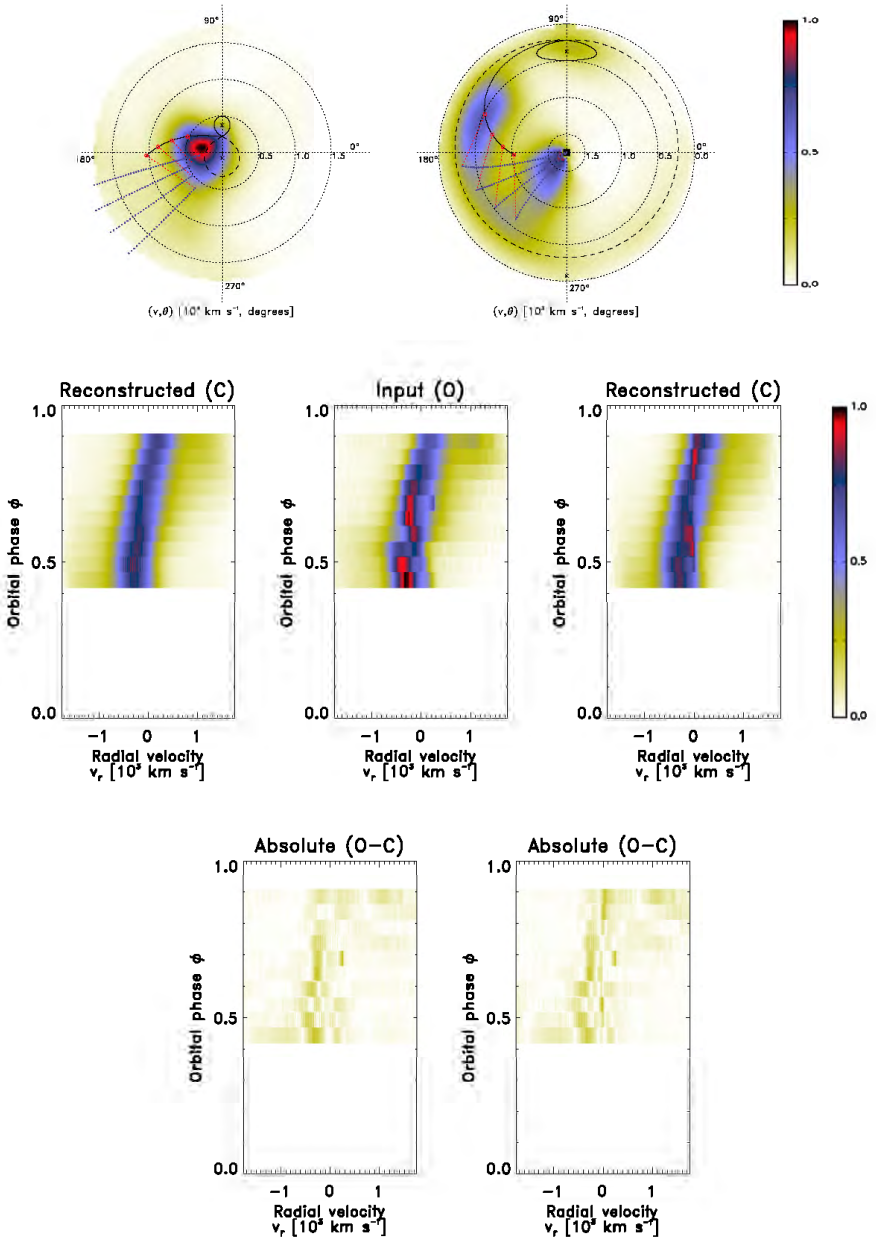

Figure A.5: Half-phase Doppler tomography of UZ For using the Hβ line taken for phases 0.4–0.9.

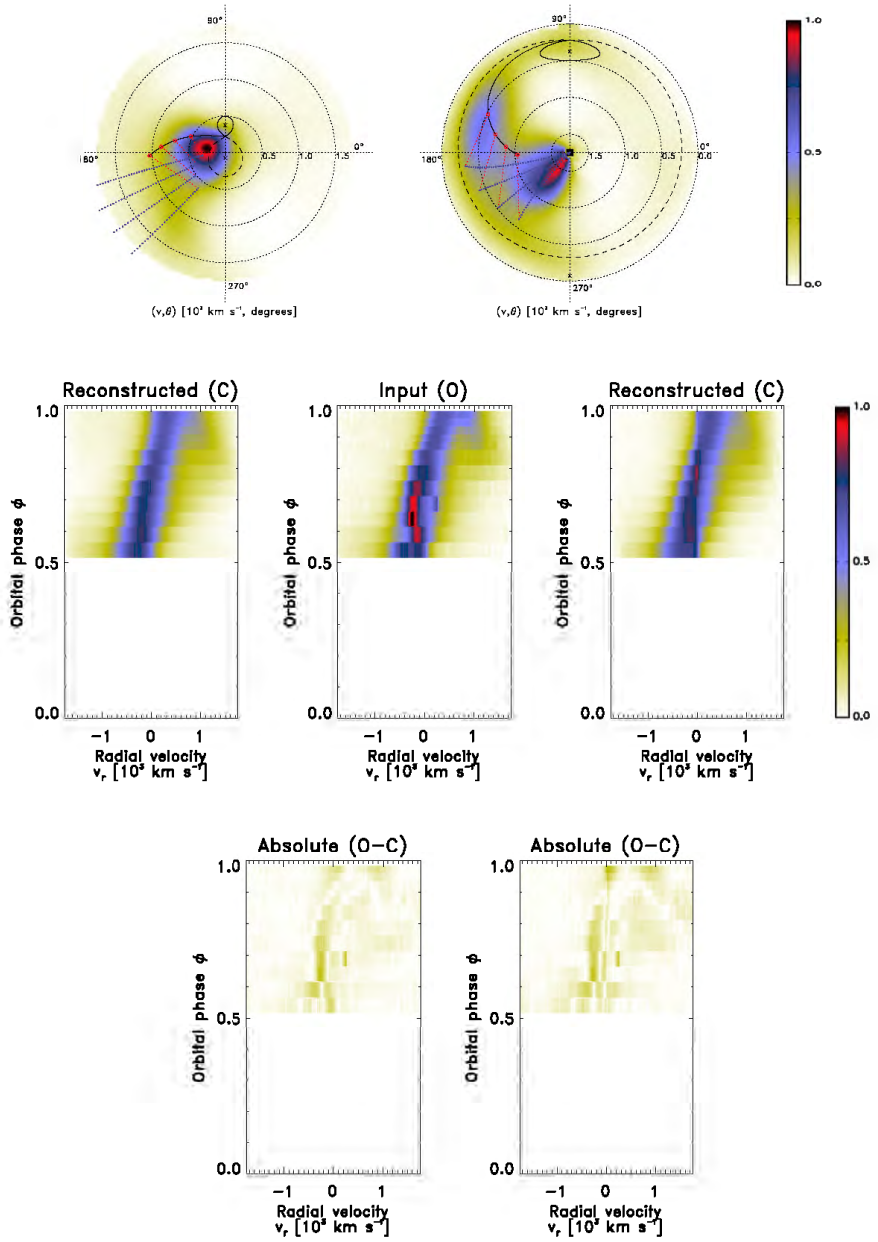

Figure A.6: Half-phase Doppler tomography of UZ For using the Hβ line taken for phases 0.5–1.0.

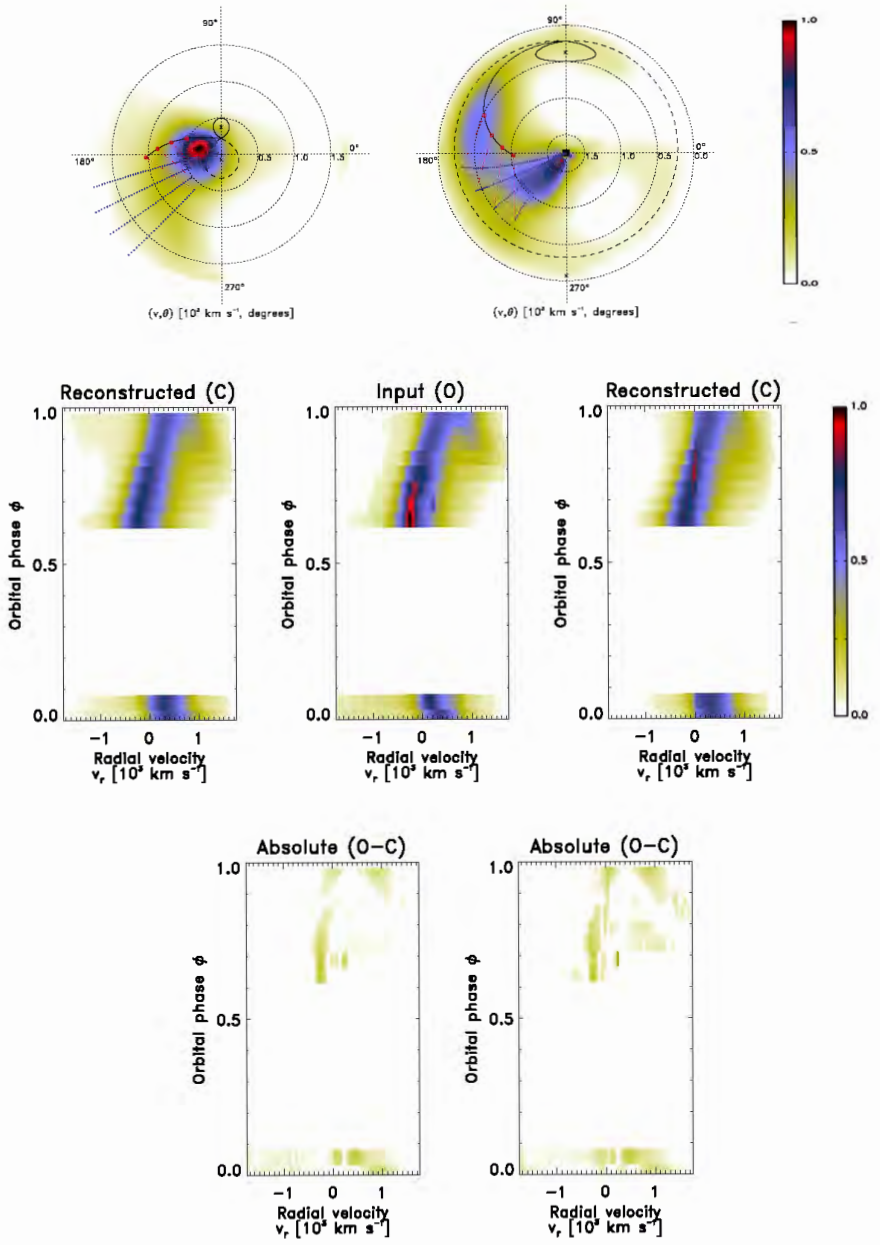

Figure A.7: Half-phase Doppler tomography of UZ For using the Hβ line taken for phases 0.6–0.1.

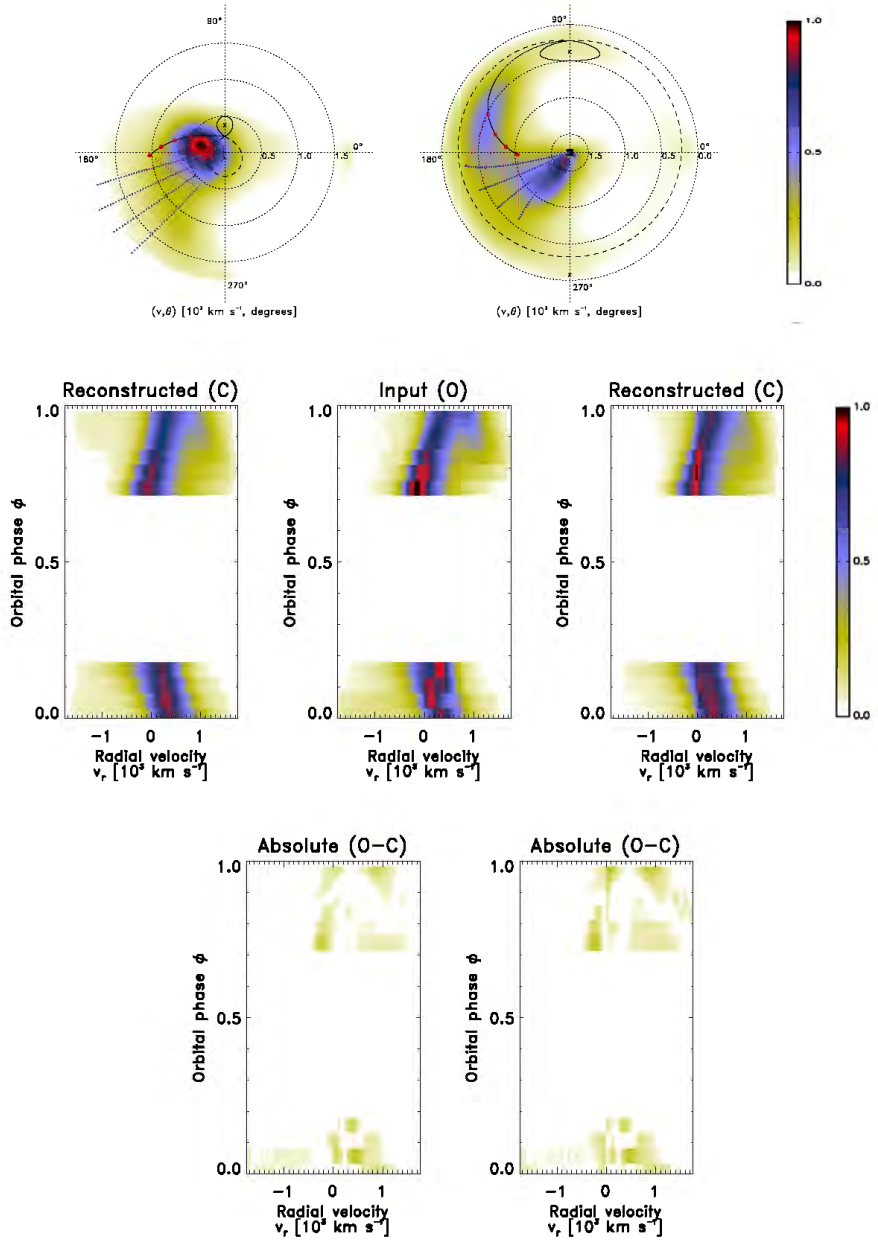

Figure A.8: Half-phase Doppler tomography of UZ For using the Hβ line taken for phases 0.7–0.2.

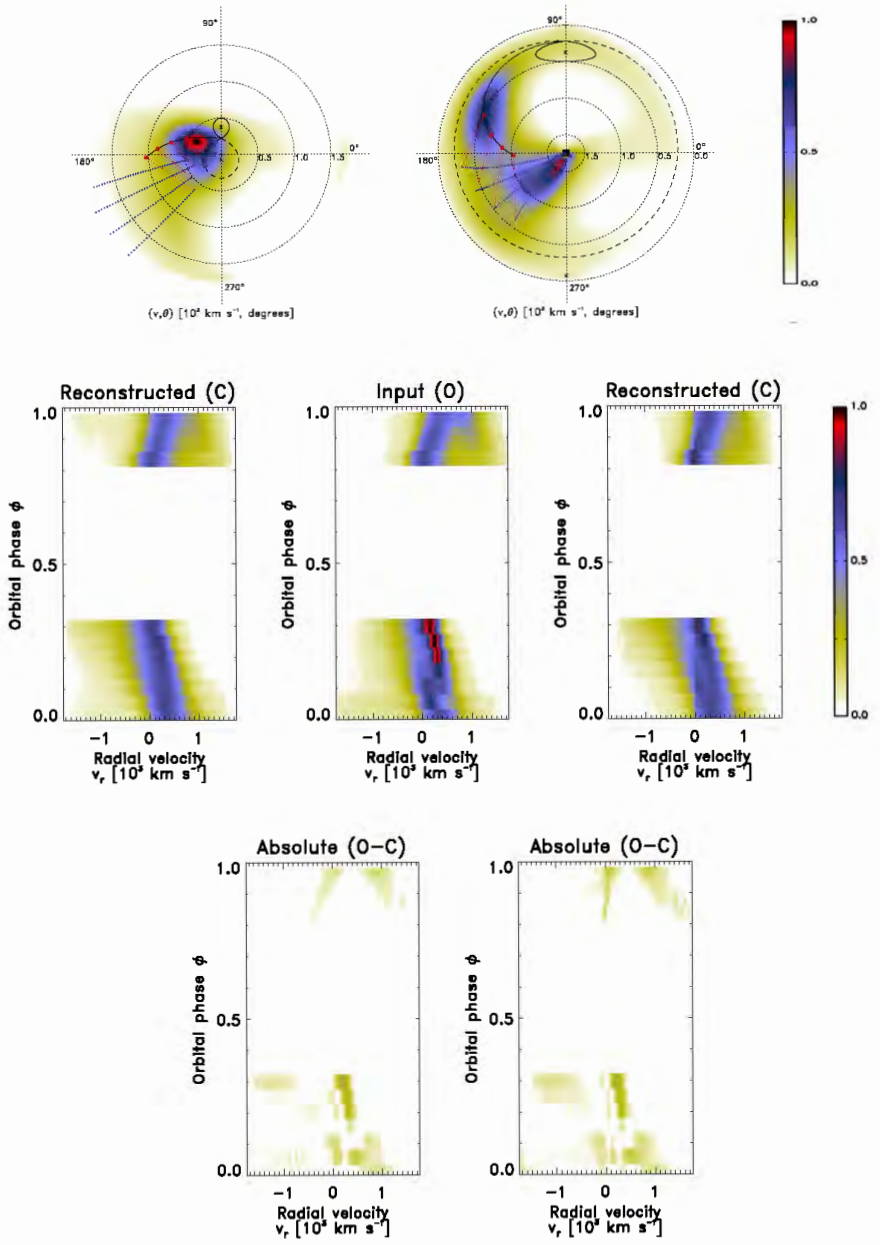

Figure A.9: Half-phase Doppler tomography of UZ For using the Hβ line taken for phases 0.8–0.3.

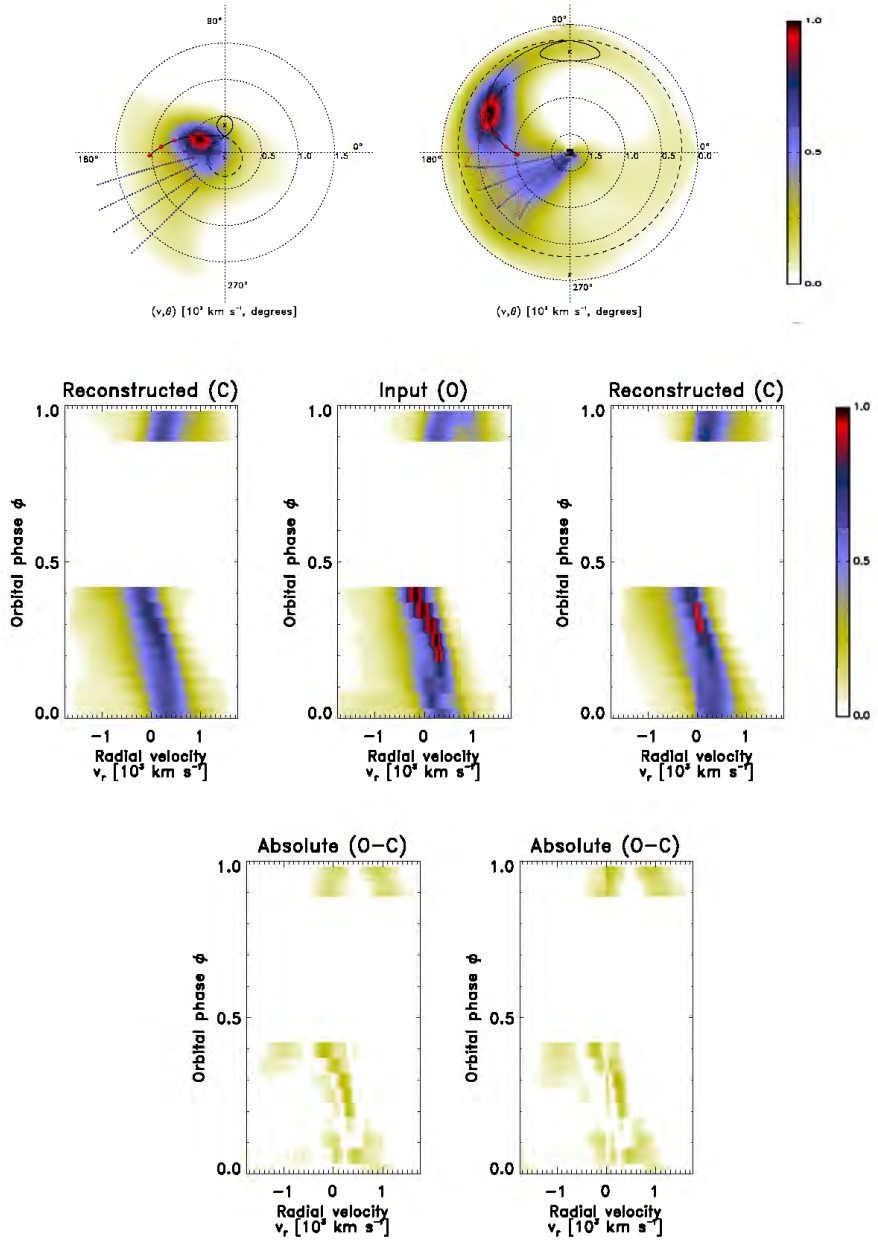

Figure A.10: Half-phase Doppler tomography of UZ For using the Hβ line taken for phases 0.–0.5.

A.2 Half-phase Doppler tomography of HeII 4686 Å

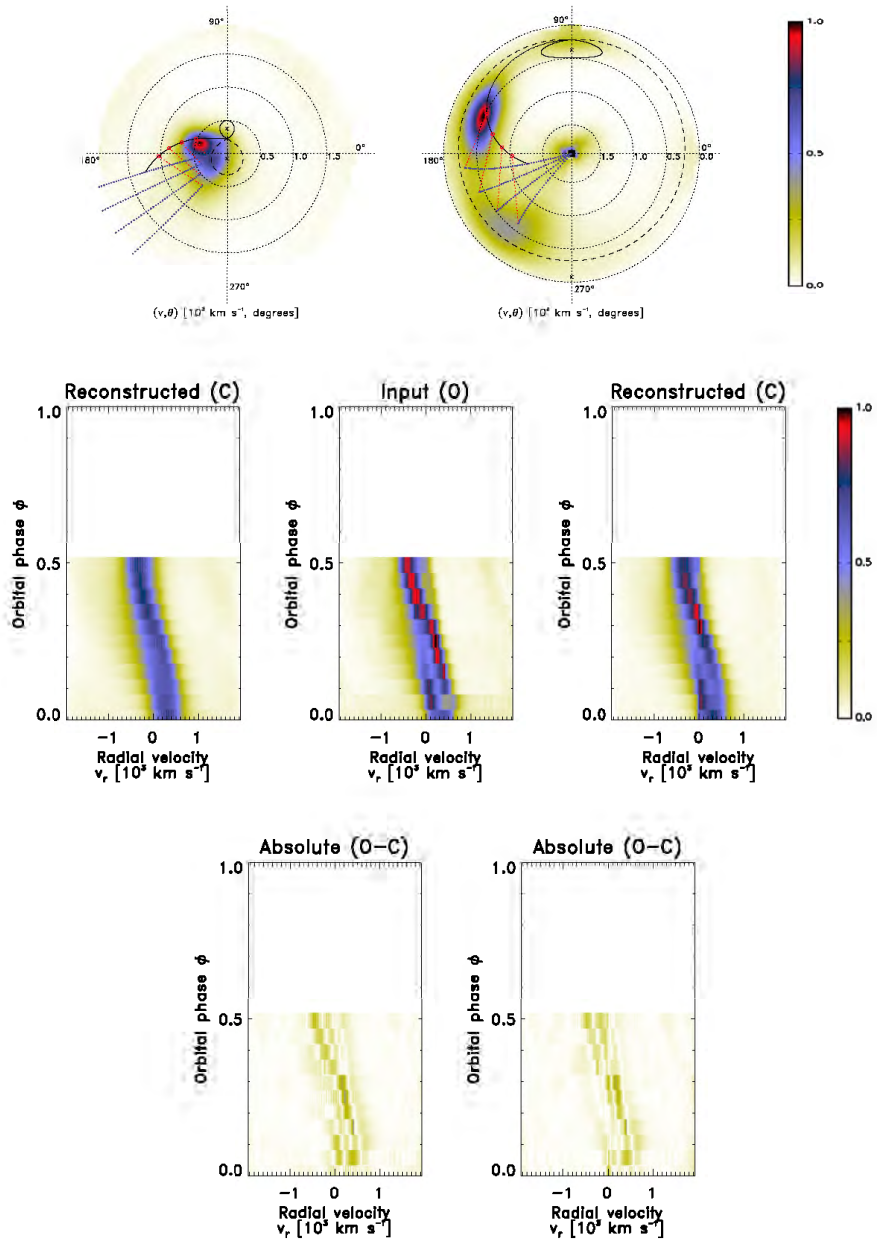

Figure A.11: Half-phase Doppler tomography of UZ For using the HeII 4686 Å line taken for phases 0.0–0.5.

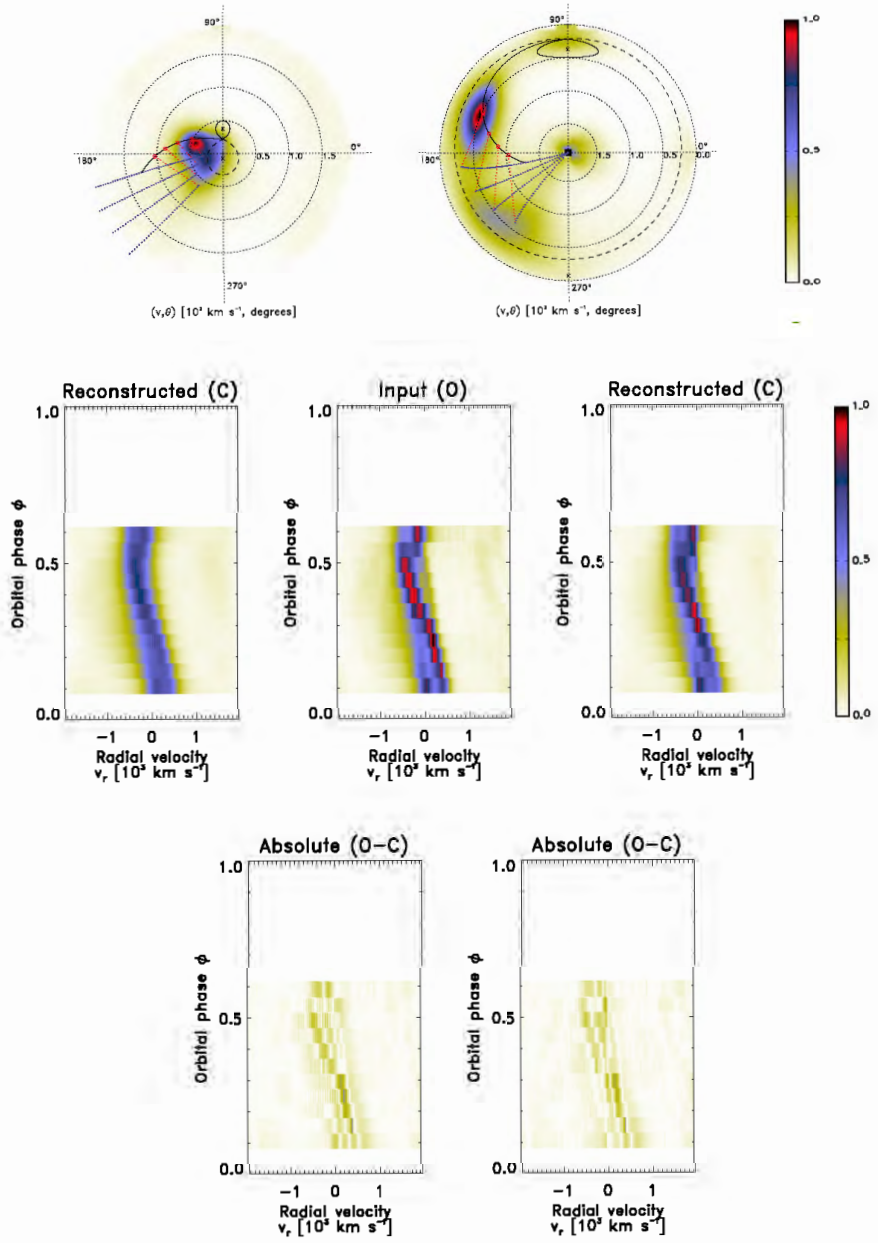

Figure A.12: Half-phase Doppler tomography of UZ For using the HeII 4686 Å line taken for phases 0.1–0.6.

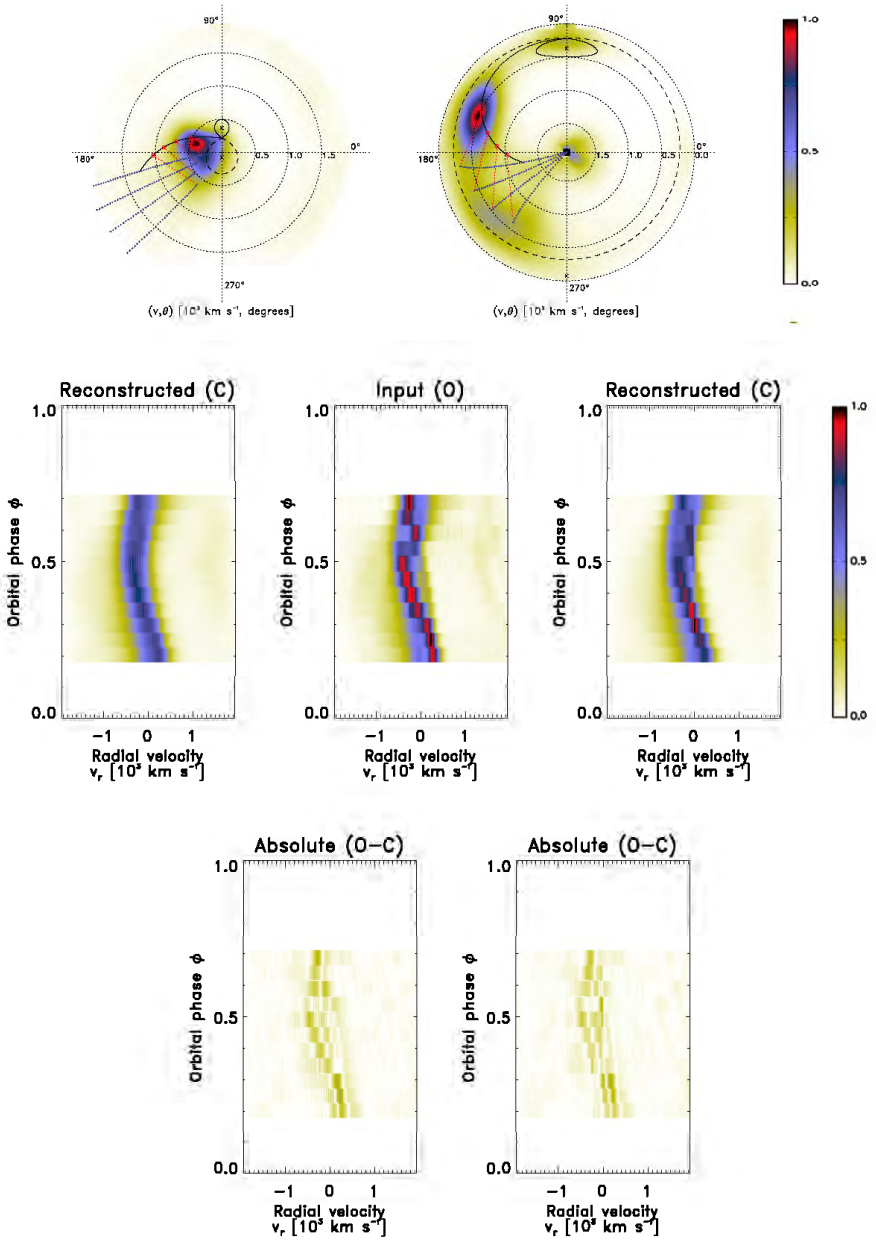

Figure A.13: Half-phase Doppler tomography of UZ For using the HeII 4686 Å line taken for phases 0.2–0.7.

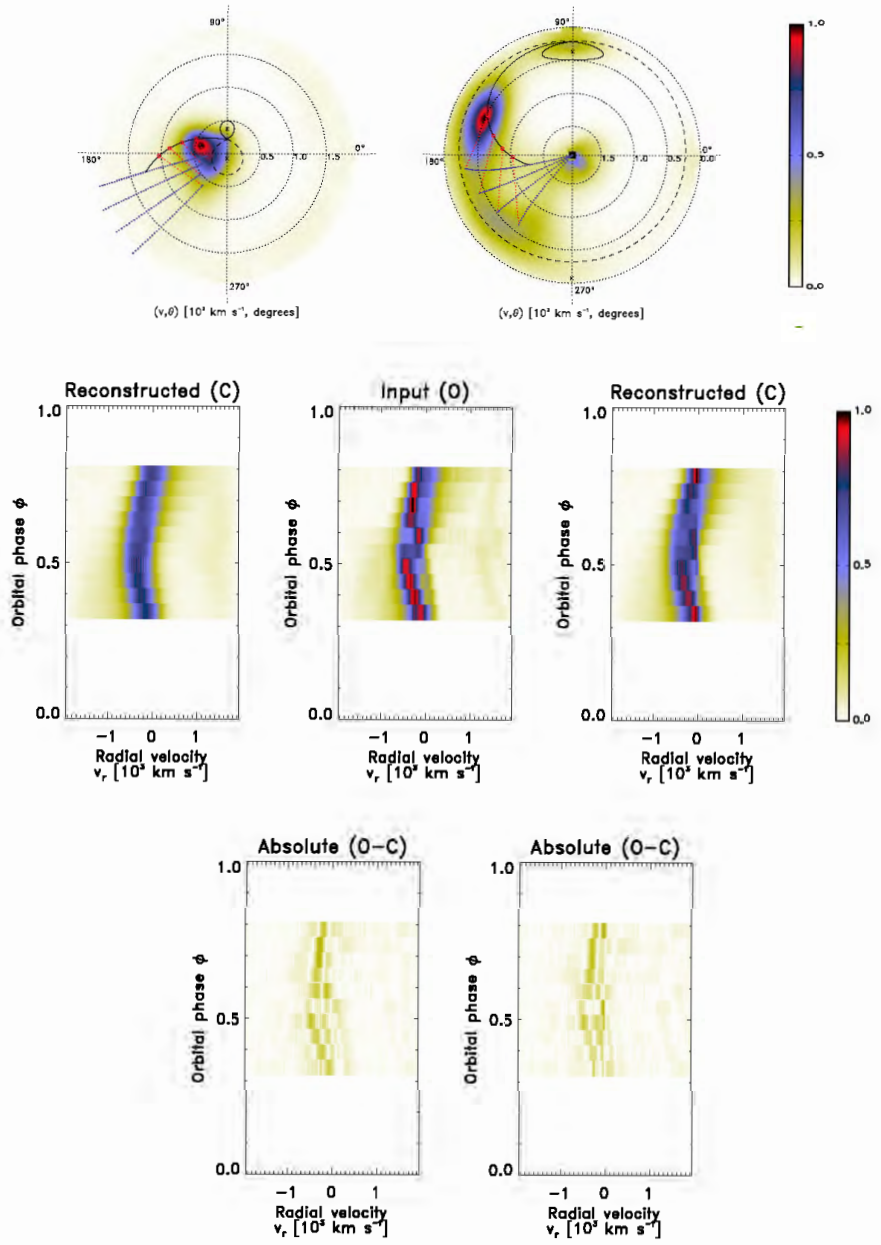

Figure A.14: Half-phase Doppler tomography of UZ For using the HeII 4686 Å line taken for phases 0.3–0.8.

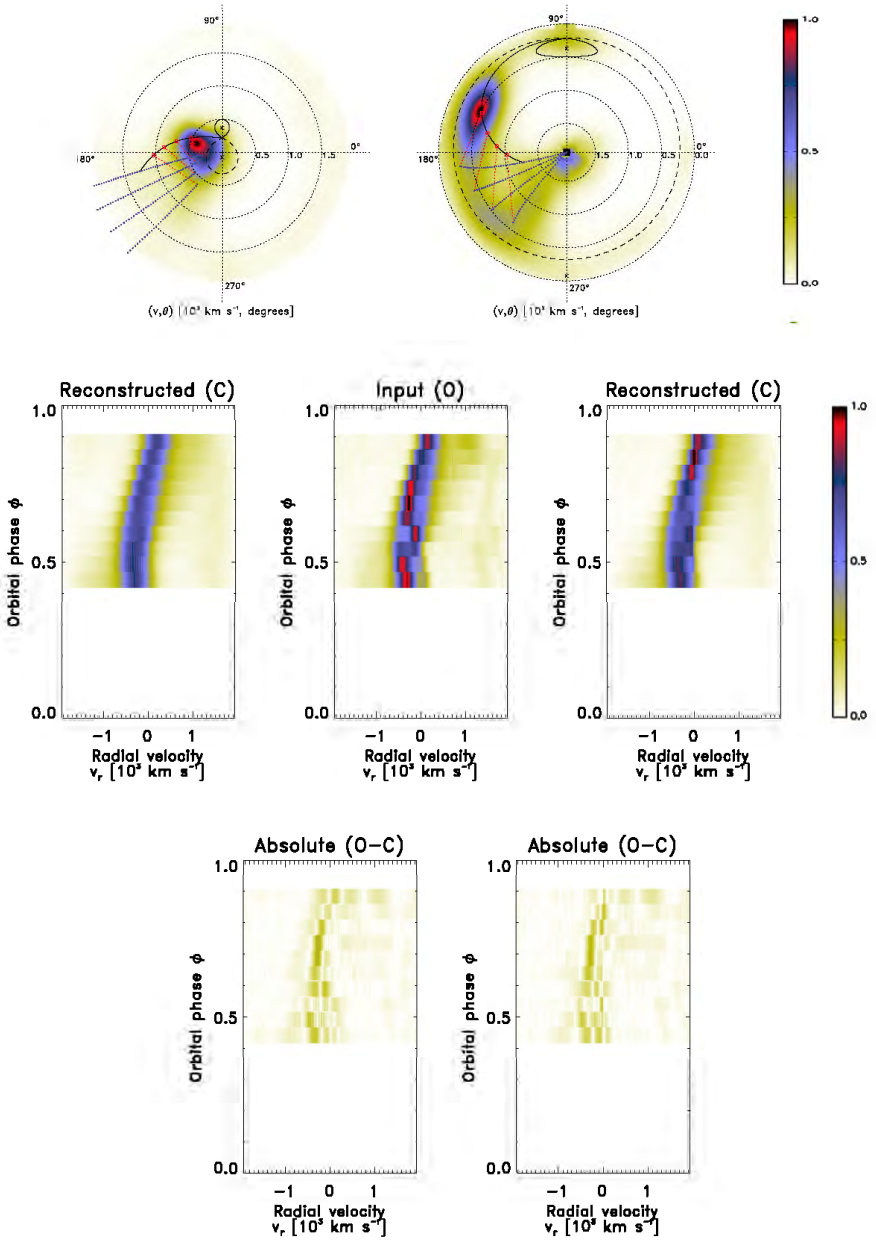

Figure A.15: Half-phase Doppler tomography of UZ For using the HeII 4686 Å line taken for phases 0.4–0.9.

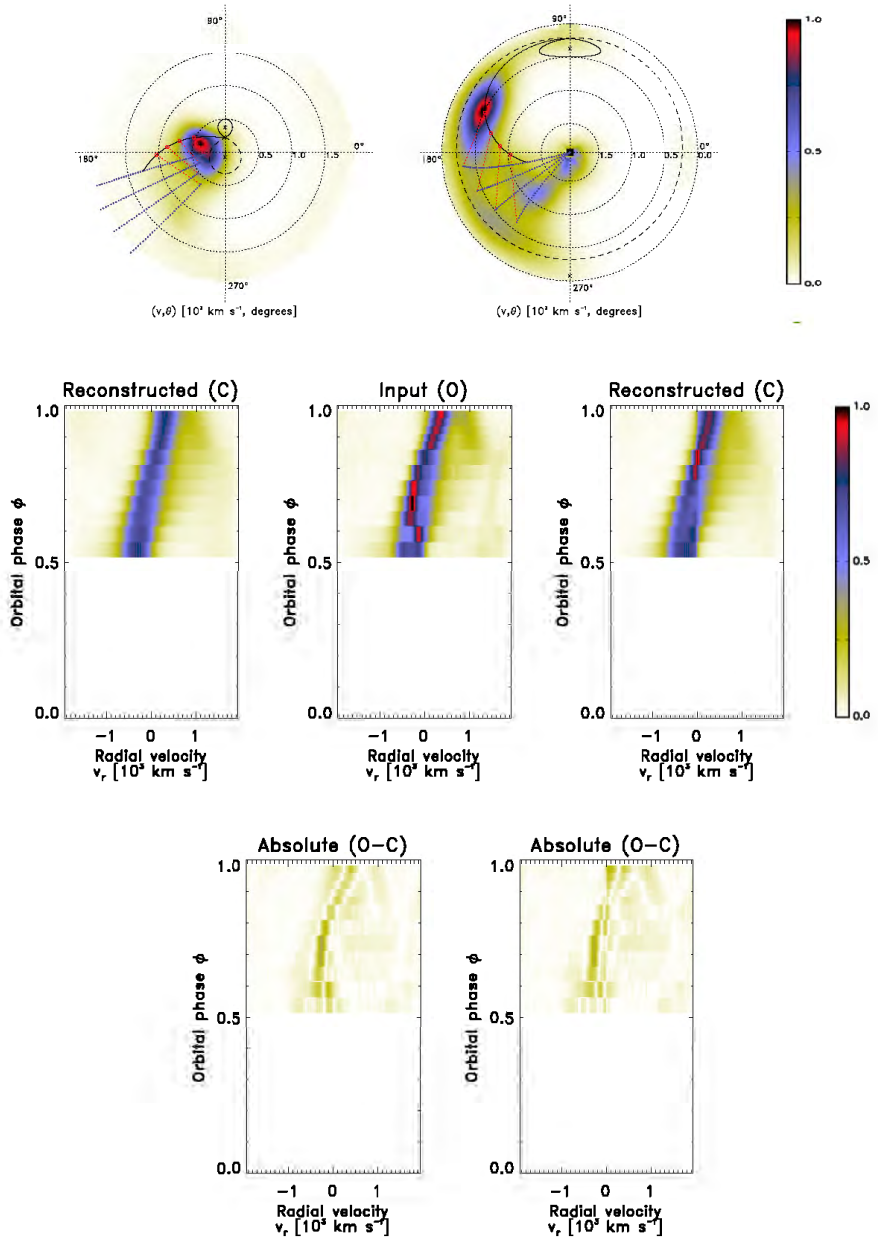

Figure A.16: Half-phase Doppler tomography of UZ For using the HeII 4686 Å line taken for phases 0.5–1.0.

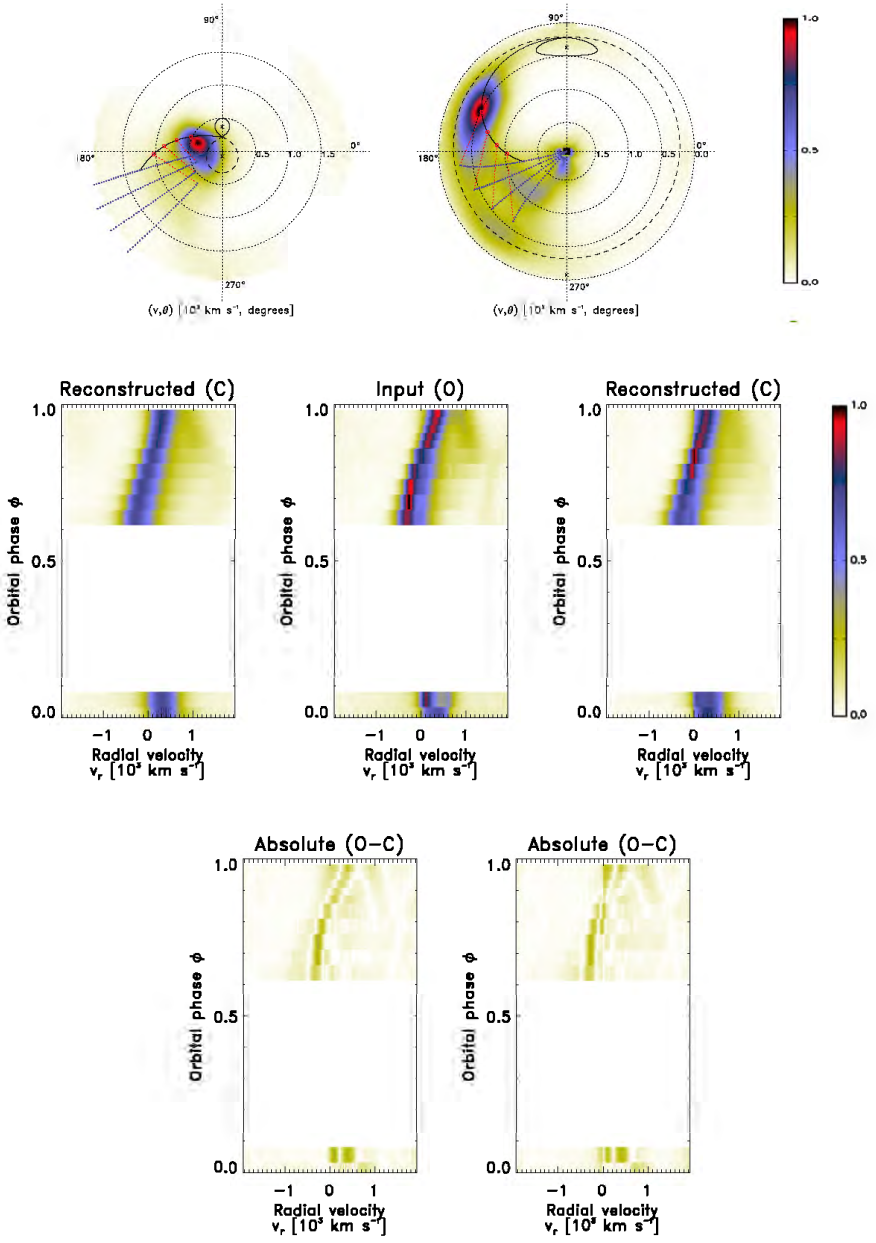

Figure A.17: Half-phase Doppler tomography of UZ For using the HeII 4686 Å line taken for phases 0.6–0.1.

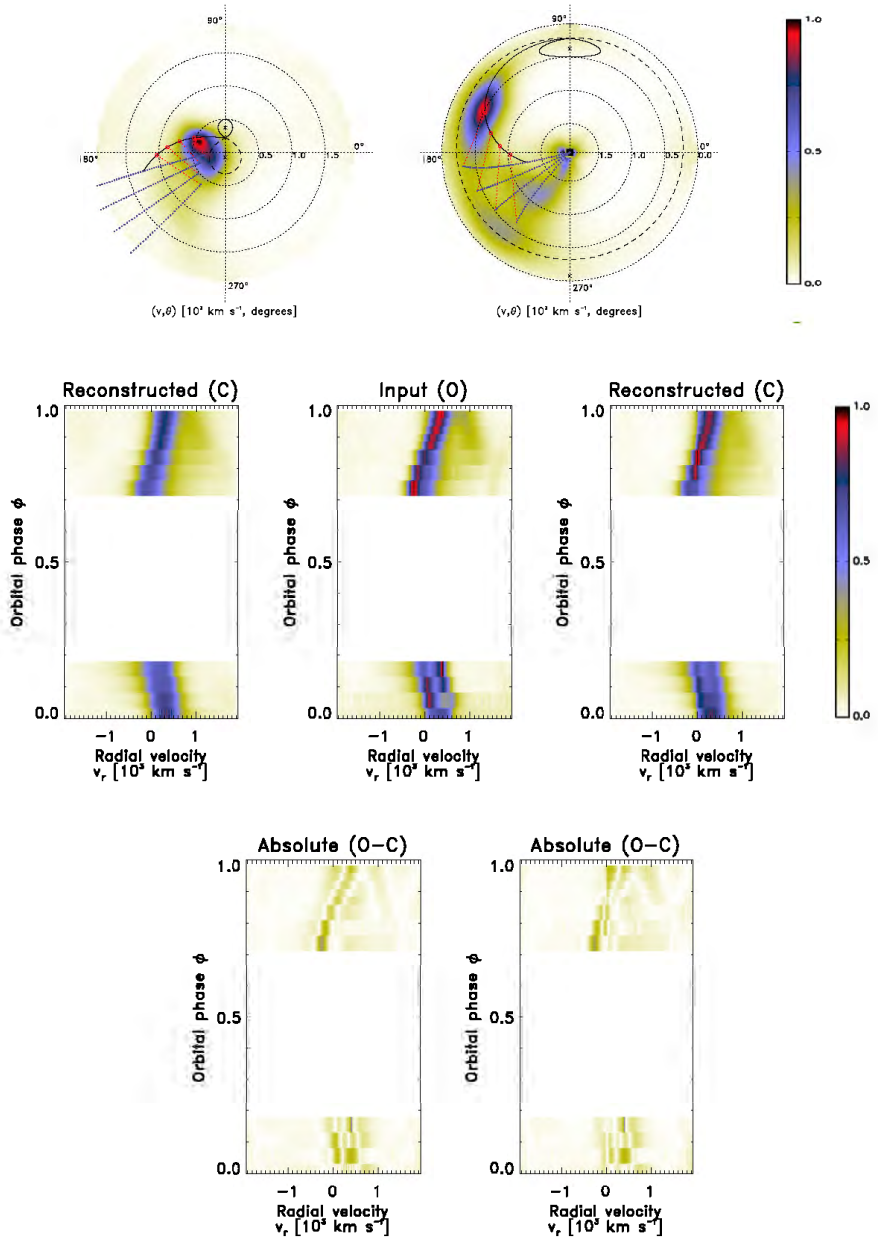

Figure A.18: Half-phase Doppler tomography of UZ For using the HeII 4686 Å line taken for phases 0.7–0.2.

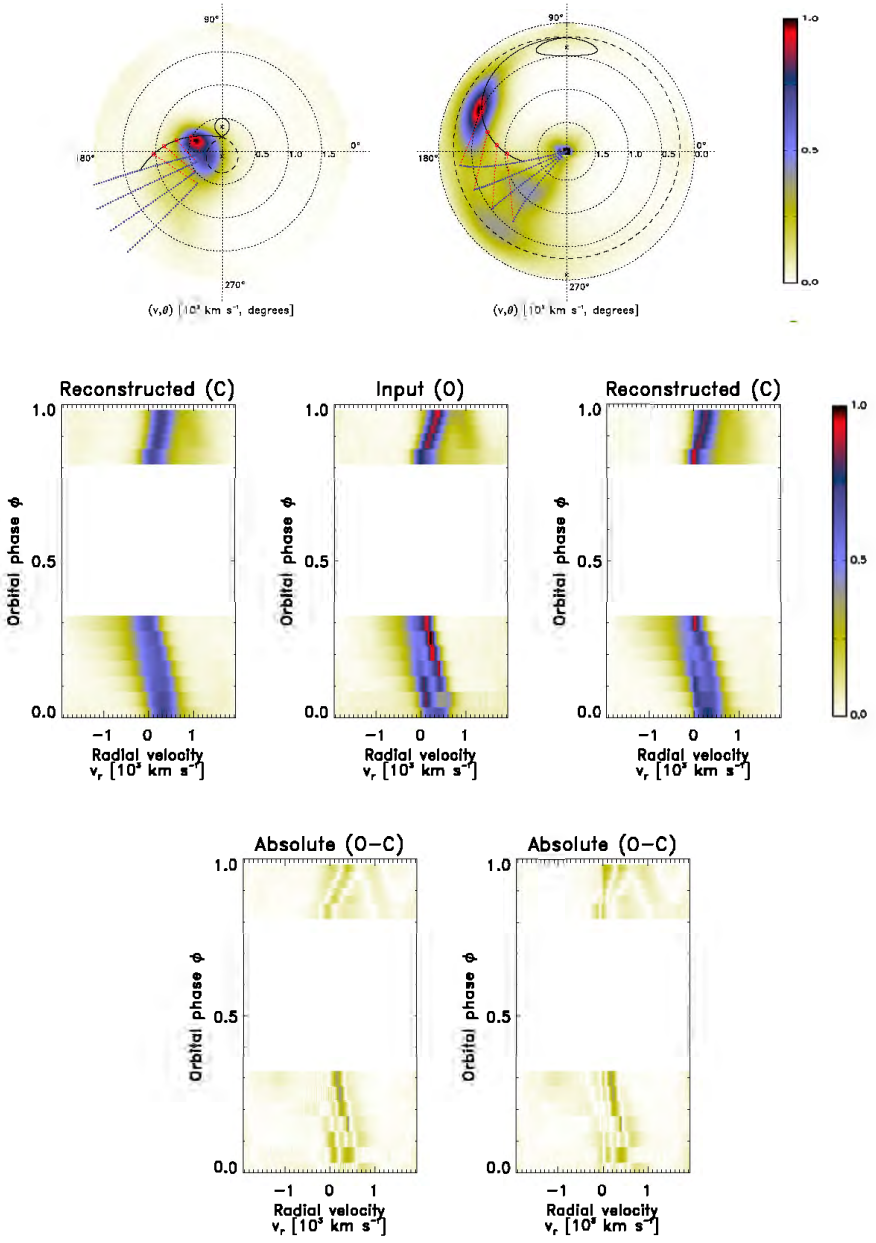

Figure A.19: Half-phase Doppler tomography of UZ For using the HeII 4686 Å line taken for phases 0.8–0.3.

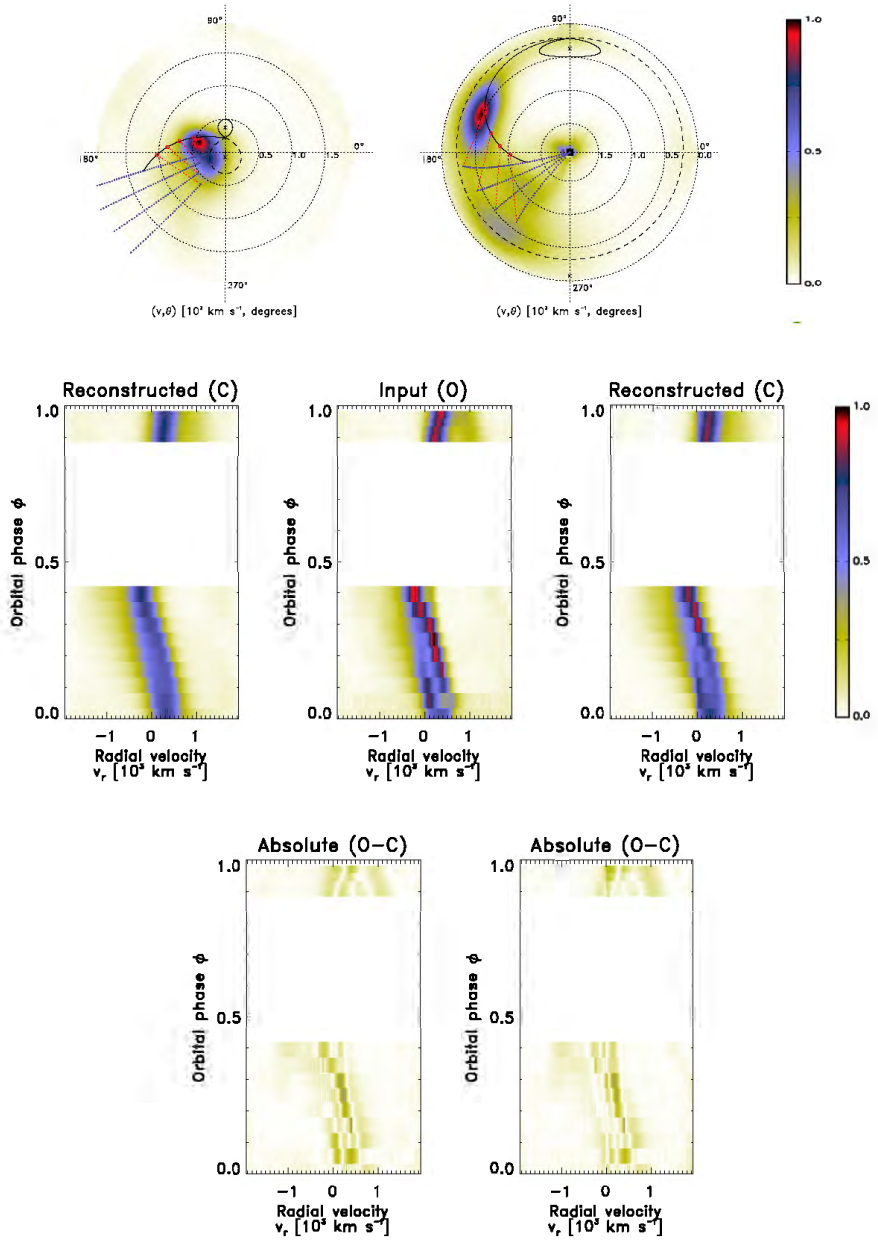

Figure A.20: Half-phase Doppler tomography of UZ For using the HeII 4686 Å line taken for phases 0.9–0.4.

A.3 Half-phase Doppler tomography of CaII 8542 Å

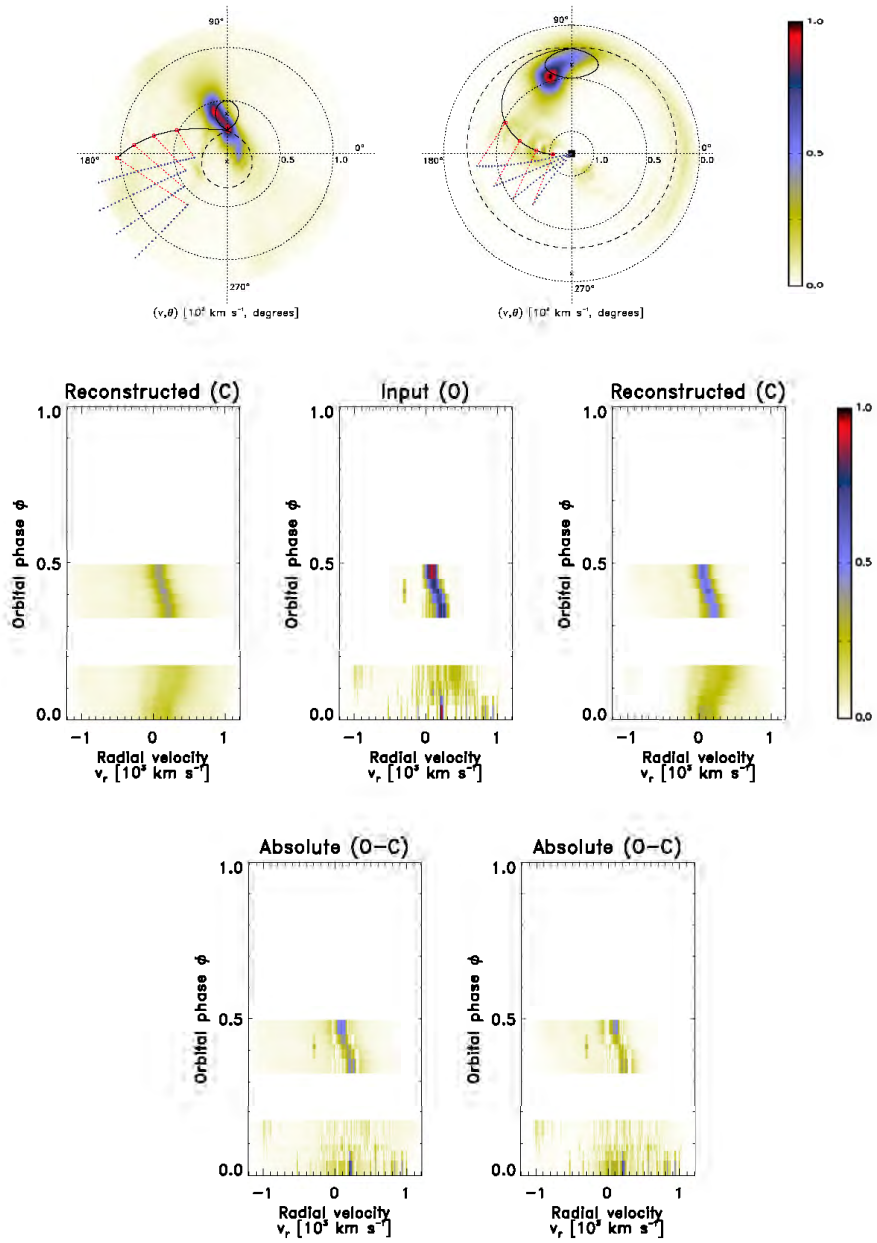

Figure A.21: Half-phase Doppler tomography of UZ For using the CaII 8542 Å line taken for phases 0.0–0.5.

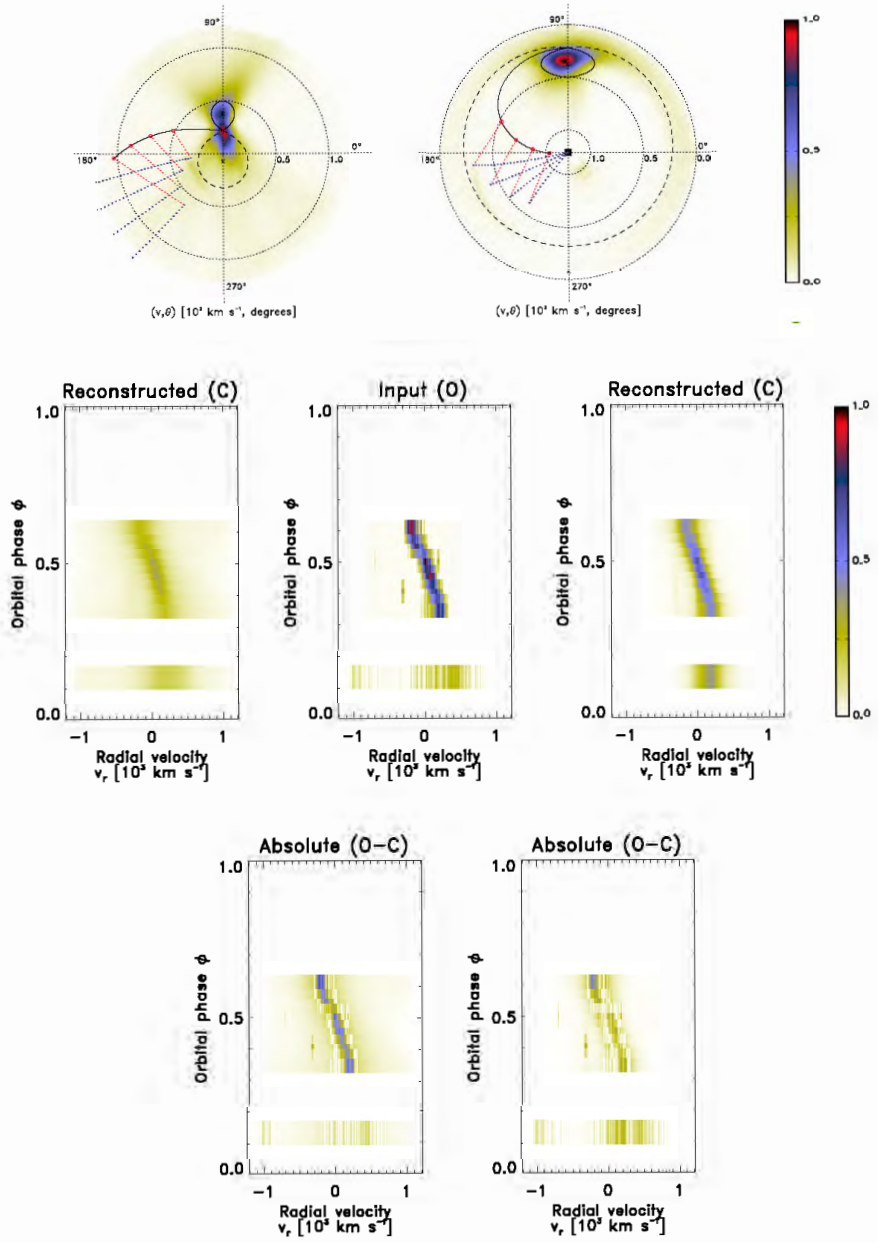

Figure A.22: Half-phase Doppler tomography of UZ For using the CaII 8542 Å line taken for phases 0.1–0.6.

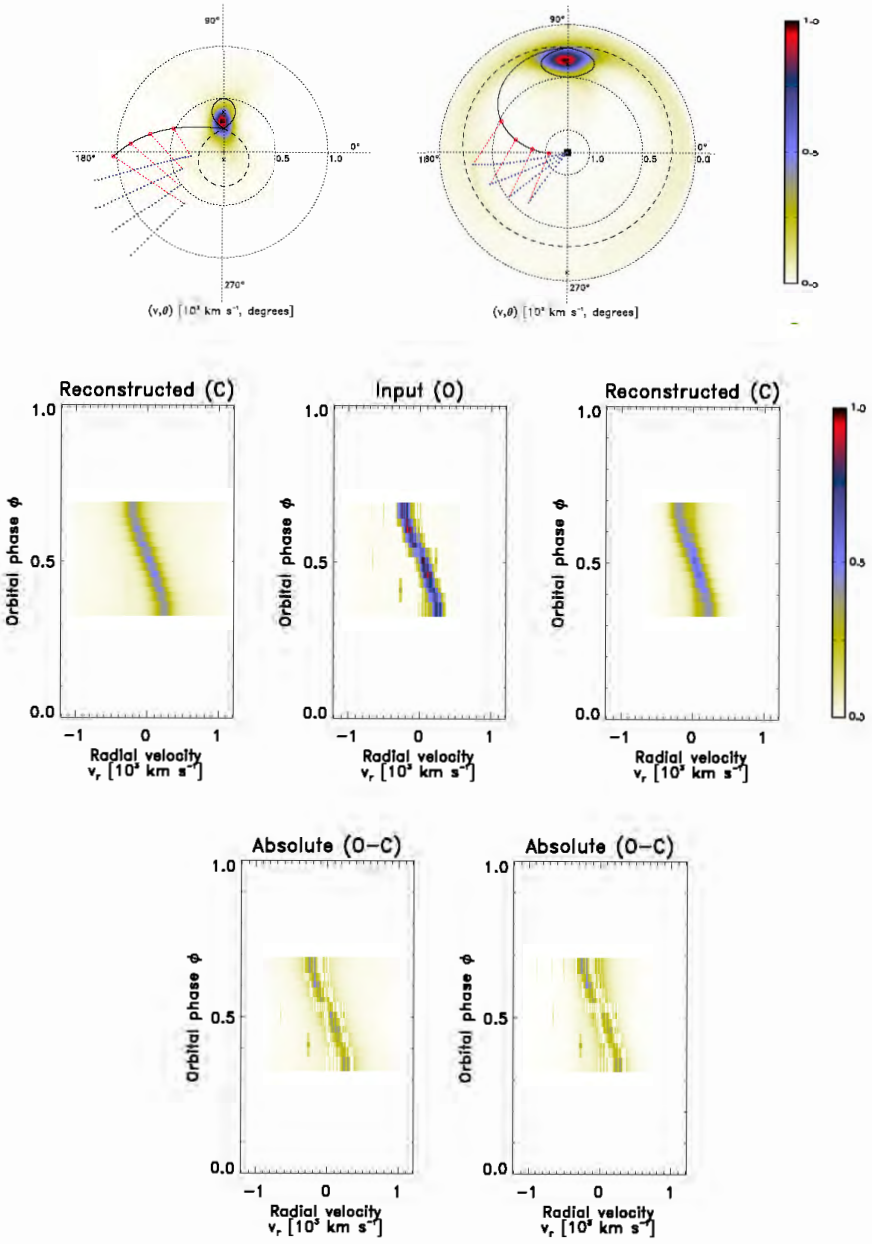

Figure A.23: Half-phase Doppler tomography of UZ For using the CaII 8542 Å line taken for phases 0.2–0.7.

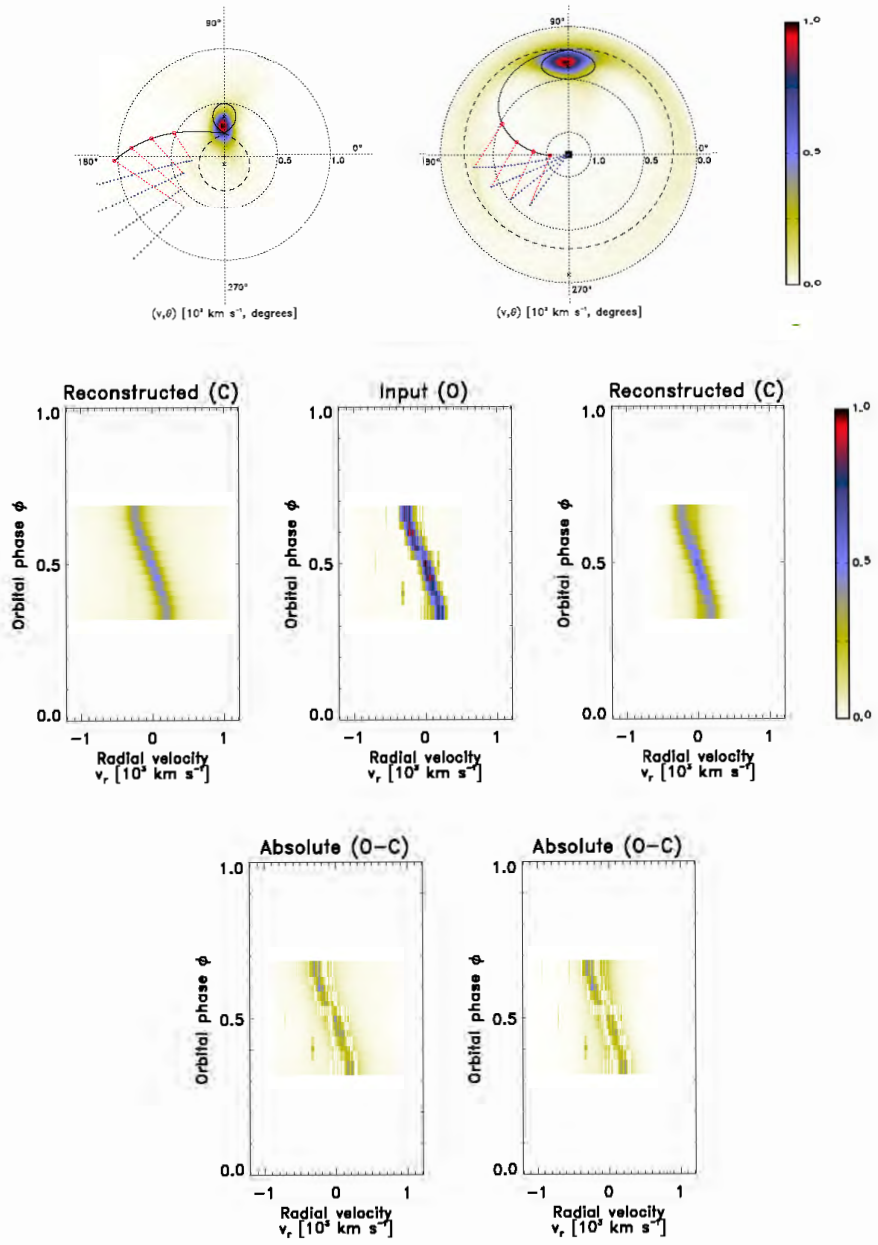

Figure A.24: Half-phase Doppler tomography of UZ For using the CaII 8542 Å line taken for phases 0.3–0.8.

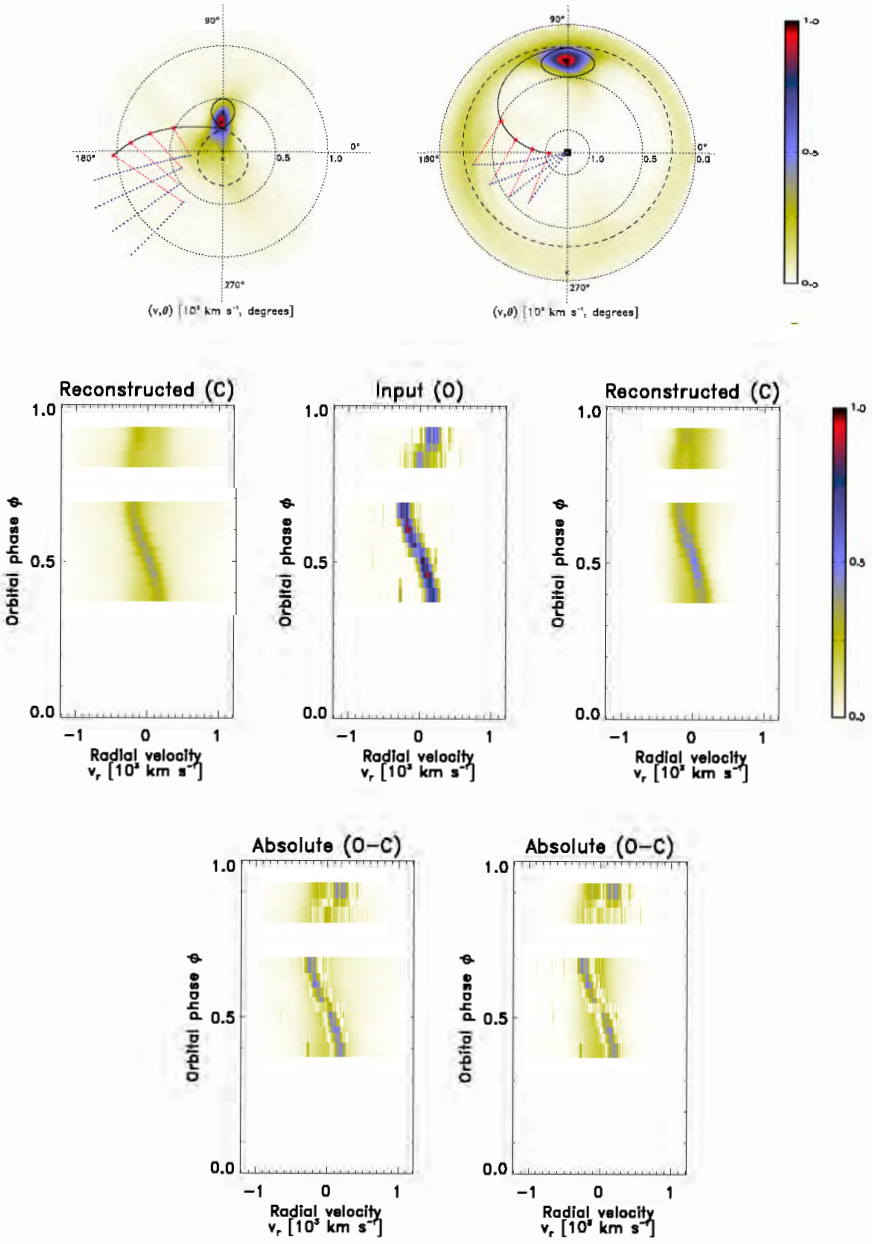

Figure A.25: Half-phase Doppler tomography of UZ For using the CaII 8542 Å line taken for phases 0.4–0.9.

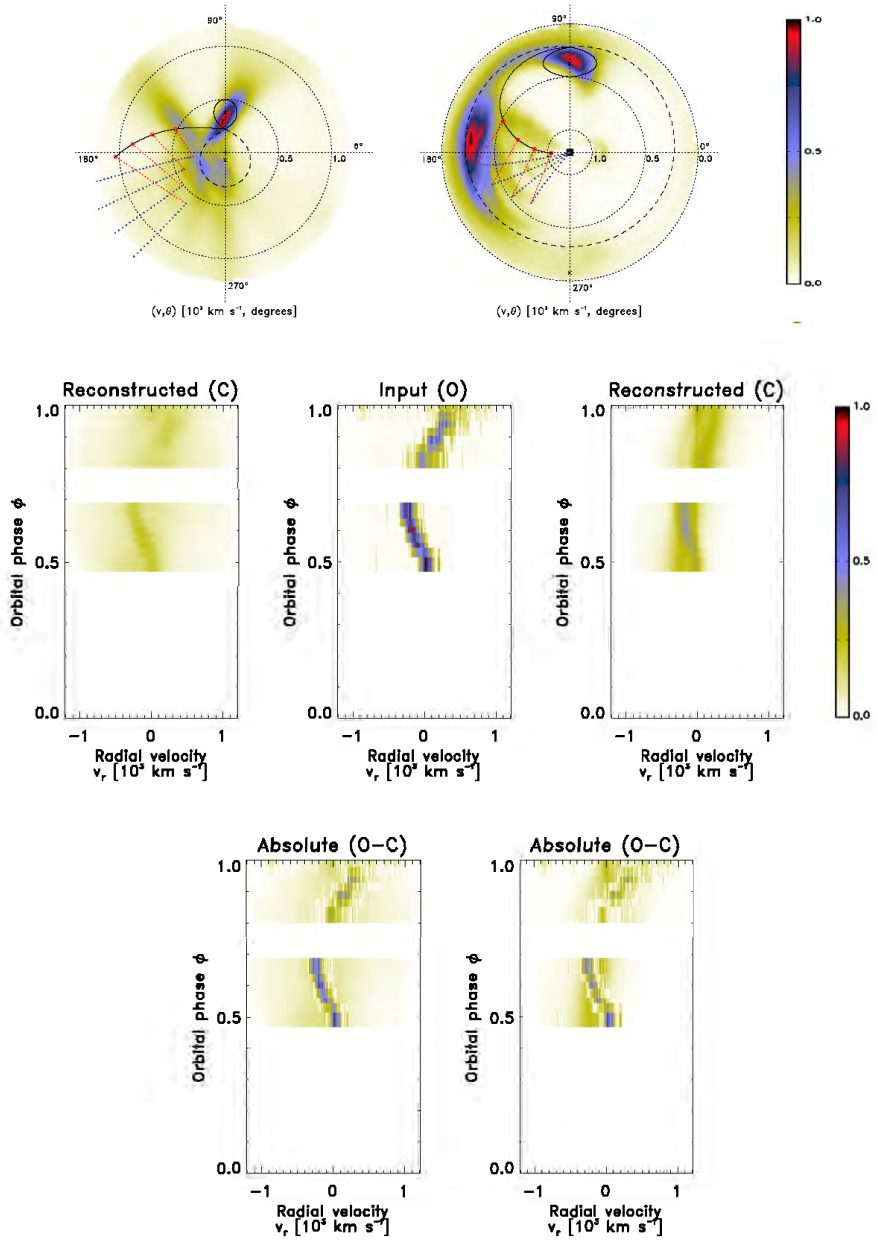

Figure A.26: Half-phase Doppler tomography of UZ For using the CaII 8542 Å line taken for phases 0.5–1.0.

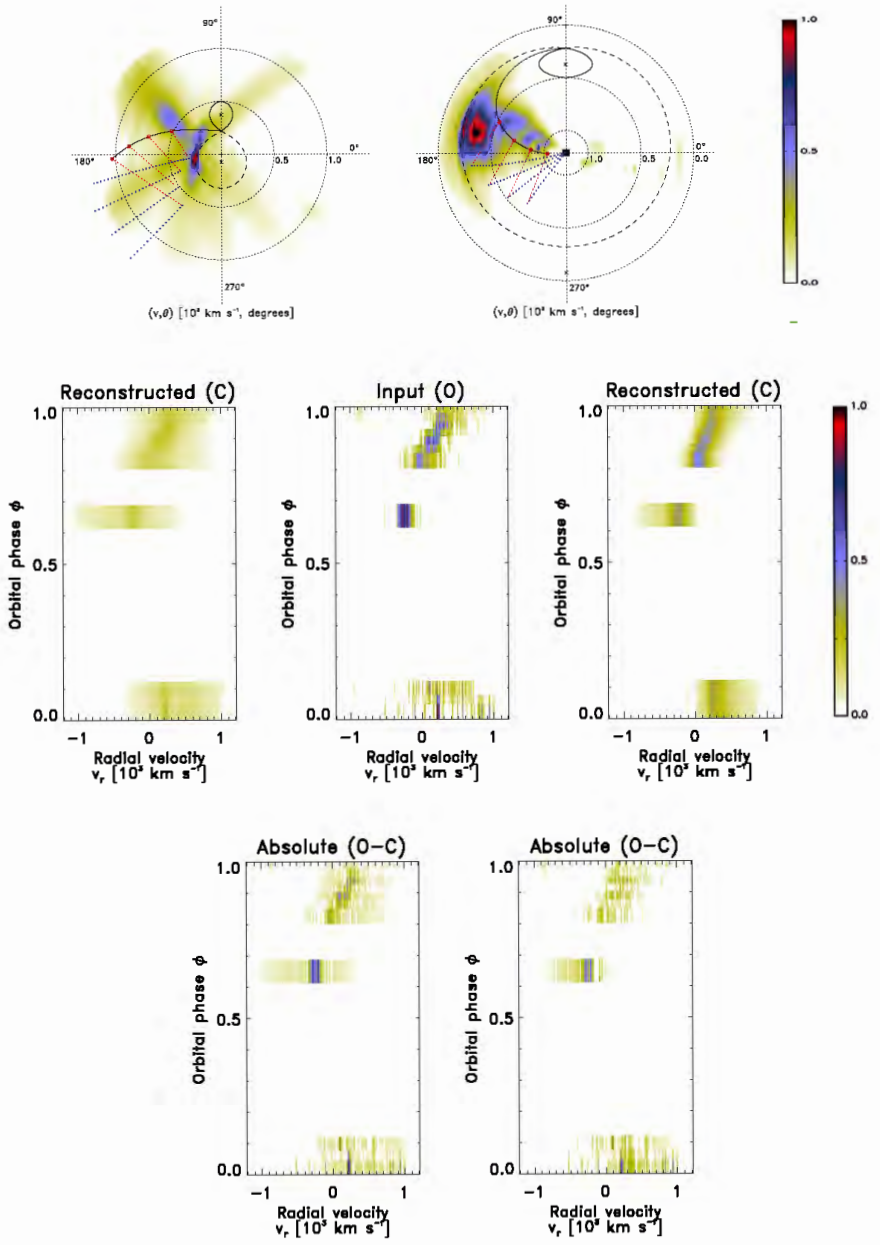

Figure A.27: Half-phase Doppler tomography of UZ For using the CaII 8542 Å line taken for phases 0.6–0.1.

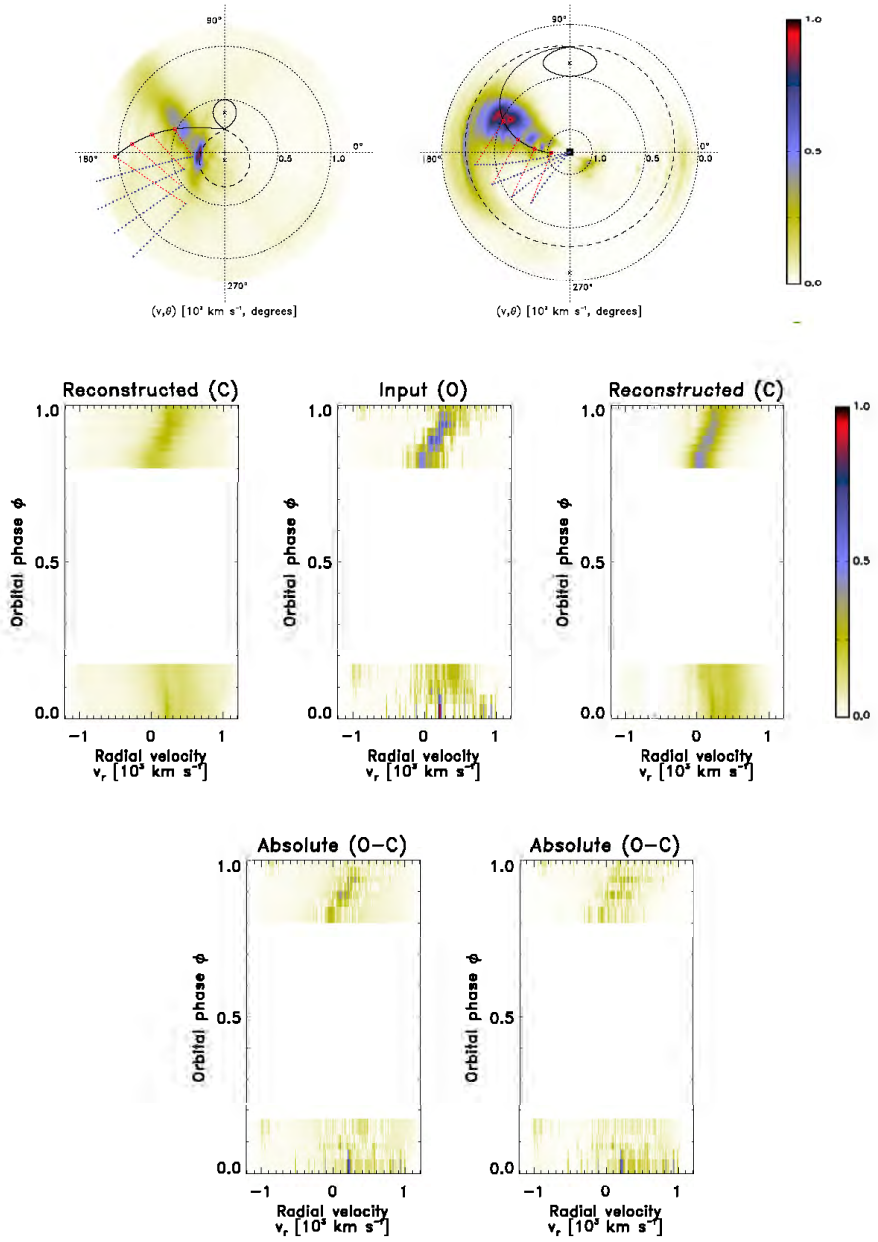

Figure A.28: Half-phase Doppler tomography of UZ For using the CaII 8542 Å line taken for phases 0.7–0.2.

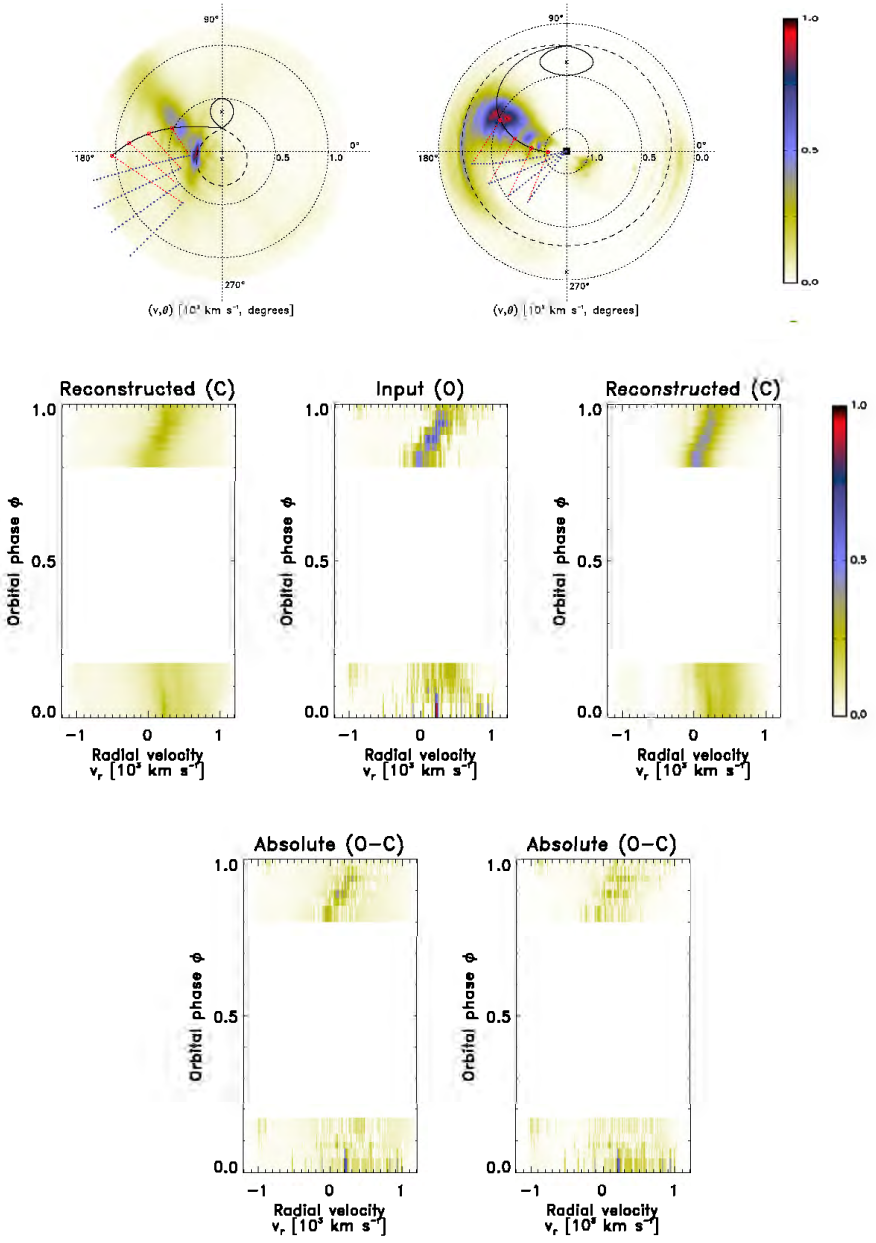

Figure A.29: Half-phase Doppler tomography of UZ For using the CaII 8542 Å line taken for phases 0.8–0.3.

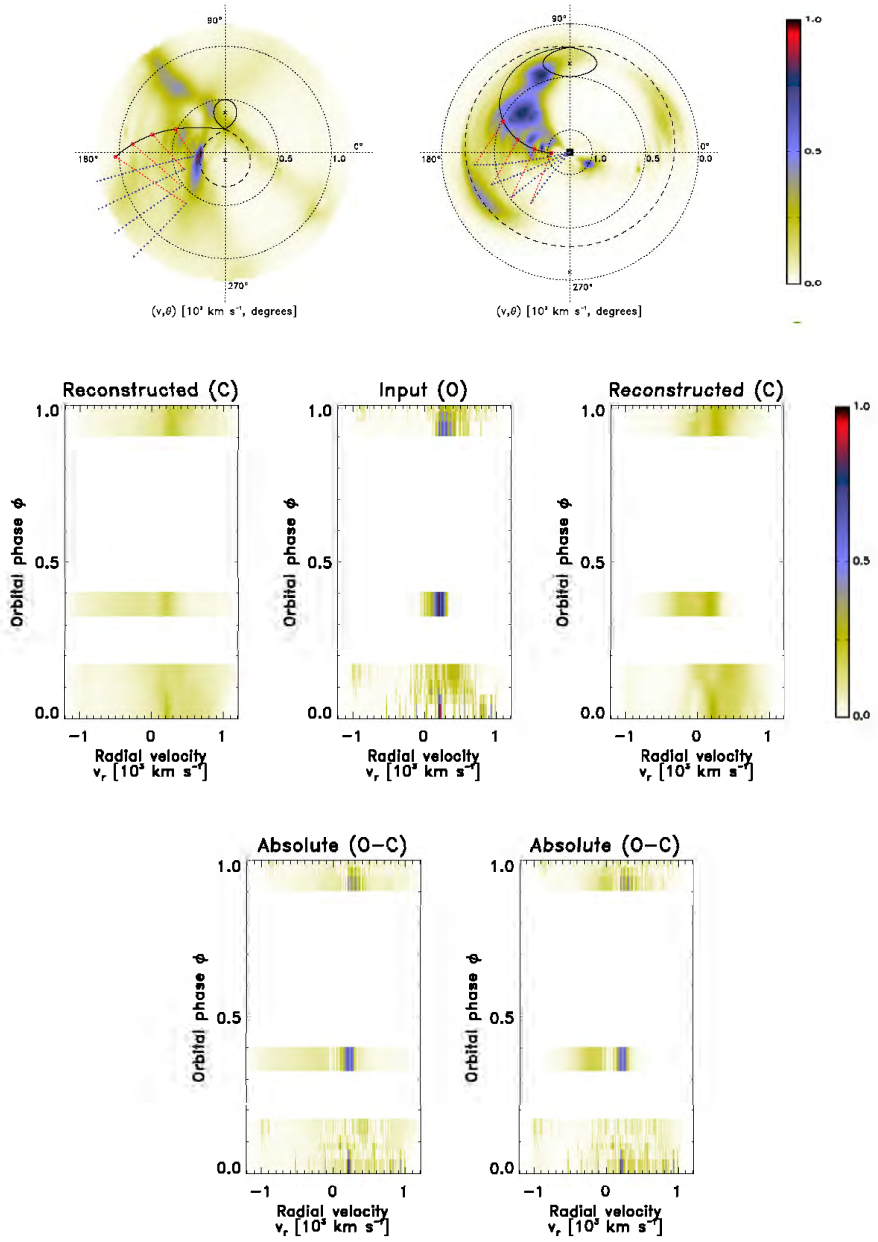

Figure A.30: Half-phase Doppler tomography of UZ For using the CaII 8542 Å line taken for phases 0.9–0.4.

Bibliography

Ables J. G., Jacka C. E., McConnell D., Schinckel A. E., Hunt A. J., 1986, Proceedings of the Astronomical Society of Australia, 6, 507

Abolfathi B., et al., 2018, ApJS, 235, 42

Achilleos N., Wickramasinghe D. T., Wu K., 1992, MNRAS, 256, 80

Aizu K., 1973, Progress of Theoretical Physics, 49, 1184

Allen R. G., Berriman G., Smith P. S., Schmidt G. D., 1989, ApJ, 347, 426

Almeida L. A., Jablonski F., 2011, in Sozzetti A., Lattanzi M. G., Boss A. P., eds, IAU Symposium Vol. 276, The Astrophysics of Planetary Systems: Formation, Structure, and Dynamical Evolution. pp 495–496, doi:10.1017/S1743921311020941

Amantayeva A., Zharikov S., Page K. L., Pavlenko E., Sosnovskij A., Khokhlov S., Ibraimov M., 2021, ApJ, 918, 58

Andreev M., Pavlenko E., Babina Y., Malanushenko V., 2013, in Krzesiński J., Stachowski G., Moskalik P., Bajan K., eds, Astronomical Society of the Pacific Conference Series Vol. 469, 18th European White Dwarf Workshop. p. 355

Andronov N., Pinsonneault M., Sills A., 2003, ApJ, 582, 358

Applegate J. H., 1992, ApJ, 385, 621

Applegate J. H., Patterson J., 1987, ApJ, 322, L99

Araujo-Betancor S., et al., 2005a, A&A, 430, 629

Araujo-Betancor S., Gänsicke B. T., Long K. S., Beuermann K., de Martino D., Sion E. M., Szkody P., 2005b, ApJ, 622, 589

Bailey J., 1978, MNRAS, 185, 73P

Bailey J., 1995, in Buckley D. A. H., Warner B., eds, Astronomical Society of the Pacific Conference Series Vol. 85, Magnetic Cataclysmic Variables. p. 10

Bailey J., Cropper M., 1991, MNRAS, 253, 27

Bailey J. A., Jones D. H. P., Parkes G. E., Mason K. O., 1978, MNRAS, 183, 73P

Bailey J., Hough J. H., Axon D. J., Gatley I., Lee T. J., Szkody P., Stokes G., Berriman G., 1982, MNRAS, 199, 801

Bailey J., et al., 1985, MNRAS, 215, 179

Bailey J., Wickramasinghe D. T., Hough J., Cropper M. S., 1987, IAU Circ., 4491, 2

Baldwin J. A., Stone R. P. S., 1984, MNRAS, 206, 241

Baptista R., 2016, Eclipse Mapping: Astrotomography of Accretion Discs. p. 155, doi:10.1007/978-3-319-39739-9_9

Barnes S. I., et al., 2008, The optical design of the Southern African Large Telescope high resolution spectrograph: SALT HRS. p. 70140K, doi:10.1117/12.788219

Barrett P. E., 2022, AJ, 163, 58

Barrett P. E., Chanmugam G., 1984, ApJ, 278, 298

Barrett P. E., Chanmugam G., 1985, ApJ, 298, 743

Barrett P. E., Dieck C., Beasley A. J., Singh K. P., Mason P. A., 2017, AJ, 154, 252

Barrett P., Dieck C., Beasley A., Mason P., Singh K. P., 2020a, in American Astronomical Society Meeting Abstracts #235. American Astronomical Society Meeting Abstracts. p. 370.03

Barrett P., Dieck C., Beasley A. J., Mason P. A., Singh K. P., 2020b, Advances in Space Research, 66, 1226

Barthelmy S. D., et al., 2005, Space Sci. Rev., 120, 143

Barwig H., Ritter H., Barnbantner O., 1994, A&A, 288, 204

Bassa C. G., Jonker P. G., Steeghs D., Torres M. A. P., 2009, MNRAS, 399, 2055

Bastian T. S., 1987, PhD thesis, University of Colorado, Boulder.

Bastian T. S., Dulk G. A., Chanmugam G., 1988, ApJ, 324, 431

Bastien P., Drissen L., Menard F., Moffat A. F. J., Robert C., St-Louis N., 1988, AJ, 95, 900

Beardmore A. P., Ramsay G., Osborne J. P., Mason K. O., Nousek J. A., Baluta C., 1995, MNRAS, 273, 742

Beasley A. J., Bastian T. S., Ball L., Wu K., 1994, AJ, 108, 2207

Belloni D., Schreiber M. R., Zorotovic M., Iłkiewicz K., Hurley J. R., Giersz M., Lagos F., 2018, MNRAS, 478, 5626

Benz A. O., Guedel M., 1989, A&A, 218, 137

Benz A. O., Fuerst E., Kiplinger A. L., 1983, Nature, 302, 45

Bera P., Bhattacharya D., 2018, MNRAS, 474, 1629

Berg R. A., Duthie J. G., 1977, ApJ, 211, 859

Berger J., Fringant A. M., 1980, A&A, 85, 367

Bernardini F., de Martino D., Mukai K., Falanga M., 2014, MNRAS, 445, 1403

Bernardini F., de Martino D., Mukai K., Russell D. M., Falanga M., Masetti N., Ferrigno C., Israel G., 2017, MNRAS, 470, 4815

Bernardini F., de Martino D., Mukai K., Falanga M., Masetti N., 2019, MNRAS, 489, 1044

Berriman G., Smith P. S., 1988, ApJ, 329, L97

Bertin E., Arnouts S., 1996, A&AS, 117, 393

Beuermann K., Burwitz V., 1995, in Buckley D. A. H., Warner B., eds, Astronomical Society of the Pacific Conference Series Vol. 85, Magnetic Cataclysmic Variables. p. 99

Beuermann K., Schwope A. D., 1994, in Shafter A. W., ed., Astronomical Society of the Pacific Conference Series Vol. 56, Interacting Binary Stars. p. 119

Beuermann K., Thomas H. C., Schwope A., Bailey J., Ferrario L., Tuohy I. R., Wickramasinghe D. T., Hough J. H., 1987, IAU Circ., 4517, 1

Beuermann K., Thomas H.-C., Schwope A., 1988, A&A, 195, L15

Beuermann K., Euchner F., Reinsch K., Jordan S., Gänsicke B. T., 2007, A&A, 463, 647

Beuermann K., et al., 2010, A&A, 521, L60

Beuermann K., et al., 2011, A&A, 526, A53

Beuermann K., Dreizler S., Hessman F. V., Deller J., 2012, A&A, 543, A138

Beuermann K., Dreizler S., Hessman F. V., 2013, A&A, 555, A133

Beuermann K., Dreizler S., Hessman F. V., Schwope A. D., 2014, A&A, 562, A63

Beuermann K., Burwitz V., Reinsch K., Schwope A., Thomas H. C., 2017, A&A, 603, A47

Beuermann K., Burwitz V., Reinsch K., Schwope A., Thomas H. C., 2020, A&A, 634, A91

Beuermann K., Burwitz V., Reinsch K., Schwope A., Thomas H. C., 2021, A&A, 645, A56

Biermann P., et al., 1985, ApJ, 293, 303

Björnsson C. I., 2019, ApJ, 873, 55

Bloemen S., Groot P., Nelemans G., Klein-Wolt M., 2015, The BlackGEM Array: Searching for Gravitational Wave Source Counterparts to Study Ultra-Compact Binaries. p. 254

Bloemen S., et al., 2016, MeerLICHT and BlackGEM: custom-built telescopes to detect faint optical transients. p. 990664, doi:10.1117/12.2232522

Boeshaar P. C., 1976, PhD thesis, Ohio State University, Columbus.

Bogensberger D., Clarke F., Lynas-Gray A. E., 2017, Open Astronomy, 26, 134

Bond I. A., Freeth R. V., 1988, MNRAS, 232, 753

Bonnet-Bidaud J. M., Mouchet M., 1987, A&A, 188, 89

Bonnet-Bidaud J. M., Somova T. A., Somov N. N., 1991, A&A, 251, L27

Bonnet-Bidaud J. M., Mouchet M., Busschaert C., Falize E., Michaut C., 2015, A&A, 579, A24

Bonnet-Bidaud J. M., et al., 2020, A&A, 633, A145

Bookbinder J. A., Lamb D. Q., 1987, ApJ, 323, L131

Bours M. C. P., et al., 2016, MNRAS, 460, 3873

Bowen I. S., 1934, PASP, 46, 146

Bowen I. S., 1935, ApJ, 81, 1

Bowyer S., Malina R. F., 1991, in Malina R. F., Bowyer S., eds, Extreme Ultraviolet Astronomy. p. 397

Bradt H. V., Rothschild R. E., Swank J. H., 1993, A&AS, 97, 355

Bramall D. G., et al., 2012, The SALT HRS spectrograph: instrument integration and laboratory test results. p. 84460A, doi:10.1117/12.925935

Breus V., Petrík K., Zola S., 2019, MNRAS, 488, 4526

Breytenbach H., Buckley D., Bonnet-Bidaud J. M., Mouchet M., 2015, in The Golden Age of Cataclysmic Variables and Related Objects - III (Golden2015). p. 18

Breytenbach H., et al., 2019, MNRAS, 484, 3831

Bridge C. M., 2004, PhD thesis, Mullard Space Science Laboratory, University College London, Holmbury St. Mary, Dorking, Surrey RH5 6NT, UK

Briggs D. S., 1995, in American Astronomical Society Meeting Abstracts. p. 112.02

Briggs G. P., Ferrario L., Tout C. A., Wickramasinghe D. T., 2018, MNRAS, 481, 3604

Brinkworth C. S., Marsh T. R., Dhillon V. S., Knigge C., 2006, MNRAS, 365, 287

Brinkworth C. S., et al., 2007, ApJ, 659, 1541

Brocklehurst M., 1971, MNRAS, 153, 471

Brown-Sevilla S. B., et al., 2021, MNRAS, 506, 2122

Buckley D. A. H., 2005, SALT First Generation Instruments. p. 273

Buckley D. A. H., 2019, in Griffin R. E., ed., IAU Symposium Vol. 339, Southern Horizons in Time-Domain Astronomy. pp 176–180, doi:10.1017/S174392131800251X

Buckley D. A. H., Ferrario L., Wickramasinghe D. T., Bailey J. A., 1998, MNRAS, 295, 899

Buckley D. A. H., Hearnshaw J. B., Nordsieck K. H., O'Donoghue D., 2003, Science drivers and first generation instrumentation for the Southern African Large Telescope (SALT). pp 264–275, doi:10.1117/12.457227

Buckley D. A. H., Charles P. A., Nordsieck K. H., O'Donoghue D., 2006a, in Whitelock P., Dennefeld M., Leibundgut B., eds, IAU Symposium Vol. 232, The Scientific Requirements for Extremely Large Telescopes. pp 1–12, doi:10.1017/S1743921306000202

Buckley D. A. H., Burgh E. B., Cottrell P. L., Nordsieck K. H., O'Donoghue D., Williams T. B., 2006b, in Society of Photo-Optical Instrumentation Engineers (SPIE) Conference Series. p. 62690A, doi:10.1117/12.673838

Burgh E. B., Nordsieck K. H., Kobulnicky H. A., Williams T. B., O'Donoghue D., Smith M. P., Percival J. W., 2003, in Iye M., Moorwood A. F. M., eds, Proc. SPIEVol. 4841, Instrument Design and Performance for Optical/Infrared Ground-based Telescopes. pp 1463–1471, doi:10.1117/12.460312

Burwitz V., Reinsch K., Beuermann K., Thomas H. C., 1997, A&A, 327, 183

Camilo F., et al., 2018, ApJ, 856, 180

Campbell R. K., Harrison T. E., Mason E., Howell S., Schwope A. D., 2008a, ApJ, 678, 1304

Campbell R. K., Harrison T. E., Kafka S., 2008b, ApJ, 683, 409

Catalán M. S., Schwope A. D., Smith R. C., 1999, MNRAS, 310, 123

Chambers K. C., et al. 2017, VizieR Online Data Catalog, p. II/349

Chandrasekhar S., 1931, ApJ, 74, 81

Chanmugam G., 1987, Ap&SS, 130, 53

Chanmugam G., Dulk G. A., 1981, ApJ, 244, 569

Chanmugam G., Dulk G. A., 1982, ApJ, 255, L107

Chanmugam G., Wagner R. L., 1978, ApJ, 222, 641

Chanmugam G., Wagner R. L., 1979, ApJ, 232, 895

Chanmugam G., Barrett P. E., Wu K., Courtney M. W., 1989, ApJS, 71, 323

Chanmugam G., Frank J., King A. R., Lasota J. P., 1990, ApJ, 350, L13

Condon J. J., 1997, PASP, 109, 166

Coppejans D. L., Knigge C., 2020, New Astronomy Reviews, 89, 101540

Coppejans R., et al., 2013, PASP, 125, 976

Coppejans D. L., Körding E. G., Miller-Jones J. C. A., Rupen M. P., Knigge C., Sivakoff G. R., Groot P. J., 2015, MNRAS, 451, 3801

Coppejans D. L., Körding E. G., Knigge C., Pretorius M. L., Woudt P. A., Groot P. J., Van Eck C. L., Drake A. J., 2016a, MNRAS, 456, 4441

Coppejans D. L., et al., 2016b, MNRAS, 463, 2229

Costa J. E. R., Rodrigues C. V., 2009, MNRAS, 398, 240

Cowley A. P., Crampton D., 1977, ApJ, 212, L121

Crampton D., Cowley A. P., Fisher W. A., 1986, ApJ, 300, 788

Crawford J. A., Kraft R. P., 1956, ApJ, 123, 44

Crawford S. M., et al., 2010, in Observatory Operations: Strategies, Processes, and Systems III. p. 773725, doi:10.1117/12.857000

Cropper M., 1985, MNRAS, 212, 709

Cropper M., 1989, MNRAS, 236, 935

Cropper M., 1990, Space Sci. Rev., 54, 195

Cropper M., Warner B., 1986, MNRAS, 220, 633

Cropper M., Wickramasinghe D. T., 1993, MNRAS, 260, 696

Cropper M., et al., 1989, MNRAS, 236, 29P

Cropper M., Mason K. O., Mukai K., 1990, MNRAS, 243, 565

Cropper M., Wu K., Ramsay G., Kocabiyik A., 1999, MNRAS, 306, 684

Cropper M., Wu K., Ramsay G., 2000, New Astronomy Reviews, 44, 57

Crosa L., Szkody P., Stokes G., Swank J., Wallerstein G., 1981, ApJ, 247, 984

Cutri R. M., et al., 2003, 2MASS All Sky Catalog of point sources.

Dai Z.-B., Qian S.-B., Fernández Lajús E., Baume G. L., 2010, MNRAS, 409, 1195

Dai Z., Qian S., Li L., 2013, ApJ, 774, 153

De Martino D., et al., 2008, Mem. Soc. Astron. Italiana, 79, 246

de Bruijne J. H., Reynolds A. P., Perryman M. A., Favata F., Peacock A. J., 2002, Optical Engineering, 41, 1158

de Kool M., 1992, A&A, 261, 188

de Martino D., et al., 2008, A&A, 481, 149

de Martino D., Bernardini F., Mukai K., Falanga M., Masetti N., 2020, Advances in Space Research, 66, 1209

Diaz M., Steiner J. E., 1994, in Braga J., Barbuy B., Leister N. V., eds, XIXth Meeting of the Brazilian Astronomical Society. p. 63

Doi M., et al., 2010, AJ, 139, 1628

Donati J. F., 1999, MNRAS, 302, 457

Doyle L. R., et al., 2011, Science, 333, 1602

Drake A. J., et al., 2009, in American Astronomical Society Meeting Abstracts #213. p. 470.07

Driessen L. N., et al., 2020, MNRAS, 491, 560

Drummond W. E., Rosenbluth M. N., 1963, Physics of Fluids, 6, 276

Dulk G. A., 1985, ARA&A, 23, 169

Dulk G. A., Bastian T. S., Chanmugam G., 1983, ApJ, 273, 249

Eastman J., Siverd R., Gaudi B. S., 2010, PASP, 122, 935

Echevarría J., Schwarzenberg-Czerny A., Jones D. H. P., Dick J. S. B., Ward M., Costero R., Gilmozzi R., 1988, Revista Mexicana Astron. Astrof., 16, 87

Echevarría J., Ramírez-Torres A., Michel R., Hernández Santisteban J. V., 2016, MNRAS, 461, 1576

Einstein A., 1905, Annalen der Physik, 322, 891

Elkholy E., Nouh M. I., 2015, Astrophysical Bulletin, 70, 333

Er H., Özdönmez A., Nasiroglu I., 2021, MNRAS, 507, 809

Esmer E. M., Başt ürk Ö., Hinse T. C., Selam S. O., Correia A. C. M., 2021, A&A, 648, A85

Euchner F., Reinsch K., Jordan S., Beuermann K., Gänsicke B. T., 2005, A&A, 442, 651

Eze R. N. C., 2015, New Astronomy, 37, 35

Ezuka H., Ishida M., 1999, ApJS, 120, 277

Fabian A. C., Pringle J. E., Rees M. J., 1976, MNRAS, 175, 43

Farihi J., Burleigh M. R., Hoard D. W., 2008, ApJ, 674, 421

Faulkner J., 1971, ApJ, 170, L99

Fender R., et al., 2017, arXiv e-prints, p. arXiv:1711.04132

Ferrario L., Wickramasinghe D. T., 1989, in Wegner G., ed., Lecture Notes in Physics, Berlin Springer Verlag Vol. 328, IAU Colloq. 114: White Dwarfs. pp 324–328, doi:10.1007/3-540-51031-1_340

Ferrario L., Wickramasinghe D. T., 1990, ApJ, 357, 582

Ferrario L., Wickramasinghe D. T., Tuohy I. R., Bailey J., 1988, IAU Circ., 4523

Ferrario L., Wickramasinghe D. T., Bailey J., Tuohy I. R., Hough J. H., 1989, ApJ, 337, 832

Ferrario L., Wickramasinghe D. T., Bailey J., Hough J. H., Tuohy I. R., 1992, MNRAS, 256, 252

Ferrario L., Bailey J., Wickramasinghe D. T., 1993, MNRAS, 262, 285

Ferrario L., Wickramasinghe D., Bailey J., Buckley D., 1995, MNRAS, 273, 17

Ferrario L., Bailey J., Wickramasinghe D., 1996, MNRAS, 282, 218

Ferrario L., Wickramasinghe D. T., Schmidt G., 2003, MNRAS, 338, 340

Ferrario L., de Martino D., Gänsicke B. T., 2015, Space Sci. Rev., 191, 111

Ferrario L., Wickramasinghe D., Kawka A., 2020, Advances in Space Research, 66, 1025

Fishman G. J., 1977, IAU Circ., 3099, 2

Foreman-Mackey D., Hogg D. W., Lang D., Goodman J., 2013, PASP, 125, 306

Frank J., King A. R., Lasota J. P., 1988, A&A, 193, 113

Frank J., King A., Raine D., 1992, Science, 258, 1015

Frank J., King A., Raine D. J., 2002, Accretion Power in Astrophysics: Third Edition

Frater R. H., Brooks J. W., 1992, J. Electr. Electron. Eng., 12, 100

Friedrich S., et al., 1996a, A&A, 306, 860

Friedrich S., Staubert R., La Dous C., 1996b, A&A, 315, 411

Fuerst E., Benz A., Hirth W., Kiplinger A., Geffert M., 1986, A&A, 154, 377

Gabdeev M. M., Borisov N. V., Shimansky V. V., Kolbin A. I., Nikolaeva E. A., 2019, in Kudryavtsev D. O., Romanyuk I. I., Yakunin I. A., eds, Astronomical Society of the Pacific Conference Series Vol. 518, Physics of Magnetic Stars. p. 100

Gaia Collaboration 2018, VizieR Online Data Catalog, p. I/345

Gänsicke B. T., 1997, PhD thesis, University of Göttingen

Gänsicke B. T., Hoard D. W., Beuermann K., Sion E. M., Szkody P., 1998, A&A, 338, 933

Gänsicke B. T., Beuermann K., de Martino D., Thomas H. C., 2000, A&A, 354, 605

Gänsicke B. T., Fischer A., Silvotti R., de Martino D., 2001a, A&A, 372, 557

Gänsicke B. T., Schmidt G. D., Jordan S., Szkody P., 2001b, ApJ, 555, 380

Gänsicke B. T., Jordan S., Beuermann K., de Martino D., Szkody P., Marsh T. R., Thorstensen J., 2004, ApJ, 613, L141

Gawroński M. P., Goździewski K., Katarzyński K., Rycyk G., 2018, MNRAS, 475, 1399

Gehrels N., et al., 2004, ApJ, 611, 1005

Gerke J. R., Howell S. B., Walter F. M., 2006, PASP, 118, 678

Giacconi R., et al., 1979, ApJ, 230, 540

Giommi P., Angelini L., Osborne J., Stella L., Tagliaferri G., Beuermann K., Thomas H.-C., 1987, IAU Circ., 4486, 1

Glenn J., Howell S. B., Schmidt G. D., Liebert J., Grauer A. D., Wagner R. M., 1994, ApJ, 424, 967

Goliasch J., Nelson L., 2015, ApJ, 809, 80

González Hernández J. I., Casares J., 2010, A&A, 516, A58

Goodman J., Weare J., 2010, Communications in Applied Mathematics and Computational Science, 5, 65

Goździewski K., et al., 2015, MNRAS, 448, 1118

Guinan E. F., Ribas I., 2001, ApJ, 546, L43

Gulbis A. A. S., O'Donoghue D., Fourie P., Rust M., Sass C., Stoffels J., 2011a, in EPSC-DPS Joint Meeting 2011. p. 1173

Gulbis A. A. S., et al., 2011b, PASP, 123, 461

Gunn J. E., et al., 1998, AJ, 116, 3040

Haghighipour N., 2015, Planet Detection; Eclipse Timing Variation. pp 1909–1912, doi:10.1007/978-3-662-44185-5_5291

Hakala P. J., 1995, A&A, 296, 164

Hakala P. J., Piirola V., Vilhu O., Osborne J. P., Hannikainen D. C., 1994, MNRAS, 271, L41

Hakala P., Cropper M., Ramsay G., 2002, MNRAS, 334, 990

Hakala P., Ramsay G., Potter S. B., Beardmore A., Buckley D. A. H., Wynn G., 2019, MNRAS, 486, 2549

Hall D. S., 1989, Space Sci. Rev., 50, 219

Hameury J. M., Lasota J. P., King A. R., 1988, A&A, 195, L12

Hardy A., et al., 2015, ApJ, 800, L24

Hardy A., et al., 2016, MNRAS, 459, 4518

Harlaftis E. T., Steeghs D., Horne K., Martín E., Magazzú A., 1999, MNRAS, 306, 348

Harrison T. E., Campbell R. K., 2015, ApJS, 219, 32

Harrison T. E., Campbell R. K., 2018, MNRAS, 474, 1572

Harrison F. A., et al., 2013, ApJ, 770, 103

Harrop-Allin M. K., Cropper M., Potter S. B., Dhillon V. S., Howell S. B., 1997, MNRAS, 288, 1033

Harrop-Allin M. K., Cropper M., Hakala P. J., Hellier C., Ramseyer T., 1999, MNRAS, 308, 807

Hartley L. E., Murray J. R., Drew J. E., Long K. S., 2005, MNRAS, 363, 285

Hastings N. C., Szkody P., Hoard D. W., Fried R., Vanmunster T., Pray D., Kowalski R. A., 1999, PASP, 111, 177

Hearn D. R., Richardson J. A., Clark G. W., 1976, ApJ, 210, L23

Heise J., Verbunt F., 1988, A&A, 189, 112

Heise J., Brinkman A. C., Gronenschild E., Watson M., King A. R., Stella L., Kieboom K., 1985, A&A, 148, L14

Hellier C., 1996, The intermediate polars. p. 143, doi:10.1007/978-94-009-0325-8_44

Hellier C., 1997, MNRAS, 288, 817

Hernández Santisteban J. V., Knigge C., Pretorius M. L., Sullivan M., Warner B., 2018, MNRAS, 473, 3241

Hessman F. V., Gänsicke B. T., Mattei J. A., 2000, A&A, 361, 952

Hettlage C., et al., 2010, Handling observation proposals for SALT. p. 77371B, doi:10.1117/12.858025

Hewitt D. M., et al., 2020, MNRAS, 496, 2542

Heywood I., 2020, oxkat: Semi-automated imaging of MeerKAT observations (ascl:2009.003)

Hilditch R. W., 2001, An Introduction to Close Binary Stars

Hillman Y., Shara M. M., Prialnik D., Kovetz A., 2020, Nature Astronomy, 4, 886

Hinse T. C., Lee J. W., Goździewski K., Haghighipour N., Lee C.-U., Scullion E. M., 2012, MNRAS, 420, 3609

Horne K., 1985, MNRAS, 213, 129

Horne K., 1986, PASP, 98, 609

Horne K., Marsh T. R., 1986, MNRAS, 218, 761

Horner J., Marshall J. P., Wittenmyer R. A., Tinney C. G., 2011, MNRAS, 416, L11

Horner J., Wittenmyer R. A., Hinse T. C., Tinney C. G., 2012a, MNRAS, 425, 749

Horner J., Hinse T. C., Wittenmyer R. A., Marshall J. P., Tinney C. G., 2012b, MNRAS, 427, 2812

Horner J., Wittenmyer R. A., Hinse T. C., Marshall J. P., Mustill A. J., Tinney C. G., 2013, MNRAS, 435, 2033

Hsu J.-C., Breger M., 1982, ApJ, 262, 732

Huang S.-S., 1966, Annales d'Astrophysique, 29, 331

Iaria R., et al., 2018, MNRAS, 473, 3490

Iben Icko J., Livio M., 1993, PASP, 105, 1373

Imamura J. N., Steiman-Cameron T. Y., 1998, ApJ, 501, 830

Irwin J. B., 1952, ApJ, 116, 211

Irwin J. B., 1959, AJ, 64, 149

Irwin J. A., 2007, Astrophysics: Decoding the Cosmos

Ishida M., 1991, PhD thesis, University of Tokyo

Jahoda K., Swank J. H., Giles A. B., Stark M. J., Strohmayer T., Zhang W., Morgan E. H., 1996, in Siegmund O. H., Gummin M. A., eds, Society of Photo-Optical Instrumentation Engineers (SPIE) Conference Series Vol. 2808, EUV, X-Ray, and Gamma-Ray Instrumentation for Astronomy VII. pp 59–70, doi:10.1117/12.256034

Jain C., Paul B., Sharma R., Jaleel A., Dutta A., 2017, MNRAS, 468, L118

Jansen F., et al., 2001, A&A, 365, L1

Jarvis M., et al., 2016, in MeerKAT Science: On the Pathway to the SKA. p. 6 (arXiv:1709.01901)

Jaynes E. T., 1957, Physical Review, 106, 620

Jonas J. L., 2009, IEEE Proceedings, 97, 1522

Jonas J., MeerKAT Team 2016, in Proceedings of MeerKAT Science: On the Pathway to the SKA. 25-27 May. p. 1

Joshi A., Pandey J. C., 2019, Bulletin de la Societe Royale des Sciences de Liege, 88, 240

Joshi A., Pandey J. C., Singh K. P., Agrawal P. C., 2016, ApJ, 830, 56

Joshi A., Pandey J. C., Singh H. P., 2019, AJ, 158, 11

Joshi A., Pandey J. C., Raj A., Singh K. P., Anupama G. C., Singh H. P., 2020, MNRAS, 491, 201

Joshi A., Pandey J. C., Rawat N., Raj A., Wang W., Singh H. P., 2022, AJ, 163, 221

Kővári Z., et al., 2021, A&A, 650, A158

Kafka S., 2020, in Observations from the AAVSO International Database, https://www.aavso.org.

Kafka S., Hoard D. W., 2009, PASP, 121, 1352

Kafka S., Honeycutt R. K., 2000, in American Astronomical Society Meeting Abstracts. p. 85.07

Kafka S., Honeycutt R. K., 2003, AJ, 125, 2188

Kafka S., Honeycutt R. K., 2005, AJ, 130, 742

Kafka S., Robertson J., Honeycutt R. K., Howell S. B., 2005a, AJ, 129, 2411

Kafka S., Honeycutt R. K., Howell S. B., Harrison T. E., 2005b, AJ, 130, 2852

Kafka S., Howell S. B., Honeycutt R. K., Robertson J. W., 2007, AJ, 133, 1645

Kalomeni B., 2012, MNRAS, 422, 1601

Kalomeni B., Yakut K., 2008, AJ, 136, 2367

Kalomeni B., Pekünlü E. R., Yakut K., 2005, A&A, 439, 823

Kalomeni B., Nelson L., Rappaport S., Molnar M., Quintin J., Yakut K., 2016, ApJ, 833, 83

Katajainen S., et al., 2003, MNRAS, 340, 1

Katysheva N., Shugarov S., 2012, Mem. Soc. Astron. Italiana, 83, 670

Kennedy M. R., et al., 2020, MNRAS, 495, 4445

Khangale Z. N., Potter S. B., Woudt P. A., 2019a, in Griffin R. E., ed., IAU Symposium Vol. 339, Southern Horizons in Time-Domain Astronomy. pp 314–317, doi:10.1017/S1743921318002867

Khangale Z. N., Potter S. B., Kotze E. J., Woudt P. A., Breytenbach H., 2019b, A&A, 621, A31

Khangale Z. N., et al., 2020, MNRAS, 492, 4298

Khangale Z. N., Potter S. B., Woudt P. A., 2021, in Bisikalo D., Giovannelli F., René H., Mason P., Mikolajewska J., Shaviv G., Sion E. M., eds, Proceedings of Science Vol. 2-7, The Golden Age of Cataclysmic Variables and Related Objects V. 2-7 September 2019. Palermo. p. 19

King A. R., Lasota J. P., 1979, MNRAS, 188, 653

King A. R., Lasota J. P., 1980, MNRAS, 191, 721

King A. R., Williams G. A., 1985, MNRAS, 215, 1P

Kippenhahn R., Meyer-Hofmeister E., 1977, A&A, 54, 539

Knigge C., 2006, MNRAS, 373, 484

Knigge C., Baraffe I., Patterson J., 2011, ApJS, 194, 28

Kobulnicky H. A., Nordsieck K. H., Burgh E. B., Smith M. P., Percival J. W., Williams T. B., O'Donoghue D., 2003, in Iye M., Moorwood A. F. M., eds, Proc. SPIEVol. 4841, Instrument Design and Performance for Optical/Infrared Ground-based Telescopes. pp 1634–1644, doi:10.1117/12.460315

Kolb U., Baraffe I., 1999, MNRAS, 309, 1034

Kolbin A. I., Serebryakova N. A., Gabdeev M. M., Borisov N. V., 2019, Astrophysical Bulletin, 74, 80

Körding E., Rupen M., Knigge C., Fender R., Dhawan V., Templeton M., Muxlow T., 2008, Science, 320, 1318

Körding E. G., Knigge C., Tzioumis T., Fender R., 2011, MNRAS, 418, L129

Kornilov V. G., et al., 2012, Experimental Astronomy, 33, 173

Kotze E. J., 2017, PhD thesis, University of Cape Town, South Africa

Kotze E. J., Potter S. B., McBride V. A., 2015, A&A, 579, A77

Kotze E. J., Potter S. B., McBride V. A., 2016, A&A, 595, A47

Kraft R. P., Mathews J., Greenstein J. L., 1962, ApJ, 136, 312

Krzeminski W., Serkowski K., 1977, ApJ, 216, L45

Kube J., Gänsicke B. T., Beuermann K., 1999, in Hellier C., Mukai K., eds, Astronomical Society of the Pacific Conference Series Vol. 157, Annapolis Workshop on Magnetic Cataclysmic Variables. p. 99 (arXiv:astro-ph/9810081)

Kuijpers J., Pringle J. E., 1982, A&A, 114, L4

Kundra E., Hric L., 2011, Ap&SS, 331, 121

Kurbatov E. P., Zhilkin A. G., Bisikalo D. V., 2019, Astronomy Reports, 63, 25

Kuulkers E., Norton A., Schwope A., Warner B., 2006, X-rays from cataclysmic variables. pp 421–460

Lamb D. Q., 1985, in Lamb D. Q., Patterson J., eds, Cataclysmic Variables and Low-Mass X-ray Binaries. p. 179, doi:10.1007/978-94-009-5319-2_21

Lamb D. Q., Masters A. R., 1979, ApJ, 234, L117

Lanza A. F., 2006, MNRAS, 369, 1773

Lanza A. F., 2020, MNRAS, 491, 1820

Lanza A. F., Rodonò M., 1999, A&A, 349, 887

Lanza A. F., Rodono M., Rosner R., 1998, MNRAS, 296, 893

Larsson S., 1987, A&A, 181, L15

Larsson S., 1989, A&A, 217, 146

Latham D. W., Liebert J., Steiner J. E., 1981, ApJ, 246, 919

Latković O., Cséki A., Djurašević G., Essam A., Hamed A. S., Youssef S. M., 2019, AJ, 157, 3

Lazaridis K., et al., 2011, MNRAS, 414, 3134

Lee J. W., Kim S.-L., Kim C.-H., Koch R. H., Lee C.-U., Kim H.-I., Park J.-H., 2009, AJ, 137, 3181

Lee J. W., Hinse T. C., Youn J.-H., Han W., 2014, MNRAS, 445, 2331

Levine A. M., Bradt H., Cui W., Jernigan J. G., Morgan E. H., Remillard R., Shirey R. E., Smith D. A., 1996, ApJ, 469, L33

Li J. K., Wu K. W., Wickramasinghe D. T., 1994, MNRAS, 268, 61

Lichfield S. J., King A. R., 1990, MNRAS, 247, 200

Liebert J., Stockman H. S., 1979, ApJ, 229, 652

Liebert J., Stockman H. S., 1985, The AM Herculis Magnetic Variables. p. 151, doi:10.1007/978-94-009-5319-2_20

Liebert J., Stockman H. S., Angel J. R. P., Woolf N. J., Hege K., Margon B., 1978, ApJ, 225, 201

Lipkin Y., Leibowitz E. M., 2004, in Vrielmann S., Cropper M., eds, Astronomical Society of the Pacific Conference Series Vol. 315, IAU Colloq. 190: Magnetic Cataclysmic Variables. p. 176

Lipkin Y. M., Leibowitz E. M., 2008, MNRAS, 387, 289

Lipunov V., et al., 2010, Advances in Astronomy, 2010, 349171

Littlefield C., Garnavich P., 2020, Research Notes of the American Astronomical Society, 4, 171

Littlefield C., et al., 2015a, MNRAS, 449, 3107

Littlefield C., Garnavich P., Magno K., Murison M., Deal S., McClelland C., Rose B., 2015b, Information Bulletin on Variable Stars, 6129, 1

Littlefield C., Garnavich P., Hoyt T. J., Kennedy M., 2018a, AJ, 155, 18

Littlefield C., Garnavich P., Kennedy M., Szkody P., Dai Z., 2018b, AJ, 155, 232

Littlefield C., Garnavich P., Mukai K., Mason P. A., Szkody P., Kennedy M., Myers G., Schwarz R., 2019, ApJ, 881, 141

Littlefield C., Garnavich P., Szkody P., Ramsay G., Howell S., Lima I., Kennedy M., Cook L., 2020, arXiv e-prints, p. arXiv:2004.08923

Livio M., Pringle J. E., 1994, ApJ, 427, 956

Livio M., Shara M. M., 1987, ApJ, 319, 819

Longair M. S., 2011, High Energy Astrophysics

Lopes de Oliveira R., Bruch A., Rodrigues C. V., Oliveira A. S., Mukai K., 2020, ApJ, 898, L40

Lucy L. B., 1974, AJ, 79, 745

Lucy L. B., 1994, A&A, 289, 983

Mai X., Mutel R. L., 2022, MNRAS, 513, 2478

Makino F., ASTRO-C Team 1987, Astrophys. Lett., 25, 223

Marsh T. R., 2001, in Boffin H. M. J., Steeghs D., Cuypers J., eds, Lecture Notes in Physics, Berlin Springer Verlag Vol. 573, Astrotomography, Indirect Imaging Methods in Observational Astronomy. p. 1 (arXiv:astro-ph/0011020)

Marsh T. R., 2005, Ap&SS, 296, 403

Marsh T. R., 2018, Circumbinary Planets Around Evolved Stars. p. 96, doi:10.1007/978-3-319-55333-7_96

Marsh T. R., Horne K., 1988, MNRAS, 235, 269

Marsh T. R., Schwope A. D., 2016, in Boffin H. M. J., Hussain G., Berger J.-P., Schmidtobreick L., eds, Astrophysics and Space Science Library, Vol. 439, Astronomy at High Angular Resolution. p. 195, doi:10.1007/978-3-319-39739-9_11

Marsh T. R., et al., 2014, MNRAS, 437, 475

Mason K. O., 1985, Space Sci. Rev., 40, 99

Mason P. A., Gray C., 2004, in Vrielmann S., Cropper M., eds, Astronomical Society of the Pacific Conference Series Vol. 315, IAU Colloq. 190: Magnetic Cataclysmic Variables. p. 237

Mason P. A., Gray C. L., 2007, ApJ, 660, 662

Mason P. A., Santana J. B., 2015, in Giovannelli F., ed., The Golden Age of Cataclysmic Variables and Related Objects - III (Golden2015). Proceedings of Science. p. 16

Mason P. A., Fisher P. L., Chanmugam G., 1996, A&A, 310, 132

Mason P. A., Ramsay G., Andronov I., Kolesnikov S., Shakhovskoy N., Pavlenko E., 1998, MNRAS, 295, 511

Mason P. A., Wells N. K., Motsoaledi M., Szkody P., Gonzalez E., 2019, MNRAS, 488, 2881

Masters A. R., 1978, PhD thesis, Illinois Univ., Urbana-Champaign.

Matese J. J., Whitmire D. P., 1983, A&A, 117, L7

Matsuoka M., et al., 2009, PASJ, 61, 999

Matt G., de Martino D., Gänsicke B. T., Negueruela I., Silvotti R., Bonnet-Bidaud J. M., Mouchet M., Mukai K., 2000, A&A, 358, 177

Mauche C. W., 2002, ApJ, 578, 439

Mazeh T., Kieboom K., Heise J., 1986, MNRAS, 221, 513

McClintock J. E., Canizares C. R., Tarter C. B., 1975, ApJ, 198, 641

McMullin J. P., Waters B., Schiebel D., Young W., Golap K., 2007, in Shaw R. A., Hill F., Bell D. J., eds, Astronomical Society of the Pacific Conference Series Vol. 376, Astronomical Data Analysis Software and Systems XVI. p. 127

McPhate J. B., Siegmund O. H. W., Welsh B. Y., Vallerga J. V., Buckley D. A. H., Gulbis A. a. A. S., Brink J. D., Rogers D., 2012, Physics Procedia, 37, 1453

Meggitt S. M. A., Wickramasinghe D. T., 1982, MNRAS, 198, 71

Melrose D. B., Dulk G. A., 1982, ApJ, 259, 844

Meyer F., Meyer-Hofmeister E., 1981, A&A, 104, L10

Middleditch J., 1982, ApJ, 257, L71

Middleditch J., Imamura J. N., Steiman-Cameron T. Y., 1997, ApJ, 489, 912

Monet D. G., et al., 2003, AJ, 125, 984

Morin J., Hill C. A., Watson C. A., 2016, in Boffin H. M. J., Hussain G., Berger J.-P., Schmidtobreick L., eds, Astrophysics and Space Science Library, Vol. 439, Astronomy at High Angular Resolution. p. 223, doi:10.1007/978-3-319-39739-9_12

Mouchet M., et al., 2017, A&A, 600, A53

Mukai K., 1988, MNRAS, 232, 175

Mukai K., 2017, PASP, 129, 062001

Mukai K., Charles P. A., 1986, MNRAS, 222, 1P

Navarrete F. H., Schleicher D. R. G., Zamponi Fuentealba J., Völschow M., 2018, A&A, 615, A81

Naylor T., 1998, MNRAS, 296, 339

Nelemans G., 2005, in Hameury J. M., Lasota J. P., eds, Astronomical Society of the Pacific Conference Series Vol. 330, The Astrophysics of Cataclysmic Variables and Related Objects. p. 27 (arXiv:astro-ph/0409676)

Neo S., Miyaji S., Nomoto K., Sugimoto D., 1977, PASJ, 29, 249

Nogami D., Gänsicke B. T., Beuermann K., 2002, in Gänsicke B. T., Beuermann K., Reinsch K., eds, Astronomical Society of the Pacific Conference Series Vol. 261, The Physics of Cataclysmic Variables and Related Objects. p. 159

Nordhaus J., Wellons S., Spiegel D. S., Metzger B. D., Blackman E. G., 2011, Proceedings of the National Academy of Science, 108, 3135

Nordsieck K., 2012, in Hoffman J. L., Bjorkman J., Whitney B., eds, American Institute of Physics Conference Series Vol. 1429, American Institute of Physics Conference Series. pp 248–251, doi:10.1063/1.3701934

Norton A. J., Somerscales R. V., Wynn G. A., 2004, in Vrielmann S., Cropper M., eds, Astronomical Society of the Pacific Conference Series Vol. 315, IAU Colloq. 190: Magnetic Cataclysmic Variables. p. 216 (arXiv:astro-ph/0301351)

Nugent J. J., et al., 1983, ApJS, 51, 1

O'Donoghue D., 1995, Baltic Astronomy, 4, 519

O'Donoghue D., et al., 2003, SALTICAM: $0.5M acquisition camera: every big telescope should have one. pp 465–476, doi:10.1117/12.460772

O'Donoghue D., et al., 2006, MNRAS, 372, 151

Offringa A. R., 2010, AOFlagger: RFI Software (ascl:1010.017)

Offringa A. R., van de Gronde J. J., Roerdink J. B. T. M., 2012, A&A, 539, A95

Oliveira A. S., Rodrigues C. V., Palhares M. S., Diaz M. P., Belloni D., Silva K. M. G., 2019, MNRAS, 489, 4032

Osborne J. P., Cropper M., Cristiani S., 1987a, Ap&SS, 131, 643

Osborne J. P., Beuermann K., Charles P., Maraschi L., Mukai K., Treves A., 1987b, ApJ, 315, L123

Osborne J. P., Giommi P., Angelini L., Tagliaferri G., Stella L., 1988, ApJ, 328, L45

Osborne J. P., Beardmore A. P., Wheatley P. J., Hakala P., Watson M. G., Mason K. O., Hassall B. J. M., King A. R., 1994, MNRAS, 270, 650

Osterbrock D. E., 1989, Astrophysics of gaseous nebulae and active galactic nuclei

Paczyński B., 1967, AcA, 17, 287

Paczynski B., 1986, ApJ, 304, 1

Paczynski B., Sienkiewicz R., 1981, ApJ, 248, L27

Paczynski B., Sienkiewicz R., 1983, ApJ, 268, 825

Padin S., Davis R. J., Lasenby A. N., 1987, MNRAS, 224, 685

Pagnotta A., Zurek D., 2016, MNRAS, 458, 1833

Pala A. F., et al., 2020, MNRAS, 494, 3799

Pandel D., Córdova F. A., 2002, MNRAS, 336, 1049

Papaloizou J. C. B., Pringle J. E., MacDonald J., 1982, MNRAS, 198, 215

Parsons S. G., et al., 2010, MNRAS, 407, 2362

Parsons S. G., Marsh T. R., Gänsicke B. T., Schreiber M. R., Bours M. C. P., Dhillon V. S., Littlefair S. P., 2013, MNRAS, 436, 241

Parsons S. G., et al., 2014, MNRAS, 438, L91

Parsons S. G., et al., 2016, MNRAS, 458, 2793

Paterson K., 2019, PhD thesis, University of Cape Town, RSA, https://open.uct.ac.za/handle/11427/29987

Patterson J., 1979, ApJ, 234, 978

Patterson J., 1984, ApJS, 54, 443

Patterson J., 1994, PASP, 106, 209

Patterson J., 1998, PASP, 110, 1132

Patterson J., Raymond J. C., 1985, ApJ, 292, 550

Patterson J., Williams G., Hiltner W. A., 1981, ApJ, 245, 618

Patterson J., et al., 2017, MNRAS, 466, 581

Pavelin P. E., Spencer R. E., Davis R. J., 1994, MNRAS, 269, 779

Pavlenko E. P., et al., 2018, MNRAS, 479, 341

Pelisoli I., et al., 2022, MNRAS, 509, L31

Perryman M. A. C., Cropper M., Ramsay G., Favata F., Peacock A., Rando N., Reynolds A., 2001, MNRAS, 324, 899

Pfeffermann E., et al., 1987, in Proc. SPIE. p. 519

Piirola V., Reiz A., Coyne G. V., 1987, Ap&SS, 130, 203

Piirola V., Coyne G. V., Takalo S. J., Takalo L., Larsson S., Vilhu O., 1994, A&A, 283, 163

Pillepich A., Porciani C., Reiprich T. H., 2012, MNRAS, 422, 44

Pletsch H. J., Clark C. J., 2015, ApJ, 807, 18

Politano M., 1996, ApJ, 465, 338

Potter S. B., 1998, PhD thesis, Mullard Space Science Laboratory, University College London, Holmbury St. Mary, Dorking, Surrey RH5 6NT, UK

Potter S. B., 2000, MNRAS, 314, 672

Potter S. B., 2016, in Boffin H. M. J., Hussain G., Berger J.-P., Schmidtobreick L., eds, Astrophysics and Space Science Library, Vol. 439, Astronomy at High Angular Resolution. p. 179, doi:10.1007/978-3-319-39739-9_10

Potter S. B., Buckley D. A. H., 2018, MNRAS, 481, 2384

Potter S. B., Cropper M., Mason K. O., Hough J. H., Bailey J. A., 1997, MNRAS, 285, 82

Potter S. B., Hakala P. J., Cropper M., 1998, MNRAS, 297, 1261

Potter S. B., Cropper M., Hakala P. J., 2000, MNRAS, 315, 423

Potter S., Ramsay G., Wu K., Cropper M., 2002, in Gänsicke B. T., Beuermann K., Reinsch K., eds, Astronomical Society of the Pacific Conference Series Vol. 261, The Physics of Cataclysmic Variables and Related Objects. p. 165

Potter S. B., Romero-Colmenero E., Watson C. A., Buckley D. A. H., Phillips A., 2004, MNRAS, 348, 316

Potter S. B., Augusteijn T., Tappert C., 2005, MNRAS, 364, 565

Potter S. B., O'Donoghue D., Romero-Colmenero E., Buckley D. A. H., Woudt P. A., Warner B., 2006, MNRAS, 371, 727

Potter S. B., et al., 2010, MNRAS, 402, 1161

Potter S. B., et al., 2011, MNRAS, 416, 2202

Potter S., Kotze E., McBride V., 2015, in Buckley D. A. H., Schroeder A., eds, SALT Science Conference 2015 (SSC2015). Proceedings of Science. p. 51

Potter S. B., et al., 2016, in Evans C. J., Simard L., Takami H., eds, Society of Photo-Optical Instrumentation Engineers (SPIE) Conference Series Vol. 9908, Proc. SPIE. p. 99082K, doi:10.1117/12.2232391

Predehl P., et al., 2010, in Arnaud M., Murray S. S., Takahashi T., eds, Society of Photo-Optical Instrumentation Engineers (SPIE) Conference Series Vol. 7732, Space Telescopes and Instrumentation 2010: Ultraviolet to Gamma Ray. p. 77320U (arXiv:1001.2502), doi:10.1117/12.856577

Pretorius M. L., Knigge C., O'Donoghue D., Henry J. P., Gioia I. M., Mullis C. R., 2007, MNRAS, 382, 1279

Pretorius M. L., Knigge C., Schwope A. D., 2013, MNRAS, 432, 570

Pretorius M. L., et al., 2021, MNRAS, 503, 3692

Prialnik D., Shara M. M., 1986, ApJ, 311, 172

Priedhorsky W., Marshall F. J., Hearn D. R., 1987, A&A, 173, 95

Pulley D., Faillace G., Smith D., Watkins A., von Harrach S., 2018, A&A, 611, A48

Qian S. B., et al., 2009a, ApJ, 695, L163

Qian S.-B., Dai Z.-B., Liao W.-P., Zhu L.-Y., Liu L., Zhao E. G., 2009b, ApJ, 706, L96

Qian S.-B., Liao W.-P., Zhu L.-Y., Dai Z.-B., 2010, ApJ, 708, L66

Qian S.-B., et al., 2011, MNRAS, 414, L16

Qian S. B., Zhu L. Y., Dai Z. B., Fernández-Lajús E., Xiang F. Y., He J. J., 2012, ApJ, 745, L23

Qian S. B., et al., 2013, MNRAS, 436, 1408

Raman G., Paul B., 2017, New Astronomy, 54, 122

Ramsay G., 1994, Information Bulletin on Variable Stars, 4075

Ramsay G., Cropper M., 2002, MNRAS, 335, 918

Ramsay G., Cropper M., 2004a, in Vrielmann S., Cropper M., eds, Astronomical Society of the Pacific Conference Series Vol. 315, IAU Colloq. 190: Magnetic Cataclysmic Variables. p. 106 (arXiv:astro-ph/0301609)

Ramsay G., Cropper M., 2004b, MNRAS, 347, 497

Ramsay G., Wheatley P. J., 1998, MNRAS, 301, 95

Ramsay G., Rosen S. R., Mason K. O., Cropper M. S., Watson M. G., 1993, MNRAS, 262, 993

Ramsay G., Mason K. O., Cropper M., Watson M. G., Clayton K. L., 1994, MNRAS, 270, 692

Ramsay G., Cropper M., Mason K. O., 1996a, MNRAS, 278, 285

Ramsay G., Cropper M., Wu K., Potter S., 1996b, MNRAS, 282, 726

Ramsay G., Cropper M., Wu K., Mason K. O., Córdova F. A., Priedhorsky W., 2004, MNRAS, 350, 1373

Ramsay G., et al., 2007, in Napiwotzki R., Burleigh M. R., eds, Astronomical Society of the Pacific Conference Series Vol. 372, 15th European Workshop on White Dwarfs. p. 425 (arXiv:astro-ph/0610357)

Ramsay G., Rosen S., Hakala P., Barclay T., 2009, MNRAS, 395, 416

Rando N., et al., 2010, in Arnaud M., Murray S. S., Takahashi T., eds, Society of Photo-Optical Instrumentation Engineers (SPIE) Conference Series Vol. 7732, Space Telescopes and Instrumentation 2010: Ultraviolet to Gamma Ray. p. 77321C, doi:10.1117/12.856825

Rappaport S., Joss P. C., Webbink R. F., 1982, ApJ, 254, 616

Rappaport S., Verbunt F., Joss P. C., 1983, ApJ, 275, 713

Raymond J. C., Black J. H., Davis R. J., Dupree A. K., Gursky H., Hartmann L., Matilsky T. A., 1979, ApJ, 230, L95

Rea N., et al., 2017, MNRAS, 471, 2902

Regős E., Tout C. A., 1995, MNRAS, 273, 146

Reimers D., Hagen H. J., 2000, A&A, 358, L45

Reimers D., Hagen H. J., Hopp U., 1999, A&A, 343, 157

Richards M. T., Albright G. E., Bowles L. M., 1994, in American Astronomical Society Meeting Abstracts. p. 21.09

Richardson W. H., 1972, Journal of the Optical Society of America (1917-1983), 62, 55

Ritter H., 2010, Mem. Soc. Astron. Italiana, 81, 849

Ritter H., 2012, Mem. Soc. Astron. Italiana, 83, 505

Ritter H., Kolb U., 2003, A&A, 404, 301

Robinson E. L., Nather R. E., Kepler S. O., 1982, ApJ, 254, 646

Rodrigues C. V., Jablonski F. J., D'Amico F., Cieslinski D., Steiner J. E., Diaz M. P., Hickel G. R., 2006, MNRAS, 369, 1972

Romero-Colmenero E., Potter S. B., Buckley D. A. H., Barrett P. E., Vrielmann S., 2003, MNRAS, 339, 685

Rosen S. R., et al., 2001, MNRAS, 322, 631

Rosen S. R., et al., 2016, A&A, 590, A1

Rothschild R. E., et al., 1981, ApJ, 250, 723

Rousseau T., Fischer A., Beuermann K., Woelk U., 1996, A&A, 310, 526

Rowland S. W., 1979, Computer implementation of image reconstruction formulas. p. 9, doi:10.1007/3-540-09417-2_2

Russell T. D., et al., 2016, MNRAS, 460, 3720

Rutten R. G. M., Dhillon V. S., 1994, A&A, 288, 773

Sambruna R. M., Chiappetti L., Treves A., Bonnet-Bidaud J. M., Bouchet P., Maraschi L., Motch C., Mouchet M., 1991, ApJ, 374, 744

Sambruna R. M., Parmer A. N., Chiappetti L., Maraschi L., Treves A., 1994, ApJ, 424, 947

Sarty G. E., Wu K., 2006, PASA, 23, 106

Savitzky A., Golay M. J. E., 1964, Analytical Chemistry, 36, 1627

Schachter J., Filippenko A. V., Kahn S. M., Paerels F. B. S., 1991, ApJ, 373, 633

Schaefer B. E., 2011, ApJ, 742, 112

Schaefer B. E., 2020, MNRAS, 492, 3323

Schmidt G. D., 2004, in Vrielmann S., Cropper M., eds, Astronomical Society of the Pacific Conference Series Vol. 315, IAU Colloq. 190: Magnetic Cataclysmic Variables. p. 22

Schmidt G. D., Stockman H. S., Margon B., 1981, ApJ, 243, L157

Schmidt G. D., Stockman H. S., Grandi S. A., 1983, ApJ, 271, 735

Schmidt G. D., Szkody P., Smith P. S., Silber A., Tovmassian G., Hoard D. W., Gänsicke B. T., de Martino D., 1996, ApJ, 473, 483

Schmidt G. D., Ferrario L., Wickramasinghe D. T., Smith P. S., 2001, ApJ, 553, 823

Schreiber M. R., et al., 2010, A&A, 513, L7

Schwarz R., Greiner J., Tovmassian G. H., Zharikov S. V., Wenzel W., 2002, A&A, 392, 505

Schwarz R., Schwope A. D., Staude A., Remillard R. A., 2005, A&A, 444, 213

Schwarz R., Schwope A. D., Staude A., Rau A., Hasinger G., Urrutia T., Motch C., 2007, A&A, 473, 511

Schwarz R., Haghighipour N., Eggl S., Pilat-Lohinger E., Funk B., 2011, MNRAS, 414, 2763

Schwope A. D., 1990, Reviews in Modern Astronomy, 3, 44

Schwope A. D., 1995, Reviews in Modern Astronomy, 8, 125

Schwope A., 2001, in Boffin H. M. J., Steeghs D., Cuypers J., eds, Lecture Notes in Physics, Berlin Springer Verlag Vol. 573, Astrotomography, Indirect Imaging Methods in Observational Astronomy. p. 127

Schwope A. D., 2018, A&A, 619, A62

Schwope A. D., Beuermann K., 1990, A&A, 238, 173

Schwope A. D., Beuermann K., 1997, Astronomische Nachrichten, 318, 111

Schwope A. D., Mengel S., 1997, Astronomische Nachrichten, 318, 25

Schwope A. D., Thinius B. D., 2018, Astronomische Nachrichten, 339, 540

Schwope A. D., Thinius B. D., 2020, Astronomische Nachrichten, 341, 424

Schwope A. D., Beuermann K., Thomas H.-C., 1990, A&A, 230, 120

Schwope A. D., Beuermann K., Jordan S., Thomas H. C., 1993, A&A, 278, 487

Schwope A. D., Thomas H. C., Beuermann K., Burwitz V., Jordan S., Haefner R., 1995a, A&A, 293, 764

Schwope A. D., Beuermann K., Jordan S., 1995b, A&A, 301, 447

Schwope A. D., Mantel K. H., Horne K., 1997a, A&A, 319, 894

Schwope A. D., Mengel S., Beuermann K., 1997b, A&A, 320, 181

Schwope A. D., Schwarz R., Staude A., Heerlein C., Horne K., Steeghs D., 1999, in Hellier C., Mukai K., eds, Astronomical Society of the Pacific Conference Series Vol. 157, Annapolis Workshop on Magnetic Cataclysmic Variables. p. 71 (arXiv:astro-ph/9810061)

Schwope A. D., Catalán M. S., Beuermann K., Metzner A., Smith R. C., Steeghs D., 2000a, MNRAS, 313, 533

Schwope A., et al., 2000b, Astronomische Nachrichten, 321, 1

Schwope A. D., Schwarz R., Sirk M., Howell S. B., 2001, A&A, 375, 419

Schwope A. D., Schreiber M. R., Szkody P., 2006, A&A, 452, 955

Schwope A. D., Horne K., Steeghs D., Still M., 2011, A&A, 531, A34

Schwope A. D., Worpel H., Webb N. A., Koliopanos F., Guillot S., 2020a, A&A, 637, A35

Schwope A. D., Worpel H., Traulsen I., Sablowski D., 2020b, A&A, 642, A134

Schwope A., Buckley D. A. H., Malyali A., Potter S., König O., Arcodia R., Gromadzki M., Rau A., 2022, A&A, 661, A43

Sebring T. A., Ramsey L. W., 1997, Hobby-Eberly Telescope: a progress report. pp 32–37, doi:10.1117/12.269069

Seibert M., et al., 2012, in American Astronomical Society Meeting Abstracts #219. p. 340.01

Shafter A. W., Reinsch K., Beuermann K., Misselt K. A., Buckley D. A. H., Burwitz V., Schwope A. D., 1995, ApJ, 443, 319

Shappee B. J., et al., 2014, ApJ, 788, 48

Shara M. M., 1989, PASP, 101, 5

Shara M. M., Livio M., Moffat A. F. J., Orio M., 1986, ApJ, 311, 163

Šimon V., 2016, MNRAS, 463, 1342

Singh K. P., et al., 2014, in Space Telescopes and Instrumentation 2014: Ultraviolet to Gamma Ray. p. 91441S, doi:10.1117/12.2062667

Sirk M. M., Warren J. K., Vallerga J. V., Christian C. A., 1994, in Bulletin of the American Astronomical Society. p. 793

Skilling J., Bryan R. K., 1984, MNRAS, 211, 111

Smak J., 1971, AcA, 21, 467

Smak J., 1984, AcA, 34, 161

Smith M. A., 1979, PASP, 91, 737

Smith D. A., Dhillon V. S., 1998, MNRAS, 301, 767

Song S., Mai X., Mutel R. L., Pulley D., Faillace G., Watkins A., 2019, AJ, 157, 184

Souza S. P., Babcock B. A., Pasachoff J. M., Gulbis A. A. S., Elliot J. L., Person M. J., Gangestad J. W., 2006, PASP, 118, 1550

Spencer R. E., Swinney R. W., Johnston K. J., Hjellming R. M., 1986, ApJ, 309, 694

Spruit H. C., 1994, A&A, 289, 441

Spruit H. C., 1998, astro-ph/9806141,

Spruit H. C., Ritter H., 1983, A&A, 124, 267

Staude A., Schwope A. D., Hedelt P., Rau A., Schwarz R., 2004, in Vrielmann S., Cropper M., eds, Astronomical Society of the Pacific Conference Series Vol. 315, IAU Colloq. 190: Magnetic Cataclysmic Variables. p. 251

Steeghs D., 2003, MNRAS, 344, 448

Steeghs D., Harlaftis E. T., Horne K., 1997, MNRAS, 290, L28

Still M., Mukai K., 2001, ApJ, 562, L71

Stockman H. S., 1977, ApJ, 218, L57

Stockman H. S., Schmidt G. D., 1996, ApJ, 468, 883

Stockman H. S., Schmidt G. D., Angel J. R. P., Liebert J., Tapia S., Beaver E. A., 1977, ApJ, 217, 815

Stratton F. J. M., 1934, Nature, 134, 974

Subebekova G., Zharikov S., Tovmassian G., Neustroev V., Wolf M., Hernandez M. S., Kučáková H., Khokhlov S., 2020, MNRAS, 497, 1475

Swank J., et al. 2010, Gravity and Extreme Magnetism SMEX (GEMS). p. 251, doi:10.1017/CBO9780511750809.038

Swinbanks D., 1987, Nature, 326, 322

Szkody P., Bailey J. A., Hough J. H., 1983, MNRAS, 203, 749

Szkody P., Vennes S., Wagner R. M., Hastings C., 1999, in Hellier C., Mukai K., eds, Astronomical Society of the Pacific Conference Series Vol. 157, Annapolis Workshop on Magnetic Cataclysmic Variables. p. 195

Szkody P., et al., 2002, AJ, 123, 430

Szkody P., et al., 2003, ApJ, 583, 902

Takahashi T., et al., 2010, in Space Telescopes and Instrumentation 2010: Ultraviolet to Gamma Ray. p. 77320Z (arXiv:1010.4972), doi:10.1117/12.857875

Takahashi T., et al., 2012, in Space Telescopes and Instrumentation 2012: Ultraviolet to Gamma Ray. p. 84431Z (arXiv:1210.4378), doi:10.1117/12.926190

Takahashi T., et al., 2014, in Space Telescopes and Instrumentation 2014: Ultraviolet to Gamma Ray. p. 914425 (arXiv:1412.1356), doi:10.1117/12.2055681

Tamor S., 1978, Nuclear Fusion, 18, 229

Tanaka Y., Inoue H., Holt S. S., 1994, PASJ, 46, L37

Tapia S., 1977a, ApJ, 212, L125

Tapia S., 1977b, IAU Circ., 3054, 1

Tasse C., et al., 2018, A&A, 611, A87

Taylor B. G., Andresen R. D., Peacock A., Zobl R., 1981, Space Sci. Rev., 30, 479

Thomas H. C., Beuermann K., 1998, in Breitschwerdt D., Freyberg M. J., Truemper J., eds, Lecture Notes in Physics, Springer Berlin Heidelberg Vol. 506, IAU Colloq. 166: The Local Bubble and Beyond. pp 247–250, doi:10.1007/BFb0104728

Thomas H. C., Beuermann K., Schwope A. D., Burwitz V., 1996, A&A, 313, 833

Thomas H. C., Beuermann K., Reinsch K., Schwope A. D., Truemper J., Voges W., 1998, A&A, 335, 467

Thomas H. C., Beuermann K., Burwitz V., Reinsch K., Schwope A. D., 2000, A&A, 353, 646

Thomas H. C., Beuermann K., Reinsch K., Schwope A. D., Burwitz V., 2012, A&A, 546, A104

Thompson A. M., Cawthorne T. V., 1987, MNRAS, 224, 425

Thorstensen J. R., 2020a, AJ, 160, 6

Thorstensen J. R., 2020b, AJ, 160, 151

Thorstensen J. R., Lépine S., Shara M., 2006, PASP, 118, 1238

Thorstensen J. R., Motsoaledi M., Woudt P. A., Buckley D. A. H., Warner B., 2020, AJ, 160, 70

Tody D., 1986, in Crawford D. L., ed., Society of Photo-Optical Instrumentation Engineers (SPIE) Conference Series Vol. 627, Instrumentation in astronomy VI. p. 733, doi:10.1117/12.968154

Tovmassian G., et al., 2017, A&A, 608, A36

Traulsen I., Reinsch K., Schwarz R., Dreizler S., Beuermann K., Schwope A. D., Burwitz V., 2010, A&A, 516, A76

Traulsen I., Reinsch K., Schwope A. D., Burwitz V., Dreizler S., Schwarz R., Walter F. M., 2011, A&A, 529, A116

Traulsen I., Reinsch K., Schwope A. D., Schwarz R., Walter F. M., Burwitz V., 2014, A&A, 562, A42

Treumann R. A., 2006, A&A Rev., 13, 229

Truemper J., 1982, Advances in Space Research, 2, 241

Turner K. C., 1985, in Hjellming R. M., Gibson D. M., eds, Astrophysics and Space Science Library Vol. 116, Radio Stars. p. 283, doi:10.1007/978-94-009-5420-5_41

Tutar D., Rennan Pekünlü E., 2013, New Astronomy, 19, 42

Udalski A., Kubiak M., Szymanski M., Kaluzny J., Mateo M., Krzeminski W., 1994, AcA, 44, 317

Vaeth H. M., Chanmugam G., 1995, ApJS, 98, 295

Vanderbosch Z. P., Clemens J. C., Dunlap B. H., Winget D. E., 2017, in Tremblay P. E., Gaensicke B., Marsh T., eds, Astronomical Society of the Pacific Conference Series Vol. 509, 20th European White Dwarf Workshop. pp 571–574

van Gend C., Lombaard B., Sickafoose A., Whittal H., 2016, The South African Astronomical Observatory instrumentation software architecture and the SHOC instruments. p. 99130R, doi:10.1117/12.2231403

van der Heyden K. J., Potter S. B., Buckley D. A. H., 2002, MNRAS, 333, 241

Vennes S., Szkody P., Sion E. M., Long K. S., 1995, ApJ, 445, 921

Verbunt F., 1984, MNRAS, 209, 227

Verbunt F., Zwaan C., 1981, A&A, 100, L7

Visvanathan N., Wickramasinghe D. T., 1979, Nature, 281, 47

Voges W., et al., 1999, A&A, 349, 389

Vogt N., Krzeminski W., Sterken C., 1980, A&A, 85, 106

Völschow M., Schleicher D. R. G., Perdelwitz V., Banerjee R., 2016, A&A, 587, A34

Völschow M., Schleicher D. R. G., Banerjee R., Schmitt J. H. M. M., 2018, A&A, 620, A42

Vreeswijk P., Paterson K., 2021, ZOGY: Python implementation of proper image subtraction (ascl:2105.010)

Vrielmann S., Schwope A. D., 2001, MNRAS, 322, 269

Walker M. F., 1956, ApJ, 123, 68

Wang Q.-S., Qian S.-B., Han Z.-T., Zejda M., Fernández-Lajus E., Zhu L.-Y., 2018, Research in Astronomy and Astrophysics, 18, 075

Warner B., 1988, Nature, 336, 129

Warner B., 1995a, Cambridge Astrophysics Series, 28

Warner B., 1995b, Ap&SS, 232, 89

Warner B., 2002, in Hernanz M., José J., eds, American Institute of Physics Conference Series Vol. 637, Classical Nova Explosions. pp 3–15 (arXiv:astro-ph/0206452), doi:10.1063/1.1518170

Warner B., McGraw J. T., 1981, MNRAS, 196, 59P

Warner B., Nather R. E., 1972, MNRAS, 156, 305

Warren J. K., Vallerga J. V., Mauche C. W., Mukai K., Siegmund O. H. W., 1993, in American Astronomical Society Meeting Abstracts #182. p. 861

Warren J. K., Sirk M. M., Vallerga J. V., 1995, ApJ, 445, 909

Watson M. G., King A. R., Osborne J., 1985, MNRAS, 212, 917

Watson M. G., King A. R., Jones M. H., Motch C., 1989, MNRAS, 237, 299

Webbink R. F., 1985, in Pringle J. E., Wade R. A., eds, Cambridge University Press, Vol. 6, Interacting Binary Stars. p. 39

Weisskopf M. C., 1999, arXiv e-prints, pp astro–ph/9912097

Weisskopf M. C., Tananbaum H. D., Van Speybroeck L. P., O'Dell S. L., 2000, in Truemper J. E., Aschenbach B., eds, Society of Photo-Optical Instrumentation Engineers (SPIE) Conference Series Vol. 4012, X-Ray Optics, Instruments, and Missions III. pp 2–16 (arXiv:astro-ph/0004127), doi:10.1117/12.391545

Wickramasinghe D. T., 1988, in Coyne G. V., Magalhaes A. M., Moffat A. F., Schulte-Ladbeck R. E., Tapia S., eds, Vatican City State: Vatican Observatory, Polarized Radiation of Circumstellar Origin. pp 199–236

Wickramasinghe D. T., Ferrario L., 1988, ApJ, 327, 222

Wickramasinghe D. T., Ferrario L., 1995, in Buckley D. A. H., Warner B., eds, Astronomical Society of the Pacific Conference Series Vol. 85, Magnetic Cataclysmic Variables. p. 43

Wickramasinghe D. T., Ferrario L., 2000a, New Astronomy Reviews, 44, 69

Wickramasinghe D. T., Ferrario L., 2000b, PASP, 112, 873

Wickramasinghe D. T., Martin B., 1985, MNRAS, 212, 353

Wickramasinghe D. T., Meggitt S. M. A., 1982, MNRAS, 198, 975

Wickramasinghe D. T., Meggitt S. M. A., 1985, MNRAS, 214, 605

Wickramasinghe D. T., Visvanathan N., Tuohy I. R., 1984, ApJ, 286, 328

Wickramasinghe D. T., Tuohy I. R., Visvanathan N., 1987, ApJ, 318, 326

Wickramasinghe D. T., Ferrario L., Bailey J., 1989, ApJ, 342, L35

Wickramasinghe D. T., Cropper M., Mason K. O., Garlick M., 1991, MNRAS, 250, 692

Wiehahn M., Potter S. B., Warner B., Woudt P. A., 2004, MNRAS, 355, 689

Willes A. J., Wu K., 2004, MNRAS, 348, 285

Willes A. J., Wu K., Kuncic Z., 2004, PASA, 21, 248

Williams G., 1983, ApJS, 53, 523

Williams G. A., 1991, AJ, 101, 1929

Winkler C., et al., 2003, A&A, 411, L1

Wittenmyer R. A., Horner J., Marshall J. P., Butters O. W., Tinney C. G., 2012, MNRAS, 419, 3258

Woelk U., Beuermann K., 1992, A&A, 256, 498

Wolf C., et al., 2018, PASA, 35, e010

Wolff M. T., Ray P. S., Wood K. S., Hertz P. L., 2009, ApJS, 183, 156

Woods T. E., Gilfanov M., 2013, MNRAS, 432, 1640

Worpel H., Schwope A. D., 2015, A&A, 583, A130

Worpel H., Schwope A. D., Granzer T., Reinsch K., Schwarz R., Traulsen I., 2016, A&A, 592, A114

Worpel H., Schwope A. D., Traulsen I., Mukai K., Ok S., 2020, A&A, 639, A17

Wright A. E., Cropper M., Stewart R. T., Nelson G. J., Slee O. B., 1988, MNRAS, 231, 319

Wu K., Kiss L. L., 2008, A&A, 481, 433

Wu K., Chanmugam G., Shaviv G., 1994, ApJ, 426, 664

Wu K., Cropper M., Ramsay G., Sekiguchi K., 2002, MNRAS, 331, 221

York D. G., et al., 2000, AJ, 120, 1579

Zackay B., Ofek E. O., Gal-Yam A., 2016, ApJ, 830, 27

Zaire B., Donati J. F., Klein B., 2021, MNRAS, 504, 1969

Zorotovic M., Schreiber M. R., 2013, A&A, 549, A95

Zorotovic M., Schreiber M. R., 2020, Advances in Space Research, 66, 1080

Zorotovic M., Schreiber M. R., Gänsicke B. T., 2011, A&A, 536, A42

Zorotovic M., et al., 2016, MNRAS, 457, 3867